CORA Cork Open Research Archive
Cartlann Taighde Oscailte Chorcaí

Title	Experimental quantification and modelling of attrition of infant formulae during pneumatic conveying
Authors	Hanley, Kevin John
Publication date	2011-08
Original Citation	Hanley, K.J. 2011. Experimental quantification and modelling of attrition of infant formulae during pneumatic conveying. PhD Thesis, University College Cork.
Type of publication	Doctoral thesis
Link to publisher's version	http://library.ucc.ie/record=b2027885~S0
Rights	© 2011, Kevin J. Hanley - http://creativecommons.org/licenses/by-nc-nd/3.0/
Download date	2024-04-16 13:17:38
Item downloaded from	https://hdl.handle.net/10468/381

UCC
University College Cork, Ireland
Coláiste na hOllscoile Corcaigh

Experimental Quantification and Modelling of Attrition of Infant Formulae during Pneumatic Conveying

A thesis presented to the National University of Ireland, Cork, in partial fulfilment of the requirements for the degree of Doctor of Philosophy

Author
Kevin John Hanley

Supervisors
Dr Edmond P. Byrne
Dr Kevin Cronin

August 2011

Department of Process and Chemical Engineering · Head: Dr Jorge Oliveira
University College Cork
Ireland

Table of Contents

Table of Contents i

Declaration vi

Abstract vii

Acknowledgements viii

List of Figures x

List of Tables xviii

List of Publications xxii

Nomenclature and Abbreviations xxiv

1 Introduction to Infant Formula 1

1.1 Infant Formula Composition and Legislative Framework 1

1.2 Overview of the Global Infant Formula Market 6

1.3 Significance of Infant Formula for Ireland 7

1.4 Infant Formula Manufacture 9

1.4.1 Overview of Manufacturing Processes 9

1.4.2 Conveying of Infant Formula within a Plant 9

1.5 Infant Formula Microstructure 13

1.5.1 SEM Images 14

1.6 Importance of Infant Formula Breakage 17

1.7 Research Motivation and Objectives 18

1.8 Thesis Structure 19

2 Effect of Pneumatic Conveying Parameters on Physical Quality Characteristics of Infant Formula 21

2.1 Introduction to the Taguchi Method 22

2.1.1 Orthogonal Arrays, Factors, Levels and Responses 23

2.1.2 Analysis of Variance (ANOVA) 25

2.1.3 Advantages and Disadvantages of the Taguchi Method 28
2.2 Materials and Methods 29
2.2.1 Raw Materials and Pneumatic Conveying Rig 29
2.2.2 Experimental Design 31
2.2.3 Product Quality Characteristics and Experimental Procedure . . . 32
2.2.4 Analytical Procedure 34
2.3 Results and Discussion 36
2.3.1 Categorical ANOVA 36
2.3.2 Polynomial Models 43
2.4 Conclusions of Chapter 2 46

3 Effect of Composition on the Mechanical Response of Agglomerates of Infant Formulae 48
3.1 Materials and Methods 49
3.1.1 Infant Formulae 49
3.1.2 Pneumatic Conveying Experiments 50
3.1.3 Measured Product Quality Characteristics and Experimental Procedure 51
3.1.4 Calculation of Relative Breakage 53
3.1.5 Texture Analysis and Compression Methodology 55
3.1.6 Uniaxial Compression Responses 57
3.1.7 Drop Tests using High-Speed Camera 58
3.2 Results and Discussion 60
3.2.1 Pneumatic Conveying Results 60
3.2.2 Results of Uniaxial Compression Tests 64
3.2.3 Drop Test Results 70
3.3 Conclusions of Chapter 3 72

4 Calibration of Discrete Element Models of Bonded Agglomerates using Taguchi Methods 74
4.1 Introduction to Discrete Element Modelling 74
4.1.1 Algorithm 75
4.1.2 DEM Particle Shape 76
4.1.3 Agglomerate Bonds and Contact Models 77
4.1.4 Agglomerate Structure Formation 78
4.2 Current Approaches to Calibration 80
4.3 DEM Simulations 81
4.3.1 Agglomerate Formation 82
4.3.2 Particle Crushing Conditions 82
4.3.3 Agglomerate Bonds and Contact Models 83

4.4 Experimental Designs 83
4.4.1 Experimental Design for Two-Dimensional Simulations 84
4.4.2 Experimental Design for Three-Dimensional Simulations 85
4.5 Simulation Responses 86
4.6 Analytical Procedure 87
4.7 Results and Discussion 89
4.7.1 Results of Two-Dimensional Simulations 89
4.7.2 Results of Three-Dimensional Simulations 94
4.7.3 Discussion 98
4.8 Conclusions of Chapter 4 100

5 Discrete Element Modelling of Agglomerates of Infant Formula 101
5.1 Physical Characterisation of the Agglomerates 102
5.1.1 Agglomerate Dimensions 103
5.1.2 SEM Characterisation of Microstructure 104
5.1.3 Experimental Impact Tests using High-Speed Camera 106
5.2 Discrete Element Modelling of Uniaxial Compression 109
5.2.1 Agglomerate Structure and Crushing Conditions 109
5.2.2 DEM Calibration 110
5.2.3 Model Sensitivity to Small Perturbations 111
5.2.4 Density Scaling 112
5.3 Comparison of DEM and Experimental Results 114
5.3.1 Probability Histograms and Density Functions 114
5.3.2 Correlation Tests of DEM Responses 116
5.3.3 Weibull Analysis 118
5.4 Additional DEM Results for Quasi-Static Loading 120
5.4.1 Characterisation of the Mechanical Response using Energy 120
5.4.2 Mode of Failure of the Agglomerates 123
5.5 DEM Simulations of Dynamic Loading 135
5.5.1 Drop Tests at 1.9 $\mathrm{m\,s^{-1}}$ 136
5.5.2 Impact Tests at 10.1 $\mathrm{m\,s^{-1}}$ 141
5.5.3 Assessment of Applicability 145
5.6 Conclusions of Chapter 5 147

6 Probabilistic Modelling of Pneumatic Conveying 149
6.1 Model Development 150
6.1.1 Assumptions 150
6.1.2 Statistics of Fluid Velocity 152
6.1.3 Statistics of Effective (Particle-Averaged) Fluid Velocity 153
6.1.4 Particle Velocity 156

6.1.5 Effective Fluid Velocity as a Random Process . . . 157
6.1.6 Statistics of Particle Velocity . . . 160
6.1.7 Autocorrelation Parameter of Effective Fluid Velocity . . . 161
6.1.8 Inter-Particle Collision Velocity Statistics . . . 164
6.1.9 Pipe Bend Collision Velocity Statistics . . . 164
6.1.10 Impact Angle Statistics . . . 166
6.1.11 Particle Impact Force Statistics . . . 168
6.1.12 Particle Strength Statistics . . . 170
6.2 Materials and Methods . . . 170
6.2.1 Model Infant Formula Particles . . . 170
6.2.2 Conveying System Geometry and Flow Conditions . . . 172
6.2.3 Determination of Weibull Parameters . . . 174
6.2.4 Monte Carlo Approach for Model Application . . . 176
6.3 Results and Discussion . . . 177
6.3.1 Effective Fluid and Particle Velocities . . . 177
6.3.2 Impact Angles and Normal Impact Velocities . . . 181
6.3.3 Impact Forces and Agglomerate Breakage Statistics . . . 183
6.3.4 Advantage of Theoretical Predictive Equations . . . 185
6.3.5 Verification of Key Model Assumptions . . . 187
6.4 Conclusions of Chapter 6 . . . 189

7 Closing Discussion and Final Conclusions **190**

References **194**

Appendices **211**
Appendix A: Orthogonal Arrays and Triangular Tables . . . 211
A.1 Orthogonal Arrays . . . 211
A.2 Triangular Tables . . . 226
Appendix B: Probability Histograms for Agglomerate Compression Experiments of Infant Formulae . . . 233
B.1 Force at Failure Histograms . . . 234
B.2 Strain at Failure Histograms . . . 236
B.3 Agglomerate Stiffness Histograms . . . 238
Appendix C: Supplementary Information on the Formation of DEM Agglomerates by Sequential Addition . . . 240
C.1 Annotated MATLAB Code . . . 244
Appendix D: Correlations of Compression Responses and Physical Characteristics of the Agglomerates . . . 252
D.1 Measured and Calculated Agglomerate Characteristics . . . 253

D.2 Correlation Results and Discussion 257
Appendix E: Convexities of Simulated Agglomerates before Mechanical Loading 260
E.1 Annotated MATLAB Code 264
E.2 Convexity Results 267
Appendix F: Illustration of DEM Calibration Difficulties in Chapter 5 269
Appendix G: Mathematical Derivations for Probabilistic Model of Pneumatic Conveying 273
G.1 Probability Density Function of Fluid Velocity 273
G.2 Derivation of Mean Fluid Velocity 274
G.3 Derivation of Variance in Fluid Velocity 276
G.4 Derivation of Effective Fluid Velocity 277
G.5 Probability Density Function of Effective Fluid Velocity 279
G.6 Proof that Effective Fluid Velocity Tends to Fluid Velocity for Infinitesimal Particles 280
G.7 Outline Derivation of Mean and Variance of Particle Velocity 281
G.8 Mean Fall Height and Velocity of Particle 281
G.9 Probability Density Function of Impact Angle 283
G.10 Derivations for Kelvin-Voigt Model 284

Declaration

The work presented in this dissertation was carried out primarily in the Department of Process and Chemical Engineering at University College Cork from October 2008. I certify that this thesis is the result of my own work and any quotation from, or description of, the work of other persons is acknowledged herein by reference to the sources. I have exercised reasonable care to ensure that the work is original and does not breach any law of copyright. This thesis has not been submitted for any other degrees, either at University College Cork or elsewhere.

_____

Kevin Hanley

3rd August 2011

Abstract

Infant formula is often produced as an agglomerated powder using a spray drying process. Pneumatic conveying is commonly used for transporting this product within a manufacturing plant. The transient mechanical loads imposed by this process cause some of the agglomerates to disintegrate, which has implications for key quality characteristics of the formula including bulk density and wettability. This thesis used both experimental and modelling approaches to investigate this breakage during conveying.

One set of conveying trials had the objective of establishing relationships between the geometry and operating conditions of the conveying system and the resulting changes in bulk properties of the infant formula upon conveying. A modular stainless steel pneumatic conveying rig was constructed for these trials. The mode of conveying and air velocity had a statistically-significant effect on bulk density at a 95% level, while mode of conveying was the only factor which significantly influenced D[4,3] or wettability. A separate set of conveying experiments investigated the effect of infant formula composition, rather than the pneumatic conveying parameters, and also assessed the relationships between the mechanical responses of individual agglomerates of four infant formulae and their compositions. The bulk densities before conveying, and the forces and strains at failure of individual agglomerates, were related to the protein content. The force at failure and stiffness of individual agglomerates were strongly correlated, and generally increased with increasing protein to fat ratio while the strain at failure decreased.

Two models of breakage were developed at different scales; the first was a detailed discrete element model of a single agglomerate. This was calibrated using a novel approach based on Taguchi methods which was shown to have considerable advantages over basic parameter studies which are widely used. The data obtained using this model compared well to experimental results for quasi-static uniaxial compression of individual agglomerates. The model also gave adequate results for dynamic loading simulations. A probabilistic model of pneumatic conveying was also developed; this was suitable for predicting breakage in large populations of agglomerates and was highly versatile: parts of the model could easily be substituted by the researcher according to their specific requirements.

Acknowledgements[†]

Initially, I must thank my supervisors in the Department of Process and Chemical Engineering, Dr Edmond Byrne and Dr Kevin Cronin. Without their support and assistance, this research would not have been possible. I consider myself fortunate to have had supervisors who were always available to provide assistance and advice, yet also allow me a significant degree of autonomy over the direction of my research.

Four other academics acted as advisors, all of whom contributed significantly to this research to the extent that they were listed as co-authors on papers arising from this work. Each advisor was involved with only a specific aspect of my research: Dr Mark Fenelon (Teagasc Food Research Centre, Moorepark, Fermoy) focused on the experimental conveying trials and measurement of physical characteristics of the infant formulae; Dr Jorge Oliveira (Department of Process and Chemical Engineering, UCC) helped to implement the Taguchi method in Chapter 2 of this thesis; Dr Séamus O'Mahony (School of Food and Nutritional Sciences, UCC) was involved with the compositions of the formulae and Dr Catherine O'Sullivan (Department of Civil and Environmental Engineering, Imperial College London) was invaluable for teaching me DEM and assisting with the simulations of individual agglomerates.

While the contributions of the people listed above have been recognised in terms of authorship credit on one or more academic papers, many others also helped me over the course of my three years as a postgraduate. The list of people at UCC that I wish to thank is particularly lengthy, which reflects the fact that I spent most of my time there. I would like to acknowledge the following academic staff: Dr John Fitzpatrick; technical staff: John Barrett, Paul Conway, Denis Ring and Tim Twomey; and administrative staff: Julie Holland and Anne-Marie McSweeney. I would like to collectively thank the other postgraduate students who are currently engaged in research in this department, and those who have since left after completing their research; in particular, I must single out Dr Darío Téllez-Medina for acknowledgement. At Moorepark, I must thank Dr Mark Auty, Bernard Corrigan and (especially) Dr Vivian Gee. At Imperial, John O'Donovan and Tom Shire introduced me to ParaView for which I am grateful. Thanks also to Dr Ignazio Cavarretta (University of Bristol, formerly Imperial) for his comments.

[†]Groups of contiguous names in this section are in alphabetical order.

A major manufacturer of infant formula was involved in my research as an industrial partner. This company supplied the infant formulae used in this research at no cost, which was very much appreciated.

Funding for this PhD was provided by the Irish Research Council for Science, Engineering and Technology (IRCSET) under the EMBARK initiative. This excellent scheme permitted me and many others to pursue postgraduate qualifications; without this financial support, the limited availability of other funding may have prevented me from conducting this research.

Finally, I would like to thank my parents for their support. This thesis is dedicated to them.

List of Figures

1.1 A flowchart showing the typical steps for infant formula production by a wet mixing/spray drying process 10
1.2 SEM micrograph of an agglomerate of infant formula B at a magnification of 150X 15
1.3 SEM micrograph of part of an agglomerate of infant formula B at a magnification of 500X 15
1.4 SEM micrograph of an agglomerate of the infant formula used for the pneumatic conveying trials described in Chapter 2 at a magnification of 400X 16
1.5 SEM micrograph at 1500X magnification showing extensive damage of an agglomerate following pneumatic conveying at a superficial air velocity of 20 $m s^{-1}$ 16

2.1 An isometric view of the conveying rig in dilute phase configuration, with an inset showing the modification for dense phase conveying 30
2.2 Line graphs showing the average percentage changes in a) bulk density, b) D[4,3] and c) wettability caused by pneumatic transport at velocities of 3, 4 or 5 $m s^{-1}$ in dense phase or 10, 20 or 30 $m s^{-1}$ in dilute phase 40
2.3 ANOVA contributions plot for S/N ratio responses 41
2.4 Stacked bar plot showing the distribution of the total sums of squares for the S/N ratio analysis as percentages allocated to each factor, interaction or error and the optimum level of each factor 42
2.5 Particle size distributions for infant formula samples before and after conveying using the optimum parameters 42
2.6 Plots of model predictions versus experimental results for four responses: a) bulk density, b) D[4,3], c) particle density and d) wettability 45
2.7 Pareto charts showing the standardised effects for each term in the fitted model for a) bulk density, b) D[4,3], c) particle density and d) wettability 46

3.1 Diagram showing the sieve stack used for isolating infant formula agglomerates in the 710–850 µm size range 50

3.2 An isometric view of the pneumatic conveying rig (modification of Figure 2.1 on p.30) . . . 51
3.3 Alternative presentations of the same particle size distributions for infant formula B before conveying and following pneumatic transport at 20 $m s^{-1}$ 53
3.4 Particle size distributions with shaded areas indicating a) the breakage potential, B_p, and b) the total breakage, B_t, according to the definitions of Hardin (1985) . . . 54
3.5 Configuration of the texture analyser used for agglomerate compression 56
3.6 Plots of force (N) versus displacement (10^{-4} m) for experimental compression of three agglomerates of infant formula B . . . 57
3.7 Four cropped frames extracted from the video of a drop test of one agglomerate . . . 59
3.8 Bar chart comparing the bulk density ($kg m^{-3}$) of infant formulae A–D before conveying, and following pneumatic transport through a rig of invariant configuration at 4 $m s^{-1}$, 10 $m s^{-1}$ and 20 $m s^{-1}$ . . . 60
3.9 As for Figure 3.8, except for volume mean diameter (µm) . . . 61
3.10 Plot of relative breakage against air velocity ($m s^{-1}$) . . . 62
3.11 As for Figure 3.8, except for wettability (s) . . . 62
3.12 As for Figure 3.8, except for Hausner ratio . . . 63
3.13 As for Figure 3.8, except for percentage surface free fat . . . 64
3.14 Probability density functions of lognormal distributions fitted to force at failure data (N) for the four infant formulae tested . . . 65
3.15 As for Figure 3.14, except for strain at failure data (%) . . . 65
3.16 As for Figure 3.14, except for agglomerate stiffness data ($N m^{-1}$) . . . 66
3.17 Scatter plot of agglomerate stiffness ($N m^{-1}$) against force at failure (N) for infant formula A . . . 70
3.18 Probability density functions of Weibull distributions fitted to coefficients of restitution of the four infant formulae tested . . . 71

4.1 Radius expansion for a 2D agglomerate containing 147 disks: a) shows the randomly-placed disks before expansion following 5000 DEM cycles and b) shows the final agglomerate after expansion . . . 79
4.2 Illustration showing how the three different layers, A, B, and C, are arranged in cubic close-packing of monosized spheres . . . 80
4.3 Illustration of uniaxial crushing of an agglomerate between two stiff horizontal platens for the 3D simulations . . . 83
4.4 Three plots of normal force (N) versus displacement (10^{-4} m) for three-dimensional agglomerate crushing trials 1, 6 and 22 . . . 87

4.5 Three plots of normal force (N) versus displacement (10^{-4} m) for two-dimensional agglomerate crushing trials 18, 65 and 75 88
4.6 ANOVA marginal means plots for four responses for the 2D simulations: a) normal force on platens at 10% strain (N); b) normal force at failure (N); c) strain at failure and d) agglomerate stiffness ($N\,m^{-1}$) 92
4.7 Plots of ANOVA predictions against the corresponding DEM simulation results for 10 randomly-selected combinations of the factor levels for the 2D analysis 94
4.8 ANOVA marginal means plots for four responses for the 3D simulations 97
4.9 ANOVA marginal means plots for the two interactions considered at three dimensions: a) bond shear strength × bond shear stiffness and b) bond shear strength × ball shear stiffness 98
4.10 Plots at three dimensions for 10 randomly-selected combinations of factor levels which compare ANOVA predictions, both including and excluding interactions 99

5.1 Screenshot showing an example of the output from the Malvern PharmaVision instrument that was used to determine average lengths and widths of the agglomerates 104
5.2 SEM micrograph at 2000X magnification of an agglomerate of infant formula B, which illustrates the methodology used to measure particle diameters and bond radius multipliers 105
5.3 Probability histogram of the particle diameters which comprise the agglomerates of infant formula B 106
5.4 Configuration of the pneumatic apparatus used to obtain high agglomerate impact velocities with the steel target 107
5.5 Chart showing the percentages of the agglomerates of infant formula B assigned to each failure category 108
5.6 Generated agglomerate containing 765 spheres, which has a length of 1.2202 mm, width of 1.0238 mm and height of 0.7613 mm 109
5.7 Plots of average force exerted on the platens against axial strain for two agglomerates using three bond normal and shear stiffnesses 112
5.8 Plots of average force exerted on the platens against axial strain for two agglomerates using three bond normal and shear strengths 113
5.9 Plots of average normal force exerted on the platens against axial strain for three simulations conducted using ball densities which varied by orders of magnitude 114
5.10 Probability histogram of the DEM force at failure responses (N) compared to PDFs of a fitted lognormal distribution and of the experimental data . 115

5.11 As for Figure 5.10, except for strain at failure (%) 115
5.12 As for Figure 5.10, except for agglomerate stiffness ($N m^{-1}$) 116
5.13 Scatter plot of agglomerate stiffness ($N m^{-1}$) against force at failure (N) for the DEM simulation results 117
5.14 Comparison of Weibull plots for the four formulae tested experimentally and the results of the DEM simulations 119
5.15 Plots of five energy terms against axial strain for compression of one representative agglomerate 121
5.16 Detailed view of the normalised force and three key energy terms for the first 10% of axial strain 122
5.17 Plots of the average normal force on the platens and bond energy against axial strain 122
5.18 Plots of the average normal force on the platens and the derivative of frictional work against axial strain 123
5.19 Plots of the number of bonds failed and the derivative of dissipated energy against axial strain 124
5.20 Plots of percentage of bonds failed against axial strain for compression of 20 randomly-selected agglomerates, using discrete data points at 5% increments of strain up to the point of failure 125
5.21 Plot showing the number of spheres contained in each daughter agglomerate for uniaxial compression of one representative agglomerate 125
5.22 Plot showing the median number of spheres remaining in the largest intact agglomerate fragment and the median number of agglomerate fragments against strain for all 130 agglomerates tested 126
5.23 Plots of percentage of bonds failed against axial strain for compression of 20 randomly-selected agglomerates, showing data at 5% of strain before and 5% after the point of failure 127
5.24 Visualisation of a representative agglomerate at an axial strain of 5%, in which the colour bar indicates the number of spheres contained in each fragment of the agglomerate 128
5.25 Visualisation of the parallel bonds within a representative agglomerate at an axial strain of 5%, in which the maximum normal stress acting on each intact bond was indicated by the diameter of the bond 128
5.26 As for Figure 5.24, except for an axial strain of 10% 129
5.27 As for Figure 5.25, except for an axial strain of 10% 129
5.28 As for Figure 5.24, except for an axial strain of 20% 130
5.29 As for Figure 5.25, except for an axial strain of 20% 130
5.30 As for Figure 5.24, except for an axial strain of 30% 131
5.31 As for Figure 5.25, except for an axial strain of 30% 131

5.32 As for Figure 5.24, except for an axial strain of 40% 132
5.33 As for Figure 5.25, except for an axial strain of 40% 132
5.34 Visualisation of the volumetric strains within an agglomerate subjected to uniaxial compression at axial strains of 20%, 30% and 40% 133
5.35 Plot showing the difference between the major and minor fabric against percentage axial strain for a representative agglomerate subjected to quasi-static uniaxial compression 134
5.36 Plot showing the orientation of the major fabric to the vertical (°) against percentage axial strain for the typical agglomerate compressed in Figure 5.35 135
5.37 Three plots of force exerted on the target platen (N) against time (ms) for simulated drop tests of agglomerates of infant formula at 1.9 ms^{-1} 137
5.38 Bar charts showing the percentage of the agglomerates tested using local damping coefficients of 0, 0.15 and 0.3 which had coefficients of restitution less than the values given on the x-axis 138
5.39 Plots of the kinetic and bond energies against time for one simulated drop test 139
5.40 Plots of four minor energy terms against time for one simulated drop test 139
5.41 Plots of the kinetic energy, bond energy and frictional work against time for one simulated drop test where damping was inactive 140
5.42 Normalised graph comparing the force exerted on the platen for a simulated drop test with plots of three energy terms 141
5.43 Visualisation of the parallel bonds within a representative agglomerate when the force exerted on the platen was at its maximum value 141
5.44 Chart showing the percentages of the agglomerates assigned to each failure category for simulated impact tests at 10.1 ms^{-1} 143
5.45 Three plots of force exerted on the target platen (N) against time (ms) for simulated impact tests of agglomerates of infant formula at 10.1 ms^{-1} . . 143
5.46 Plots of the kinetic energy, bond energy and frictional work against time for one simulated drop test 144
5.47 Normalised graph comparing the force exerted on the platen for a simulated impact test with plots of three energy terms 144
5.48 Plots of the number of bonds failed and the derivative of bond energy against time for a simulated impact test 145
5.49 Comparison of the volumetric strains at two times during a drop test of a representative agglomerate at 10.1 ms^{-1} 146

6.1 Illustration showing the turbulent velocity profile in a pipeline 152

6.2 Probability density functions of fluid velocity for $u_m = 20\ \mathrm{m\,s^{-1}}$ and n values of 2, 4 and 6 153
6.3 Comparison of the approximation of u_e given by Eq. 6.7 with the more theoretically-precise expression for u_e given by Eq. G.14 155
6.4 Comparison of $P(u_f)$ and $P(u_e)$ for $u_m = 20\ \mathrm{m\,s^{-1}}$ 155
6.5 Comparison of the drag coefficients predicted by Eqs. 6.19 and 6.20 for $1 \leq Re_p \leq 500$ 158
6.6 Illustration showing u_f and u_e for the hypothetical radial motion of a particle in a cross-section of the pipe 159
6.7 Geometry used to derive the trigonometric relationship between θ and y given as Eq. 6.42 166
6.8 Probability density functions of impact angle for a constant $\frac{r_p}{R}$ of 0.01 and $\frac{R_b}{R}$ values of 1, 5 and 10 167
6.9 Variation of the mean impact angle (rad) obtained both by numerical integration and using Eq. 6.46, with the ratio of bend radius to pipe radius, $\frac{R_b}{R}$ 168
6.10 Variation of the standard deviation in impact angle (rad) obtained both by numerical integration and using Eq. 6.47, with the ratio of bend radius to pipe radius, $\frac{R_b}{R}$ 169
6.11 Plot of the maximum impact force against normal impact velocity, showing the linear relationship required by Eq. 6.50 172
6.12 Plot showing the non-linear variation of impact angle with displacement from the centre of the pipe cross-section (m) 173
6.13 Weibull plot for the 50 simulated agglomerates which failed when subjected to impact loading at $20\ \mathrm{m\,s^{-1}}$ 175
6.14 Probability density functions of the Weibull distributions in a) σ and b) F for the parameters determined in Section 6.2.3 175
6.15 Three realisations of the effective fluid velocity and particle velocity against distance along the pipeline for $\phi = 116\ \mathrm{s^{-1}}$ 178
6.16 As for Figure 6.15, except for $\phi = 9.24\ \mathrm{s^{-1}}$ 179
6.17 Plots of the particle Reynolds number against distance along the pipeline for both values of ϕ tested 181
6.18 Plot of the variance in particle velocity ($\mathrm{m^2\,s^{-2}}$) against ϕ ($\mathrm{s^{-1}}$) 181
6.19 Probability density function of the Weibull distribution fitted to the simulation data for $|F(t)|\big|_{\max}$ 184
6.20 Identification of F^*: the point of intersection of the Weibull PDFs for force at failure and for the maximum impact forces in the conveying system 185
6.21 Plot of the mean probability of survival of an agglomerate against the maximum air velocity 186

6.22 Plot of the particle and effective fluid velocities against distance for a representative conveying simulation in which the particle was initially at rest . . . 187

B.1 Probability histogram of the force at failure data (N) for compression of agglomerates of infant formula A, compared with the PDF of a fitted lognormal distribution . . . 234
B.2 As for Figure B.1, except for infant formula B instead of A . . . 234
B.3 As for Figure B.1, except for infant formula C instead of A . . . 235
B.4 As for Figure B.1, except for infant formula D instead of A . . . 235
B.5 Probability histogram of the strain at failure data (%) for compression of agglomerates of infant formula A, compared with the PDF of a fitted lognormal distribution . . . 236
B.6 As for Figure B.5, except for infant formula B instead of A . . . 236
B.7 As for Figure B.5, except for infant formula C instead of A . . . 237
B.8 As for Figure B.5, except for infant formula D instead of A . . . 237
B.9 Probability histogram of the stiffness data ($\mathrm{N\,m^{-1}}$) for compression of agglomerates of infant formula A, compared with the PDF of a fitted lognormal distribution . . . 238
B.10 As for Figure B.9, except for infant formula B instead of A . . . 238
B.11 As for Figure B.9, except for infant formula C instead of A . . . 239
B.12 As for Figure B.9, except for infant formula D instead of A . . . 239

C.1 Simplified flowchart of the MATLAB code used to form agglomerates by sequential addition . . . 242
C.2 Orthographic projection of a sample agglomerate containing 200 spheres produced by sequential addition . . . 243

D.1 Preparation of the *.tif* images for calculating the fractal dimensions of agglomerate outlines using ImageJ . . . 256
D.2 Logarithmic plot showing the data calculated by FracLac for N_ε and ε, where the fractal dimension of the agglomerate outline is the absolute slope of the linear regression . . . 256
D.3 An example of fractal dimension calculation for agglomerate compression data using FracLab . . . 257

E.1 Example of a convex hull fitted to 100 randomly-generated points . . . 260
E.2 An agglomerate composed of two identical contacting spheres which has a convexity of 0.8 . . . 263
E.3 Effect of varying the number of points used per sphere on the calculated convexity . . . 263

E.4 Plot showing the percentages of simulated agglomerates which had convexities ≤ the corresponding values given on the x-axis 268

F.1 ANOVA contributions plots for three responses: force at failure (N), strain at failure (%) and agglomerate stiffness ($N\,m^{-1}$) 272

G.1 Illustration of a spherical particle in the cross-section of the pipeline . . . 277
G.2 Diagram showing the assumption made that the cross-section of each particle is a segment of an annulus rather than a circle 278
G.3 Geometry for more accurate integration used to quantify u_e 278
G.4 Relationship between L and s which is quantified by Eq. G.13 279
G.5 Geometry for the integral used to quantify the mean fall height of a particle under gravity, μ_h 282
G.6 Cross-section through the pipe bend showing the geometry used to derive Eq. 6.45 for $P(\theta)$ 284

List of Tables

1.1 Approximate percentage compositions of typical bovine and mature human milk . . . 3
1.2 Restrictions placed on the composition of infant formulae manufactured from cows' milk proteins by European Commission Directive 2006/141/EC, Annex I, §4–10.1 . . . 4
1.3 Indispensable and conditionally indispensable amino acids in breast milk as stated by European Commission Directive 2006/141/EC . . . 5
1.4 Major infant formula manufacturers and corresponding brands . . . 8
1.5 Main raw materials for infant formula manufacture, along with mineral additives, common vitamins and emulsifiers used (Písecký, 1997) . . . 9

2.1 Standard form of the L_9 orthogonal array, where the numbers 1 to 3 represent factor levels . . . 24
2.2 Control factors and levels used for the L_{18} experimental design . . . 31
2.3 L_{18} array showing the columns used after assigning all factors to the array 32
2.4 Responses for all four quality characteristics in terms of smaller-is-better S/N ratios . . . 36
2.5 Partial ANOVA table for S/N ratio responses . . . 37
2.6 Partial ANOVA table for raw data analysis of percentage changes of four responses . . . 38
2.7 Partial ANOVA table for analysis of standard deviations between replicates for three responses . . . 39
2.8 Parameters and p-values of polynomial models fitted to percentage data for four quality characteristics . . . 43
2.9 Correlation matrix for parameters of the model shown as Eq. 2.12 . . . 44
2.10 Metrics quantifying goodness of fit of the polynomial models . . . 44

3.1 Compositions of the infant formulae used in terms of their major components, in order of increasing protein to fat ratio . . . 50

3.2 Configuration selected for the pneumatic conveying experiments to investigate the effect of composition on quality characteristics of infant formulae . . . 51
3.3 Descriptors of powder flowability based on the Hausner ratio . . . 52
3.4 Sample relative breakage values calculated using three different baseline sizes: 20 µm, 63 µm and 74 µm . . . 55
3.5 Settings chosen for the configurable parameters of the texture analyser . 56
3.6 Means, standard deviations and extreme values of impact velocities for drop tests conducted using agglomerates in the 710–850 µm size range . 59
3.7 Means and standard deviations of the results obtained for force at failure (N), strain at failure (%) and agglomerate stiffness ($N m^{-1}$), and the parameters of the associated fitted lognormal (L/N) distributions . . . 66
3.8 Results of the Shapiro-Wilk W test for normality of the force at failure, strain at failure and agglomerate stiffness data sets . . . 68
3.9 Spearman R and Kendall τ rank correlations of all combinations of force at failure, strain at failure and agglomerate stiffness for infant formula A 69
3.10 As for Table 3.9, except for infant formula B instead of A . . . 69
3.11 As for Table 3.9, except for infant formula C instead of A . . . 69
3.12 As for Table 3.9, except for infant formula D instead of A . . . 69
3.13 Means, standard deviations and extreme values of coefficients of restitution 70

4.1 Factors varied, levels used and column of the standard L_{81} array assigned to each factor for the 2D simulations . . . 84
4.2 Factors varied, levels used and column of the standard L_{27} array assigned to each factor for the 3D simulations . . . 85
4.3 ANOVA results for the four responses for the 2D simulations . . . 89
4.4 Two-way interactions, sums of squares, p-values and columns containing those interactions identified as statistically-significant at a 90% level for the 2D simulations . . . 91
4.5 Factor settings that maximise normal force on the platens at 10% strain for the 2D simulations . . . 93
4.6 ANOVA results for the four response parameters for the simulations in 3D 95

5.1 Mean agglomerate dimensions for each infant formula . . . 104
5.2 Means, standard deviations and extreme values of particle diameters and bond radius multipliers . . . 106
5.3 Calibrated parameters used for the DEM simulations . . . 111
5.4 Means, standard deviations and parameters of the lognormal distributions fitted to the results obtained for force at failure (N), strain at failure (%) and agglomerate stiffness ($N m^{-1}$) for the DEM simulation results . . 116

5.5 Spearman R and Kendall τ rank correlations for all combinations of force at failure, strain at failure and agglomerate stiffness for the DEM simulation results . . . 117
5.6 Weibull moduli, the characteristic stresses at which 37% of agglomerates survive and coefficients of determination of the linear regressions . . . 119
5.7 Basic statistics comparing the coefficient of restitution data for drop tests conducted using sets of 20 agglomerates having three different local damping coefficients: 0, 0.15 and 0.3 . . . 138

6.1 Quantities calculated for the Kelvin-Voigt model from m, ε and t_c . . . 171
6.2 Means, standard deviations and extreme values of the particle velocity ($\mathrm{m\,s^{-1}}$), averaged over the 5,000 simulations conducted at each value of ϕ, compared to the means and standard deviations calculated using theoretical predictive equations . . . 180
6.3 As for Table 6.2, except for impact angle . . . 182
6.4 As for Table 6.2, except for normal impact velocity ($\mathrm{m\,s^{-1}}$) . . . 182
6.5 Contributions made by each term of Eq. 6.41 to the variance in normal impact velocity, σ^2_{un} . . . 183
6.6 Means, standard deviations and extreme values of the maximum impact forces (N), averaged over 10,000 simulations, compared to the means and standard deviations calculated using theoretical predictive equations . . . 184
6.7 Means, standard deviations and extreme values of the probability of survival, averaged over 10,000 simulations, compared to the mean calculated using Eq. 6.59 . . . 185

A.1 Standard form of the L_8 orthogonal array . . . 211
A.2 Standard form of the L_{18} orthogonal array . . . 212
A.3 Standard form of the L_{27} orthogonal array . . . 213
A.4 Standard form of the L_{81} orthogonal array . . . 214
A.5 Triangular table for the L_8 orthogonal array . . . 226
A.6 Triangular table for the L_9 orthogonal array . . . 226
A.7 Triangular table for the L_{27} orthogonal array . . . 226
A.8 Triangular table for the L_{81} orthogonal array . . . 228

D.1 Spearman R rank correlations of force at failure, strain at failure or agglomerate stiffness, and the physical characteristics of 92 agglomerates of infant formula B . . . 258
D.2 Spearman R rank correlations of pairs of agglomerate physical characteristics . . . 258

E.1 Median times required to fit convex hulls and find their enclosed volumes using the MATLAB function *convhulln* 262

F.1 Control factors and levels used for the L_8 experimental design 269
F.2 L_8 array showing the columns used after assigning all factors to the array 270
F.3 Partial ANOVA table for the three simulation responses for the agglomerate containing 633 spheres 270
F.4 Partial ANOVA table for the three simulation responses for the agglomerate containing 746 spheres 271

List of Publications[†]

Academic Papers Published in Refereed Journals

- Hanley, K.J., Cronin, K., O'Sullivan, C., Fenelon, M.A, O'Mahony, J.A., and Byrne, E.P.: Effect of composition on the mechanical response of agglomerates of infant formulae. *Journal of Food Engineering*, **107**(1): 71–79.

- Hanley, K.J., Byrne, E.P., Cronin, K., Oliveira, J.C., O'Mahony, J.A., and Fenelon, M.A.: Effect of pneumatic conveying parameters on physical quality characteristics of infant formula. *Journal of Food Engineering*, **106**(3): 236–244.

- Hanley, K.J., O'Sullivan, C., Oliveira, J.C., Cronin, K., and Byrne, E.P.: Application of Taguchi methods to DEM calibration of bonded agglomerates. *Powder Technology*, **210**(3): 230–240.

Presentations and Posters at Conferences

- Hanley, K.J., O'Sullivan, C., Oliveira, J.C., Cronin, K., and Byrne, E.P., July 2011. Application of Taguchi methods to DEM calibration of bonded agglomerates. *UK–China Particle Technology Forum III*, Birmingham, UK.

Continued on page xxiii

[†]The publications in each category are arranged in chronological order by publication date.

Continued from page xxii

Presentations and Posters at Conferences (cont.)

- Hanley, K.J., Cronin, K., O'Sullivan, C., Fenelon, M.A, O'Mahony, J.A., and Byrne, E.P., April 2011. Effect of composition on changes in physical quality characteristics of infant formulae caused by mechanical loading. *40th Annual UCC Food Research Conference*, Cork, Ireland.

- Hanley, K.J., Byrne, E.P., Cronin, K., and Fenelon, M.A., April 2010. An investigation into the minimisation of variation of infant formula quality characteristics during pneumatic conveying by Taguchi methods. *6th World Congress on Particle Technology*, Nuremberg, Germany.

Nomenclature and Abbreviations

The following table lists and briefly defines all the nomenclature and abbreviations used in the text in alphabetical order†, along with the chapter or section and the page on which they first appear, where the reader may find a more detailed description. Greek letters are grouped at the end of the table. The variables used in the MATLAB code given in Appendices C and E are not included in this table.

Symbol/ Abbreviation	Section/ Chapter	Page	Brief Definition
2B	2.2.1	29	A smooth, semi-reflective steel finish
316L	2.2.1	29	Low-carbon austenitic stainless steel grade
a	i) 3.2.3 ii) G.6	i) 71 ii) 280	i) Scale parameter of Weibull PDF; ii) Designation of any numerator in l'Hôpital's rule
A	3.1.1	50	Label assigned to a stage 1 infant formula containing 28.8% fat
a_0	2.2.4	35	Model offset
a_1	2.2.4	35	Linear model parameter for mode of conveying
a_2	2.2.4	35	Linear model parameter for length of vertical rig section
a_{22}	2.2.4	35	Quadratic model parameter for length of vertical rig section
a_{31}	2.2.4	35	Linear model parameter for air velocity in dense phase
a_{32}	2.2.4	35	Linear model parameter for air velocity in dilute phase
a_{331}	2.2.4	35	Quadratic model parameter for air velocity in dense phase

Continued on next page

†Note that a distinction is made between equivalent symbols in text and mathematical fonts, e.g., i/i or n/n.

Symbol/ Abbreviation	Section/ Chapter	Page	Brief Definition
a_{332}	2.2.4	35	Quadratic model parameter for air velocity in dilute phase
a_4	2.2.4	35	Linear model parameter for number of passes through rig
a_5	2.2.4	35	Linear model parameter for radii of 90° bends
a_{55}	2.2.4	35	Quadratic model parameter for radii of 90° bends
a_{61}	2.2.4	35	Linear model parameter for plug length
a_{62}	2.2.4	35	Linear model parameter for solids feed rate
a_{662}	2.2.4	35	Quadratic model parameter for solids feed rate
ANOVA	2.1.2	25	Analysis of Variance
ASTM	3.1.1	50	American Society for Testing and Materials
b	i) 3.2.3 ii) G.6	i) 71 ii) 280	i) Shape parameter of Weibull PDF; ii) Designation of any denominator in l'Hôpital's rule
B	3.1.1	50	Label assigned to a stage 2 infant formula containing 22.1% fat
B_p	3.1.4	53	Breakage potential, defined by Hardin (1985)
B_r	3.1.4	53	Relative breakage, defined by Hardin (1985)
B_t	3.1.4	53	Total breakage, defined by Hardin (1985)
bcc	4.1.4	79	A body-centred cubic lattice
c	i) 5.4.2 ii) 6.1.11	i) 134 ii) 169	i) Index of a contact between spheres in a simulated agglomerate; ii) Damping coefficient assigned to the dashpot in the Kelvin-Voigt model
C	3.1.1	50	Label assigned to a stage 3 infant formula containing 17.1% fat
c_D	6.1.4	156	Drag coefficient for an individual sphere in an unbounded fluid
CFD	5	101	Computational Fluid Dynamics

Continued on next page

Symbol/ Abbreviation	Section/ Chapter	Page	Brief Definition
d	i) 3.1.5 ii) 5.3.3 iii) 6.2.4 iv) E	i) 56 ii) 118 iii) 177 iv) 261	i) Distance between the bottom of the platen and the top surface of the glass plate for compression of agglomerates using a texture analyser; ii) Size of the agglomerate defined for Weibull analysis; iii) Diameter of a particle (equivalent to $2r_p$); iv) Sphere diameter/ cylinder height for the calculation of theoretical convexity in Eq. E.5
D	3.1.1	50	Label assigned to a stage 4 infant formula containing 15.2% fat
d_i	E	261	Diameter of sphere i in a simulated agglomerate
d_o	3.1.5	56	d at the instant when the trigger force was attained for a compression test
D[4,3]	2.2.3	32	Volume mean diameter/De Brouckere mean diameter
DEM	4.1	74	Discrete Element Modelling
DOE	2.1	23	Design of Experiments
ds	G.4	278	Width of a narrow strip of length L in the derivation of Eq. G.14
dx	G.8	281	Width of a narrow strip of length $2y$ in the derivation of Eq. 6.35
dy	G.9	283	Width of a narrow strip of length $2L$ in the derivation of Eq. 6.45
F	i) 5.3.3 ii) 6.1.11	i) 118 ii) 169	i) Force at failure of an agglomerate in Eq. 5.4; ii) Force exerted on a particle due to a deflection x in the Kelvin-Voigt impact model
F^*	6.3.3	184	The force at which Weibull PDFs for force at failure of the particles and the maximum impact forces in the conveying system intersect
F_1	2.2.4	35	Coded mode of conveying factor (-1, 1)
F_2	2.2.4	35	Coded length of vertical rig section factor (-1, 0, 1)
F_3	2.2.4	35	Coded air velocity factor
F_4	2.2.4	35	Coded number of passes through rig factor

Continued on next page

Symbol/ Abbreviation	Section/ Chapter	Page	Brief Definition
F_5	2.2.4	35	Coded radii of 90° bends factor
F_6	2.2.4	35	Coded plug length/solids feed rate pseudo-factors
f_c	6.1.7	162	Collision frequency: the reciprocal of t_ϕ
F_D	6.1.4	156	Drag force acting on the particle in the probabilistic model
F_i	4.1.1	75	Resultant force on a simulated disk or sphere
F_n	4.1.3	77	Normal contact force in a DEM simulation
F_o	6.2.3	175	37% characteristic force for Weibull analysis of a material
fcc	4.1.4	79	A face-centred cubic lattice
FDII	1.3	7	Food and Drink Industry Ireland
g_i	4.1.1	75	Body force acceleration vector acting on a simulated disk or sphere
H	6.1.7	164	Fall height within any vertical strip in a cross-sectional plane of the pipeline
i	C	240	Index of the active sphere in the sequential addition algorithm used to form 3D DEM agglomerates
i	5.3.3	118	Index of a particular agglomerate when ordered by increasing σ for the mean rank position approach
I	4.1.1	76	Moment of inertia of a simulated disk or sphere
I_{xx}	D.1.1	254	A summation term in the covariance matrix M used to calculate roundness
I_{xy}	D.1.1	254	As for I_{xx}
I_{yy}	D.1.1	254	As for I_{xx}
IBEC	1.3	7	Irish Business and Employers Confederation
INRIA	D.1.4	256	Institut National de Recherche en Informatique et en Automatique (eng.: National Institute for Research in Computer Science and Control)
ISO	3.1.1	50	International Standards Organisation

Continued on next page

Symbol/ Abbreviation	Section/ Chapter	Page	Brief Definition
j	C	241	Index of a sphere which contacts sphere i in the sequential addition algorithm used to form 3D DEM agglomerates
k	C	241	Index of a sphere which overlaps sphere i in the sequential addition algorithm used to form 3D DEM agglomerates
k	6.1.11	169	Stiffness of the linear spring in the Kelvin-Voigt model
K_n	4.1.3	77	Normal contact stiffness (secant) in a DEM simulation
k_n^{α}	4.1.3	77	Normal stiffness of entity α in a DEM contact
k_n^{β}	4.1.3	77	Normal stiffness of entity β in a DEM contact
K_s	4.1.3	77	Shear contact stiffness (tangent) in a DEM simulation
k_s^{α}	4.1.3	77	Shear stiffness of entity α in a DEM contact
k_s^{β}	4.1.3	77	Shear stiffness of entity β in a DEM contact
L	i) G.4 ii) G.9	i) 278 ii) 283	i) Length of a narrow strip of thickness ds in the derivation of Eq. G.14; ii) Half-length of a narrow strip of width dy in the derivation of Eq. 6.45
L_n	2.1.1	24	Standard designation of a Taguchi orthogonal array, where n is the number of rows
m	i) 4.1.1 ii) 5.3.3 iii) E	i) 75 ii) 118 iii) 261	i) Mass of a simulated disk/sphere, or of a particle in the probabilistic model of pneumatic conveying; ii) Weibull modulus, e.g., the exponent in Eq. 5.1; iii) Number of spheres comprising a simulated agglomerate
M	D.1.1	254	Identifier assigned to the covariance matrix used to calculate roundness
M_i	4.1.1	75	Resultant moment on a simulated disk or sphere
n	i) 2.1.1 ii) C	i) 24 ii) 240	i) Number of rows in an orthogonal array; ii) Specified maximum permissible number of spheres in 3D DEM agglomerates produced by sequential addition

Continued on next page

Symbol/ Abbreviation	Section/ Chapter	Page	Brief Definition
n	i) 1.4.2 ii) 5.3.3 iii) 6.1.2	i) 12 ii) 118 iii) 152	i) Exponent in the power-law relationship between particle velocity and erosion; ii) Total number of data points recorded for Weibull analysis; iii) Parameter in the $1/7^{th}$ power law velocity profile which is a function of Re
n_f	2.1.2	27	Total number of factors
n_{fi}	2.1.2	27	Total number of factors and interactions
n_j	2.1.2	26	Number of levels of factor j
n_m	2.1.2	27	Number of levels of factor m
n_p	2.1.2	26	Total number of data points
n_{pv}	6.1.7	162	Number of particles per unit volume in the pipe
n_x^c	5.4.2	134	x-component of a unit vector describing the normal orientation of contact c
n_y^c	5.4.2	134	As for n_x^c, except for the y-component
n_z^c	5.4.2	134	As for n_x^c, except for the z-component
N_ε	D.1.2	255	Number of boxes of side length ε which intersect the agglomerate outline
p {-value}	2.1.2	27	Indicator of significance level, e.g., a factor is significant at the 95% level if p < 0.05
p	6.1.4	156	Inertial rate constant of the conveyed particle
P	6.1.11	169	Impulse: the product of particle mass and normal impact velocity
p_e	6.1.4	157	Effective inertial rate constant of the particle
$P_s(d)$	5.3.3	118	Probability of survival of agglomerates of size d under a stress σ
$P_s(V_o)$	5.3.3	118	Probability of survival of a volume V_o of material when exposed to a uniform tensile stress σ
$P(u_e)$	6.1.3	154	PDF of effective fluid velocity
$P(u_f)$	6.1.2	152	PDF of fluid velocity
$P(\theta)$	6.1.10	167	PDF of impact angles between particles and the pipe bend
PDF	3.2.2	64	Probability Density Function

Continued on next page

Symbol/ Abbreviation	Section/ Chapter	Page	Brief Definition
PFC	4.1.1	75	Particle Flow Code
r	3.2.2	68	Pearson product moment correlation coefficient
r	i) 2.1.2 ii) 6.1.2	i) 26 ii) 152	i) Number of repetitions of each trial in an experimental design; ii) Radial distance from the pipe centreline
r_p	6.1.3	154	Radius of a particle
R	3.2.2	69	Spearman R rank correlation coefficient
R	i) 2.2.4 ii) 4.1.1 iii) 6.1.2	i) 35 ii) 76 iii) 152	i) Response of polynomial model; ii) Radius of a simulated disk or sphere; iii) Internal radius of a pipeline
R^2	2.3.2	43	Coefficient of determination: the amount of variance of the data explained by a fitted model
R^2_{adjusted}	2.3.2	43	Form of R^2 that is corrected for the number of parameters used in a model
R_b	6.1.10	166	Mean radius of the pipe bend
R_{ue}	6.1.5	159	A first-order autoregressive function to describe autocorrelation
R_ϕ	6.1.5	159	A characteristic dimension required in the calculation of ϕ
RE	1.1	5	All *trans* retinol equivalent of vitamin A
Re	6.1.2	152	Pipe Reynolds number
Re_p	6.1.4	156	Particle Reynolds number
s	G.4	278	Radial distance between the centreline of the pipe and any strip of length L and thickness ds in the derivation of Eq. G.14
SEM	1.5.1	14	Scanning Electron Microscope
S/N	2.1.2	26	Signal-to-Noise
SS_e	2.1.2	27	ANOVA sum of squares of the error
SS_{f_j}	2.1.2	26	ANOVA sum of squares due to factor j
$SS_{f_j \times f_m}$	2.1.2	27	Sum of squares of the two-way interaction between factors j and m
SS_t	2.1.2	26	ANOVA total sum of squares

Continued on next page

Symbol/ Abbreviation	Section/ Chapter	Page	Brief Definition
$S_f(\omega)$	6.3.5	188	Fluid turbulence energy spectrum
$S_p(\omega)$	6.3.5	188	Particle energy spectrum
t	6.1.5	160	Time elapsed during the probabilistic modelling simulations
T	6.3.5	188	Integral time scale
t_c	6.1.11	169	Contact time for a particle impact
t_ϕ	6.1.7	162	Time required for any particle to travel along its mean free path
t^*	6.3.5	188	Particle relaxation time
TE	1.1	5	d-α-tocopherol equivalent of vitamin E
$\overline{u}$	6.1.7	162	Average speed of a particle
$\overline{u}_c$	6.1.7	163	Average collision velocity between particles
u_e	6.1.3	154	Effective fluid velocity, i.e., the average spatial fluid velocity acting on the particle projected area
$u_e^*(t)$	G.7	281	Random component in the calculation of effective fluid velocity
u_f	6.1.2	152	Fluid velocity at a radial distance r from the pipe centreline
u_m	6.1.2	152	Maximum fluid velocity at the pipe centreline
u_n	6.1.9	165	Normal component of impact velocity at the pipe bend
u_p	6.1.4	156	Axial velocity of the conveyed particle
u_t	6.1.7	163	Terminal velocity of a particle falling under gravity
u_v	6.1.7	163	Vertical velocity of a particle falling under gravity and retarded by fluid drag
u_ϕ	6.1.5	158	Characteristic velocity at which conveyed particles move in the radial direction
V	2.1.2	27	Variance
V_e	2.1.2	27	Variance of the error
V_h	E	261	Volume of a convex hull
V_j	2.1.2	27	Variance of factor (or interaction) j

Continued on next page

Symbol/ Abbreviation	Section/ Chapter	Page	Brief Definition
V_o	i) 5.3.3 ii) 5.4.2	i) 118 ii) 132	i) Volume of material exposed to a uniform tensile stress σ for Weibull analysis; ii) Volume of a tetrahedron before compression
V_S	E	261	Total volume occupied by all m spheres in a simulated agglomerate
V_t	5.4.2	132	Volume of a tetrahedron at any stage of the compression process
W statistic	3.2.2	68	Result from Shapiro-Wilk W test for normality
$W(t)$	G.7	281	Random variate drawn from the normal distribution with a mean of 0 and a variance of σ_{ue}^2
x	C	240	Specified length of the 3D DEM agglomerates produced by sequential addition
x	i) 3.2.2 ii) 6.1.11 iii) 6.2.4	i) 64 ii) 169 iii) 176	i) Raw data for a response, i.e., force at failure, strain at failure, agglomerate stiffness or coefficient of restitution; ii) Deflection of the particle during the duration of impact; iii) Horizontal displacement from the centre of the pipe cross-section
$x'(t)$	G.10	285	Velocity of a particle at any time t
x_i	D.1.1	254	The x-coordinate of agglomerate pixel p_{ij}
$\ddot{x}_i$	4.1.1	75	Acceleration of a simulated disk or sphere
x_n	4.1.3	77	Normal displacement at a contact in a DEM simulation
x_p	6.2.4	176	Axial displacement of a particle along the pipeline
y	C	240	Specified width of the 3D DEM agglomerates produced by sequential addition
y	i) 3.2.2 ii) 6.1.10 iii) G.8	i) 64 ii) 166 iii) 281	i) Probability density; ii) Vertical displacement from the centre of the pipe cross-section; iii) Half-height of vertical strip of width dx defined in the derivation of Eq. 6.35
$\overline{y}$	2.1.2	26	Global mean of all data points

Continued on next page

Symbol/ Abbreviation	Section/ Chapter	Page	Brief Definition
$y_{\text{estimated}}$	2.1.2	28	Estimated ANOVA prediction by addition of marginal means
y_i	2.1.2	26	Raw response for trial i before applying S/N transformation
$y_{i\|k}$	2.1.2	26	Subset of data points (ANOVA) in which a factor was tested at level k
$y_{i\|l\,k}$	2.1.2	27	Subset of data points (ANOVA) in which one factor was tested at level l and another factor was tested at level k concurrently
y_j	D.1.1	254	The y-coordinate of agglomerate pixel p_{ij}
$\overline{y_k}$	2.1.2	26	Mean of the data subset designated as $y_{i\|k}$
$\overline{y}\|_{k_j}$	2.1.2	28	Mean of the data subset where factor j is at its optimum level
$\overline{y_{l\,k}}$	2.1.2	27	Mean of the data subset designated as $y_{i\|l\,k}$
y_{target}	2.1.2	26	Specified target value for a nominal-is-better S/N optimisation
z	C	240	Specified height of the 3D DEM agglomerates produced by sequential addition
z_t	6.1.5	160	A random term in the algorithm to calculate u_e which is sampled from the normal distribution
α	i) 2.3.1 ii) 3.2.2 iii) 4.1.3 iv) C	i) 37 ii) 68 iii) 77 iv) 241	i) Shortened designation for mode of conveying; ii) Alternative way of expressing the level of significance, e.g., $\alpha = 0.1$ for a significance level of 90%; iii) An identifier for the first entity in a DEM simulation contact; iv) Initial position of sphere i in the sequential addition algorithm
β	i) 2.3.1 ii) 4.1.3 iii) C	i) 37 ii) 77 iii) 241	i) Shortened designation for length of vertical rig section; ii) An identifier for the second entity in a DEM simulation contact; iii) Position of sphere i in the sequential addition algorithm when point contact is achieved with sphere j

Continued on next page

Symbol/ Abbreviation	Section/ Chapter	Page	Brief Definition
$\gamma_{1/2/3}$	6.2.4	176	Variates randomly selected from the uniform distribution on the interval [0,1]
ΔF_s	4.1.3	77	Increment of shear contact force in a DEM simulation
Δt	6.1.5	160	The time step used in the algorithm to calculate u_e and u_p
Δx_s	4.1.3	77	Increment of shear displacement at a contact in a DEM simulation
ε	i) 6.1.11 ii) D.1.2	i) 169 ii) 255	i) Coefficient of restitution of a particle; ii) Side length of the boxes used to calculate the box-counting fractal dimension
ζ	6.1.11	169	Dimensionless damping factor for the impact of a particle in the Kelvin-Voigt model
ϑ	4.1.1	76	A dimensionless multiplier which is 0.5 for a simulated disk and 0.4 for a sphere
Θ	6.1.7	163	Granular temperature for pneumatic conveying
θ	6.1.9	165	Impact angle for a particle collision with the pipe bend
θ_c	6.1.10	167	Impact angle for a particle collision with the bend with is collinear with the centreline of the straight pipe
θ_{max}	6.1.10	167	Maximum impact angle for a particle collision with the pipe bend
λ	6.1.7	162	Mean free path between collisions for the probabilistic model developed
$\bar{\lambda}$	4.1.3	78	Dimensionless parameter which gives the radius of a parallel bond when multiplied by the radius of the smaller of the two particles interacting in the bond
$\lambda_{1/2}$	D.1.1	254	Eigenvalues of the covariance matrix M used to calculate roundness
μ	3.2.2	64	Mean of the normal distribution corresponding to a fitted lognormal distribution

Continued on next page

Symbol/ Abbreviation	Section/ Chapter	Page	Brief Definition
μ_h	6.1.7	163	Average height through which a particle falls under gravity when placed randomly in the pipeline
μ_{Ps}	6.3.3	184	Mean probability of survival of an agglomerate
μ_{uc}	6.1.8	164	Mean impact velocity for pairwise collisions of conveyed particles
μ_{ue}	6.1.6	161	Mean effective fluid velocity (equivalent to μ_{uf})
μ_{uf}	6.1.2	153	Mean fluid velocity
μ_{un}	6.1.9	165	Mean normal impact velocity for collisions with the pipe bend
μ_{up}	6.1.6	161	Mean particle velocity
μ_θ	6.1.9	165	Mean impact angle for collisions with the pipe bend
ν	6.1.4	156	Kinematic viscosity of the conveying fluid (air)
ρ	6.1.4	156	Density of the conveying fluid (air)
ρ_p	6.1.7	163	Density of the conveyed particle
ρ_{ue}	6.1.5	160	Autocorrelation coefficient in the algorithm used to calculate u_e from its value at the preceding step
$\rho_{u_p,\theta}$	6.1.9	165	Cross-correlation coefficient of particle velocity and impact angle
σ	i) 3.2.2 ii) 5.3.3	i) 64 ii) 118	i) Standard deviation of the normal distribution corresponding to a fitted lognormal distribution; ii) Uniform tensile stress applied to a volume V_o for Weibull analysis
σ_o	5.3.3	118	37% characteristic stress for Weibull analysis of a material
σ^2_{ue}	6.1.5	160	Variance in effective fluid velocity
σ^2_{uf}	6.1.2	153	Variance in fluid velocity
σ^2_{un}	6.1.9	165	Variance in normal impact velocity of a particle with the pipe bend
σ^2_{up}	6.1.6	161	Variance in particle velocity

Continued on next page

Symbol/ Abbreviation	Section/ Chapter	Page	Brief Definition
σ_{ut}^2	6.3.5	188	Variance in fluid velocity caused by turbulence
σ_θ	6.1.9	165	Standard deviation in impact angle with the pipe bend
τ	i) 3.2.2 ii) 6.1.5	i) 69 ii) 159	i) Kendall τ rank correlation coefficient; ii) Separation time
τ_c	6.1.5	159	Correlation (or decorrelation) time constant
υ	2.1.2	27	Degrees of freedom
υ_{error}	2.1.2	27	Degrees of freedom of the error
$\upsilon_{\text{factor}_j}$	2.1.2	27	Degrees of freedom of factor (or interaction) j
υ_{total}	2.1.2	27	Degrees of freedom of the data
ϕ	6.1.5	159	Autocorrelation parameter in the first-order autoregressive function R_{ue}
Φ_1	5.4.2	134	Eigenvalue of the fabric tensor which is the magnitude of the major fabric
Φ_2	5.4.2	134	As for Φ_1, except for the intermediate fabric
Φ_3	5.4.2	134	As for Φ_1, except for the minor fabric
Φ_{ij}	5.4.2	134	Element ij of the 3D second-order fabric tensor for contact orientations
ω	6.3.5	188	Spectral frequency
ω_d	6.1.11	169	Damped natural frequency for the underdamped impact of a particle in the Kelvin-Voigt model
$\dot{\omega}_i$	4.1.1	75	Angular acceleration of a simulated disk or sphere
ω_n	6.1.11	169	Natural frequency for the underdamped impact of a particle in the Kelvin-Voigt model

1

Introduction to Infant Formula

Many organisations have published definitions which specify precisely what infant formulae are. As might be expected, all of these definitions are similar. The principal European Commission directive governing infant formulae, which is discussed in Section 1.1, defines infant formulae as "foodstuffs intended for particular nutritional use by infants during the first months of life and satisfying by themselves the nutritional requirements of such infants until the introduction of appropriate complementary feeding" (European Commission, 2006). The Codex Alimentarius Commission, a body created in 1963 by the Food and Agriculture Organisation of the United Nations and the World Health Organisation to develop food standards, guidelines and related texts (FAO/WHO Food Standards Codex Alimentarius, 2010, ¶1), defines infant formula as "a breast-milk substitute specially manufactured to satisfy, by itself, the nutritional requirements of infants during the first months of life up to the introduction of appropriate complementary feeding" (Codex Alimentarius, 2007).

1.1 Infant Formula Composition and Legislative Framework

The composition of infant formulae must satisfy strict criteria. The standards required for infant formula marketed in the European Union are detailed in the Annexes of European Commission Directive 2006/141/EC (European Commission, 2006). Usually infant formulae are manufactured from cows' milk proteins and/or soy protein isolates. Since the implementation of 2006/141/EC, it is now permissible to market infant formulae manufactured from protein hydrolysates in the EU (European Commission, 2006, Annex I, §2). Soy-based infant formulae are an option for babies who are intolerant or allergic to cow milk formula or lactose. Protein hydrolysate formulae are intended for babies who have a family history of milk or soy allergies. These are easier

to digest and are less likely to cause allergic reactions than other types of formula. For this reason, they are also known as hypoallergenic formulae (Mayo Clinic, 2010). The criteria which are provided for the composition (in terms of proteins, carbohydrates, lipids, vitamins, minerals and certain other ingredients) of both infant and follow-on formulae vary slightly depending on whether the formula is manufactured from cows' milk proteins, protein hydrolysates or soy protein isolates.

The Codex Alimentarius Commission has also issued guidelines for the nutritional content of infant formula; these correspond closely to 2006/141/EC. For proteins, lipids and chloride, for example, both the upper and lower limits are identical. For other components (particularly vitamins), no upper limits are stated (Codex Alimentarius, 2007, §3.1). Directive 2006/141/EC was transposed into Irish law by passing S.I. No. 852 of 2007 (European Communities (Infant Formulae and Follow-On Formulae) Regulations, 2007, p.2). Minor amendments were made by passing S.I. No. 209 of 2009 (European Communities (Infant Formulae and Follow-On Formulae) (Amendment) Regulations, 2009). In England, S.I. 3521 was used to implement the directive (The Infant Formula and Follow-on Formula (England) Regulations, 2007, p.13). In the United States, infant formulae are governed by the Food and Drug Administration, who list requirements for infant formulae in Section 412(i) of the Federal Food, Drug and Cosmetic Act. Limits are placed on permissible amounts of 29 different nutrients, in a similar manner to European Commission Directive 2006/141/EC (U.S. Food and Drug Administration, 2010).

Manufacturers typically divide their core infant formula ranges into between two and four age-based categories (Norton-Smith, 2008; Pasricha et al., 2009). Some of the most common definitions of the age categories are the following:

Stage 1 For use from birth to six (sometimes twelve) months

Stage 2 For use from six to twelve months

Stage 3 For use from one to three years

Stage 4 For use from three years on

Nutri Seven and PBM International divide their ranges into stage 1, 2 and 3 formulae (Nutri Seven Pty. Ltd., 2010; PBM International Ltd., 2011). Infant Formula Australia categorise their products from stages 1 to 4 (Infant Formula Australia, 2009). Novalac infant formulae, manufactured by United Pharmaceuticals (United Pharmaceuticals, 2010) and distributed by Bayer Healthcare in Australia and New Zealand, refer directly to stage 1 and 2 formulae (Bayer Healthcare, n.d.). In Europe, manufacturers seldom refer directly to the stages in their marketing material, e.g., SMA Nutrition refer to stages 1, 2 and 3 as first infant milk, follow-on milk and toddler milk, respectively (Advertising Standards Authority, 2010; SMA Nutrition, 2011).

There are some differences between the compositions of typical stage 1/2/3/4 infant formulae, particularly regarding proteins. Dairy proteins can be subdivided into 2 groups: caseins and whey proteins. In bovine milk, caseins (α_{s1}, α_{s2}, β, κ, γ) comprise approximately 78% of the protein content, while the remainder is predominantly (approximately 19%) whey proteins (α-lactalbumin, β-lactoglobulin, bovine serum albumin, casein derived peptides, immunoglobulins) (Walstra et al., 1999, ch.2). Compared to the relatively invariant nature of cow milk, the composition of human milk changes over time. A high ratio of whey to casein (> 80% whey) is present at the initiation of lactation, which is reduced to a 60:40 whey:casein ratio in mature milk, and still further to a 50:50 ratio in extended lactation (Lien, 2003). Not only does the amino acid profile change, but the overall mean protein content is approximately halved during the first month of lactation (Harzer et al., 1986). There are also significant diurnal variations in fat content (Jenness, 1979), a factor which is significantly influenced by the diet of the mother (Lönnerdal, 1986). The compositions of typical bovine milk and human milk are compared in Table 1.1 (Písecký, 1997, p.121).

Table 1.1: *Approximate percentage compositions of typical bovine and mature human milk*

	Bovine Milk	Human Milk
Water	87.35	87.3
Fat	3.75	4.1
Lactose	4.85	6.9
Casein	2.78	0.6
Lactalbumin	0.47	0.9
Minerals	0.8	0.2
Total	100	100

Stage 1 infant formulae, or first milks, are generally whey-dominant, with a 60:40 whey:casein ratio: the same ratio as in mature human milk (Nicholson, 2009). Second milks are casein-dominant, with a 20:80 whey:casein ratio (Nicholson, 2009). This closely reflects the protein composition of bovine milk (Rudloff and Kunz, 1997). Follow-on formulae for children over one year old (stage 3) contain more protein than formulae intended for consumption by infants, although the nutritional benefit of this protein increase is questionable (Fox and McSweeney, 2003, p.633).

When concentrations of individual proteins are assessed, α-lactalbumin is found to be the dominant protein in human milk (28% of total protein), while this is present in relatively low concentrations in traditional infant formulae manufactured from cows' milk proteins. β-lactoglobulin, a protein which is not found in human milk, is the most dominant whey protein in traditional infant formulae (Lien, 2003). Differences between the amino acid compositions of bovine and human milks are largely attributable

to differences in their α-lactalbumin contents (Heine et al., 1991). Recently, whey sources with elevated concentrations of α-lactalbumin have become available; this has permitted the development of formulae with increased concentrations of this protein and correspondingly decreased concentrations of β-lactoglobulin (Lien, 2003).

In most cases, both lower and upper limits are required for permitted amounts of nutrients. While it is obvious that insufficient amounts of nutrients may lead to deficiency illnesses or stunt growth, an excess of certain components could also be deleterious to the health of the infant. Formula that is too strong can lead to hypernatraemic dehydration or kidney problems (Laing, 2002; Oates, 1973). Table 1.2 shows some of the restrictions placed on the composition of infant formulae manufactured from cows' milk proteins in the European Union.

Table 1.2: *Restrictions placed on the composition of infant formulae manufactured from cows' milk proteins by European Commission Directive 2006/141/EC, Annex I, §4–10.1*

Criterion	Permitted Minimum	Permitted Maximum
Energy†	250 kJ/100 ml	295 kJ/100 ml
Carbohydrates	2.2 g/100 kJ	3.4 g/100 kJ
Lactose	1.1 g/100 kJ	—
Lipids	1.05 g/100 kJ	1.4 g/100 kJ
Proteins	0.45 g/100 kJ	0.7 g/100 kJ
Choline	1.7 mg/100 kJ	12 mg/100 kJ
Inositol	1 mg/100 kJ	10 mg/100 kJ
Linoleic Acid	70 mg/100 kJ	285 mg/100 kJ
Taurine	—	2.9 mg/100 kJ
Minerals		
Calcium	12 mg/100 kJ	33 mg/100 kJ
Chloride	12 mg/100 kJ	38 mg/100 kJ
Copper	8.4 µg/100 kJ	25 mg/100 kJ
Fluoride	—	25 µg/100 kJ
Iodine	2.5 µg/100 kJ	12 µg/100 kJ
Iron	0.07 mg/100 kJ	0.3 mg/100 kJ
Magnesium	1.2 mg/100 kJ	3.6 mg/100 kJ
Manganese	0.25 µg/100 kJ	25 µg/100 kJ
Phosphorous	6 mg/100 kJ	22 mg/100 kJ
Potassium	15 mg/100 kJ	38 mg/100 kJ
Selenium	0.25 µg/100 kJ	2.2 µg/100 kJ
Sodium	5 mg/100 kJ	14 mg/100 kJ

Continued on page 5

Criterion	Permitted Minimum	Permitted Maximum
Zinc	0.12 mg/100 kJ	0.36 mg/100 kJ
Vitamins		
Biotin	0.4 µg/100 kJ	1.8 µg/100 kJ
Folic Acid	2.5 µg/100 kJ	12 µg/100 kJ
Niacin	72 µg/100 kJ	375 µg/100 kJ
Pantothenic Acid	95 µg/100 kJ	475 µg/100 kJ
Riboflavin	19 µg/100 kJ	95 µg/100 kJ
Thiamin	14 µg/100 kJ	72 µg/100 kJ
Vitamin A	14 µg-RE/100 kJ‡	43 µg-RE/100 kJ‡
Vitamin B_6	9 µg/100 kJ	42 µg/100 kJ
Vitamin B_{12}	0.025 µg/100 kJ	0.12 µg/100 kJ
Vitamin C	2.5 mg/100 kJ	7.5 mg/100 kJ
Vitamin D	0.25 µg/100 kJ	0.65 µg/100 kJ
Vitamin E	0.1 mg α-TE/100 kJ*	1.2 mg α-TE/100 kJ*
Vitamin K	1 µg/100 kJ	6 µg/100 kJ

† All other figures in this table are per 100 kJ of energy. It is assumed that the formula has been made up exactly in accordance with the manufacturer's specifications.

‡ Expressed as all *trans* retinol equivalent.

* Expressed as d-α-tocopherol equivalent.

The exact composition of infant formula in terms of individual proteins is not defined by legislation. Instead, requirements such as the following are included in legislation: "…the infant formula must contain an available quantity of each indispensable and conditionally indispensable amino acid at least equal to that contained in the reference protein (breast milk, as defined in Annex V)" (European Commission, 2006, Annex I, §2). The minimum required amounts of 11 amino acids are stated in Annex V, and are provided in Table 1.3.

Table 1.3: *Indispensable and conditionally indispensable amino acids in breast milk as stated by European Commission Directive 2006/141/EC*

Amino Acid	Minimum Concentration† (mg/100 kJ)
Cystine	9
Histidine	10
Isoleucine	22

Continued on page 6

Amino Acid	Minimum Concentration
Leucine	40
Lysine	27
Methionine	5
Phenylalanine	20
Threonine	18
Tryptophan	8
Tyrosine	18
Valine	21

† As in Table 1.2, it is assumed that the formula has been made up in accordance with the manufacturer's specifications.

Even though the legislative requirements may appear all-encompassing, and manufacturers must take great care to ensure that they are satisfied, they cannot account for the largest source of error in infant formula reconstitution: those made by the caregiver. In one representative study of 19 mothers, Lucas et al. (1991) showed that slightly under half of the participants consistently reconstituted infant formula with an error of less than 20% and only two of the 19 consistently made up milk with less than 10% error. Usually the issue is over-concentration of the feed (Renfrew et al., 2003). As a result, powdered infant formula is linked with higher rates of fat deposition in infants (Lucas et al., 1992).

1.2 Overview of the Global Infant Formula Market

Based on 2009 figures, the global infant formula market is valued at approximately US$10 billion, accounting for almost half of the US$21 billion global baby food sector (Dept. of Agriculture, Fisheries and Food, 2010, p.7). While it is clear that the global infant formula sector is experiencing rapid growth, estimates of the annual growth vary; two estimates of market growth are 9% in 2009 (Ubic Consulting, 2010) or 15% as an average year-on-year growth (Dept. of Agriculture, Fisheries and Food, 2010). Global Industry Analysts, Inc. project a market worth of $23.8 billion by 2015, which indicates a future slowdown in the growth rate (Global Industry Analysts, Inc. Report, 2010). The United States and Western Europe are the traditional markets for baby food and infant formula products; however, these regions offer little opportunities for growth due to declining birth rates, static market conditions and industry consolidation. As a result, manufacturers are placing an increasing emphasis on the more lucrative and populous markets in Asia-Pacific, particularly India and China. The Asian market is the

largest and also has the highest growth rates. 2009 estimates for the Asian market share from the sources above are 39% (Dept. of Agriculture, Fisheries and Food, 2010) and 53% (Ubic Consulting, 2010). The United States, Asia-Pacific and Europe collectively accounted for approximately 82% of the global infant nutrition market in 2009 (Global Industry Analysts, Inc. Report, 2010).

A large number of firms manufacture infant formula worldwide, although in individual countries, the market is usually dominated by a small number of brands. One example for which data are readily available is the United States infant formula market. In 2000, just three companies controlled 99% of the domestic market: Mead Johnson Nutrition (Bristol-Myers Squibb), Ross Laboratories (Abbott Laboratories) and Carnation (Nestlé) (Oliveira et al., 2001). The first two of these still controlled 80% of the market in 2009 (Ubic Consulting, 2010). Globally, the infant formula market leader in 2009 was Mead Johnson Nutrition with a 20% market share, followed by Nestlé (18%), Abbott Laboratories (16%), Groupe Danone (12%) and Wyeth Nutrition with a 10% share (Dept. of Agriculture, Fisheries and Food, 2010).

Like the pharmaceutical industry, many significant acquisitions and mergers have occurred in the infant nutrition sector in recent times. Some examples are listed below:

April 2007 Nestlé acquired Gerber from Novartis for US$5.5 billion (Martin and Sorkin, 2007).

August 2007 Groupe Danone purchased Royal Numico N.V. for €12.3 billion (Michelson and Stevenson, 2007).

January 2008 Nutribio was established as an equal joint venture between Groupe Sodiaal and Groupe Entremont Alliance by merging their existing subsidiaries Sodiaal Industrie and Cofranlait (Entremont Alliance, n.d.).

January 2009 Pfizer agreed to purchase Wyeth, including their infant formula interests, for a total of US$68 billion (Bawden, 2009).

May 2010 Perrigo Co. acquired PBM Holdings, Inc. for approximately US$808 million (PR Newswire, 2010).

Examples of the infant formula brands produced by some of the major infant formula manufacturers are listed in Table 1.4, along with their parent companies (where applicable).

1.3 Significance of Infant Formula for Ireland

Ireland has a strong food and agri-business sector, supporting an estimated 230,000 jobs at present (Ryan, 2010). The Food and Drink Industry Ireland (FDII) sector of the Irish

Table 1.4: *Major infant formula manufacturers and corresponding brands*

Manufacturer [Parent Company]	Brands[†]
Abbott Laboratories	Gain · Isomil · Similac
Groupe Danone	Bebiko · Bebilon · Cow & Gate · Mellin · Milupa · Neocate
H.J. Heinz Company	Nurture
Mead Johnson Nutrition [Bristol-Myers Squibb]	Enfalac · Enfamil
Nestlé	Carnation · Good Start · NAN
PBM Nutritionals	Bright Beginnings
Wyeth Nutrition [Pfizer Inc.]	Progress · Promil · S-26 · SMA

[†]Brand information was obtained from the manufacturers' corporate websites.

Business and Employers Confederation (IBEC) state that the manufacture of food and drink products is Ireland's primary indigenous industry with a turnover approaching €24 billion (Food and Drink Industry Ireland, 2011). The value of exports from this sector in 2009 was €7.1 billion (Noonan, 2010), equivalent to more than $^2/_3$ of exports by indigenous manufacturers. This represented a reduction of €1 billion on 2008 figures due to volatility in dairy markets (Food and Drink Industry Ireland, 2011). 43% of exports go to the UK and 33% to the remainder of the EU (Food and Drink Industry Ireland, 2011). The dairy sector is the largest single contributor to Ireland's food and drink exports, accounting for 27% of total exports (National Dairy Council, 2008).

In Ireland, the dairy sector is heavily linked to infant formula manufacture. Ireland is the world's largest single producer of infant formulae, accounting for approximately 15% of world production (European Commission Food and Veterinary Office, 2007, §4.2). Total sales in 2008 were €667 million, virtually all of which was exported. More than 120,000 metric tonnes of infant formula is produced annually in Ireland, using over 100,000 metric tonnes of Irish dairy ingredients (Dept. of Agriculture, Fisheries and Food, 2010, p.8).

These infant formula manufacturing plants are not localised in one area, but are found in different parts of the country. Abbott Ireland's infant nutrition plant in Cootehill, Co. Cavan processes around 500,000 litres of milk daily (Abbott Ireland, n.d.). Pfizer Ireland (formerly Wyeth Nutritionals Ireland) produce infant formula in Askeaton, Co. Limerick; this is one of the largest purpose-built infant nutrition manufacturing plants in the world with an annual production capacity of approximately 50 million kilograms (Pfizer Ireland, 2011). Nutricia Ireland (part of Groupe Danone), who are the market

leader in Ireland and the UK, have manufacturing sites in Macroom, Co. Cork and in Rocklands, Co. Wexford (Nutricia, 2011).

1.4 Infant Formula Manufacture

1.4.1 Overview of Manufacturing Processes

Powdered infant formula can be manufactured using two general types of processes: a dry blending process and a wet mixing/spray drying process. It is also possible to use both of these processes in combination (U.S. Food and Drug Administration, 2003, ¶1). The wet mixing/spray drying process is more commonly used, and a flowchart showing the typical steps involved is shown in Figure 1.1.

The typical raw materials, mineral additives, the most common vitamins and the emulsifiers included in infant formula are shown in Table 1.5 (Písecký, 1997, p.122).

Table 1.5: *Main raw materials for infant formula manufacture, along with mineral additives, common vitamins and emulsifiers used (Písecký, 1997)*

Raw Materials	Lactose · demineralised whey powder · whey protein concentrate · caseinate · maltodextrin · lactulose · fractionated coconut oil · sunflower, corn and soya oil
Mineral Additives	Tricalciumphosphate · sodium and potassium citrate · magnesium and potassium chloride · calcium carbonate · zinc, ferrous, cupric and manganese sulfates
Common Vitamins	Ascorbic acid · alpha-tocopheryl acetate · riboflavin · vitamin A palmitate · vitamin D_3
Emulsifiers	Mono-glycerol-stearate · di-glycerol-stearate · lecithin · carrageenin

1.4.2 Conveying of Infant Formula within a Plant

Figure 1.1 shows that the infant formula that is formed in the spray dryer must be transported to the can filling line, often via an intermediate silo. Note that the conveying distances involved are typically 50–200 m in the horizontal direction, and 10–20 m in the vertical direction. Production-scale spray dryers are physically large items of equipment; hence, the base of the dryer, from which the dried product is removed, will invariably be at a low level in the plant, whereas the silo entrance will usually be at a higher level.

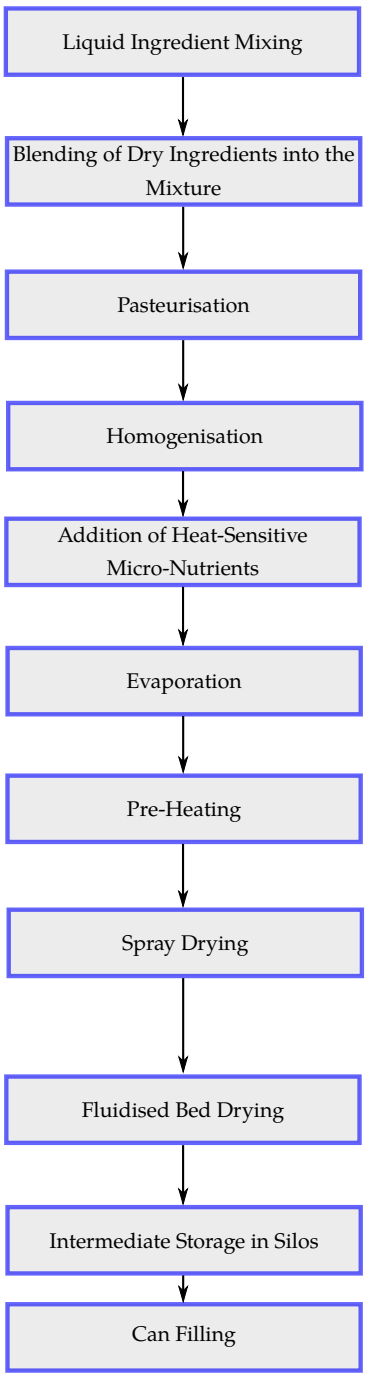

Liquid raw materials (water, oils etc.) are stored in large tanks which are mounted on load cells (Sørensen et al., 1992). When required, the liquid ingredients are pumped into mixing vessels in the appropriate proportions and may be emulsified.

The dry ingredients, which are stored either in silos or in large bags in a warehouse, are blended into the mixture until the desired concentration is achieved.

The mixture is pumped to a heat exchanger for pasteurisation. This pasteurization process must ensure that the vegetative cells of harmful bacteria are destroyed (U.S. Food and Drug Administration, 2003).

The mixture is filtered and homogenised to reduce the size of fat globules in the liquid. Some manufacturers homogenise prior to pasteurisation.

At this stage, thermally-labile micro-nutrients, particularly certain vitamins and amino acids, are added to the product (U.S. Food and Drug Administration, 2003).

A multiple-effect evaporator is often used to concentrate the premix before spray drying, largely for economic reasons. It is generally cheaper to remove water in an evaporator than in a spray dryer (Sørensen et al., 1992).

The viscous mixture resulting from evaporation is pre-heated to 70–90°C before being pumped under high pressure to the spray dryers.

In the spray dryers, the liquid is atomised by either a wheel or pressure nozzle type atomiser and falls under gravity through air at 140–200°C. The powder temperature at the spray dryer outlet is 45–80°C (U.S. Food and Drug Administration, 2003).

The warm powder discharged from the dryer is passed through one or several fluidised beds for final drying and cooling of the powder to room temperature. The fluidised beds also enhance agglomeration, and hence improve flowability and instant properties of the final product (Písecký, 1997).

The product is sifted to remove lumps and may be stored in silos as an intermediate step before filling.

The infant formula is filled into tin-plated steel cans on an automated filling line. The cans are flushed with an inert gas during the packaging process.

Figure 1.1: *A flowchart showing the typical steps for infant formula production by a wet mixing/spray drying process*

This elevation disparity necessitates transport of the infant formula produced in the vertical direction.

There are many different conveying technologies that could potentially be selected for this operation, including screw conveyors, belt conveyors and sliding/vibratory conveyors. These listed conveyors are rarely selected for this application, as all have at least one major disadvantage that mitigates against their widespread use: screw

conveyors are restricted to short distances of only a few metres; belt conveyors would need to be used in conjunction with another form of conveyor, such as a bucket elevator, for vertical transport; and sliding/vibratory conveyors have both of these disadvantages, being restricted to distances of 8–10 m and capable of tolerating only small deviations from the horizontal (Yanko, 2007).

Pneumatic conveying is typically selected for transporting infant formula between the fluidised bed drying and can filling stages of the manufacturing process. This form of gas-solid multiphase flow is described by Fraige and Langston (2006) as the use of a gas, which is usually air, to transport solid particles through a pipeline. The advantages of pneumatic conveying include the following (Fraige and Langston, 2006; Marcus et al., 1990, p.2; Molerus, 1996):

- It allows for dust-free transportation of a wide range of products.
- In contrast to the other conveyors listed above, pneumatic conveying is very flexible as regards layout. Products may be conveyed horizontally, vertically or at inclined angles and conveyor lengths may exceed 1000 m.
- Pneumatic conveying is safe and easily automated.
- A system may contain multiple product pick-up and distribution points.
- Pneumatic conveyors are low-maintenance.
- The system is easy to design and operate hygienically, which is crucial for infant formula production to comply with regulatory requirements.

For infant formula transport, flexibility of the system routing is often the primary reason for selecting pneumatic conveying. However, pneumatic conveying does have some disadvantages which must be taken into account (Fraige and Langston, 2006; Marcus et al., 1990; Molerus, 1996):

- The power consumption is often high.
- Significant wear and abrasion of the equipment may occur, particularly at bends when high gas velocities are used.
- While the conveyor may experience damage due to repeated impacts from the conveyed product, it is also possible for degradation of the product to occur during conveying.

The last two disadvantages can be mitigated in a well-designed pneumatic conveying system. Much research has been conducted on erosion and wear in pneumatic conveyors, e.g., Agarwal et al. (1985), Deng et al. (2005), Mason and Smith (1972), and Mills and Mason (1981). This phenomenon is strongly related to particle velocity by the

power-law relationship in Eq. 1.1, in which the exponent, n, is often around 3 (Marcus et al., 1990, p.431):

$$\text{Erosion} = \text{constant} \times \text{velocity}^n \tag{1.1}$$

The final disadvantage listed above, product attrition in pneumatic conveying systems, is the primary focus of this research. This is a very active area of research; some of the academic papers published in this area in the last 10 years include Aarseth (2004), Chapelle et al. (2004), Frye and Peukert (2002), Han et al. (2003), Konami et al. (2002), Rajniak et al. (2008), Salman et al. (2002), and Zhang and Ghadiri (2002).

Pneumatic conveying may be divided into two broad categories:

1. Dilute/lean phase
2. Dense phase

Dilute phase transport is characterised by low mass flow ratios[†][0–15 (Marcus et al., 1990, p.8), although often around 1 (Klinzing, 2001⋆)] and relatively high velocities (often 15–40 $\mathrm{m\,s^{-1}}$). Note that these figures are indicative; for example, Yanko (2007) suggests that mass flow ratios for dense phase conveying are typically 10–50. Dilute phase is the most commonly used type of conveying in industry. However, the use of high velocities exacerbates pipeline erosion and attrition of the conveyed product, although the latter may become irrelevant if accurate control of the product's physical properties (e.g., particle size distribution) is unimportant. This may be true if, for example, the material is dissolved after conveying. If the velocity is reduced below the saltation velocity, the conveying transitions to the dense phase regime. The saltation velocity is the gas velocity below which the particles begin to separate from the gas phase and thereafter are transported by sliding or rolling along the bottom of the pipeline (Hong and Tomita, 1995). The saltation velocity is usually measured experimentally, although theoretical and empirical expressions exist to allow its calculation from some properties of the material and conveying system (Jones and Leung, 1978).

Dense phase conveying came into use in the 1970s. Mass flow ratios in dense phase are greater than around 15 (Marcus et al., 1990, p.8) and typical conveying velocities are 4–10 $\mathrm{m\,s^{-1}}$ (Yanko, 2007). By conveying in dense phase, all three of the disadvantages of pneumatic conveying listed on p.11 are reduced. There is an overall energy saving compared to dilute phase: the respective specific energy consumptions are 150–250 $\mathrm{J\,kg^{-1}\,m^{-1}}$ for dilute phase and $< 10\ \mathrm{J\,kg^{-1}\,m^{-1}}$ for dense phase (Laouar and Molodtsof, 1998). Furthermore, the major reduction in conveying velocity lessens both pipeline abrasion and product attrition (Klinzing, 2001). The reduction in product breakage makes dense phase pneumatic conveying particularly suitable for transport-

[†]Mass flow ratio is the mass of solids per unit mass of conveying air (Marcus et al., 1990, p.8)

ing infant formula to the can filling line, where the minimisation of product breakage is highly desirable (see Section 1.6).

Of course, dense phase conveying also has some disadvantages compared to dilute phase conveying. It is not possible to convey all materials satisfactorily in dense phase whereas dilute phase conveying is more widely applicable. Dense phase conveying is most suitable for products which have a narrow distribution in particle size and little variation in shape (Yanko, 2007). Dense phase pneumatic conveying systems which operate by forming plugs of material in the pipeline may have problems when conveying either very fine powders or granular, permeable products. The conveyance of sticky products can also be problematic (Marcus et al., 1990, p.346). The capital and maintenance costs of a dense phase conveying system are usually considerably higher than those of an equivalent dilute phase system, as it is often necessary to incorporate apparatus for plug formation, plug destruction (for conveying in the strand or dune regimes) or supplementary air injection. Even with such devices in place, blockages of the conveying line can still occur when conveying sub-optimal materials, and reliability tends to be poorer than for a similar dilute phase system. For hygienic transport, dense phase systems are not self-cleaning, and therefore must be blown empty at regular intervals using a high-velocity pulse of air (Yanko, 2007). The system designer must also consider how to restart a dense phase conveying system following a power failure, when the pipeline may be obstructed by the conveyed material. In general, these potential disadvantages mitigate against the selection of dense phase conveying, unless either pipeline erosion or product attrition are critical considerations.

There are two additional points to be made regarding pneumatic conveying. The first is that the flow profile in dilute phase is homogeneous and essentially invariant. However, the conveyed solids are distributed non-uniformly over the pipe cross-section in the dense phase regime and a number of flow profiles exist. These were originally categorised by visual observation of flows in glass pipes (Wen and Simons, 1959), e.g., slug flow, dune flow, plug flow and ripple flow. The second point is that all of the pneumatic conveying experiments in this thesis make use of a conventional positive-pressure system, in which air enters the equipment under pressure. It is also possible to use a negative-pressure, or vacuum, system, although these are used less frequently than the positive-pressure equivalents (Yanko, 2007).

1.5 Infant Formula Microstructure

The three main components in infant formulae, comprising typically around 95% of any formula by mass, are carbohydrate, fat and protein. For example, the experimental infant formula used by Guo et al. (1998) to examine the distribution of components at

the microstructural level contained 56% carbohydrate, 28% fat, 12% protein, with the remainder divided between ash and residual moisture.

The carbohydrate is predominantly the disaccharide lactose (4-o-β-D-galactopyranosyl-D-glucopyranose), with very small amounts of others such as glucose, fructose and galactose. This can be treated as forming a continuous, crystalline phase in which other components are suspended. Lactose crystals can be obtained in a variety of forms, depending on the conditions of crystallisation (Wong et al., 1988, p.284). The principal factor governing the crystalline habit is the ratio of lactose concentration to its solubility. In infant formula, the additional components in the lactose lead to crystals which may be irregularly shaped and clumped, rather than having a regular form.

The fat which is present in the infant formulae is not distributed uniformly throughout the particle, but is instead localised in globules. These globules are much smaller than in raw milk due to breakage during high-pressure homogenisation. These globules have a large surface area collectively, and are bounded by artificial membranes of casein micelles and denatured whey protein clusters (Guo et al., 1996). These membrane-bounded fat globules can become attached to each other to form short-chained structures.

The vast majority of casein in bovine milk (approximately 95%) exists in the form of large colloidal particles, known as micelles. These micelles are generally spherical in shape, with an average diameter of 120 nm and a range from 50–500 nm (Fox and McSweeney, 1998, p.180). The same is true for infant formula, where the casein is predominantly in the form of micelles. Whey proteins exist in two main forms (α-lactalbumin and β-lactoglobulin), and in infant formula production, these can be denatured by pasteurisation (forming denatured whey protein clusters). These denatured whey proteins have a tendency to form appendages to casein micelles, leading to large protein aggregates.

1.5.1 SEM Images

As part of this research, some representative samples of infant formula were visualised using the scanning electron microscope (SEM) at the Teagasc Food Research Centre in Moorepark, Fermoy, Co. Cork. The instrument was a Carl Zeiss Gemini Supra 40VP field emission SEM (Carl Zeiss SMT AG, Oberkochen, Germany). Samples of infant formula for analysis were affixed to aluminium stubs using double-sided carbon tape and sputter-coated with a thin layer of chromium ($\ll$ 50 nm thick) for either 90 s or 120 s using an Emitech K550X coater (Quorum Technologies Ltd, Ashford, Kent, UK). The accelerating voltage used for the SEM was constant at 2 kV, while the magnification was varied from 50X to 5000X.

Figures 1.2 and 1.3 show micrographs of two agglomerates taken at different magnifications. Both are of infant formula B: this designation was given to a particular stage 2 infant formula which had the composition shown in Table 3.1 (p.50).

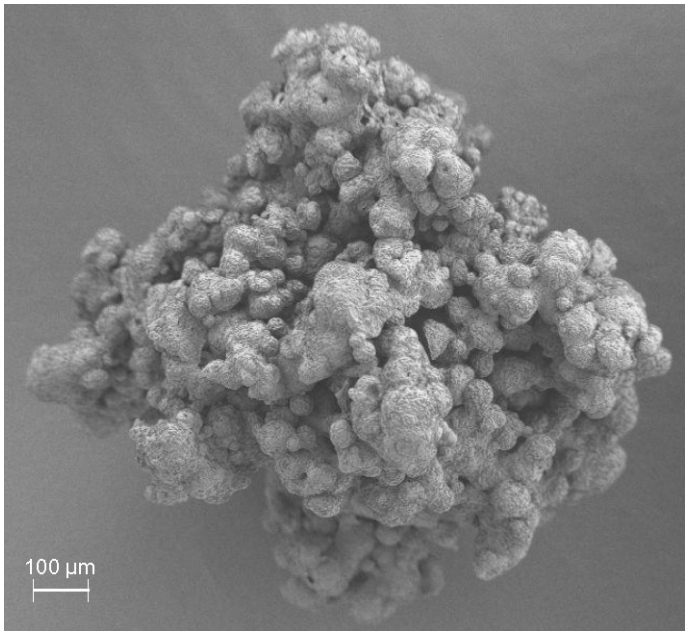

Figure 1.2: *SEM micrograph of an agglomerate of infant formula B at a magnification of 150X, where the scale bar has a length of 100 µm*

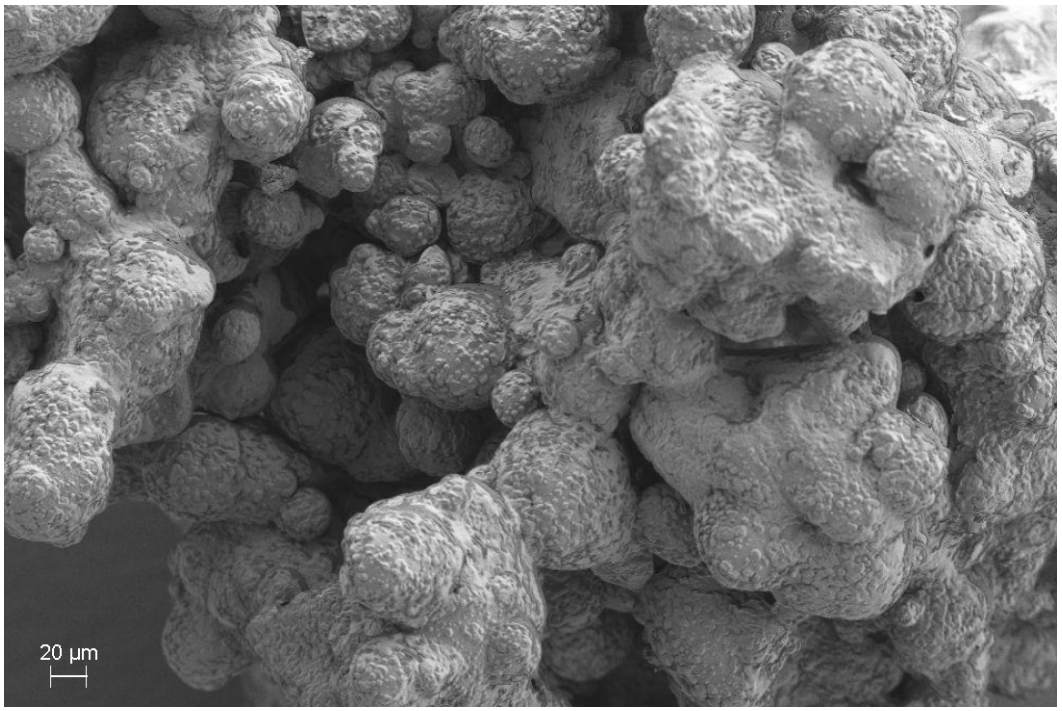

Figure 1.3: *SEM micrograph of part of an agglomerate of infant formula B (size range 710–850 µm) at a magnification of 500X, where the scale bar has a length of 20 µm*

The SEM was particularly useful for visualising damage of the agglomerates caused by mechanical loading. Figures 1.4 and 1.5 show representative micrographs of two agglomerates of the same infant commercial formula that was used for the pneumatic

conveying trials described in Chapter 2. The former shows one such agglomerate before conveying where there is no visible damage of the overall structure or of the component particles. Conversely, Figure 1.5 shows extensive damage; this was caused by multiple passes of the powder through a pneumatic conveying rig at 20 ms^{-1}.

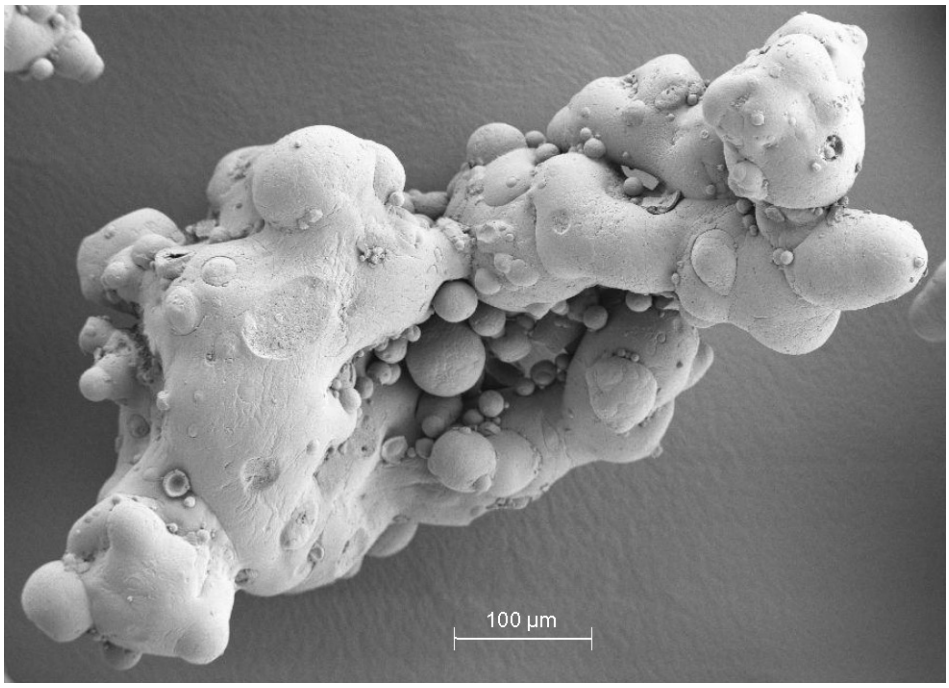

Figure 1.4: *SEM micrograph of an agglomerate of the infant formula used for the pneumatic conveying trials described in Chapter 2 at a magnification of 400X, where the scale bar has a length of 100 µm*

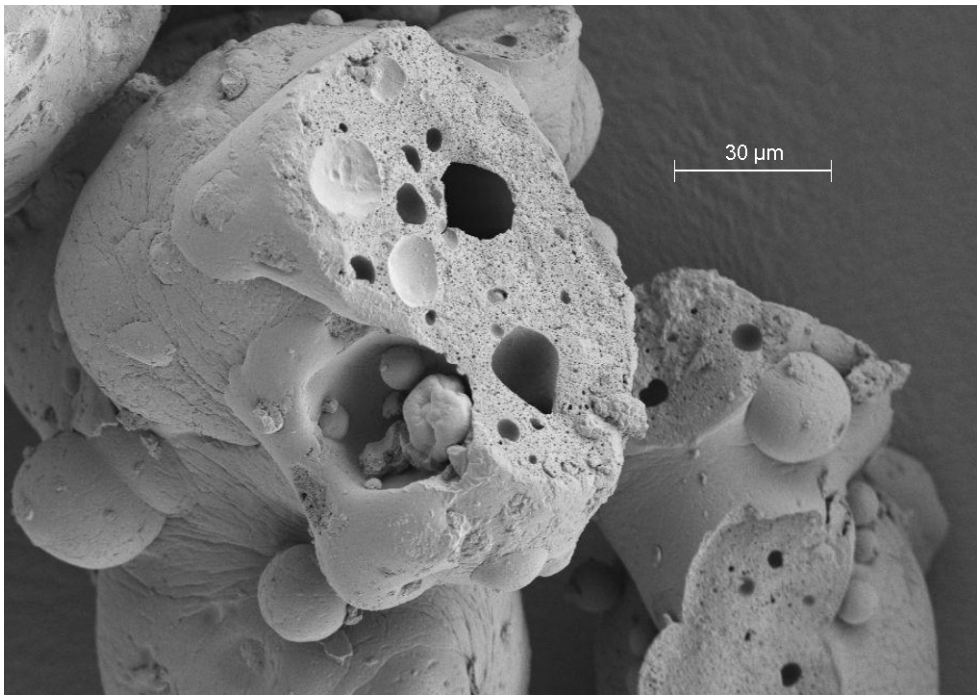

Figure 1.5: *SEM micrograph at 1500X magnification showing extensive damage of an agglomerate following pneumatic conveying at a superficial air velocity of 20 ms^{-1}*

1.6 Importance of Infant Formula Breakage

In Section 1.4.2, it was stated that pneumatic conveying is commonly used to transport infant formula from the spray dryers to the can filling line. These pneumatic conveyors are operated in dense phase mode; however, it is still possible for significant attrition of infant formula to occur. It must be noted that many infant formulae with different compositions exist, even within each stage (Section 1.1), and these formulae can vary considerably in terms of friability. Therefore, the attrition of one particular formula when conveyed through a pneumatic conveying system may be deemed acceptable, while a formula with a different composition may break down excessively using the same system and operating conditions. The fact that infant formula is an agglomerated product greatly increases the likelihood of disintegration upon impact with the walls of the pneumatic conveyor (Malave-Lopez and Peleg, 1986; Yan and Barbosa-Cánovas, 2000).

It may not be immediately apparent why attrition is of concern to infant formula manufacturers, since the formula must be reconstituted with water prior to consumption. The main reason why excessive breakage of the product is undesirable is because powdered infant formula is dispensed on a volume basis, rather than gravimetrically. A designated number of scoops of the powder are added to boiled water which has been allowed to cool sufficiently and either stirred well or shaken. As discussed in Section 1.1 on p.6, it is essential that the caregiver measures out powders accurately to achieve the correct liquid formula composition which fully meets the nutritional needs of the infant. Some details of the legislation governing infant formulae were also provided in Section 1.1. This legislation specifies the essential composition of infant formula when reconstituted in accordance with manufacturer's preparation instructions.

Since infant formula is dispensed by volume, bulk density is a key quality parameter for manufacturers, as this affects the quantity of powder which fills the scoop. If the bulk density was lower than specified, the reconstituted feed would be nutritionally deficient, while if too high, the feed would be too concentrated. Bulk density is one of the quality characteristics which is heavily influenced by breakage (Yan and Barbosa-Cánovas, 2000). Therefore, it is necessary for manufacturers to factor in an allowance in bulk density exiting the final dryer to compensate for powder breakage which inevitably occurs during in-plant handling and transport. If this breakage estimation is inaccurate, product bulk densities may be out of compliance with in-plant specifications and regulatory requirements may not be satisfied for the nutritional content of the reconstituted formula. While this is the main problem, there are other detrimental effects of infant formula attrition:

1. Attrition tends to disimprove the product's instant properties, such as wettability

(Hogekamp and Schubert, 2003). Since the primary reason for agglomeration was to benefit from improved rehydration characteristics, a process referred to as instantisation (Ortega-Rivas, 2009), it is clearly undesirable for some of the agglomerates to revert to primary particles during conveying.

2. The particle size distribution affects flowability (Peleg, 1977); hence, attrition of infant formula may negatively influence the can filling operation.
3. The fine dust generated by agglomerate breakage may have health consequences for employees in infant formula production facilities.

When these issues associated with attrition are considered, it is clear that it is beneficial for an infant formula manufacturer to minimise breakage of the product between spray drying and can filling. The ideal scenario would be conveyance of the infant formula without any attrition. In this case, the spray drying conditions could be controlled by the manufacturer to give an optimal product and obviate the requirement to add on estimated allowances for expected downstream powder breakage.

1.7 Research Motivation and Objectives

In Section 1.6, the importance of infant formula attrition was discussed. Although a major issue, little has been published on the subject of infant formula breakage during conveying. Manufacturers have some proprietary information regarding breakage of the specific formulae which they produce; however, such information is never published for confidentiality reasons. Efforts are rarely made to identify the root causes of attrition as knowing the breakage behaviour of each product manufactured without understanding these root causes is generally deemed sufficient for large-scale production. Furthermore, infant formula manufacturers rarely develop models which may provide additional insight into the agglomerate breakage process. As long as the infant formula produced consistently satisfies quality requirements, irrespective of how this is achieved (even using empirical observations), this is often acceptable for manufacturing purposes.

This lack of fundamental understanding can create a problem when the production process is changed, e.g., if a formula with a different composition is manufactured. The only way to estimate potential breakage is by comparison with other formulae of similar composition. There is no guarantee that predictions thus made will be reliable, which could result in the initial batches produced failing to meet specifications. Of course, knowledge of the product's breakage behaviour would be gained over time, thereby permitting breakage to be predicted accurately.

This scenario is clearly not ideal. It would be far better to supplement qualitative experimental knowledge with quantitative relationships between process or compositional

parameters and the bulk properties of the infant formula (and their susceptibility to variation) during conveying, based on an understanding of fundamental physical phenomena. The aim of this research was to address this gap in the current knowledge, with reference to the following three specific objectives:

1. Establish relationships between the geometry and operating conditions of a pneumatic conveying system, and the resulting changes in bulk properties of infant formula, including particle size, bulk density and wettability, upon conveying through the system.
2. Identify which infant formula components (e.g., fat, protein) have the greatest influence on attrition of the product.
3. Develop mathematical models at two scales to investigate both the breakage of individual agglomerates and the attrition of a large volume of powder when conveyed.

1.8 Thesis Structure

The subsequent chapters of this thesis are largely self-contained (with the exception of Chapter 7: a discussion of the overall findings of this work). Each chapter contains its own introduction with literature review, description of materials and methods, presentation of results with discussion, and conclusions sections. Where it is necessary to refer to other parts of the text, this is clearly indicated with reference to the appropriate section, table or figure and these internal references are often supplemented by a page number. Each of the remaining six chapters contained in this thesis is described briefly below:

Chapter 2 investigates the effect of varying seven pneumatic conveying parameters on four quality characteristics of infant formula to determine which parameters are most influential and the optimum combination of parameters to minimise variations in these quality characteristics.

Chapter 3 is similar to Chapter 2, except the effect of infant formula composition is investigated, rather than the pneumatic conveying parameters. This chapter also investigates the relationships between the mechanical responses of individual agglomerates of four infant formulae and their compositions.

Chapter 4 establishes a novel approach for calibrating discrete element models of bonded agglomerates using Taguchi methods for both 2D and 3D simulations.

Chapter 5 develops a discrete element model which simulates the key features of the uniaxial compression response of individual agglomerates, making use of the

calibration approach outlined in Chapter 4. The applicability of this discrete element model to dynamic loading was also evaluated.

Chapter 6 develops a probabilistic model which may be applied to predict attrition of a large volume of infant formula when conveyed through a pneumatic conveying system. The broad approach discussed in this chapter may be applied to any friable product.

Chapter 7 discusses the results obtained in the preceding chapters as an integrated body of work and states the main conclusions arising from this research.

The material contained in these chapters is supplemented by seven appendices, the content of which is discussed at the appropriate point in the main text.

2

Effect of Pneumatic Conveying Parameters on Physical Quality Characteristics of Infant Formula

Globally, most infant formula is sold in powdered form, and typically these powders are agglomerated for improved reconstitution. It is inevitable that some breakage of these agglomerates occurs during in-plant handling, transport and packaging; however, quantifying and controlling the amount of breakage which occurs is a very important issue for manufacturers which has major implications for product quality (as discussed in Section 1.6).

Dense-phase pneumatic conveying is often used in plants for transporting infant formulae from the drying operation to the filling line in order to minimise breakage of the agglomerates. While it is generally true that dense-phase pneumatic conveying causes low levels of product attrition (Section 1.4.2), there are three circumstances in which significant, undesirable amounts of product breakage may still occur:

1. If the infant formula being conveyed is extremely friable
2. If the operating conditions of the pneumatic conveying system are inappropriate
3. If the design of the pneumatic conveying system is sub-optimal

There is often limited scope to change either the composition of an infant formula or the production process to make the product less susceptible to breakage. The composition is largely dictated by regulatory authorities, who require specific nutritional requirements of infant formulae sold within their jurisdictions (Section 1.1). Other factors which influence the composition include financial considerations, since it is desirable to use less-expensive ingredients where possible, and regional preferences for sweetness or flavour. Altering the production process to reduce product breakage has many disadvantages: there would be "knock-on" effects on other product properties which would need careful consideration; key processes may require re-validation, which is

expensive and time-consuming; new equipment would constitute a capital expense; lost production time (and profit); operating procedures and other documentation would require revision; etc. The effect of composition on changes in key quality characteristics of infant formulae is discussed in Chapter 3; however, the easiest way to minimise infant formula breakage is to ensure that the dense-phase pneumatic conveying system is well-designed and is operated correctly. While this is an important issue, there is no published work which relates the design and operating conditions of a pneumatic conveying system to the corresponding effects on key quality characteristics of infant formula.

It has been demonstrated conclusively that increasing the air or particle velocity in a pneumatic conveying system increases product attrition (e.g., Kalman and Goder, 1998; Taylor, 1998; Zhang and Ghadiri, 2002). Most attrition in pneumatic conveying systems occurs around bends (Kalman, 1999), which makes the selection of bend type critical (Aarseth, 2004; Chapelle et al., 2004; Salman et al., 2002; Wypych and Arnold, 1993). Other influential factors include the length of the conveying line or number of passes through an experimental system (Kalman, 2000; Konami et al., 2002), the mass flow ratio (Han et al., 2003; Kalman, 2000) and structural characteristics of the conveyed product (Samimi et al., 2003).

This chapter details a comprehensive study that was carried out on seven pneumatic conveying parameters which may affect key quality characteristics of infant formulae, such as bulk density, particle size and wettability. A lab-scale modular pneumatic conveying rig was constructed, which allowed the selected parameters to be varied according to a Taguchi experimental design, and four responses were measured. The aim was to identify which parameters have the most significant effect on these responses, as it is more important to control these parameters accurately than those which are less influential. In practice, while the settings chosen by the system designer for some of the tested parameters (e.g., the vertical conveying length) would be constrained by physical restrictions, it is still important to understand how these parameters influence the key quality characteristics of infant formula. Another objective was to determine the optimum pneumatic conveying parameters to minimise variations in the measured product quality characteristics. This research also investigates whether the significant parameters are the same for different responses, and if any of the responses are relatively unaffected by conveying.

2.1 Introduction to the Taguchi Method

Genichi Taguchi is a Japanese researcher who introduced some new concepts on the objectives of quality management and selected a set of statistical methods and tools

to reach those objectives. He is widely regarded as pioneering the modern quality-by-design approach (Ross, 1988). The Taguchi approach, developed during the 1950s as an integrated process improvement technique (Taguchi, 1987), is now a key part of the 6σ methodology for world-class manufacturing. The Taguchi robust engineering design method has become very popular in industrial practice as a valuable tool to achieve quality by design and minimise non-conformity costs by establishing the optimum settings of a process that optimise its performance and the consistency of that performance (Taguchi, 1987). Many researchers have made use of Taguchi methods for this purpose, e.g., Hou et al. (2007), Kim et al. (2003), Mahapatra et al. (2008), Oktem et al. (2007), Ozbay et al. (2009), and Wu et al. (2005).

Taguchi's approach is one of a large range of Design of Experiments (DOE) methods, all of which share a common objective: to find the relationship between the process parameters and the process output by using a structured pre-planned methodology for obtaining experimental data. Appropriate DOE methods maintain an efficient balance between the amount of data required (resource intensity) and the precision and confidence of the conclusions (information quality), which also implies minimising the bias that may be induced by the sampling design. It should be noted that it is rarely feasible to eliminate biases completely from an experimental study, e.g., the composition of milk varies seasonally, yet experiments involving dairy powders (including those discussed in this thesis) seldom account for this effect because of practical considerations.

2.1.1 Orthogonal Arrays, Factors, Levels and Responses

The Taguchi method is often viewed as a three step process (Ross, 1988, p.168):

1. System design
2. Parameter design
3. Tolerance design

System design involves determining which parameters may have the greatest influence on the response and selecting suitable test settings for those parameters. The chosen parameters are the *factors* of the design, and the settings of the factors are referred to as *levels*. Those outputs which are recorded and analysed are the *responses*, e.g., profit margin or a suitable product quality characteristic. Parameter design is used to find the optimum levels for each factor from those identified by the system design. This requires the selection of a suitable orthogonal array which depends on the number of factors and levels to be tested (Ross, 1988, p.74). It is not necessary for the researcher to develop these arrays, since the commonly-used arrays are provided both in the literature and in many statistical software packages. These orthogonal arrays were

not developed by Taguchi, rather they originate from a variety of sources including fractional factorial and Plackett-Burman designs (Box et al., 1988). It is crucial to choose an array which is suitable for the application. Selecting a two-level array minimises experimental requirements but does not identify points of optimum operation within the solution space, rather only at its limits. Therefore, a three-level design is effectively the minimum for a typical optimisation procedure.

For the Taguchi method, orthogonal arrays are traditionally designated by L_n, where n is the number of rows. As an example, the simplest three-level orthogonal array is the L_9, which is shown as Table 2.1.

Table 2.1: *Standard form of the L_9 orthogonal array, where the numbers 1 to 3 represent factor levels*

Trial Number	Column			
	1	2	3	4
1	1	1	1	1
2	1	2	2	2
3	1	3	3	3
4	2	1	2	3
5	2	2	3	1
6	2	3	1	2
7	3	1	3	2
8	3	2	1	3
9	3	3	2	1

This array contains nine rows and four columns. Each control factor is allocated to one column of the array. The number of trials for each set of experiments is equal to the number of rows; thus, an L_9 array requires nine trials and can accommodate up to four three-level factors. It is conventional to denote the factor levels numerically so that the lowest level of any factor is 1, the second-lowest is 2 etc. If the actual levels of a factor are 5, 20 and 30, then these would correspond to 1, 2 and 3 in a three-level array. Levels do not necessarily need to be numerical, and if a factor is discontinuous, such as colour, then the levels may be assigned arbitrarily. If all columns of an array contain factors, the array is saturated; however, columns may be left unused, in which case they may permit some interactive effects to be tested for significance.

A relatively small set of basic arrays is used for the Taguchi method, although a range of techniques may be used to modify these arrays without loss of orthogonality (Taguchi et al., 1992). This is the defining property of orthogonal arrays and ensures balanced comparison of all factors. In an orthogonal array, each factor is tested at each level

the same number of times, and for any pair of columns, all possible permutations of levels are tested, and each permutation is tested an equal number of times. For the L_9, each factor is tested at levels 1, 2 and 3 on three occasions, and for any two columns, each of the nine possible permutations of levels are tested; thus, it satisfies the requirement for orthogonality. Following system and parameter design, tolerance design is used to tighten tolerances on statistically-significant parameters to reduce variation (Ross, 1988, p.168).

One disadvantage of the Taguchi approach is the creation of intricate confoundings between effects of factors and of interactions (Montgomery, 2009). This means that a column may contain a number of partial or full interactions, in addition to a factor. As an example, the interaction between the factors in columns 1 and 2 is distributed between columns 3 and 4 for any three-level array (e.g., the L_9 in Table 2.1). If factors are allocated to columns 1, 2 and 3 of this array, it would become impossible to distinguish between the effect of the factor in column 3 and the partial interactive effect due to the factors in columns 1 and 2, both of which are contained in column 3. The presence of confounding has significant implications for analysis of the results: in certain cases, it may be impossible to distinguish between the effects of factors and confounded interactions. The Taguchi method uses triangular tables and linear graphs to aid with column allocation. These identify the columns of a particular array which contain the interaction between any pair of columns (Taguchi, 1987). For this reason, the initial allocation of factors to columns should ideally be done with the knowledge of which interactions might be relevant or negligible.

2.1.2 Analysis of Variance (ANOVA)

The Taguchi method uses Analysis of Variance (ANOVA) for data interpretation (Ross, 1988; Taguchi et al., 1992). This is a statistical method used to quantify how much of the variability of the response can be attributed to each factor or interaction. The use of ANOVA obviates the requirement to establish an inference (interpolative) model to relate the system factors to responses. Taguchi's belief was that these inference models are often underpinned by patterns, or surfaces in the solution space, that do not reflect the behaviour of the real system. This results in the identification of points of optimum operation that are due to mathematical artefacts and may not exist in reality. Furthermore, using inference models pools the lack of fit of the model with all other sources of error. Since analysing sources of variability is one of the main reasons to use the Taguchi method, adding lack of fit, which is a limitation of the method of analysis and not a system characteristic, would not be beneficial.

If multiple data sets are available, Taguchi recommends combining repetitions of each

trial into signal-to-noise (S/N) ratios prior to analysis (Maghsoodloo et al., 2004). There are two main advantages of analysing the data with S/N ratios:

1. The mean response may be optimised while simultaneously taking the reduction of process variability into account.
2. The response is logarithmised prior to analysis which extends the region of linearity; this is advantageous as this method ultimately makes extensive use of linear statistics.

The disadvantage is that S/N ratios confound the effect on the average value of quality with the effect on the variability, so it does not elucidate which factors influence one and not the other, which could be useful for a full interpretation of the results. Three different equations are used for calculating the S/N ratio depending on the objective of the optimisation (Ross, 1988, p.172). These are given below as Eq$^{\underline{s}}$. 2.1–2.3:

$$\mathrm{S/N}_{\text{smaller-is-better}} = -10\log_{10}\left(\frac{1}{r}\sum_{i=1}^{r} y_i^2\right) \tag{2.1}$$

$$\mathrm{S/N}_{\text{larger-is-better}} = -10\log_{10}\left(\frac{1}{r}\sum_{i=1}^{r} \frac{1}{y_i^2}\right) \tag{2.2}$$

$$\mathrm{S/N}_{\text{nominal-is-better}} = -10\log_{10}\left(\frac{1}{r}\sum_{i=1}^{r} (y_i - y_{\text{target}})^2\right) \tag{2.3}$$

r is the number of repetitions of each trial, y_i is the (raw) response for trial i and y_{target} is the specified target value for the optimisation. The same equations are used for ANOVA, irrespective of whether the raw data or S/N ratios are used for the data analysis. The key ANOVA equations are provided below (Eq$^{\underline{s}}$. 2.4–2.11); for further detail, the reader is directed to Ross (1988).

The first quantity calculated in ANOVA is the total sum of squares (SS_t), which is a measure of the total variability of the data:

$$SS_t = \sum_{i=1}^{n_p} (y_i - \overline{y})^2 \tag{2.4}$$

n_p is the total number of data points and $\overline{y}$ is the global mean of the data.

The sums of squares due to factor j (SS_{f_j}) is the portion of SS_t that is explained by the fact that factor j changed settings in the design n_k times (n_j is the number of levels of factor j):

$$SS_{f_j} = SS_t - \sum_{k=1}^{n_j}\left(\sum_{i=1}^{n_p/n_j} (y_{i|k} - \overline{y_k})^2\right) \tag{2.5}$$

$y_{i|k}$ is the subset of data points in which factor j was tested at level k and $\overline{y_k}$ is the mean of this data subset. Note that this form of Eq. 2.5 requires orthogonality to be valid.

The sum of squares of the error, SS_e, is the portion of SS_t that is not accounted for by any of the factors, where n_f is the number of factors:

$$SS_e = SS_t - \sum_{j=1}^{n_f} SS_{f_j} \tag{2.6}$$

If main effects are of interest only, columns which do not contain factors are not considered and their effects form part of SS_e. It is also possible to analyse interactions in a similar manner to factors if sufficient degrees of freedom are available, unless this is prevented by confounding. The two-way interaction between factors j and m has a sum of squares ($SS_{f_j \times f_m}$) which is given by Eq. 2.7:

$$SS_{f_j \times f_m} = SS_t - SS_{f_j} - SS_{f_m} - \sum_{l=1}^{n_j} \left[\sum_{\substack{k=1 \\ k \neq l}}^{n_m} \left(\sum_{i=1}^{n_p/(n_j \times n_m)} \left(y_{i|lk} - \overline{y_{lk}} \right)^2 \right) \right] \tag{2.7}$$

n_j and n_m are the numbers of levels of factors j and m, respectively. Note that $n_j = n_m$ is not a requirement. $y_{i|lk}$ is the subset of data points in which factor j was tested at level l and factor m was tested at level k concurrently. $\overline{y_{lk}}$ is the mean of this data subset.

To test for significance, variances (V) are calculated by dividing the sums of squares by the respective degrees of freedom (υ). Three different degrees of freedom are defined:

$$\upsilon_{\text{total}} = n_p - 1 \tag{2.8}$$

$$\upsilon_{\text{factor}_j} = n_j - 1 \tag{2.9}$$

$$\upsilon_{\text{error}} = \upsilon_{\text{total}} - \sum_{j=1}^{n_{fi}} \upsilon_{\text{factor}_j} \tag{2.10}$$

n_{fi} is the number of factors and interactions analysed. For a valid ANOVA, it is necessary for $\upsilon_{\text{error}} \geq 0$. If $\upsilon_{\text{error}} = 0$, it is impossible to test for significance without pooling, i.e., without removing some factors or interactions from the analysis. Statistical significance can be determined for factor (or interaction) j by dividing V_j by the variance of the error, V_e, and comparing the result to the f-distribution value for the specified confidence level. This is equivalent to using the p-value to assess statistical significance: effects are deemed to be significant at the 90%, 95% or 99% significance levels if their p-values are less than 0.1, 0.05 or 0.01, respectively.

It is straightforward to identify the point of optimum using the Taguchi method when all interactions are neglected. The optimum level is selected for each factor as that which gives the desired trend in the response. For example, the objective of an optimisation procedure is always to maximise the response if the analysis was conducted using S/N ratios.

The corresponding response is then estimated by addition of the marginal means, which are the differences between the means of the subsets of data where each factor is at its selected optimum level, k ($\overline{y}|_{k_j}$), and the global mean, $\overline{y}$:

$$y_{\text{estimated}} = \overline{y} + \sum_{j=1}^{n_f} (\overline{y}|_{k_j} - \overline{y}) \tag{2.11}$$

Eq. 2.11 shows that the Taguchi method only considers as solutions combinations of those factor settings used in the design. Once the optimum response has been found, a confirmation experiment should be carried out unless the optimal factor levels correspond exactly to one of the rows of the orthogonal array; this is an unlikely event due to the experimental efficiency of these designs.

2.1.3 Advantages and Disadvantages of the Taguchi Method

The main advantages of the Taguchi approach are as follows:

- The experimental designs which make use of orthogonal arrays minimise the amount of data required, i.e., the method has good experimental efficiency.
- The analysis methods clearly identify what is being analysed and relate only to actual system behaviour (no pooling lack of fit of an inference model with the other error terms: Section 2.1.2).
- The method is capable of analysing discontinuous variables (e.g., colour), and if a factor is numerical, there is no requirement for its levels to be equi-spaced.

However, a theoretical analysis of the implications of Taguchi's choice of statistical tools identifies a number of limitations (Box et al., 1988; Montgomery, 2009); the most important is that the DOE with orthogonal arrays generates very intricate confoundings, as discussed in Section 2.1.1. It is often impossible to definitively distinguish between the effects of factors and confounded interactions. Therefore, while it is true that the analysis is very clear on which effects one is analysing, it must be understood that many of the effects being analysed are not individualised and actually pool a complex mix of effects. More data would be needed in order to distinguish and separate those effects, if desired. Of course, in systems where interactions are all negligible, the method works perfectly with no complications.

2.2 Materials and Methods

2.2.1 Raw Materials and Pneumatic Conveying Rig

A commercial infant formula was used for these trials containing approximately 57% carbohydrate, 28% fat, 11% protein, 2% ash and 2% moisture. The pneumatic conveying rig was assembled from hygienically-designed modular components using tri-clover clamps. The components were manufactured from 316L stainless steel with a 2B internal surface finish, except for the powder collection vessel which was made of polypropylene. The basic rig configuration was invariant, with two horizontal sections linked to a vertical section by two 90° bends. This configuration was selected to provide a close analogue of a real industrial system, in which inclined pipe sections are seldom used and a vertical conveying section is required to transport formulae from the spray dryer outlet to the silo inlet. Three different bend radii (50, 200, 300 mm) and three different vertical section lengths (340, 650, 960 mm) were available. The rig incorporated two in-line sight-glasses to allow visual observation of the powder transport operation. Dry compressed air entered the rig at the point indicated on Figure 2.1. The pressure of the air was regulated to provide different air velocities. The air velocity could be measured by inserting a 3 mm diameter pitot-static tube into a small resealable hole in one horizontal length. All air velocities in this chapter are stated in terms of the maximum superficial air velocities in the pipeline containing no powder, which could be measured more accurately than average velocity. After measuring the velocity, the pitot-static tube was removed and the measurement hole sealed before commencing powder conveying to avoid disruption of the flow.

For dilute phase operation, the powder was poured into the air stream using a funnel. To simulate dense phase (plug flow) operation, the funnel was removed and the opening sealed off with a blank. The first sight glass was filled with infant formula to create a single plug in the line before reassembling the rig and switching on the air supply with a ball valve. This plug was not compressed to avoid breakage of the powder before conveying.

The pipe diameter was constant at 25 mm, except for a 50 mm diameter terminal section. This section of larger diameter minimised breakage at the capture point by reducing the velocity of the air stream immediately before the capture vessel. The typical pipe diameter in an infant formula manufacturing plant is approximately 100 mm. Although the ratio of pipe diameter to particle diameter remained very large for the lab-scale rig, there are often issues when scaling up results obtained using small-scale pneumatic conveying systems to industrial-scale systems. This possible limitation must be remembered for the results given in this chapter. The end vessel incorporated filters

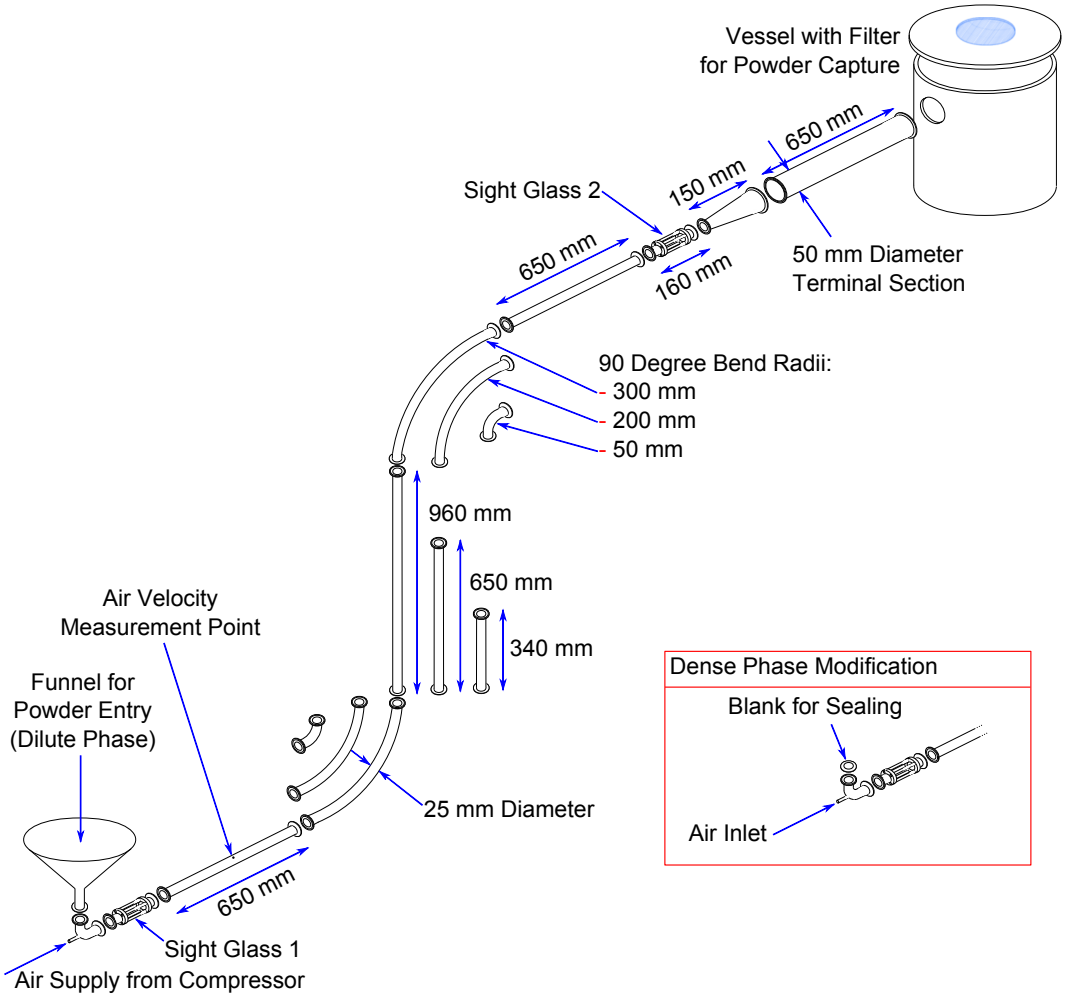

Figure 2.1: *An isometric view of the conveying rig in dilute phase configuration, with an inset showing the modification for dense phase conveying*

for separation of powder from the air, and air stream entry into the vessel was offset to create a swirling fluid motion and further reduce powder breakage.

Since infant formula is a hygroscopic material, it was stored in bulk in air-tight plastic bags inside stiff paper sacks. Smaller quantities were transferred into Ziploc bags for experiments. Any infant formula that was unnecessarily exposed to atmosphere for more than approximately 30 minutes was discarded. The experiments were also conducted in a manner which minimised the duration of exposure of the infant formula to the open air. The pneumatic conveying rig shown in Figure 2.1 was too large to place inside any available humidity-controlled environment. Therefore, all testing apparatus (Section 2.2.3) was prepared in advance and each experiment was carried out without interruption to minimise the exposure time.

2.2.2 Experimental Design

Seven factors were varied in these experiments, with all others held constant. Noise factors were not included in these experiments so only an inner array was used. All factors were controlled at three levels only, except mode of conveying (dilute or dense phase), which must be a two-level factor. The control factors and levels used for this experiment are shown in Table 2.2. Note that the number of passes for this experimental system was analogous to the length of an industrial conveying system, i.e., increasing the number of passes increased the effective length.

Table 2.2: *Control factors and levels used for the L_{18} experimental design*

Control Factors	Levels		
	1	2	3
Mode of Conveying	Dense	Dilute	
Plug Length *(Dense)*	50 mm	100 mm	150 mm
Solids Feed Rate *(Dilute)*	1 $g s^{-1}$	2 $g s^{-1}$	3 $g s^{-1}$
Air Velocity *(Dense)*	3 $m s^{-1}$	4 $m s^{-1}$	5 $m s^{-1}$
Air Velocity *(Dilute)*	10 $m s^{-1}$	20 $m s^{-1}$	30 $m s^{-1}$
Number of Passes through Rig	1	2	5
Length of Vertical Rig Section	340 mm	650 mm	960 mm
Radii of 90° Bends	50 mm	200 mm	300 mm

An L_{18} orthogonal array was chosen; this mixed-level array allows for one two-level factor and up to seven three-level factors to be tested. The standard form of the L_{18} array is provided in Appendix A (Table A.2; p.212) for information. The blocking of the design must be noted. For dense phase, the plug length factor exists but solids feed rate does not, and *vice versa* for the dilute phase. Furthermore, the mode of conveying determines the levels used for air velocity: if dense phase is specified, air velocity must be less than the saltation velocity for horizontal flow (Marcus et al., 1990), which was found during preliminary experiments. This situation may be interpreted using the trans-factor technique – a specific type of pseudo-factor design – to assign the orthogonal array (Taguchi, 1987). Mode of conveying is a branching factor, while plug length and solids feed rate are pseudo-factors or nested factors. A narrow range of velocities was used for dense phase conveying (3–5 $m s^{-1}$) as the velocity had to be less than the saltation velocity, yet also sufficient to ensure reliable conveying.

The L_{18} array provides 17 degrees of freedom for studying effects. Since the two-level factor requires one degree of freedom, and each three-level factor requires two, the factors in Table A.2 collectively account for 13 degrees of freedom. The vertical rig section length was assigned to column two of the array to allow its interaction with

the two-level factor to be studied; this is the only interaction which can be studied (Maghsoodloo et al., 2004) as others are partially confounded with the remaining three-level columns (Taguchi et al., 1992). Sufficient degrees of freedom are available to allow this interaction to be tested for statistical significance without pooling. After assigning the remaining factors to columns, the array in Table 2.3 was obtained.

Table 2.3: *L_{18} array showing the columns used after assigning all factors to the array*

Row	Column							
	Mode	Vertical Length	–	–	Air Velocity	No. of Passes	Bend Radii	Plug Length/ Solids Feed Rate
1	Dense	340 mm	1	1	3 ms^{-1}	1	50 mm	50 mm
2	Dense	340 mm	2	2	4 ms^{-1}	2	200 mm	100 mm
3	Dense	340 mm	3	3	5 ms^{-1}	5	300 mm	150 mm
4	Dense	650 mm	1	1	4 ms^{-1}	2	300 mm	150 mm
5	Dense	650 mm	2	2	5 ms^{-1}	5	50 mm	50 mm
6	Dense	650 mm	3	3	3 ms^{-1}	1	200 mm	100 mm
7	Dense	960 mm	1	2	3 ms^{-1}	5	200 mm	150 mm
8	Dense	960 mm	2	3	4 ms^{-1}	1	300 mm	50 mm
9	Dense	960 mm	3	1	5 ms^{-1}	2	50 mm	100 mm
10	Dilute	340 mm	1	3	30 ms^{-1}	2	200 mm	1 gs^{-1}
11	Dilute	340 mm	2	1	10 ms^{-1}	5	300 mm	2 gs^{-1}
12	Dilute	340 mm	3	2	20 ms^{-1}	1	50 mm	3 gs^{-1}
13	Dilute	650 mm	1	2	30 ms^{-1}	1	300 mm	2 gs^{-1}
14	Dilute	650 mm	2	3	10 ms^{-1}	2	50 mm	3 gs^{-1}
15	Dilute	650 mm	3	1	20 ms^{-1}	5	200 mm	1 gs^{-1}
16	Dilute	960 mm	1	3	20 ms^{-1}	5	50 mm	2 gs^{-1}
17	Dilute	960 mm	2	1	30 ms^{-1}	1	200 mm	3 gs^{-1}
18	Dilute	960 mm	3	2	10 ms^{-1}	2	300 mm	1 gs^{-1}

2.2.3 Product Quality Characteristics and Experimental Procedure

Four product quality characteristics were measured:

1. Bulk density
2. D[4,3] – volume mean diameter
3. Particle density
4. Wettability

For infant formula manufacture, bulk density is one of the most critical quality characteristics, as this determines the mass of powder which fills a measuring scoop used for dispensing powder on reconstitution. This was measured using a Stampfvolumeter STAV 2003 (J. Engelsmann AG, Luwigshafen, Germany). For each measurement, 100 g of powder was weighed into the graduated cylinder and tapped 1250 times to the extreme powder bulk density (GEA Niro, 2006).

The particle size distribution of the infant formula agglomerates was measured by laser diffraction using a Malvern Mastersizer S with dry powder feeder (Malvern Instruments Limited, Malvern, Worcestershire, UK). Although the air dispersion method has been shown to cause some attrition of the formula being tested (Kwak et al., 2009), it remains much more widely used than the alternative wet dispersion method. The particle size distribution was measured twice for each trial to increase accuracy, and the mean result was used for analysis. The volume mean diameter/De Brouckere mean diameter (D[4,3]) was used as the single measure to compare particle size results.

Agglomerates of infant formula contain internal cavities; however, it was not known whether or not these voids were impermeable to air for the formula tested. Particle density was found by nitrogen pycnometry using a Micromeritics Multivolume Pycnometer 1305 (Micromeritics Instrument Corporation, Norcross, GA, USA). By assessing the changes in particle density upon conveying, inferences could be made about the permeability of the subsurface cavities to air. The particle density was determined three times for each trial using the same sample and the mean result was used.

Wettability was measured using the GEA Niro Analytical Method (GEA Niro, 2009) based on the International Dairy Federation standard for determining the dispersibility and wettability of instant dried milk (International Dairy Federation, 1979). Ten grams of infant formula were placed inside a steel ring on top of a flat stainless steel plate. The plate was placed on top of a 600 ml beaker containing 250 ml of water at 25°C. The infant formula was scattered on the water surface by slowly withdrawing the plate. The wettability was recorded as the time required for all particles to become wetted, by visual inspection, from when the plate began being withdrawn. Note that low wettability times are desirable, indicating good wettability behaviour.

Three complete sets of replicates were carried out, giving 54 trials in total. Complete randomisation was used to minimise bias in the results, i.e., trials were randomly selected until all trials had been completed for a replicate, before proceeding on to the next replicate. Wettability was measured for only one replicate, while bulk density, particle density and D[4,3] were measured for all three replicates. These four quality characteristics were also measured prior to conveying: measurements were taken for four samples of infant formula per replicate, e.g., bulk density was measured for twelve

samples before conveying. The mean bulk density, D[4,3], particle density and wettability of the infant formula before conveying were 462 $kg\,m^{-3}$, 312 µm, 1107 $kg\,m^{-3}$ and 18 s, respectively.

2.2.4 Analytical Procedure

All data analysis was conducted using the percentage change in each measured powder quality characteristic before and after passage through the rig. The data were analysed using STATISTICA (v.7.1, StatSoft, Inc., Tulsa, OK, USA). The complete analysis may be divided into two parts:

1. The pseudo-factors were treated as categorical and an ANOVA was done using S/N ratios for each quality characteristic.
2. A polynomial model was fitted to the data, taking into account the nesting of factors.

Categorical ANOVA

As recommended by Taguchi, the trial replicates were combined into S/N ratios for each of the four responses. This was done for wettability even though data were available for only a single replicate. S/N ratios were calculated using the lower-is-best definition, since the smaller is the change in a quality characteristic during infant formula handling, the easier it is to control final product properties in the manufacturing plant. Ideally, the properties of the infant formula immediately after drying would be unchanged when the consumer reconstitutes the product. In that case, the spray drying conditions could be controlled to give an optimal product rather than needing to add estimated allowances for subsequent powder breakage.

An ANOVA was performed on the S/N ratios for each quality characteristic to identify statistically-significant factors. All factors were analysed without the inclusion of nesting in the array to avoid intricate confoundings which would prevent certain factor effects from being uniquely distinguished. For instance, no distinction was made between air velocities of 5 $m\,s^{-1}$ (the highest value for dense phase) and 30 $m\,s^{-1}$ (the highest for dilute phase), as both have the meaning "velocity as high as possible" in terms of the categorical classification. The same is true for equivalent levels of plug length and solids feed rate (both as high as possible, or as low as reasonable, or the mid-point).

Effects were calculated and contributions found by subtracting the global mean of the S/N ratios for each quality characteristic from the marginal means. These effects were tested for statistical significance. Contributions plots were drawn for each factor which

show the average effect of selecting any factor level on the responses. A second ANOVA was performed for four selected factors, taking nesting into account: mode of conveying, air velocity, plug length and solids feed rate. By omitting all other factors, confounding was avoided. The main purpose of the second ANOVA was to obtain contributions plots for air velocity and the pseudo-factors which show the required dependence on mode of conveying. It is noted that this procedure does not lead to any loss of information, because the impact of ignoring the nesting in the first ANOVA was that the importance of the nested factors may have been overestimated. Thus, the main outcome of the first ANOVA was to identify those factors which were not statistically-significant. The second ANOVA then gave a more accurate and real view of the results by considering the nesting.

Optimum factor levels were determined using the maximum S/N ratio contributions, and estimates of each product quality characteristic at these optimum levels were calculated. A verification experiment was done using the optimum settings to check the results of the analysis.

Polynomial Models

It is likely that the influence of certain factors on a characteristic depends on the mode of conveying, i.e., the air velocity might be expected to have far greater importance for dilute phase conveying than for dense phase. However, the ANOVAs did not consider this when evaluating the statistical significance of factors, including the air velocity and pseudo-factors. A complementary analysis was performed in which a polynomial model was fitted to the data. This allows the statistical significance of most factors to be evaluated while taking nesting into account, i.e., distinguishing between effects for dense and dilute phase conveying. This polynomial model was fitted to the raw data for each quality characteristic: bulk density, D[4,3], particle density and wettability. The model took the form of Eq. 2.12, where F_n represents the levels of factor n when coded between -1 and 1 and R is the model response:

$$\begin{aligned} R = a_0 &+ a_1F_1 + a_2F_2 + a_{22}{F_2}^2 + 0.5a_{31}F_3(1-F_1) + 0.5a_{32}F_3(1+F_1) + 0.5a_{331}{F_3}^2(1-F_1) \\ &+ 0.5a_{332}{F_3}^2(1+F_1) + a_4F_4 + a_5F_5 + a_{55}{F_5}^2 + 0.5a_{61}F_6(1-F_1) \\ &+ 0.5a_{62}F_6(1+F_1) + 0.5a_{662}{F_6}^2(1+F_1) \end{aligned} \tag{2.12}$$

By omitting quadratic effects of the number of passes and the plug length, a unique set of model parameters could be determined for each quality characteristic by least-squares regression. The linear and quadratic terms for F_3 and F_6 in Eq. 2.12 are multiplied by $(1 \pm F_1)$ to ensure that certain parameters are present in the models only if dense phase conveying is used, i.e., if F_1 = -1, while those parameters that are multiplied by $(1 + F_1)$ appear only if dilute phase conveying is used.

In the model fitting, the residual sums of squares for bulk density, D[4,3] and particle density were partitioned into pure error and lack of model fit components. This was not possible for wettability due to the lack of replicated measurements. Plots of model predicted values against experimental data were drawn to highlight bias, if present. Standardised effects were calculated for these parameters and these were shown on Pareto charts using a 95% significance level.

2.3 Results and Discussion

2.3.1 Categorical ANOVA

The results obtained for smaller-is-better S/N ratios of the four measured quality characteristics (bulk density, D[4,3], particle density and wettability) are provided in Table 2.4.

Table 2.4: *Responses for all four quality characteristics in terms of smaller-is-better S/N ratios*

Row	Bulk Density	D[4,3]	Particle Density	Wettability
1	−4.538	−9.335	−13.118	−24.952
2	−1.526	−7.946	−13.868	−23.380
3	−2.694	−13.514	−8.720	−32.168
4	−2.491	−20.124	−15.875	−37.938
5	−11.610	−9.152	−13.784	−28.227
6	−3.877	−12.273	−7.169	−31.846
7	−6.436	−13.803	−2.661	−34.299
8	−4.235	−15.296	−3.059	−26.680
9	−7.268	−13.093	−8.698	−35.530
10	−28.037	−27.381	−7.615	−41.213
11	−23.796	−23.101	−10.248	−32.349
12	−25.178	−21.136	−15.578	−32.033
13	−27.733	−28.024	−12.028	−45.385
14	−20.636	−21.168	−12.068	−28.014
15	−27.158	−27.634	−11.686	−42.457
16	−28.629	−29.566	−5.889	−39.563
17	−28.463	−28.099	−12.454	−46.194
18	−19.591	−19.239	−6.105	−30.120

Table 2.5 is the partial ANOVA table obtained by analysing these four sets of S/N ratios

as the responses, and ignoring nesting in the array. A significance level of 95% was selected as standard in this work.

Table 2.5: *Partial ANOVA table for S/N ratio responses. υ is the number of degrees of freedom, SS the sum of squares associated to each element of the table and p the p-value calculated with the respective variances. Statistically-significant effects at a 95% confidence level are denoted in bold and with an asterisk*

Factor	υ	Bulk Density		D[4,3]	
		SS	p	SS	p
Mode of Conveying (α)	1	1892.06	**0.000***	682.17	**0.007***
Vertical Length (β)	2	7.75	0.439	29.65	0.610
Air Velocity	2	61.52	**0.039***	52.16	0.448
Number of Passes	2	37.82	0.082	5.28	0.907
Radii of 90° Bends	2	29.41	0.116	24.62	0.658
Plug Length/Solids Feed Rate	2	7.75	0.439	8.14	0.862
$\alpha \times \beta$ Interaction	2	11.47	0.325	3.80	0.932
Error	4	15.23		105.54	
Total	17	2063.01		911.36	

Factor	υ	Particle Density		Wettability	
		SS	p	SS	p
Mode of Conveying (α)	1	2.51	0.731	215.70	0.097
Vertical Length (β)	2	114.88	0.153	81.37	0.483
Air Velocity	2	20.12	0.618	186.24	0.249
Number of Passes	2	13.09	0.722	16.01	0.847
Radii of 90° Bends	2	19.95	0.620	80.51	0.486
Plug Length/Solids Feed Rate	2	13.31	0.718	27.95	0.755
$\alpha \times \beta$ Interaction	2	15.30	0.687	4.87	0.949
Error	4	73.93		185.16	
Total	17	273.08		797.81	

Mode of conveying and air velocity had a statistically-significant effect on bulk density at the 95% level ($p < 0.05$). For D[4,3], mode of conveying was the only factor which was significant while for wettability, mode of conveying was significant at the 90% level. Air velocity had the second-highest sum of squares for both of these responses, but was not significant in either case, even at the 90% level. None of the factors had a significant influence on particle density. Since dense phase conveying is invariably

used for pneumatic transport of infant formula, the air velocity is the most critical factor which manufacturers must control to avoid attrition issues.

The raw data were also analysed to supplement this S/N ratio analysis, expressed as percentage changes from the mean value of the appropriate quality characteristic before conveying. The results are given in Table 2.6.

Table 2.6: *Partial ANOVA table for raw data analysis of percentage changes of four responses, where υ is the number of degrees of freedom, SS the sum of squares and p the p-value. Statistically-significant effects at a 95% confidence level are denoted in bold and with an asterisk*

Factor	υ	Bulk Density		D[4,3]	
		SS	p	SS	p
Mode of Conveying (α)	1	5381.26	**0.000***	2876.86	**0.007***
Vertical Length (β)	2	8.55	0.702	536.67	0.063
Air Velocity	2	601.38	**0.000***	275.39	0.231
Number of Passes	2	156.64	**0.003***	205.81	0.331
Radii of 90° Bends	2	167.31	**0.002***	233.76	0.286
Plug Length/Solids Feed Rate	2	57.70	0.103	182.42	0.374
$\alpha \times \beta$ Interaction	2	10.97	0.636	53.23	0.747
Error	40	478.82		3617.90	
Total	53	6862.62		7982.03	

Factor	υ	Particle Density		Wettability	
		SS	p	SS	p
Mode of Conveying (α)	1	3.59	0.597	15099	0.059
Vertical Length (β)	2	70.31	0.074	4784	0.420
Air Velocity	2	3.73	0.863	15108	0.135
Number of Passes	2	5.41	0.808	2876	0.568
Radii of 90° Bends	2	12.89	0.604	7214	0.302
Plug Length/Solids Feed Rate	2	5.29	0.812	973	0.811
$\alpha \times \beta$ Interaction	2	5.29	0.812	636	0.870
Error	40/4	504.70		8795	
Total	53/17	611.21		55485	

The results were broadly similar to those for the S/N ratio analysis in Table 2.5; the main difference was the increased number of statistically-significant factors caused by the rise in degrees of freedom of the error from 4 to 40 for all responses except wettability. For

bulk density, the number of passes and bend radii factors became significant at the 95% level. Mode of conveying and air velocity remained significant with the two highest sums of squares. For D[4,3], vertical length became significant at the 90% level and had the second-highest sum of squares after mode of conveying, whereas this factor was not close to significance in the S/N ratio analysis (p = 0.610). There was little change for the particle density and wettability results: for particle density, vertical length retained the highest SS and for wettability, the differences between S/N ratio and raw data analyses were minimal, as expected because of the absence of data replicates.

For those three responses where replicates were available, it was also possible to carry out an ANOVA on standard deviations between replicates, the results of which are given in Table 2.7. It is interesting that mode of conveying was statistically-significant for bulk density and D[4,3]. This indicates that this factor is important not only for minimising changes in quality characteristics caused by conveying but also for minimising the variability between results. However, it must be remembered that there is usually a large difference between the dense and dilute levels of this factor since pneumatic conveyors in industry seldom use velocities close to saltation.

Table 2.7: *Partial ANOVA table for analysis of standard deviations between replicates for three responses. υ is the number of degrees of freedom, SS the sum of squares and p the p-value. Statistically-significant effects at a 95% confidence level are denoted in bold and with an asterisk*

Factor	υ	Bulk Density		D[4,3]		Particle Density	
		SS	p	SS	p	SS	p
Mode of Conveying (α)	1	11.80	**0.023***	217.06	**0.009***	0.56	0.713
Vertical Length (β)	2	1.68	0.471	14.56	0.525	4.66	0.568
Air Velocity	2	1.34	0.536	19.61	0.437	6.25	0.484
Number of Passes	2	0.47	0.787	29.11	0.323	3.22	0.666
Radii of 90° Bends	2	4.42	0.206	7.35	0.704	0.20	0.972
P. Length/S. Feed Rate	2	2.25	0.384	12.09	0.577	4.74	0.563
$\alpha \times \beta$ Interaction	2	2.46	0.359	54.03	0.172	2.65	0.711
Error	4	3.67		38.27		14.27	
Total	17	28.09		392.08		36.56	

A more straightforward way of visualising these results was to partition the raw percentage data into six categories: one for each combination of mode of conveying and air velocity (the two most important factors). The mean percentage changes in bulk density, D[4,3] and wettability were calculated for each of these combinations, and are plotted on Figure 2.2. For example, using dilute phase conveying and an air velocity of

30 $m s^{-1}$ caused the bulk density to increase by 25.3%, on average, whereas selecting the same conditions reduced D[4,3] by an average of 21.8%.

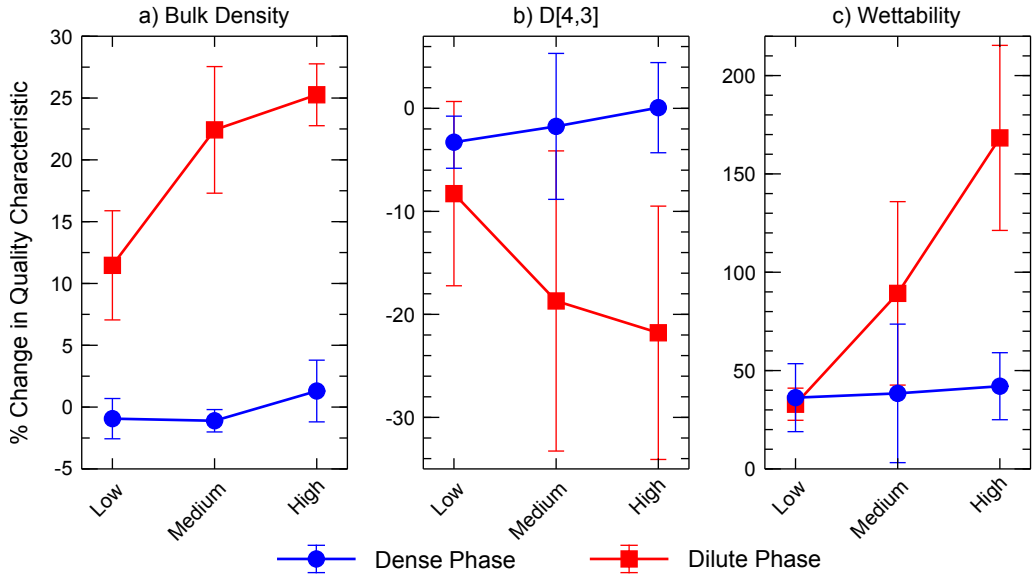

Figure 2.2: *Line graphs showing the average percentage changes in a) bulk density, b) D[4,3] and c) wettability caused by pneumatic transport at velocities of 3, 4 or 5 $m s^{-1}$ in dense phase or 10, 20 or 30 $m s^{-1}$ in dilute phase, where error bars indicate one standard deviation*

Figure 2.3 shows the ANOVA plot for S/N ratios using contributions, which shifts all data to be centred on the x-axis. Note that the air velocity and plug length/solids feed rate factors showed a strong dependence on the mode of conveying. The optimum level for each factor was selected as that which gave the maximum S/N ratio contribution.

Figure 2.4 compares the percentages of the total sums of squares attributed to each factor, and identifies the optimum level for each factor. For example, mode of conveying accounted for more than 90% of the total sum of squares for bulk density and the optimum level of this factor was 1, or dense phase by reference to Table 2.2. This sum of squares was calculated from Table 2.5 by dividing 1892.06 by 2063.01, and the level was selected from Figure 2.3.

Figure 2.4 was used to select the optimum settings. It is clear that dense phase conveying, the lowest air velocity of 3 $m s^{-1}$ and the shortest plug length of 50 mm should be chosen. The number of passes was set at 2, since this was the optimum for all responses except particle density, where it was not statistically-significant. The fact that 2 passes was selected as the optimum rather than 1 pass implies that the additional breakage caused by multiple passes through the conveying rig was negligible. The ANOVA confirms this: the number of passes was not significant for any quality characteristic except bulk density, where it was barely significant at the 90% level. A small amount of experimental variability could have caused 2 passes to be identified as being preferable to 1 pass, whereas there was minimal difference between the results obtained using these levels in

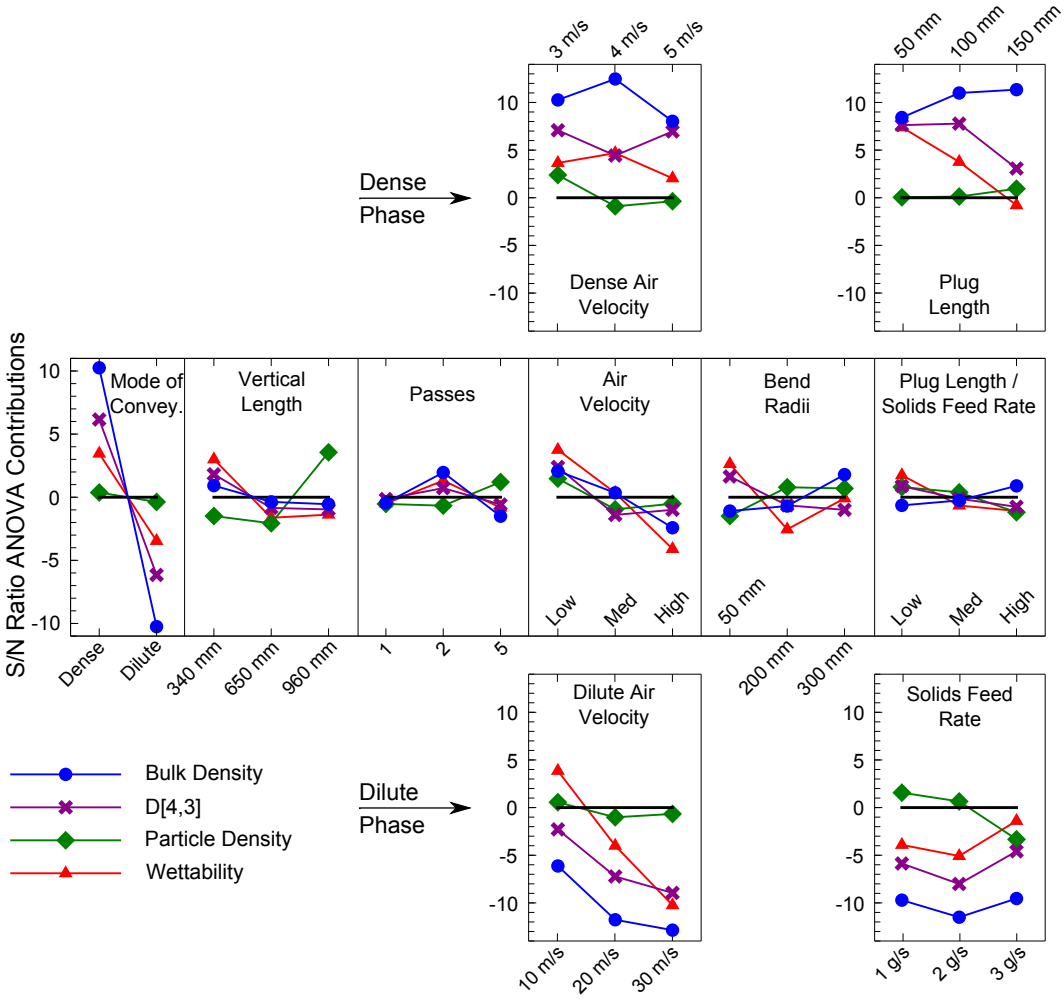

Figure 2.3: *ANOVA contributions plot for S/N ratio responses*

reality. A vertical section length of 960 mm was selected; this factor made the dominant contribution to the total sum of squares for particle density. Finally, a bend radius of 50 mm was chosen. This was the optimum setting for both D[4,3] and wettability. However, neither the radii of the bends nor the vertical conveying length were significant factors. The estimated percentage bulk density and D[4,3] changes at these optimum settings were negligible at 1.15% and -1.90%, based on S/N ratios. These were obtained by summing the contributions corresponding to the optimum settings (including the interaction) to the global mean of the S/N ratios for each quality characteristic.

Since the combination of settings identified as the optimum was not among the 18 experiments in the Taguchi design, a verification test was required. The bulk density and particle size distribution were measured before and after conveying a 600 g sample of infant formula through the rig using the optimal rig geometry and operating parameters. Bulk densities of this sample before and after were 457.1 $kg\,m^{-3}$ and 461.2 $kg\,m^{-3}$ respectively and the corresponding D[4,3] results were 310.36 µm and 306.91 µm. These were changes of 0.90% and -1.11%. These results were close to the predicted results and were essentially equivalent within the limits of experimental error. In addition to the

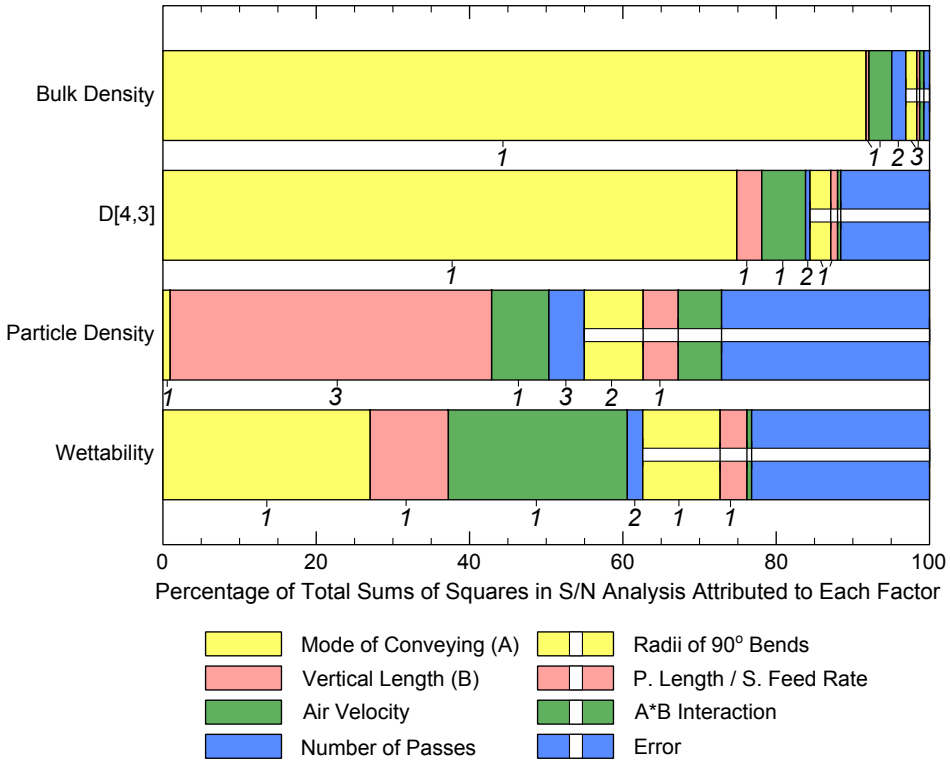

Figure 2.4: *Stacked bar plot showing the distribution of the total sums of squares for the S/N ratio analysis as percentages allocated to each factor, interaction or error and the optimum level of each factor*

means, the particle size distributions were almost identical, as can be seen from Figure 2.5.

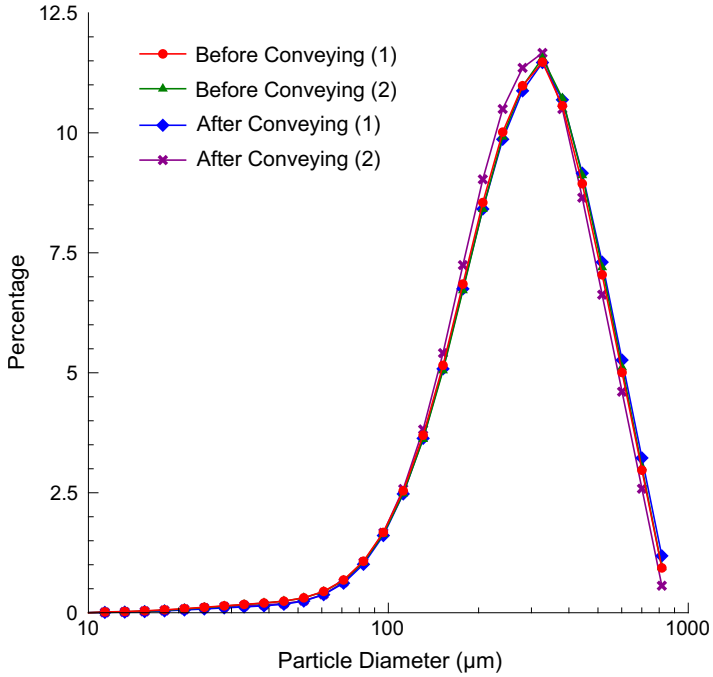

Figure 2.5: *Particle size distributions for infant formula samples before and after conveying using the optimum parameters*

2.3.2 Polynomial Models

The parameters obtained by fitting the polynomial model shown as Eq. 2.12 to the raw data for bulk density, D[4,3], particle density and wettability are shown in Table 2.8, while the correlations between model parameters are given in Table 2.9.

Table 2.8: *Parameters and p-values of polynomial models fitted to percentage data for four quality characteristics, where factors which are statistically-significant at a 95% level are indicated by an asterisk and are highlighted in bold*

Factor	Bulk Density		D[4,3]		Particle Density		Wettability	
	Param.	p	Param.	p	Param.	p	Param.	p
a_0	13.221	**0.000***	-15.715	**0.002***	-2.104	0.287	87.653	0.057
a_1	11.746	**0.000***	-8.827	**0.018***	1.301	0.375	36.204	0.214
a_2	0.462	0.330	-3.513	**0.020***	1.110	0.065	16.249	0.176
a_{22}	0.267	0.744	2.773	0.276	1.470	0.155	-20.099	0.306
a_{31}	1.054	0.281	2.284	0.448	0.019	0.987	5.561	0.798
a_{32}	-0.715	0.642	3.245	0.496	1.351	0.483	9.663	0.779
a_{331}	6.962	**0.000***	-7.361	**0.018***	0.362	0.765	65.061	**0.033***
a_{332}	-2.056	0.186	0.560	0.906	-0.451	0.814	2.416	0.944
a_4	1.272	0.121	-2.080	0.408	-0.197	0.845	2.046	0.910
a_5	-1.049	0.185	1.545	0.525	0.216	0.825	10.463	0.559
a_{55}	-1.678	0.253	1.132	0.802	-0.718	0.693	-8.759	0.789
a_{61}	-0.901	0.288	-0.435	0.867	0.595	0.572	9.880	0.606
a_{62}	-0.199	0.813	2.064	0.430	-0.599	0.570	6.067	0.749
a_{662}	-3.950	**0.020***	7.269	0.156	-1.328	0.517	-14.480	0.695

Table 2.10 contains the R^2 and $R^2_{adjusted}$ values for the model fits, along with the percentages of the total model sum of squares attributed to error, subdivided into pure error and lack of model fit components. The model fit was particularly good for bulk density, where less than 5% of the total sum of squares was due to error, and less than 1% of this total was due to lack of model fit. However, the model fit for particle density was extremely poor: more than 80% of the total sum of squares was due to error. This result, in conjunction with the lack of any statistically-significant factors in Table 2.5, confirmed that the particle density of the infant formula tested was not affected by pneumatic conveying. Since agglomerates of such formulae contain internal cavities, there must be sufficient surface fissures or pores to permit the ingress of nitrogen into most of these voids when measuring particle density by pycnometry. Therefore, when the agglomerates were damaged during conveying, the change in particle density was negligible.

Table 2.9: *Correlation matrix for parameters of the model shown as Eq. 2.12*

	a_{662}	a_{62}	a_{61}	a_{55}	a_5	a_4	a_{332}	a_{32}	a_{331}
a_1	0.707	0.000	0.000	0.000	0.000	0.000	0.707	0.000	-0.707
a_2	0.000	0.000	0.000	0.000	0.000	0.000	0.000	0.000	0.000
a_{22}	0.000	0.000	0.000	0.000	0.000	0.000	0.000	0.000	0.000
a_{31}	0.000	0.000	0.000	0.408	-0.047	0.283	0.000	0.000	0.000
a_{331}	-0.500	0.000	0.000	0.000	-0.287	0.208	-0.500	0.000	1.000
a_{32}	0.000	0.000	0.000	-0.408	0.047	-0.283	0.000	1.000	
a_{332}	0.500	0.000	0.000	0.000	0.287	-0.208	1.000		
a_4	-0.208	-0.283	0.283	0.000	0.000	1.000			
a_5	-0.115	-0.375	0.375	-0.115	1.000				
a_{55}	-0.250	0.204	-0.204	1.000					
a_{61}	0.000	0.000	1.000						
a_{62}	0.000	1.000							
a_{662}	1.000								

	a_{31}	a_{22}	a_2	a_1
a_1	0.000	0.000	0.000	1.000
a_2	0.000	0.000	1.000	
a_{22}	0.000	1.000		
a_{31}	1.000			

Table 2.10: *Metrics quantifying goodness of fit of the polynomial models*

Response	R^2	$R^2_{adjusted}$	% Sum of Squares		
			Error	*Pure Error*	*Lack of Fit*
Bulk density	0.954	0.939	4.616	3.911	0.705
D[4,3]	0.620	0.497	37.976	34.223	3.753
Particle density	0.192	-0.070	80.775	75.908	4.867
Wettability	0.915	0.639	8.484	—	—

In all cases, some of the sum of squares attributed to error was caused by the omission of two quadratic effects from the model; however, the proportion of the sum of squares caused by lack of model fit was always low, indicating that neither quadratic effect was very important. The contributions plot for the plug length factor confirmed this, since it did not exhibit a marked curvature for any response. However, the contributions plot for the number of passes was notably curved for bulk density with the maximum S/N occurring at the intermediate level. This factor was also significant at a 90% level in

the categorical analysis, yet the omission of the quadratic effect did not significantly affect the model fit: a result which demonstrated the dominance of the mode of conveying factor for the bulk density response. Plots of model predicted values against experimental data are shown in Figure 2.6.

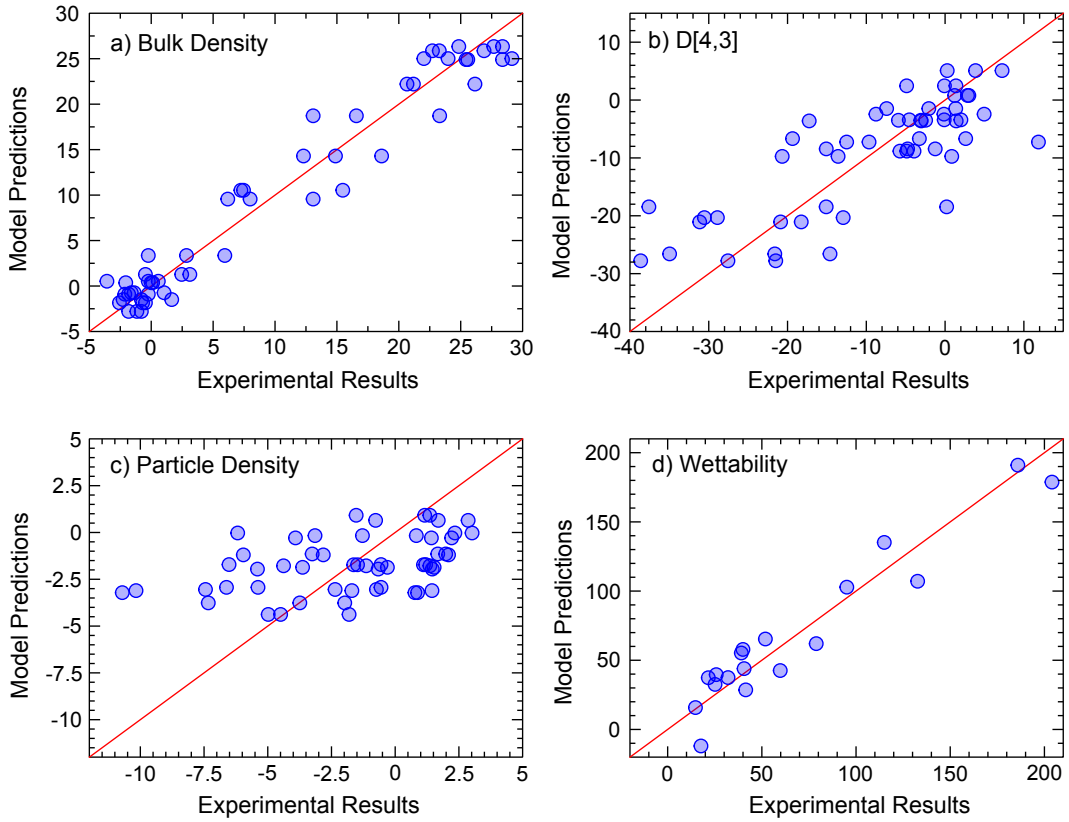

Figure 2.6: *Plots of model predictions versus experimental results for four responses: a) bulk density, b) D[4,3], c) particle density and d) wettability*

No bias was apparent for bulk density or wettability. The model for D[4,3] showed a slight tendency to under-predict the degree of product breakage at high attrition levels, e.g., the largest absolute percentage change in D[4,3] was 38.6%, whereas the model predicted a difference of 27.8%: a considerable disparity. The bias in the model for particle density was even more evident. This model under-predicted large changes in particle density and overestimated small density changes.

Pareto charts for the four quality characteristics are shown in Figure 2.7. Mode of conveying was significant for both bulk density and D[4,3], while the linear parameter for air velocity in dilute phase was significant for all quality characteristics except particle density. It is interesting to note that the equivalent parameter for dense phase conveying was not close to significance for any response. Therefore, if dense phase conveying is used for infant formula transport, air velocity is not likely to have a significant effect on measured quality characteristics. However, the choice of air velocity remains critical to ensure consistent, reliable flow through the pneumatic conveying system. It should be noted that there are considerations other than the effect on product quality

characteristics which influence the choice of settings of a factor. For example, the air velocity and solids feed rate or plug length affect the throughput of a conveying system, and if a certain mass flow rate is required, this imposes restrictions on the settings chosen for these parameters. Other influential parameters were the quadratic parameter for solids feed rate for bulk density and the linear parameter for length of the vertical rig section. The latter was statistically-significant only for D[4,3], but had the largest standardised effect for particle density and the second-largest for wettability.

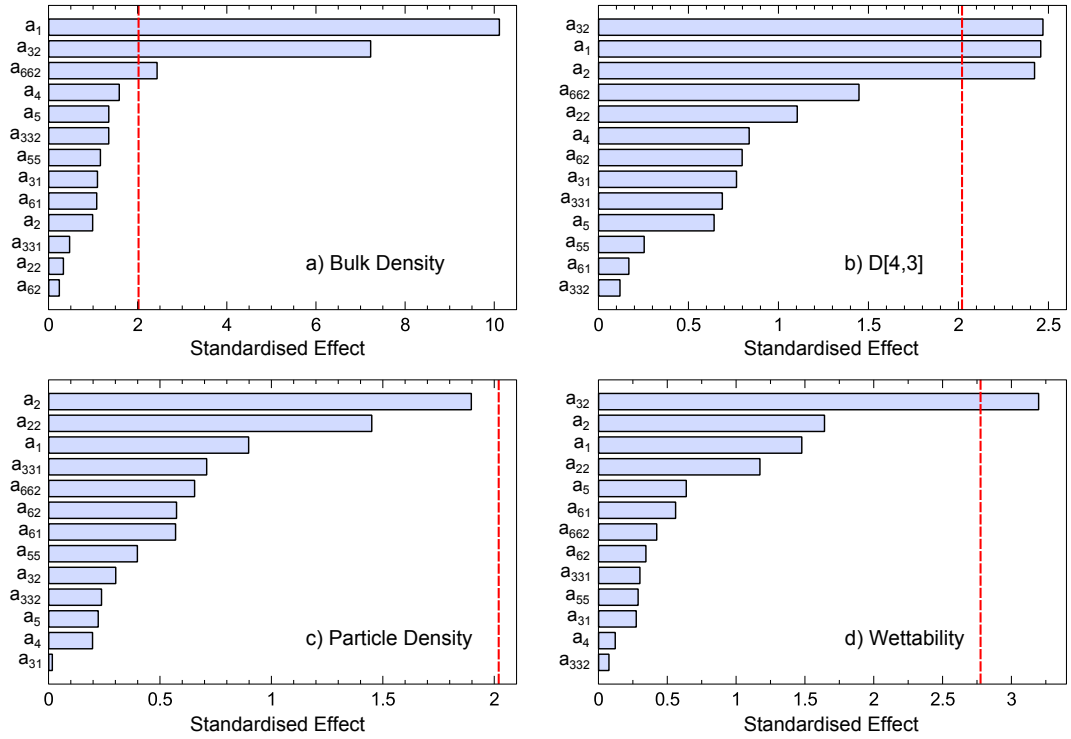

Figure 2.7: *Pareto charts showing the standardised effects for each term in the fitted model for a) bulk density, b) D[4,3], c) particle density and d) wettability, where the dashed lines indicate the 95% significance level*

2.4 Conclusions of Chapter 2

A lab-scale modular pneumatic conveying rig with a diameter of 25 mm was used to investigate the effect of varying seven factors on four product quality characteristics: bulk density, volume mean diameter, particle density and wettability. The main conclusions of this chapter are summarised as follows:

1. Mode of conveying and air velocity had a statistically-significant effect on bulk density at a 95% level. For D[4,3] and wettability, mode of conveying was the only significant factor, at only a 90% level for the latter. None of the factors had a statistically-significant influence on particle density.

2. Optimum settings for this system were dense phase conveying with a 50 mm

plug length, 960 mm vertical section, 3 $m s^{-1}$ air velocity, 2 passes and 50 mm bend radii. Estimated bulk density and D[4,3] changes at these optimum settings were 1.15% and -1.90%. A verification test obtained similar changes of 0.90% and -1.11%.

3. By fitting a polynomial model to the raw data, it was shown that air velocity was significant for only dilute phase conveying, and not for dense phase. These results imply that the resulting changes in infant formula quality characteristics caused by conveying will be negligible, irrespective of the settings chosen for the other conveying parameters, provided that the air velocity is selected to ensure dense phase conveying.

3

Effect of Composition on the Mechanical Response of Agglomerates of Infant Formulae

Agglomeration is widely used to enhance the reconstitution properties of dried powders, such as infant formulae (Ortega-Rivas, 2009). Breakage of infant formula agglomerates during in-plant handling and transport is undesirable: implications range from deterioration of the product's instant properties such as wettability (Hogekamp and Schubert, 2003), to failure of product bulk densities to comply with predetermined quality control limits, a subject discussed in Section 1.6 on p.17. The issue of agglomerate breakage is often significant since agglomerates tend to be considerably more fragile, and therefore more liable to disintegrate under mechanical loading, than the primary particles from which they are formed.

Dense phase pneumatic conveying is often used for transporting infant formula to powder storage silos and packaging lines after spray drying (Section 1.4.2), during which the agglomerates experience many transient contacts with other agglomerates and the inner wall of the pipeline. It is known that the composition of dairy powders affects quality characteristics such as flowability (Benkovic and Bauman, 2009; Fitzpatrick et al., 2007). However, little information is available in the literature to relate the composition of infant formulae to the macro-scale changes in key quality characteristics that occur during pneumatic conveying. As discussed in Chapter 2, there might be limited scope to change the composition of an infant formula to reduce attrition following spray drying. However, it is important to quantify the changes in product properties, even if they are very large, so that these changes may be predicted accurately.

The forces experienced by individual agglomerates at any instant during conveying are very difficult to quantify experimentally. One feasible alternative is to study the breakage behaviour of single agglomerates under controlled laboratory conditions using diametrical compression. Using this approach, detailed information about the force-

deformation response is provided (Adams et al., 1994; Antonyuk et al., 2005; Khanal et al., 2008), mechanical properties such as agglomerate strength and toughness may be measured (Bika et al., 2001), and expressions such as those developed by Rumpf (1962) and Kendall (1988) may be applied to relate the agglomerate strength to properties of the primary particles and inter-particle bonds (Ghadiri et al., 2007, p.840; Samimi et al., 2003). Advances in technology have also made it possible to study individual agglomerates under dynamic loading by recording high-speed video footage of agglomerate impacts (e.g., Samimi et al., 2004; Subero and Ghadiri, 2001). Both the static and dynamic loading cases can provide valuable insights into the micro-scale behaviour of the agglomerates during loading which influences the macro-scale changes in quality characteristics.

The research detailed in this chapter had two main objectives:

1. To investigate the relationship between composition and the resulting changes in key quality characteristics, such as bulk density and wettability, when subjected to conveying. This potential relationship was assessed via pneumatic conveying trials using four formulae of differing compositions.
2. To establish whether the mechanical response characteristics of the individual infant formula agglomerates, including stiffnesses and coefficients of restitution, may be predicted by compositional trends. Static uniaxial compression tests as well as dynamic drop tests were used.

In addition to their application in this chapter, some of the results of the uniaxial compression tests are also used in Chapter 5 to calibrate a discrete element model.

3.1 Materials and Methods

3.1.1 Infant Formulae

Four typical infant formulae were tested in this work. Their compositions are shown in Table 3.1 in order of increasing protein to fat ratio. As discussed in Section 1.1, manufacturers typically (though not always) divide their core infant formula ranges into four or fewer age-based categories. The tabulated compositions of formulae A–D approximate those of typical stage 1–4 infant formulae, respectively.

The size range of the agglomerates was restricted for both the uniaxial compression and drop test experiments, both to control one of the sources of variability and to simplify agglomerate handling. A sieve shaker was used to isolate the fraction of the infant formulae between 710 µm and 850 µm using the apparatus shown in Figure 3.1. A sieving time of 5 min was used. The action of the sieve shaker was likely to cause some attrition of the infant formula agglomerates; however, little could be done to prevent

Table 3.1: *Compositions of the infant formulae used in terms of their major components, in order of increasing protein to fat ratio*

Formula	Percentages					Protein:Fat
	Carbohydrate	Fat	Protein	Ash	Moisture	
A	56.5	28.8	10.7	2.0	2.0	0.372
B	56.1	22.1	15.4	4.4	2.0	0.697
C	58.9	17.1	14.8	5.2	4.0	0.865
D	58.9	15.2	16.7	5.2	4.0	1.099

this. Once isolated, the agglomerates were stored in an air-tight container with a large quantity of silica gel desiccant beads to inhibit moisture absorption. The remaining fractions (< 355 µm; 355–710 µm; > 850 µm) were discarded.

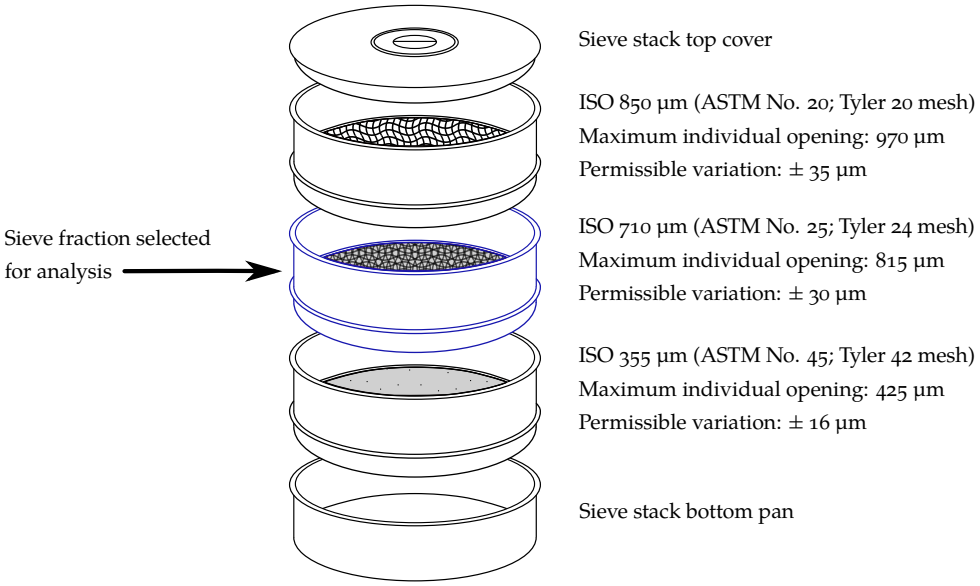

Figure 3.1: *Diagram showing the sieve stack used for isolating infant formula agglomerates in the 710–850 µm size range*

3.1.2 Pneumatic Conveying Experiments

The pneumatic conveying rig was the same modular 316L stainless steel system used for the experiments in Chapter 2. This rig is described in detail in Section 2.2.1 on p.29. However, the configuration of the rig was standardised for all experiments in this chapter, since the only variables of interest related to composition of the formulae. A diagram of this standardised pneumatic conveying rig is given as Figure 3.2 while Table 3.2 shows the invariant settings chosen for these experiments. Three air velocities were used for this study: one in the dense phase regime (4 $m\,s^{-1}$) and two in the dilute phase regime (10 $m\,s^{-1}$ and 20 $m\,s^{-1}$).

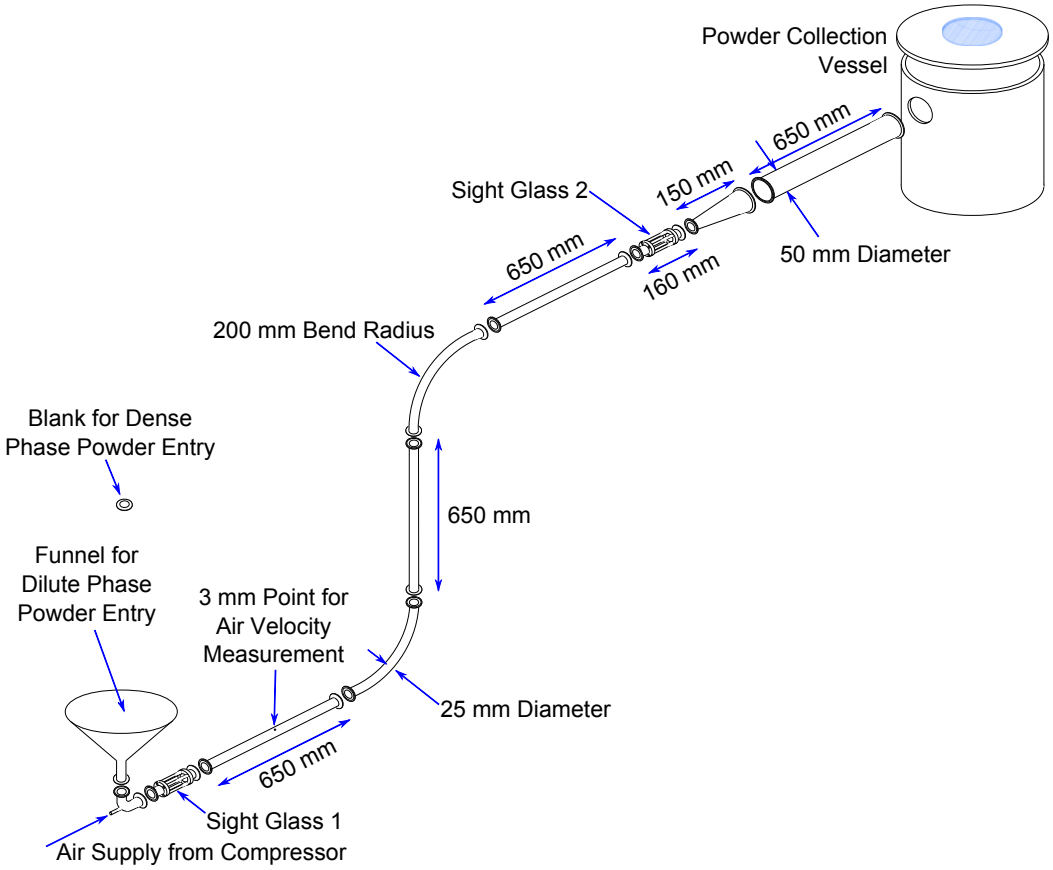

Figure 3.2: *An isometric view of the pneumatic conveying rig (modification of Figure 2.1 on p.30)*

Table 3.2: *Configuration selected for the pneumatic conveying experiments to investigate the effect of composition on quality characteristics of infant formulae*

Parameter	Chosen Setting
Plug Length *(Dense)*	100 mm
Solids Feed Rate *(Dilute)*	1 $g s^{-1}$
Number of Rig Passes	1
Length of Vertical Rig Section	650 mm
Radii of 90° Bends	200 mm

3.1.3 Measured Product Quality Characteristics and Experimental Procedure

Five product quality characteristics were measured:

1. Bulk density
2. D[4,3]
3. Wettability
4. Hausner ratio

5. Percentage surface (solvent extractable) free fat

The first three of these were measured using the same methods outlined in Section 2.2.3. Hausner ratio is an indicator of powder flowability, which may be calculated from the tapped bulk density using Eq. 3.1 (Hausner, 1967).

$$\text{Hausner ratio} = \frac{\text{Tapped bulk density}}{\text{Poured bulk density}} \tag{3.1}$$

A funnel (11.8 mm outlet diameter) was used when slowly pouring the infant formula into the graduated cylinder. In cases where cohesive arching prevented smooth flow, the side of the funnel was tapped to initiate movement. A Hausner ratio of 1 indicates that the bulk solid is incompressible, and the larger the Hausner ratio is, the poorer the flowability (Schulze, 2008, p.179). Table 3.3 shows a descriptive flowability scale which is sometimes used (e.g., Sanganwar and Gupta, 2008) to describe the flow properties of a powder based on the Hausner ratio.

Table 3.3: *Descriptors of powder flowability based on the Hausner ratio*

Flow Character	Hausner Ratio
Excellent	1.00–1.11
Good	1.12–1.18
Fair	1.19–1.25
Passable	1.26–1.34
Poor	1.35–1.45
Very poor	1.46–1.59
Very, very poor	> 1.60

The percentage free fat of the infant formulae was determined using the relevant GEA Niro Analytical Method (GEA Niro, 2005). Free fat is an important property for infant formula manufacturers: if it is excessively high, a fatty layer would appear on the surface of the reconstituted formula which is organoleptically undesirable. It was measured by agitating 10 g of infant formula with 50 ml of petroleum ether for 15 minutes using a Stuart SF1 flask shaker (Bibby Scientific Limited, Stone, Staffordshire, UK), filtering the resulting solution through Whatman Grade 113 filter paper and evaporating 25 ml of the filtrate to dryness. Most of the ether was evaporated in a fume hood before the samples were dried in an oven at 105°C for 90 minutes: a more rigorous criterion than the one hour drying time required by the standard (GEA Niro, 2005). The mass of the residue was then measured. The petroleum ether used had a boiling point of 40–60°C (min. 95%) and a density of 0.640–0.655 $\mathrm{g\,ml^{-1}}$ at 20°C (ACS Grade, Sigma-Aldrich, St. Louis, MO, USA).

All pneumatic conveying trials were conducted three times. The Hausner ratio and the free fat were measured for only one replicate, whereas the other three quality

characteristics were measured for all replicates. For each replicate, bulk density and wettability were measured once, giving three measurements in total for each pneumatic conveying trial. D[4,3] was measured twice for each replicate, giving six measurements for each trial. Free fat and Hausner ratio measurements were carried out in duplicate to allow the variability in the measurements to be estimated. Properties of the infant formulae before conveying were also measured for comparison. In all cases, the order of the trials was completely randomised to minimise the bias in the results.

3.1.4 Calculation of Relative Breakage

Rather than using the change in D[4,3] (or any similar definition of average particle size) to quantify particle breakage, the approach proposed by Hardin (1985) which gives insight into the breakage which occurs in different size fractions of the material under loading was used. This method for quantifying breakage using particle size distributions is commonly used in the field of soil mechanics (e.g., Coop et al., 2004; Donohue et al., 2009). Particle size distributions are often presented as shown in Figure 3.3a, with percentages of the particles contained in each size category shown on a linear vertical axis. To apply Hardin's method, it is necessary to present cumulative particle size distributions, where the vertical axis shows the percentage of the particles which is finer than the corresponding particle diameter. The particle diameter must be displayed on a logarithmic axis. This is shown in Figure 3.3b for the same particle size distributions considered in Figure 3.3a.

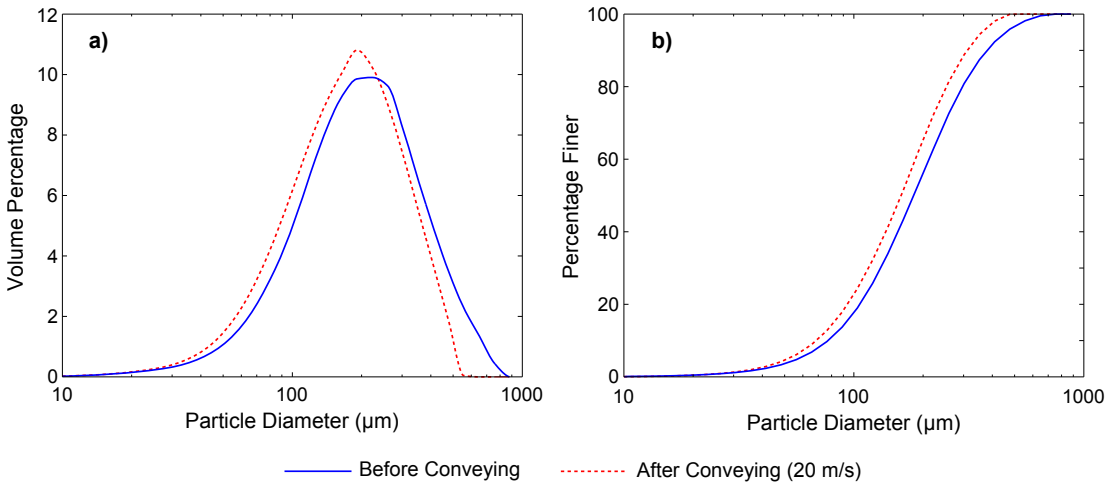

Figure 3.3: *Alternative presentations of the same particle size distributions for infant formula B before conveying and following pneumatic transport at 20 ms^{-1}*

Hardin defined three measures: breakage potential (B_p), total breakage (B_t) and relative breakage (B_r). The breakage potential, B_p, and the total breakage, B_t, represent the shaded areas on Figure 3.4. A baseline particle size must be selected; Hardin used 74 μm although other researchers have used different values, e.g., Coop et al. (2004) and

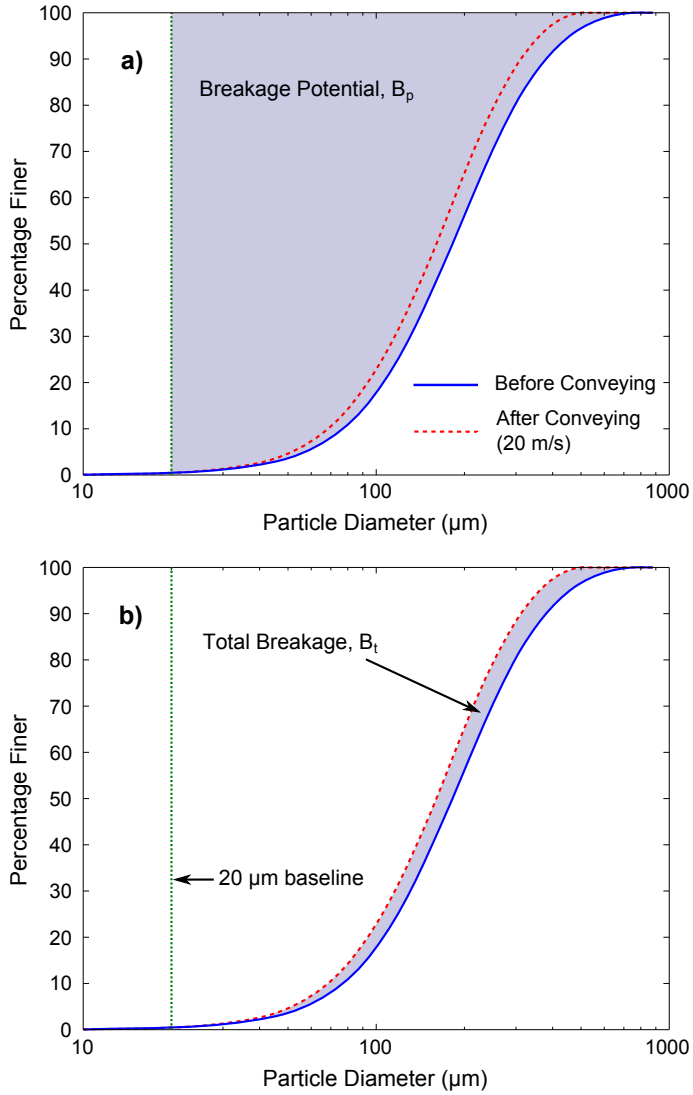

Figure 3.4: *Particle size distributions with shaded areas indicating a) the breakage potential, B_p, and b) the total breakage, B_t, according to the definitions of Hardin (1985)*

Donohue et al. (2009) both used 63 μm. For this work, 20 μm was chosen as measured changes in the particle size distributions of infant formulae below this threshold were negligible, even where attrition was high. B_p is the area enclosed between the particle size distribution before breakage and the baseline size (Figure 3.4a), while B_t is the area enclosed between the particle size distributions before and after breakage for particle diameters greater than the baseline particle size (Figure 3.4b). Thus, B_t is a measure of the actual breakage that occurs whereas B_p quantifies the breakage if all the particles had final sizes below the baseline size. The relative breakage, B_r, may then be calculated from Eq. 3.2.

$$B_r = \frac{B_t}{B_p} \tag{3.2}$$

For the analysis of the laser diffraction data, two particle size distributions were averaged since measurements were duplicated for each of the three replicates. Thus, three values of relative breakage were obtained for each combination of air velocity and infant

formula. Note that while changing the baseline particle size had a major effect on the magnitude of B_r, it did not significantly affect the relative trends observed for B_r. For example, selecting Hardin's baseline size of 74 µm instead of 20 µm would increase B_r results by 107%, on average; however, the minimum and maximum increases would be 74% and 139%. Table 3.4 shows values of B_r calculated using different baseline sizes for five randomly-selected combinations of infant formula and air velocity. This table demonstrates that choosing a different baseline size simply caused the results to scale proportionally for the infant formulae tested.

Table 3.4: *Sample relative breakage values calculated using three different baseline sizes: 20 µm, 63 µm and 74 µm*

Formula | Velocity	Baseline Sizes (µm)		
	20	63	74
A | 10 ms^{-1}	0.0541	0.0920 {+70%}	0.1016 {+88%}
B | 4 ms^{-1}	0.0076	0.0156 {+106%}	0.0181 {+139%}
B | 20 ms^{-1}	0.0502	0.0988 {+97%}	0.1119 {+123%}
C | 10 ms^{-1}	0.0329	0.0619 {+88%}	0.0703 {+114%}
D | 4 ms^{-1}	0.0258	0.0468 {+81%}	0.0518 {+101%}
D | 20 ms^{-1}	0.0549	0.1030 {+87%}	0.1163 {+112%}

3.1.5 Texture Analysis and Compression Methodology

The uniaxial compression experiments were carried out using a Stable Micro Systems TA.HD*plus* texture analyser (Stable Micro Systems Ltd., Godalming, Surrey, UK). A 5 kg load cell was used. The force resolution of this load cell is 0.1 g, force accuracy is 0.025%, the range resolution is 0.001 mm and the speed accuracy is better than 0.1% (TA.HD*plus* Texture Analyzer, 2011). Individual agglomerates were compressed on a flat, 120 mm square glass plate that was 4 mm thick: a surface with extremely low surface friction. Since the agglomerates were not fixed in place, they were always in a stable orientation before compression. A 75 mm compressive platen was used; the diameter of this platen was large enough to ensure that fragments which broke off the agglomerates remained underneath the platen, where they may have been compressed again subsequently. The configuration of the texture analyser is shown in Figure 3.5.

It was essential to ensure that the platen and glass plate were parallel during the tests. Otherwise, the edge of the platen could contact the glass plate before fully compressing the agglomerate, leading to spurious results. The small size of the infant formula agglomerates being compressed made it necessary to insert small cardboard shims underneath the bottom surface of the texture analyser to bring the two compressing

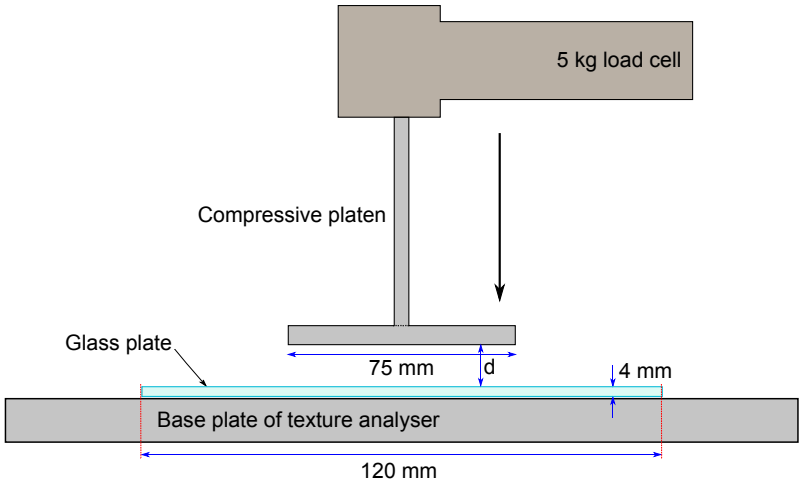

Figure 3.5: *Configuration of the texture analyser used for agglomerate compression*

surfaces perfectly into alignment. The settings chosen for the parameters of the texture analyser software, Exponent (v.4.0.5.0), are shown in Table 3.5.

Table 3.5: *Settings chosen for the configurable parameters of the texture analyser*

Parameter	Setting
Trigger force†	0.2 g (≈ 0.002 N)
Target force‡	30 g (≈ 0.29 N)
Pre-test speed	0.01 mm s^{-1}
Test speed	0.01 mm s^{-1}
Post-test speed	5 mm s^{-1}
Data acquisition rate	500 points/s

†The trigger force is the force at which to begin recording data.

‡The target force is the force at which to stop recording data and write the results to a file.

Four variables were recorded, with the last three variables being interrelated: force, distance, strain and time. It may not be immediately obvious how strain was determined, so this is briefly outlined here. The load cell and range of the texture analyser were calibrated daily before use. Thus, the distance between the bottom of the platen and the top surface of the glass plate (d) was known precisely at all times, and this decreased as the test proceeded. The agglomerate height is this distance at the instant when the trigger force was reached (d_o). As the agglomerate was compressed ($d < d_o$), the strain was found as $\frac{d_o - d}{d_o}$.

3.1.6 Uniaxial Compression Responses

Three responses were taken from the raw data obtained from the texture analyser:

1. The normal force at the point of failure of the agglomerate (N)
2. The strain at the point of failure of the agglomerate (%)
3. The agglomerate stiffness ($N\,m^{-1}$)

Identifying one unique point of failure for strain-controlled crushing can be problematic as each plot features a number of local maxima, so it may not be straightforward to identify which corresponds to the failure point. Figure 3.6 shows three representative plots of force versus displacement for compression of three agglomerates of infant formula B.

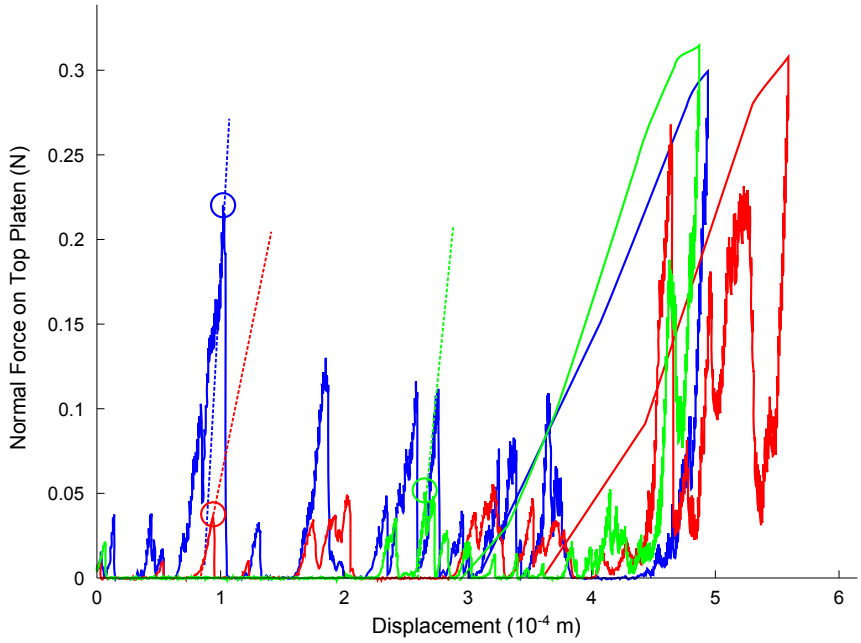

Figure 3.6: *Plots of force (N) versus displacement (10^{-4} m) for experimental compression of three agglomerates of infant formula B, indicating points of failure of the agglomerates using circles and agglomerate stiffnesses using dashed lines*

Each plot has a number of peaks and troughs and it is not easy to define exactly which is the failure point. It is also clear from Figure 3.6 that simply selecting the point at which the maximum force occurs as the point of failure is not a reliable criterion; often, the agglomerate fails before the point of maximum force is attained. In these cases, the maximum force is for compressive failure of the residual agglomerate fragments created by the initial crushing cycle. For consistency, an algorithm was developed to identify the points at which agglomerates fail using MATLAB (v.7.0.1 [R14SP1], The MathWorks, Natick, MA, USA). In brief, the point of failure is the first point, ordered by increasing strain, which satisfies three conditions:

1. It is a local maximum on a plot of force versus deformation, and has the highest force value within a small (< 2%) strain range surrounding this point.
2. The difference between the force at failure and the force at the subsequent local minimum must be greater than 0.01 N, and when normalised by the force at failure, the difference must be greater than 25%.
3. The maximum force attained in a 10% strain range following the point of failure must be less than the force at failure (otherwise, this is indicative of asperity failure, not agglomerate failure).

These specific numeric values were chosen as they identified the point of failure reliably when the algorithm was tested using a subset of the experimental data. Since the points of failure of the agglomerates were not identified in real time, the compression tests could not be stopped immediately after failure and a target force was instead specified as the stopping condition. The agglomerate stiffness was defined as the slope of the linear region prior to the point of failure on a plot of force versus deflection. Stiffnesses were calculated automatically by initially finding the slope for a small region of displacement, and successively extending the region used to calculate the slope. The stiffness was taken to be the first slope at which either the difference between successively-calculated slopes exceeded a defined tolerance or this difference became negative, i.e., stiffness began to decrease. In fewer than 2% of cases, stiffnesses were calculated which were not valid as the slope of the fitted linear trendline deviated markedly from the force-displacement plot. In these cases, the number of data points used to calculate the stiffness was changed manually to obtain a realistic value for stiffness. The circles and dashed lines on Figure 3.6 identify the points of failure and stiffnesses obtained using this approach. The total numbers of agglomerates which were judged to have failed using the criteria in this section, and thus, which are considered in the results below, were 486, 457, 464 and 447 for infant formulae A–D, respectively.

3.1.7 Drop Tests using High-Speed Camera

Thirty agglomerates of each infant formula were dropped individually onto a flat, horizontal, stainless steel plate. Each agglomerate was gently pushed off a smooth stainless steel platform which was at a fixed elevation of 450 mm above the target plate. This ensured that the impact velocities were consistent at approximately 1.9 $\mathrm{m\,s^{-1}}$: an important consideration since the coefficient of restitution generally decreases with increasing impact velocity, e.g., Schwager (2007). Basic statistics are provided in Table 3.6 which indicate the variation between impact velocities more precisely. None of the agglomerates were seen to fail when subjected to this dynamic loading.

The impacts were recorded at 1000 frames/s using an AOS X-Motion high-speed camera

Table 3.6: *Means, standard deviations and extreme values of impact velocities for drop tests conducted using agglomerates in the 710–850 µm size range*

Infant Formula	Impact Velocity Statistics ($m\,s^{-1}$)			
	Mean	Std. Dev.	Minimum	Maximum
A	1.793	0.168	1.416	2.105
B	1.894	0.154	1.552	2.162
C	1.856	0.150	1.576	2.166
D	1.911	0.128	1.593	2.196
Overall	1.865	0.155	1.416	2.196

with a remote trigger (AOS Technologies AG, Baden Daettwil, Switzerland) and a Navitar 50 mm F0.95 TV lens adjusted to a focal length of 0.6 m. Each frame had a resolution of 1280×600 and the total sequence length was 1.74 s, including the pre-trigger buffer (20% of total sequence length, or 0.348 s). Illumination was provided by a pair of Dedolight Asperics^2 DLH4 lamps which were fully switched on and focused on the target plate. The camera was mounted horizontally on a Manfrotto 055XB tripod with a Manfrotto #222 joystick head.

The camera operating software was AOS Imaging Studio (v.2.5.2.2, AOS Technologies AG). Each resulting *.mpg* file was analysed subsequently using ProAnalyst (v.1.5.3.0, Professional ed., Xcitex, Inc., Cambridge, MA, USA). This software allowed the position of each agglomerate to be tracked over time, and thus provided the raw data required to calculate the coefficient of restitution, i.e., the magnitude of the normal velocity after impact divided by the normal velocity before impact. The mean normal velocities were calculated for six consecutive frames directly before and after impact. These velocities, averaged over a 0.005 s period, were used to calculate the coefficient of restitution. This was more accurate than using only two frames. Figure 3.7 shows four non-consecutive cropped sample frames for one drop test with a mm scale in the background.

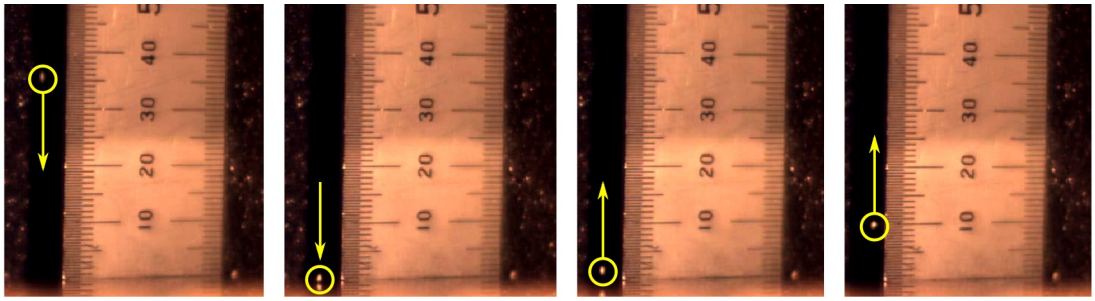

Figure 3.7: *Four cropped frames (numbers 50, 69, 72 and 83) extracted from the video of a drop test of one agglomerate of infant formula C, where the agglomerate is circled and its direction of motion is indicated by arrows*

3.2 Results and Discussion

3.2.1 Pneumatic Conveying Results

The variation of bulk density with conveying velocity for the four infant formulae listed in Table 3.1 is given in Figure 3.8.

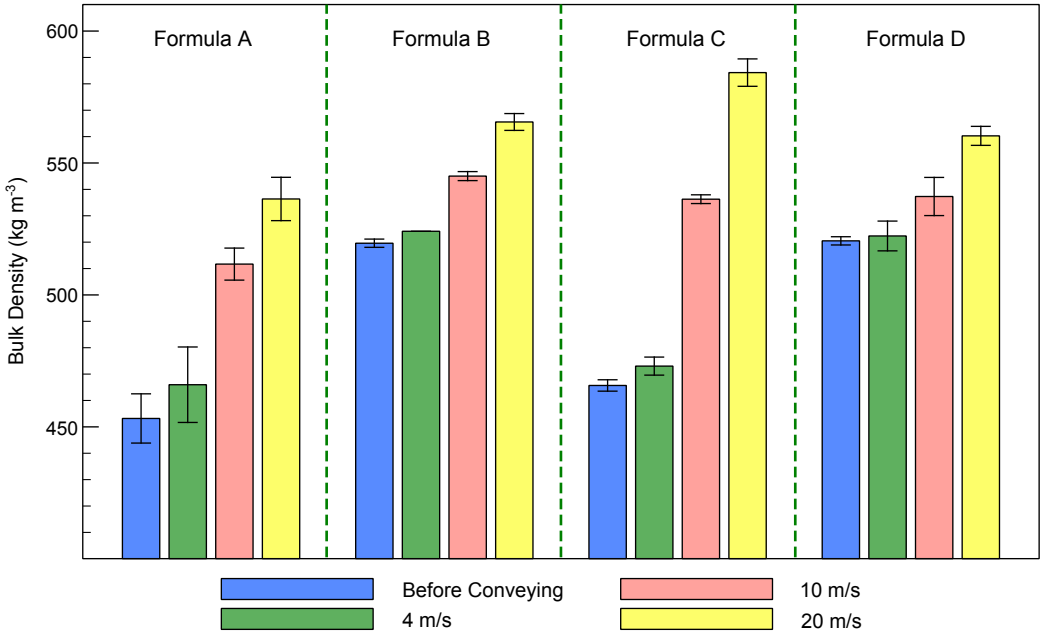

Figure 3.8: *Bar chart comparing the bulk density ($kg\,m^{-3}$) of infant formulae A–D before conveying, and following pneumatic transport through a rig of invariant configuration at 4 ms^{-1}, 10 ms^{-1} and 20 ms^{-1}, where the error bars indicate one standard deviation*

For all four infant formulae, there was a steady increase in bulk density with conveying velocity, as expected. It is interesting to compare the magnitudes of the bulk density increases. The densities of formulae B and D showed the least variation: the percentage differences between the bulk densities before conveying and after conveying at 20 $m\,s^{-1}$ were 8.9% and 7.7%, respectively. The corresponding differences for formulae A and C were much larger at 18.4% and 25.5%. Even within the dense phase regime, differences between the densities before conveying and after conveying at 4 $m\,s^{-1}$ were more pronounced for formulae A and C: the percentage differences were 2.8%, 0.9%, 1.6% and 0.4% respectively for formulae A–D. This means that attrition is potentially of greatest concern for formulae A and C. The bulk densities of the formulae before conveying were related to the percentage of protein in their compositions. Infant formula A contained the least protein (10.7%) and had the lowest bulk density before conveying of 452.6 $kg\,m^{-3}$; C contained the second-lowest amount of protein and had the second-lowest bulk density of 465.1 $kg\,m^{-3}$; etc.

The bulk density increased due to attrition of the powder, which is also shown by

the decreasing trends in D[4,3] on Figure 3.9. This is as expected from results in the literature (e.g., Kalman and Goder, 1998; Taylor, 1998; Zhang and Ghadiri, 2002).

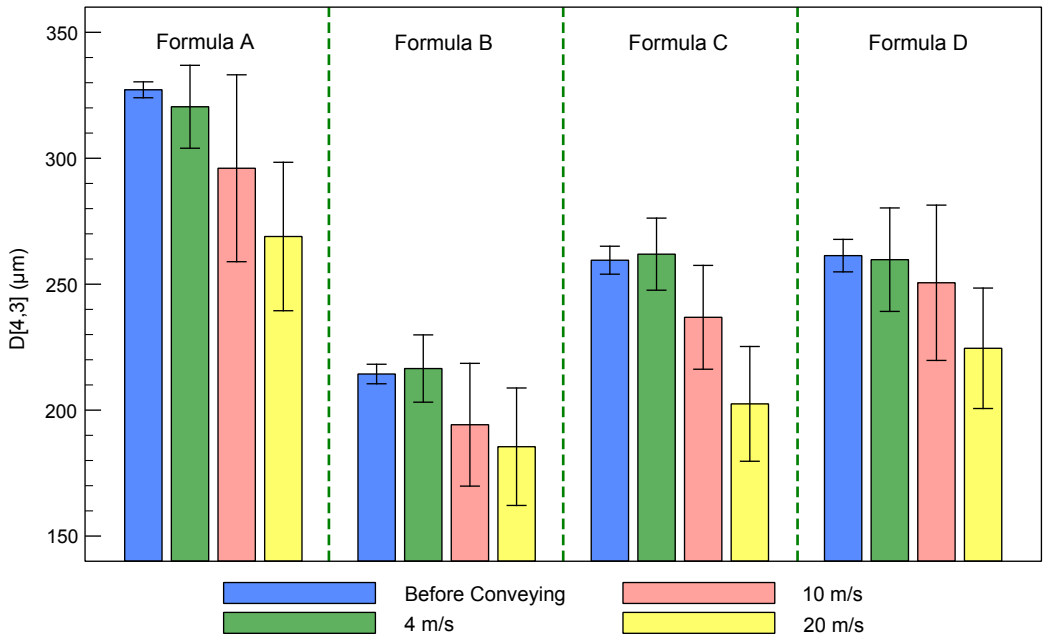

Figure 3.9: *Bar chart comparing the volume mean diameter (µm) of infant formulae A–D before conveying, and following pneumatic transport at 4 ms^{-1}, 10 ms^{-1} and 20 ms^{-1}, where the error bars indicate one standard deviation*

The differences between mean diameters for the formulae before conveying and following passage through the rig at 4 ms^{-1} were low: the difference of 2.1% for formula A was the largest. The differences between mean diameters before conveying and after transport at 20 ms^{-1} were 58 µm, 29 µm, 57 µm and 37 µm respectively for formulae A–D. These were percentage differences of 17.8%, 13.5%, 22.0% and 14.1% respectively. The marked differences between D[4,3] values on Figure 3.9 before conveying were attributable to factors such as spray dryer and fluidised bed configurations. The error bars were quite large for the results recorded at high conveying velocities, which is due to the difficulty associated with taking a small (< 1 g), representative sample for laser diffraction from a relatively large bulk of approximately 200 g.

These D[4,3] results may be compared to the relative breakage results shown in Figure 3.10. B_r generally increased with air velocity, except for infant formula A for which B_r remained constant at around 0.06. For any particular velocity, the trends in B_r were related to the percentage differences in D[4,3], e.g., at 20 ms^{-1}, formula C had the largest percentage difference in D[4,3] compared to the value before conveying of 22%, and this formula correspondingly had the highest B_r of 0.096. Similarly, the smallest percentage difference of 13.5% was for formula B which had the lowest B_r of 0.050.

As discussed in Section 1.6, one of the primary disadvantages of infant formula attrition

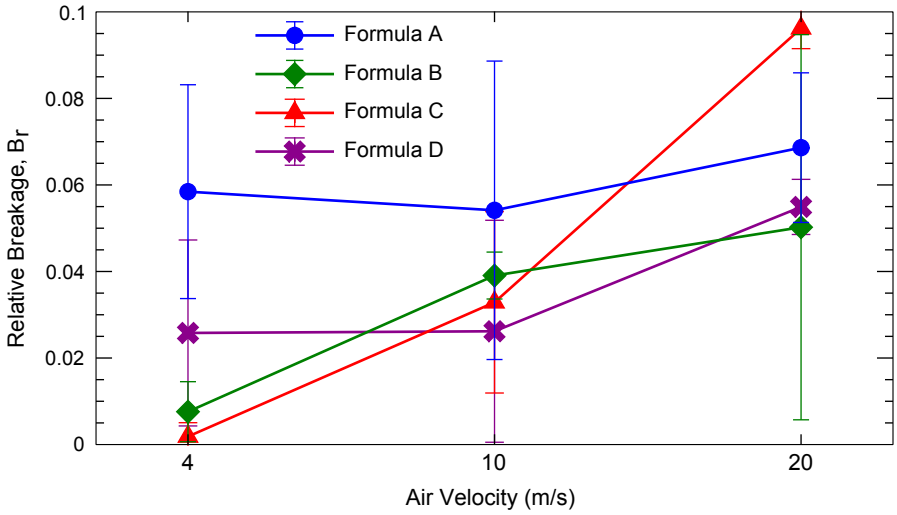

Figure 3.10: *Plot of relative breakage against air velocity (ms^{-1}), where the error bars indicate one standard deviation*

is deterioration of the product's rehydration characteristics. Figure 3.11 shows the increase in wettability time that is commensurate with increased attrition.

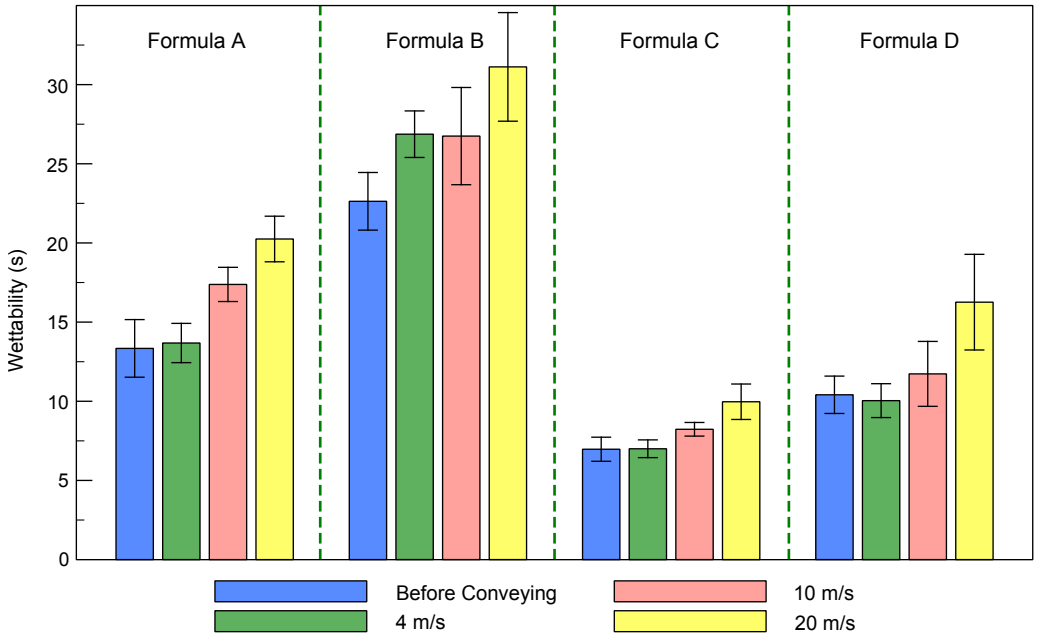

Figure 3.11: *Bar chart comparing the wettability (s) of infant formulae A–D before conveying, and following pneumatic transport at 4 ms^{-1}, 10 ms^{-1} and 20 ms^{-1}, where the error bars indicate one standard deviation*

It is interesting to note the very poor wettability of infant formula B. The minimum wettability recorded for this formula (22.6 s, measured before conveying) was higher than any of the measurements for the other three formulae, even where attrition was high. Note that wettability is related to particle size (Ortega-Rivas, 2009), and B also had the smallest D[4,3] values of the four formulae tested.

Yan and Barbosa-Cánovas (2000) found that the Hausner ratios of instant coffee and

milk powders increased with increasing attrition. Figure 3.12 shows the opposite result for infant formula B: as conveying velocity increased, so too did attrition (Figure 3.9), yet the Hausner ratio decreased which indicates improved flowability.

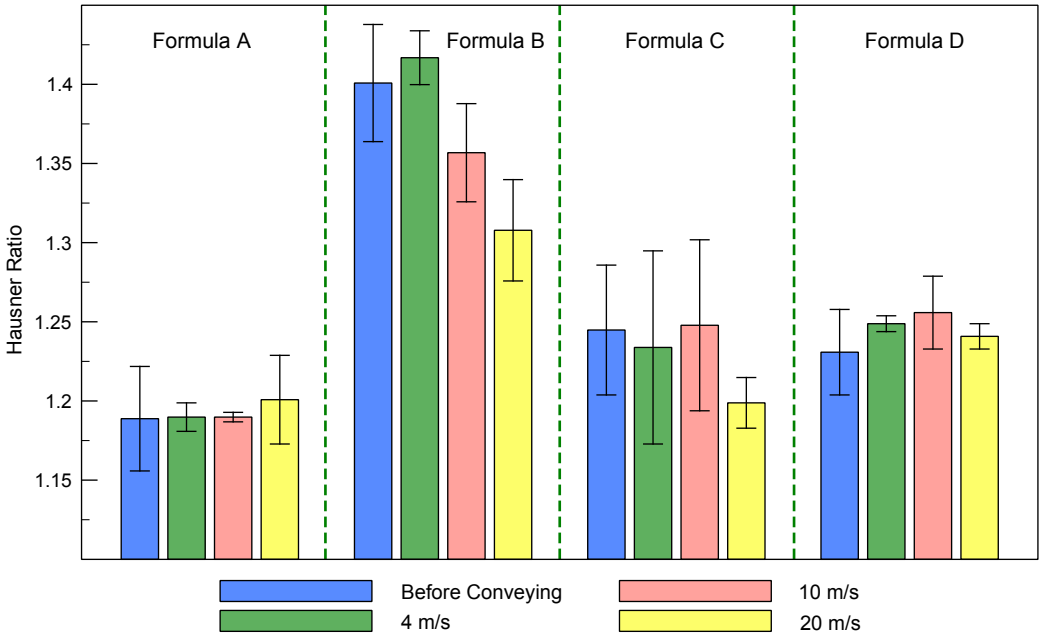

Figure 3.12: *Bar chart comparing the Hausner ratio of infant formulae A–D before conveying, and following pneumatic transport at 4 ms^{-1}, 10 ms^{-1} and 20 ms^{-1}, where the error bars indicate one standard deviation*

The Hausner ratios were particularly high for infant formula B, ranging from 1.31 (20 ms^{-1}) to 1.42 (4 ms^{-1}). These values indicate flowabilities ranging from passable to poor, which was confirmed by the powder's tendency to form cohesive arches when flowing out of the funnel. Yan and Barbosa-Cánovas (2000) also found that larger agglomerates have higher Hausner ratios; again, comparing results for the four formulae on Figures 3.9 and 3.12 does not confirm this. No clear trends are observed for powders other than formula B. This fact, along with sizes of the error bars and the use of only two replicates per data point, implies that these Hausner ratio results for infant formula B should be interpreted with caution.

The results for percentage free fat are shown on Figure 3.13. Formula A had a very high free fat content, which increased from 0.75% before conveying to a maximum of 1.46% after conveying at 20 ms^{-1}. This increasing trend in percentage free fat was not observed for the other formulae; however, this may be due to their relatively low values of free fat compared to formula A. The progressive reduction in percentage free fat as the protein to fat ratio increased reflected a similar trend in the overall fat content of these powders: powder A contained the most fat (28.8%) while powder D contained the least (15.2%). It is hypothesised that the regions which contained high concentrations of fat coincided with the points of structural weakness for agglomerates of infant formula A. This explanation accounts for the observed free fat results as

breakage of the agglomerates during conveying exposed surfaces containing high levels of fat.

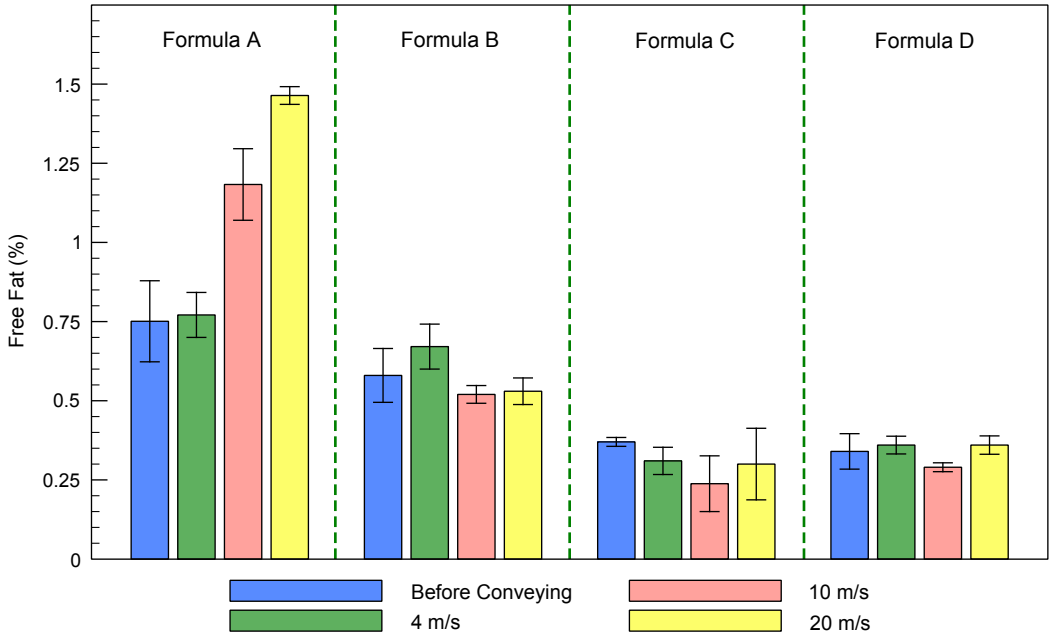

Figure 3.13: *Bar chart comparing the percentage surface (solvent extractable) free fat of infant formulae A–D before conveying, and following pneumatic transport at 4 ms^{-1}, 10 ms^{-1} and 20 ms^{-1}, where the error bars indicate one standard deviation*

3.2.2 Results of Uniaxial Compression Tests

The results recorded for force at failure, strain at failure and agglomerate stiffness for the four infant formulae tested were displayed as probability histograms; however, these are confined to Appendix B for reasons of space. The Freedman-Diaconis rule was used to set the bin widths and locations. Note that the heights of the bars were scaled so that the sum of the bar areas on each figure was one. All of the distributions showed a pronounced positive skew. Both Weibull and lognormal distributions were fitted to these data sets for each infant formula using the *dfittool* command in MATLAB. The lognormal distribution gave a better fit of the data for each response. The associated probability density function (PDF) was overlaid on each histogram in Appendix B as a solid red line. These PDFs were calculated using Eq. 3.3:

$$y = f(x \mid \mu, \sigma) = \frac{1}{x\sigma\sqrt{2\pi}} e^{\frac{-(\ln x - \mu)^2}{2\sigma^2}} \tag{3.3}$$

The lognormal PDFs for the four infant formulae tested are compared on Figures 3.14–3.16, while Table 3.7 shows means and standard deviations of the raw data and parameters of the lognormal distributions.

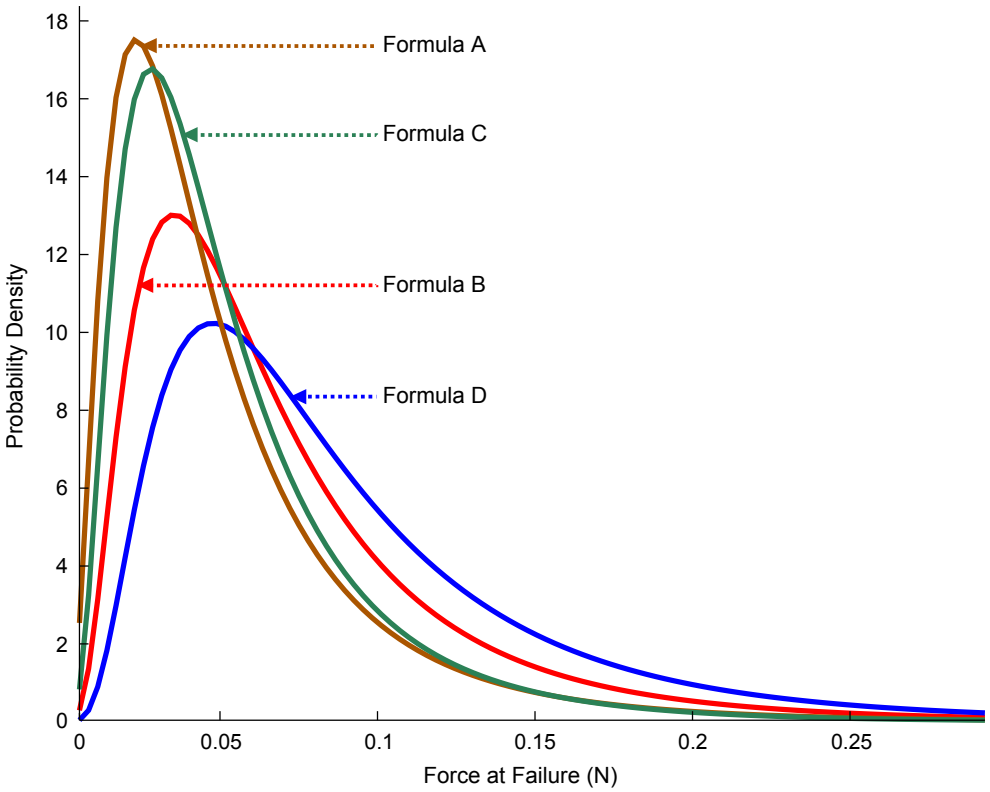

Figure 3.14: *Probability density functions of lognormal distributions fitted to force at failure data (N) for the four infant formulae tested*

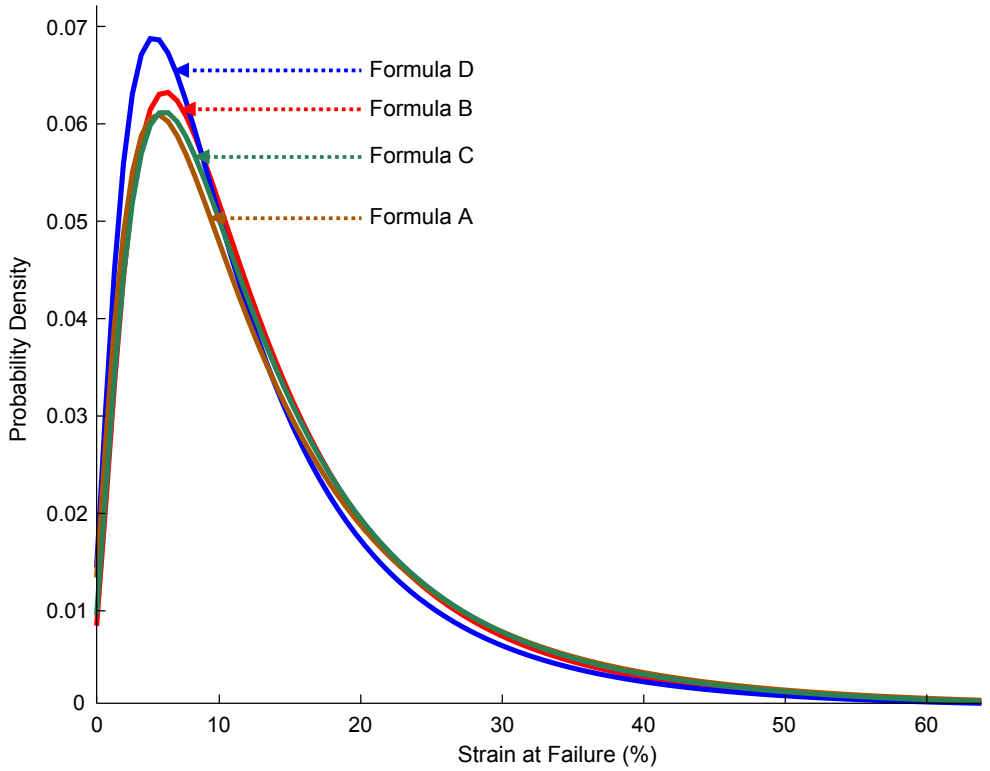

Figure 3.15: *Probability density functions of lognormal distributions fitted to strain at failure data (%) for the four infant formulae tested*

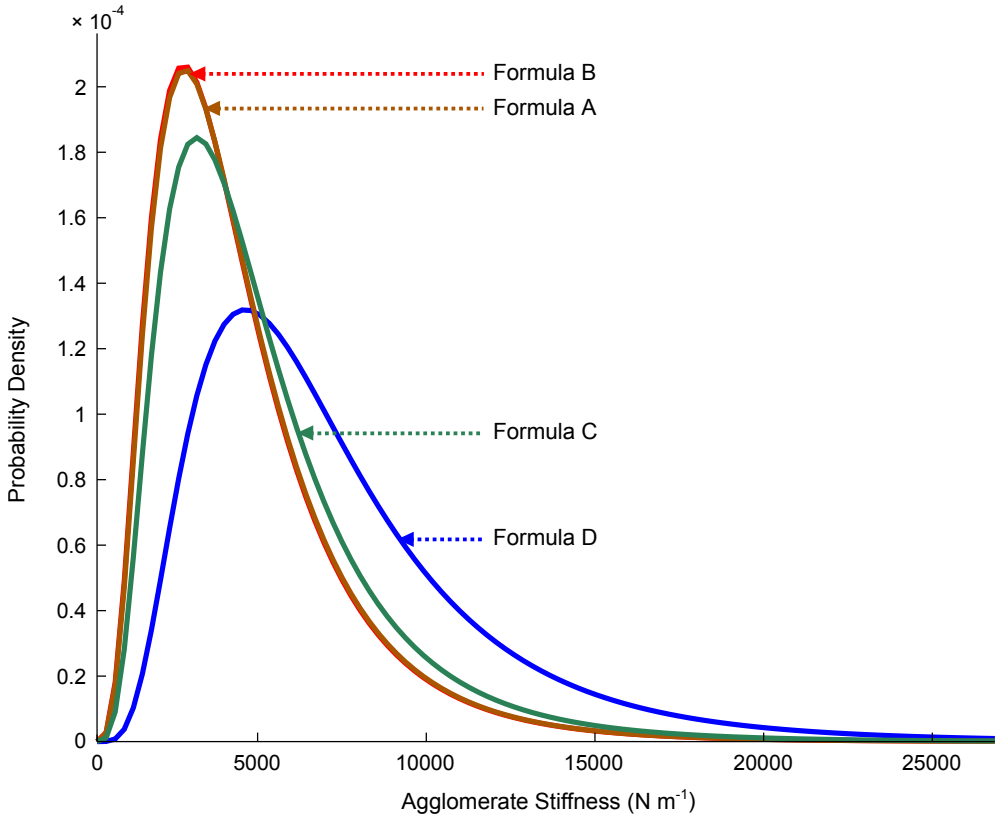

Figure 3.16: *Probability density functions of lognormal distributions fitted to agglomerate stiffness data ($N\,m^{-1}$) for the four infant formulae tested*

Table 3.7: *Means and standard deviations of the results obtained for force at failure (N), strain at failure (%) and agglomerate stiffness ($N\,m^{-1}$), and the parameters of the associated fitted lognormal (L/N) distributions*

	Force (N)	Strain (%)	Stiffness ($N\,m^{-1}$)
Formula A			
Mean (Exp.)	0.05301	15.1448	4695.79
Std. Dev. (Exp.)	0.04156	11.4917	2964.44
$\mu^{\dagger}$ (L/N) {Std. Error}	-3.20912 {0.03373}	2.41042 {0.03753}	8.28542 {0.02630}
$\sigma^{\dagger}$ (L/N) {Std. Error}	0.74351 {0.02388}	0.82737 {0.02658}	0.57981 {0.01863}
Formula B			
Mean (Exp.)	0.07140	14.4088	4648.45
Std. Dev. (Exp.)	0.05275	10.4331	2921.23
$\mu^{\dagger}$ (L/N) {Std. Error}	-2.87162 {0.03199}	2.40225 {0.03573}	8.27756 {0.02719}
$\sigma^{\dagger}$ (L/N) {Std. Error}	0.68387 {0.02266}	0.76379 {0.02531}	0.58124 {0.01926}
Formula C			
Mean (Exp.)	0.05603	14.9298	5232.35

Continued on page 67

	Force (N)	Strain (%)	Stiffness ($N\,m^{-1}$)
Std. Dev. (Exp.)	0.04372	10.8541	3169.15
$\mu^{\dagger}$ (L/N) {Std. Error}	-3.11709 {0.03129}	2.42275 {0.03654}	8.39819 {0.02668}
$\sigma^{\dagger}$ (L/N) {Std. Error}	0.67391 {0.02216}	0.78705 {0.02588}	0.57468 {0.01890}
Formula D			
Mean (Exp.)	0.09047	13.3854	7358.42
Std. Dev. (Exp.)	0.06005	10.2184	4201.11
$\mu^{\dagger}$ (L/N) {Std. Error}	-2.60941 {0.03110}	2.30463 {0.03733}	8.75345 {0.02639}
$\sigma^{\dagger}$ (L/N) {Std. Error}	0.65754 {0.02203}	0.78934 {0.02644}	0.55795 {0.01869}

$^{\dagger}\mu$ and σ are the mean and standard deviation of the corresponding normal distribution, as returned by the MATLAB function *lognfit*.

By comparing the means, a number of general trends became apparent. In general, the force at failure and agglomerate stiffness increased with the protein to fat ratio while the strain at failure decreased. For all responses and formulae, the standard deviations were very large, exceeding 50% of the corresponding means, which illustrates the inherent variability between individual spray-dried agglomerates of this natural product. There was a clear correspondence between the force at failure and the percentage of protein in the formulae: the lowest protein level of 10.7% for formula A resulted in the lowest mean force at failure of 0.05301 N, whereas the maximum mean force at failure of 0.09047 N was for formula D which contained 16.7% protein. The protein content was inversely related to the strain at failure. As the percentage of protein increased, the strain at failure decreased. Since the percentage of protein was related to the bulk densities of the formulae before conveying, formulae with low bulk densities before conveying had low mean forces at failure and high mean strains at failure. There is an interesting link between mean forces at failure of the agglomerates and changes in bulk density due to conveying. It is intuitively sensible that formulae containing strong agglomerates with high forces at failure would break less under mechanical loading, and thus exhibit less change in bulk density, than a formula containing weaker agglomerates. Infant formulae B and D had the largest mean forces at failure, and also showed the least change in bulk density on Figure 3.8. The agglomerates of formulae A and C were comparatively weak, and their bulk densities varied the most with conveying velocity.

The mean strain at failure was also related to the differences between bulk densities before conveying and after conveying at 4 $m\,s^{-1}$: the smallest bulk density difference (0.4%) and mean strain at failure (13.4%) were both for infant formula D, while the highest values (2.8% and 15.1% respectively) were recorded for formula A. There was a relationship between carbohydrate content and agglomerate stiffness, although this

was not as clear as the others. It is true that increasing the percentage of carbohydrate increased the agglomerate stiffness. However, formulae C and D had identical carbohydrate contents but markedly different stiffnesses, which indicated that the observed relationship may be caused by other factors. It must be noted that all of these observations were based on only four data points and more formulae would need to be tested to confirm these general trends.

Correlation Tests of Experimental Responses

It was instructive to determine whether or not significant correlations existed between any pairs of responses from a data set. Correlations are often determined using the Pearson product moment correlation coefficient (r). However, this is only applicable if the data are normally distributed. Visual inspection of the probability histograms (Figures B.1–B.12) indicated that this was not the case. A rigorous test was provided by the Shapiro-Wilk W test for normality (similar to the Kolmogorov-Smirnov and Lilliefors tests), as implemented in STATISTICA. If the p-value < α for the chosen significance level (α is one minus the significance level expressed as a decimal, e.g., $\alpha = 0.05$ for a significance level of 95%), the null hypothesis that the data are normally distributed should be rejected. Results of the W test for the four infant formulae are given in Table 3.8.

Table 3.8: *Results of the Shapiro-Wilk W test for normality of the force at failure, strain at failure and agglomerate stiffness data sets*

Response	Formula A		Formula B	
	W statistic	p-value	W statistic	p-value
Force at Failure	0.8375	0.0000	0.8268	0.0000
Strain at Failure	0.8916	0.0000	0.8868	0.0000
Agglomerate Stiffness	0.8482	0.0000	0.8377	0.0000

Response	Formula C		Formula D	
	W statistic	p-value	W statistic	p-value
Force at Failure	0.7864	0.0000	0.8733	0.0000
Strain at Failure	0.8998	0.0000	0.8748	0.0000
Agglomerate Stiffness	0.8794	0.0000	0.8891	0.0000

Since the distributions were not normal, the degree of relationship between the responses was instead determined using rank correlation coefficients. Two of the most

commonly used are the Spearman R and Kendall τ coefficients, which are both available in STATISTICA. The results of these calculations are given in Tables 3.9–3.12.

Table 3.9: *Spearman R and Kendall τ rank correlations of all combinations of force at failure, strain at failure and agglomerate stiffness for infant formula A*

Correlation	Spearman R		Kendall τ	
	R	p-value	τ	p-value
Force ⟷ Strain	0.1418	0.0017	0.0924	0.0023
Force ⟷ Stiffness	0.8511	0.0000	0.6608	0.0000
Strain ⟷ Stiffness	0.1874	0.0000	0.1259	0.0000

Table 3.10: *Spearman R and Kendall τ rank correlations for all combinations of force at failure, strain at failure and agglomerate stiffness for infant formula B*

Correlation	Spearman R		Kendall τ	
	R	p-value	τ	p-value
Force ⟷ Strain	0.2363	0.0000	0.1604	0.0000
Force ⟷ Stiffness	0.7370	0.0000	0.5428	0.0000
Strain ⟷ Stiffness	0.1357	0.0037	0.0913	0.0035

Table 3.11: *Spearman R and Kendall τ rank correlations for all combinations of force at failure, strain at failure and agglomerate stiffness for infant formula C*

Correlation	Spearman R		Kendall τ	
	R	p-value	τ	p-value
Force ⟷ Strain	0.2067	0.0000	0.1388	0.0000
Force ⟷ Stiffness	0.8430	0.0000	0.6548	0.0000
Strain ⟷ Stiffness	0.2418	0.0000	0.1634	0.0000

Table 3.12: *Spearman R and Kendall τ rank correlations for all combinations of force at failure, strain at failure and agglomerate stiffness for infant formula D*

Correlation	Spearman R		Kendall τ	
	R	p-value	τ	p-value
Force ⟷ Strain	0.2368	0.0000	0.1580	0.0000
Force ⟷ Stiffness	0.8180	0.0000	0.6293	0.0000
Strain ⟷ Stiffness	0.2444	0.0000	0.1635	0.0000

Sufficient data points were available to ensure that all results were statistically-significant, even at a 99% level. There was a strong positive correlation between force at

failure and agglomerate stiffness, with infant formula A having the highest Spearman R of 0.8511 (Kendall τ of 0.6608). This can be visualised on a scatter plot of stiffness against force with a linear trendline, which is shown for formula A as Figure 3.17. Spearman R coefficients for the other two combinations of responses were much lower (maximum of 0.2444).

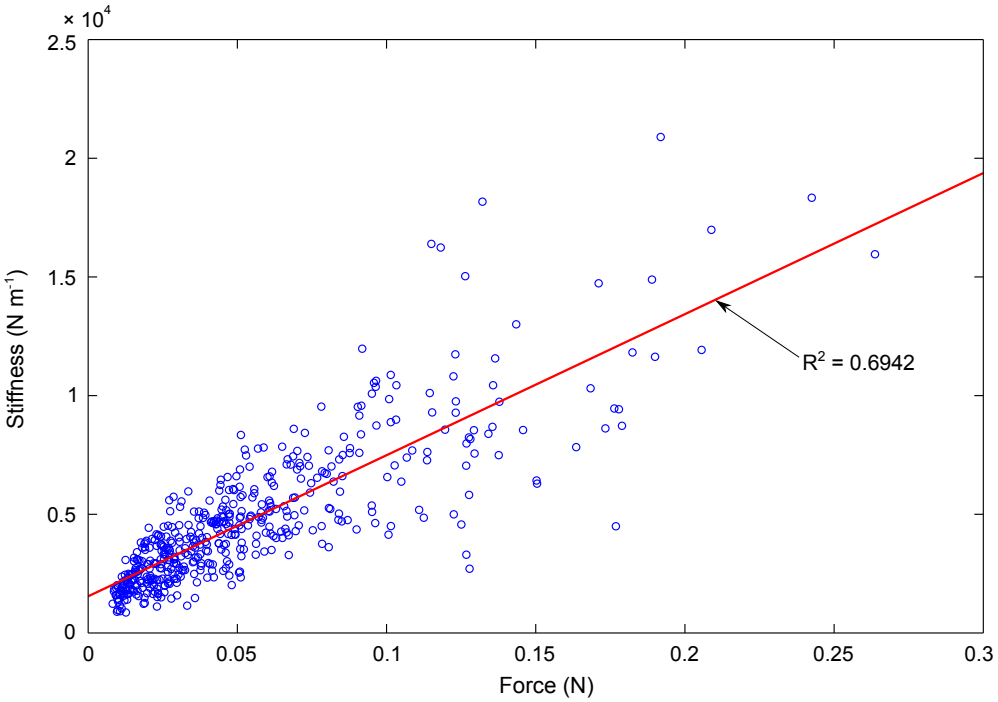

Figure 3.17: *Scatter plot of agglomerate stiffness ($N\,m^{-1}$) against force at failure (N) for infant formula A, with a linear trendline to highlight the positive correlation between the responses*

3.2.3 Drop Test Results

Table 3.13 shows means, standard deviations and extreme values of the coefficients of restitution which were obtained by video analyses of agglomerate drop tests.

Table 3.13: *Means, standard deviations and extreme values of coefficients of restitution*

Infant Formula	Coefficient of Restitution Statistics			
	Mean	Std. Dev.	Minimum	Maximum
A	0.2460	0.0950	0.0244	0.4191
B	0.3258	0.0979	0.0901	0.4743
C	0.3009	0.1030	0.0929	0.5007
D	0.2768	0.1089	0.0500	0.5852
Overall	0.2883	0.1044	0.0244	0.5852

Formula A had the lowest mean coefficient of restitution of 0.2460, and also had the

lowest minimum and maximum coefficients of restitution of 0.0244 and 0.4191, respectively. Formula B had the highest mean coefficient of restitution of 0.3258. Since a large dispersion existed in these results (standard deviations for any formula were greater than the maximum differences between means of different formulae), a more appropriate way of displaying coefficients of restitution was by fitting a probability density function to the data. The most suitable was a Weibull PDF (Eq. 3.4), where a is the scale parameter, b is the shape parameter and $x \geq 0$:

$$y = f(x \mid a, b) = b a^{-b} x^{b-1} e^{-\left(\frac{x}{a}\right)^b} \tag{3.4}$$

The PDFs obtained are shown on Figure 3.18.

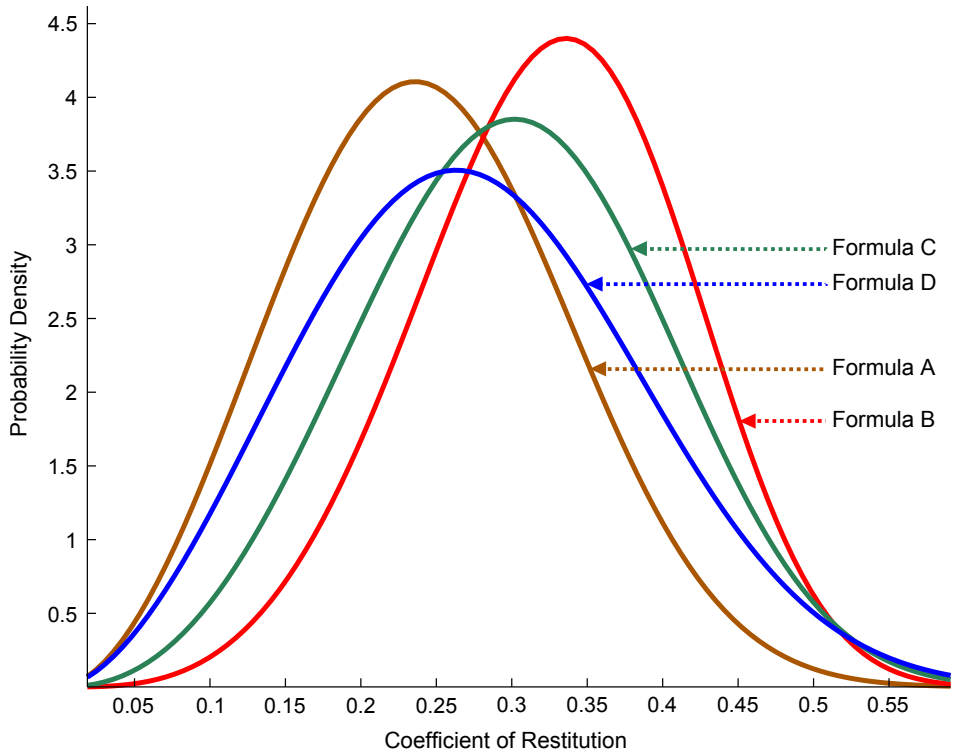

Figure 3.18: *Probability density functions of Weibull distributions fitted to coefficients of restitution of the four infant formulae tested*

Note the relationship that exists between the coefficient of restitution and the relative breakage results for low velocity conveying at 4 $\mathrm{m\,s^{-1}}$. Where coefficients of restitution were low, this implies that extensive breakage of either bonds or primary particles occurred which absorbed energy. Since these agglomerates were particularly susceptible to damage, it might be expected that the infant formula would be more friable than other formulae under similar loading conditions. Infant formula A, which had the lowest coefficient of restitution, had the highest B_r for conveying at 4 $\mathrm{m\,s^{-1}}$ (0.058), formula D had the second-lowest coefficient of restitution and the second-highest B_r of 0.026, while the B_r results for formulae B and C were transposed, but were very close as seen on Figure 3.10.

None of the agglomerates were seen to fail during the drop tests. There are two reasons for this. Firstly, the impact velocity was around 1.9 ms^{-1}, and it was shown that attrition was low using a considerably higher conveying velocity of 4 ms^{-1}. Secondly, the agglomerates for the uniaxial compression experiments and the drop tests were isolated using a sieve shaker which applied significant mechanical loading to the powder. This process is likely to have broken any friable agglomerates, so those remaining with a size between 710 µm and 850 µm were likely to be particularly resistant to breakage.

3.3 Conclusions of Chapter 3

In this chapter, the relationships between the compositions of infant formulae, the changes in key quality characteristics when transported by pneumatic conveying and the mechanical properties obtained by uniaxial compression and drop testing of individual agglomerates were investigated. As conveying velocity increased, so too did the bulk density, although the increases in bulk densities for those formulae containing the least protein (A and C) were considerably greater than for others (B and D). As the percentage of protein increased, the bulk densities before conveying of the four formulae increased accordingly. The wettability of formula B was poor, which may be caused by its generally smaller particle size. The surface (i.e., solvent extractable) free fat decreased progressively as the protein to fat ratio increased, which is commensurate with the decreasing fat contents of these powders. Since it is desirable to minimise the changes in bulk properties of the infant formulae caused by conveying, this implies that manufacturers should consider maximising the protein content of their formulae while obviously remaining in compliance with regulatory requirements for energy, micro-nutrient content etc. Reducing the fat content to the minimum permissible should also be beneficial, as this would correspondingly reduce the percentage surface free fat.

The force at failure and agglomerate stiffness generally increased with increasing protein to fat ratio while the strain at failure decreased. Strong positive correlations existed between force at failure and agglomerate stiffness. Both force and strain at failure were related to the percentage of protein: increasing the protein content caused an increase in the mean force at failure and a decrease in the mean strain at failure. Agglomerates of infant formulae B and D had the largest mean forces at failure, which explains why these formulae showed the least variation in bulk density when pneumatically conveyed. The strain at failure was also related to the differences between bulk densities before conveying and after conveying at 4 ms^{-1}. When drop tests were conducted at around 1.9 ms^{-1}, infant formula A had the lowest mean coefficient of restitution and B had the highest (0.3258). The coefficients of restitution decreased as the relative breakage

results increased, which is likely to be due to the increased number of bonds or primary particles broken during loading.

4

Calibration of Discrete Element Models of Bonded Agglomerates using Taguchi Methods

The primary emphasis of Chapters 2 and 3 has been on the "macro" effects of infant formula attrition, i.e., quantification of the effect of attrition on bulk product quality characteristics. Even where infant formula breakage has been assessed on a single-particle, "micro" level (Sections 3.2.2 and 3.2.3), it has not been possible to gain any insights into the evolution of the microstructure of the agglomerates under loading, which could potentially be very useful. For example, it might be possible to develop simulated infant formula agglomerates which are geometrically similar to the physical agglomerates but which are stronger. The simulation outputs could inform modifications made to the operating parameters of the spray dryer, or the composition of the formula, and thus aid the development of products which are less prone to attrition when pneumatically conveyed. Chapters 4 and 5 both make extensive use of discrete element modelling (DEM), which can provide detailed microstructural information to the researcher. Chapter 4 introduces this simulation tool and details a novel approach to calibration of such models. This approach was applied for model calibration in Chapter 5.

4.1 Introduction to Discrete Element Modelling

Discrete element modelling[†] is a computational or simulation tool used to model complex systems of particulates at the particle scale by specifying a relatively small number of microstructural parameters. The fundamental algorithm for DEM was established

[†]DEM may also be read as an abbreviation of distinct element method; in the literature, they are often treated as interchangeable (Bobet et al., 2009) although the categorisation of Cundall and Hart (2004) suggests that discrete element modelling is a broader, more inclusive term.

during the 1970s by P.A. Cundall and O.D.L. Strack (Cundall and Strack, 1979). However, the method did not become widely used until the 1990s, and its popularity has grown rapidly since. This increase in usage of DEM is commensurate with the rise in computational power, which has made it possible to run useful simulations on affordable desktop computers (Cundall, 2001). The availability of commercial software has also contributed to the increased popularity of the method.

4.1.1 Algorithm

The two categories in particulate DEM are the "hard sphere" and "soft sphere" approaches. The calculations in the former approach assume instantaneous binary collisions, and use momentum and energy balances (Di Renzo and Di Maio, 2004; Zhu et al., 2007). The discussion below is restricted to the soft sphere, or force-displacement method, which is used most often. It is so called because particles in the model are assigned finite stiffnesses and deformations of particles at the contact points are captured by permitting overlaps between the interacting bodies (Cheng et al., 2003). For this work, simulations were conducted in both two and three dimensions using the commercial DEM software packages PFC2D v.4.0 and PFC3D v.4.0[†] (Itasca Consulting Group, Minneapolis, MN, USA), respectively. These software packages are implementations of the DEM algorithm proposed by Cundall and Strack (1979). Note that while particulate materials of interest in engineering applications are three-dimensional, 2D models are useful analogues of real 3D materials as the models are easier to create, have shorter simulation times, and deformation and failure mechanisms can be more easily observed.

Both of these software packages apply an explicit conditionally-stable central difference algorithm to calculate the time steps necessary to represent the dynamic behaviour of the particles. Since the assumption is made that velocities and accelerations are constant within each time step, this requires time steps to be extremely small for stability (Potyondy and Cundall, 2004).

At each successive time step, inter-particle forces are evaluated at contact points using some force-displacement relations and resultant forces are calculated for each particle. Newton's second law is then applied to determine particle accelerations, both translational and angular (O'Sullivan, 2008). Eq. 4.1 relates resultant force (F_i) and acceleration ($\ddot{x}_i$) for a disk/sphere of mass m and Eq. 4.2 gives the relationship between resultant moment (M_i) and angular acceleration ($\dot{\omega}_i$) (Itasca Consulting Group, 2008).

$$F_i = m(\ddot{x}_i - g_i) \tag{4.1}$$

[†]PFC is an abbreviation of "Particle Flow Code".

$$M_i = I\dot{\omega}_i \tag{4.2}$$

g_i is a body force acceleration vector and I is the moment of inertia of the disk/sphere. Since the centre of mass coincides with the centre of a disk or sphere of radius R, Eq. 4.2 may be rewritten as Eq. 4.3, where the multiplier ϑ is 0.5 for a disk and 0.4 for a sphere.

$$M_i = \vartheta m R^2 \dot{\omega}_i \tag{4.3}$$

These acceleration terms are integrated numerically to find particle velocities and displacements; hence, positions may be updated after each time step. Note that disks have three degrees of freedom while spheres, in three dimensions, have six: one translation and spin in each Cartesian direction (Cundall, 2001).

4.1.2 DEM Particle Shape

The simplest particle shapes to select for use in DEM are disks (2D) or spheres (3D) (O'Sullivan, 2008). This is because knowledge of the location of the centrepoint and the radius is sufficient to describe these particles fully as orientation is unimportant. Furthermore, contact equations involving disks and spheres are usually easier to solve computationally (linear) than for alternative geometries, e.g., using ellipsoidal particles requires non-linear equations to be solved at the contact points.

While choosing disks or spheres has significant computational benefits, there are also disadvantages. If the real particles being modelled have a non-circular aspect, yet are being modelling using disks or spheres, the model particles may be more prone to rotation or rolling than in reality.

Where it is desirable to use particles other than disks or spheres, there are two approaches:

1. Many authors have used fundamental particles of alternative shapes, e.g., ellipses (Ting et al., 1993), ellipsoids (Lin and Ng, 1997; Ng, 2004), polygons (D'Addetta et al., 2002; Issa and Nelson, 1993), polyhedra (Ghaboussi and Barbosa, 1990; Hart et al., 1988), and particles of specific shape, e.g., tablet-shaped particles (Song et al., 2006). Additional references are given by Donzé et al. (2008).

2. The second option is to bond multiple disks or spheres together to form clumps or clusters (O'Sullivan, 2008). These clusters may be of any arbitrary shape and can experience damage due to bond failure. This latter property is crucial for simulating crushing. Some examples of papers which have used clusters of bonded particles include Cheng et al. (2003), Favier et al. (1999), Hosseininia and Mirghasemi (2006), Jensen et al. (1999), McDowell and Harireche (2002), Robertson and Bolton (2001), and Thornton and Liu (2004).

4.1.3 Agglomerate Bonds and Contact Models

At each contact, it is necessary to include a rheological model to relate the inter-particle force (whether tensile or compressive) with the overlap. Cundall and Strack calculated forces by placing conceptual springs, dashpots and sliders at the contact points between particles (Zhang and Whiten, 1996). In general, the springs may be linear and elastic, non-linear and elastic, or elasto-plastic. The dashpots allow for viscous dissipation of energy. A slider in the contact tangential direction permits relative motion of particles when the Coulomb frictional strength is exceeded (O'Sullivan, 2008).

PFC2D/3D includes two contact models: the linear model and the Hertz-Mindlin model (Itasca Consulting Group, 2008). The PFC implementation of the Hertz-Mindlin model is a non-linear approximation to the theory outlined by Mindlin and Deresiewicz (1953). It is not as popular as the linear model as it is considerably more computationally expensive (Zhu et al., 2007), and will not be considered further here. The contact stiffness in the PFC linear model is calculated from the normal or shear stiffnesses of the two contacting entities (either two disks/spheres or one disk/sphere and one wall). For two contacting entities, α and β, which have normal stiffnesses of k_n^α and k_n^β and shear stiffnesses of k_s^α and k_s^β, the contact normal and shear stiffnesses, K_n and K_s, are given by Eq§. 4.4–4.5, respectively (Itasca Consulting Group, 2008):

$$K_n = \frac{k_n^\alpha k_n^\beta}{k_n^\alpha + k_n^\beta} \tag{4.4}$$

$$K_s = \frac{k_s^\alpha k_s^\beta}{k_s^\alpha + k_s^\beta} \tag{4.5}$$

Note that the normal stiffness is a secant stiffness (relates total displacement and force), while the shear stiffness is a tangent stiffness (relates incremental displacement and force). Thus, the normal contact force, F_n, is calculated from Eq. 4.6 and the elastic shear force increment, ΔF_s, from Eq. 4.7:

$$F_n = K_n x_n \tag{4.6}$$

$$\Delta F_s = -K_s \Delta x_s \tag{4.7}$$

If the second approach listed in Section 4.1.2 is applied, it is necessary to bond disks or spheres together at contacts to form agglomerates. PFC includes two standard bond types: contact bonds and parallel bonds (Itasca Consulting Group, 2008⋆). Contact bonds are simpler; these take the form of a pair of elastic springs at the contact point between bonded entities. Two parameters are required to specify contact bonds: the bond normal and shear strengths. In 3D, parallel bonds may be envisioned as an annular region centred on the contact point which contains a number of uniformly-distributed elastic springs. In 2D where the contact is between disks of unit thickness, the analogue

is parallel springs distributed over a rectangular region. Parallel bonds require the specification of five parameters in the software: the bond normal and shear strengths, normal and shear stiffnesses and the bond radius. These spring stiffnesses cause a force and moment to be developed if the bonded particles move relative to one another. The maximum normal and shear stresses acting at the periphery of the parallel bond are calculated from beam theory and compared to the corresponding bond strengths. If the maximum normal tensile stress is greater than the bond normal strength, the parallel bond is deemed to have failed and is deleted from the model. The same occurs if the maximum shear stress exceeds the bond shear strength. The bond radius is set by specifying the parameter $\bar{\lambda}$ in the software; the bond radius is the product of $\bar{\lambda}$ and the radius of the smaller of the two particles interacting in the bond (equivalent to the radius of the circular region containing springs in 3D). $\bar{\lambda}$ must be positive; if it is equal to 1, the bond radius is the same as the radius of the smaller particle in the bond. Further details of parallel bonding are provided by Potyondy and Cundall (2004).

Although parallel bonds are more computationally expensive than contact bonds, they have one major advantage. Parallel bonds transmit both force and moment (bending and twisting in three dimensions; bending only in two dimensions), whereas contact bonds are restricted to the transmission of force only.

4.1.4 Agglomerate Structure Formation

A great deal of research has been conducted on packing of disks and spheres (e.g., Feng et al., 2003; Nolan and Kavanagh, 1992; Santiso and Muller, 2002; Visscher and Bolsterli, 1972). Three different methods were used to produce the agglomerates for use in this research:

1. Radius expansion (2D)
2. Close-packed cubic lattices (3D)
3. Sequential addition (3D)

Radius expansion has been used by numerous authors to produce agglomerates for use in 2D simulations (e.g., Belheine et al., 2009; Chareyre and Villard, 2002; Yan et al., 2009). Disks are randomly generated within a rigid confining wall and their radii are gradually increased until the maximum overlap between disks reaches a low limiting value, as illustrated by Figure 4.1. The wall is then deleted. A related method which is sometimes used to generate 2D agglomerates is to randomly generate disks within a confining wall, as for radius expansion, but then impose a centripetal gravitational field to pack the disks together closely (e.g., Lian et al., 1998; Ning et al., 1997). Such methods have

also been applied to 3D simulations (Moreno-Atanasio and Ghadiri, 2006; Thornton et al., 1999).

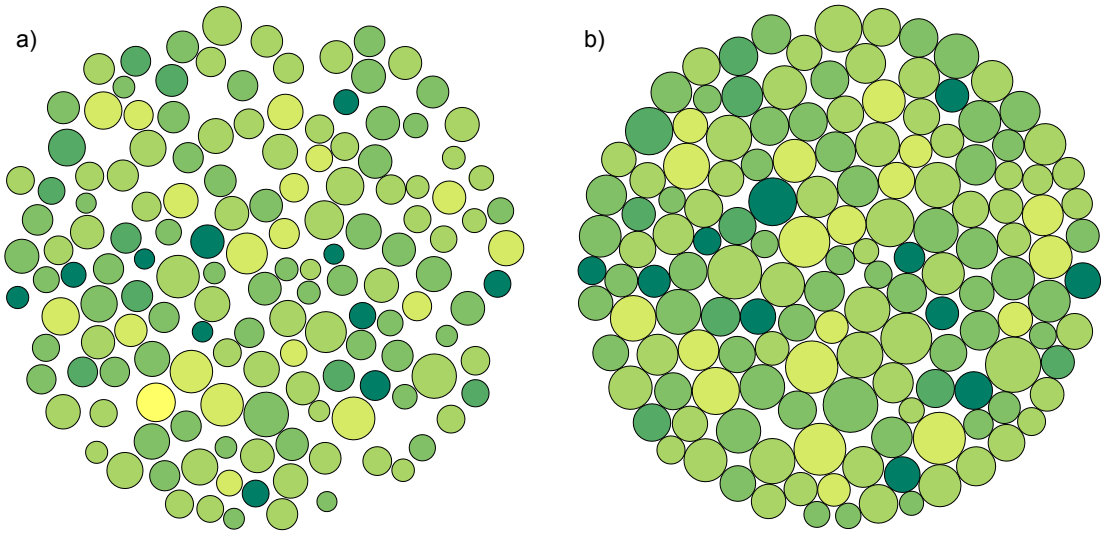

Figure 4.1: *Radius expansion for a 2D agglomerate containing 147 disks: a) shows the randomly-placed disks before expansion following 5000 DEM cycles and b) shows the final agglomerate after expansion*

Agglomerates for use in three-dimensional simulations are often produced from ideal cubic lattices, e.g., Cheng et al. (2003), Harireche and McDowell (2003), Kafui and Thornton (2000), and McDowell and Harireche (2002). Two types of close-packing of monosized spheres are possible: hexagonal and cubic close-packing. Both are equally efficient (74.05%) at filling space with spheres, but result in different lattices: hexagonal and face-centred cubic (fcc), respectively (West, 1999, p.20). A body-centred cubic (bcc) lattice may also be generated, but this is not close-packed (efficiency $\approx 68.02\%$). Irrespective of the lattice chosen, no initial overlaps are included between the spheres. Flaws in the lattice may be simulated by randomly deleting some of the spheres. For the simulations below, cubic close-packing was used, in which there are three alternating layers. These layers, often denoted as A, B and C, are illustrated in Figure 4.2.

The third method listed above, sequential addition, is less commonly used, and yields agglomerates with low density packings (Al-Raoush and Alsaleh, 2007). One seed sphere is placed at the origin. Other spheres are then placed successively and randomly within a geometry of defined volume surrounding this seed sphere. Each active sphere is moved randomly until it comes into contact with another sphere, when it is fixed in position (ensuring no overlaps). Since many different variants of these deposition methods exist, some details of the sequential addition method used in this research are provided in Appendix C.

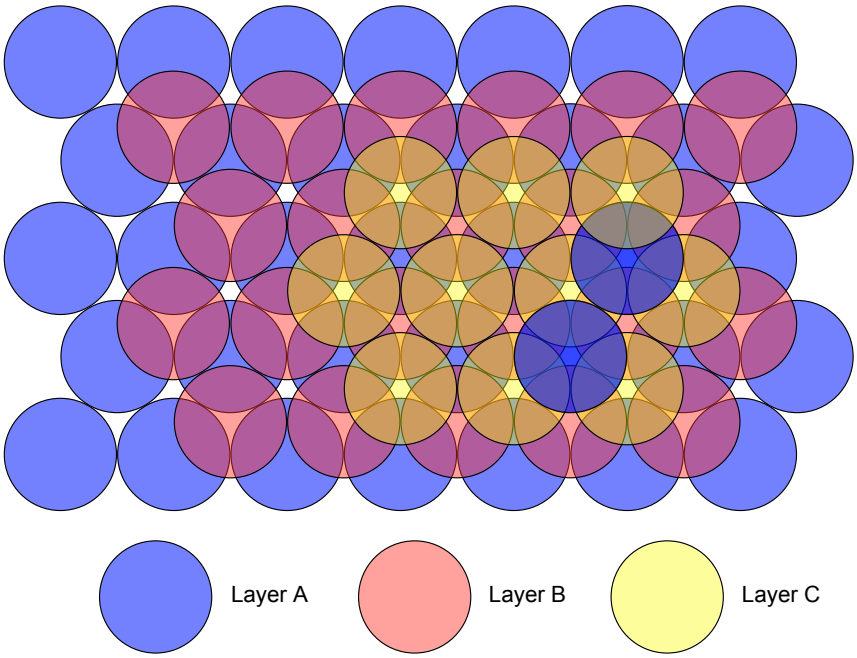

Figure 4.2: *Illustration showing how the three different layers, A, B, and C, are arranged in cubic close-packing of monosized spheres*

4.2 Current Approaches to Calibration

A key challenge in DEM analysis is to select appropriate parameters so that the response of real, physical systems can be accurately simulated. Some of the input parameters, such as the particle dimensions or the density, can be measured or estimated with a large degree of confidence. However, the rheological parameters for input to the contact constitutive models are often more difficult to determine accurately by experiment. It is not generally possible to infer a complete set of appropriate parameters for a DEM simulation directly from properties of the physical material, as might be expected for a complex system. Therefore a calibration approach is often used to select these parameters. Typically calibration involves varying the DEM parameters until the model response corresponds closely to the equivalent experimental response. This approach is widely used (e.g., Asaf et al., 2006; Coetzee and Els, 2009; Doležalová et al., 2002). This calibration is often conducted using very basic parametric studies, where parameters are varied individually and the effect on the model response is monitored. While conceptually simple, this approach to calibration has many disadvantages:

- It may take a long time to obtain an appropriate set of parameters.
- It is impossible to know in advance how many DEM simulations are required for calibration.
- The final parameters obtained may not be optimal.
- The mechanistic insight gained is limited.

Recently there have been proposals to develop more efficient DEM calibration approaches using design of experiments (DOE) methods. Yoon (2007) applied a Plackett-Burman design and response surface analysis to determine suitable DEM micro-parameters for uniaxial compression of bonded rock particles. Favier et al. (2010) used DOE methods to calibrate discrete element models for a mixer and a hopper, based on measurements of torque and discharge flow rate, respectively. Johnstone and Ooi (2010) applied DOE methods to find appropriate model parameters based on experimental measurements of flow in a rotating drum device and mechanical response during a confined compression test. A large range of DOE methods are in use in the scientific field, but all these methods have the same objective: to find the relationship between the process parameters and the process output by using a structured pre-planned methodology for obtaining experimental data that ensures the desired balance between the amount of data to be obtained and the precision and confidence required of the results.

An introduction to the Taguchi method was given in Chapter 2, beginning on p.22. This DOE approach has become very popular in industrial practice as a tool to achieve quality by design and minimise non-conformity costs, by establishing the optimum settings of a process that optimise its performance and the consistency of that performance (Taguchi, 1987). As it has proved to be effective in ensuring robust operation in practice (i.e., obtaining the set of parameters that minimise system variability resulting from the inevitable variability of its inputs), it should also be ideally suited to calibration (identifying the set of model parameters that minimise the variability of model predictions). However, a literature review revealed no published work which applied Taguchi methods to DEM calibration.

The objective of this chapter was to evaluate the Taguchi method as a tool for calibrating agglomerates of bonded disks (2D) and spheres (3D). If the method proved successful, it could be applied subsequently to calibrate a DEM using experimental data. Simulations of agglomerate crushing were conducted in both two and three dimensions using the commercial DEM software packages PFC2D and PFC3D, which were introduced in Section 4.1.1.

4.3 DEM Simulations

Due to the range of potential applications and level of interest in the modelling of particles using bonded agglomerates (Section 4.1.2), it was chosen here as an exemplar application of the Taguchi method to DEM calibration. It should be noted that these simulations were not intended to capture the behaviour of any particular material, and so could feasibly represent many different agglomerated products. This approach also

allowed parameters such as stiffnesses to be varied to investigate their effect on the responses without needing to consider physical implications.

4.3.1 Agglomerate Formation

The agglomerates used for the 2D calibration study were produced in the DEM simulation by bonding disks together. These disks were produced by radius expansion within a circular confining wall with a 500 µm diameter. The random placement of the disks inside the confining wall is dictated by the seed of the random number generator: a dimensionless integer. If two simulations were run using identical parameters, disks would be generated in the same positions; however, changing only the random number seed would cause the disks to be generated in different positions. The ball diameters before radius expansion were normally distributed around 30 µm with a lower cut-off of 20 µm. Following expansion, the average ball diameter was 38 µm with a standard deviation of 7 µm. On average, each agglomerate contained 130 disks with a standard deviation of 11 disks.

A lattice-based methodology was used to produce the agglomerates in three dimensions, placing monosized spheres in a face-centred-cubic lattice packing without any initial overlaps. Flaws in the lattice were simulated by randomly deleting either 10% or 20% of the spheres, as described in Section 4.4.2. Each agglomerate contained 846 spheres of diameter 60 µm before deletion. The agglomerate dimensions were ellipsoidal, with equal major and intermediate radii of approximately 350 µm and a minor radius of 250 µm. The PFC damping coefficient was 0.3. This local non-viscous damping is necessary to dissipate kinetic energy in the DEM (Potyondy and Cundall, 2004). Ball density was 600 $\mathrm{kg\,m^{-3}}$ which is a reasonable estimate for light dairy agglomerates. The damping coefficient and ball density were the same for the 2D and 3D simulations.

4.3.2 Particle Crushing Conditions

To simulate a particle crushing test, each agglomerate was subject to uniaxial compression between stiff, horizontal, frictionless platens, as shown in Figure 4.3. This form of DEM agglomerate crushing is similar to the work of Cheng et al. (2003) and Thornton et al. (2004).

This compression was strain-controlled, and all agglomerates were compressed to a strain of 20%. In both the two- and three-dimensional cases, the bottom platen remained at rest and the upper platen moved towards it at 10 $\mathrm{mm\,s^{-1}}$. This velocity was sufficiently low to ensure that forces on the top and bottom platens were equivalent during crushing, i.e., quasi-static loading was attained. The initial distance between the platens was

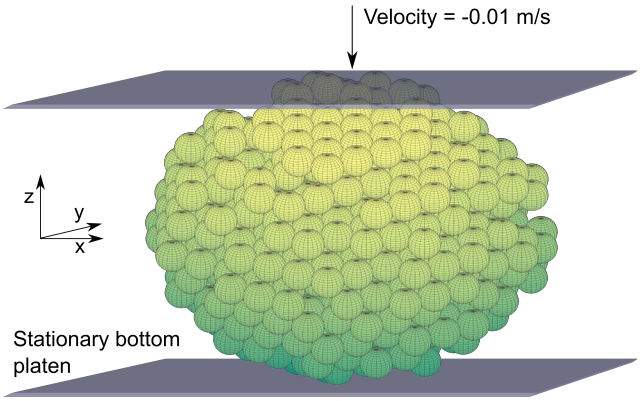

Figure 4.3: *Illustration of uniaxial crushing of an agglomerate between two stiff horizontal platens for the 3D simulations*

equal to the agglomerate height. Stable time steps were calculated automatically by the software and were approximately 1×10^{-4} s for 2D and 3×10^{-5} s for 3D.

4.3.3 Agglomerate Bonds and Contact Models

The inter-sphere contacts were modelled using a standard linear contact model and parallel bonds were used to cement the disks or spheres together to form a bonded agglomerate (see Section 4.1.3). Once a bond breaks, or if a new contact is formed after the cementing stage of the simulation, the contact interaction between two particles is frictional.

4.4 Experimental Designs

The 2D and 3D models needed to be assessed independently because although many parameters were the same, the range of values of certain parameters which gave a feasible response differed by orders of magnitude in many cases. This could be attributed to the kinematic constraints imposed in 2D compared to the 3D case; in 2D, each base particle has three, rather than six, degrees of freedom and particle motion is restricted to a single plane. In ANOVA, whether a factor or interaction is important or negligible is a comparative result which depends on the range of values tested. This implies that the 2D and 3D results may not be comparable. However, since the underlying physical phenomena represented by each parameter are the same, some insights obtained in one case may be considered for the other. As 2D simulations are much less computationally expensive, it was decided to consider these first, and use the insights gained to inform the experimental design for the 3D simulations.

4.4.1 Experimental Design for Two-Dimensional Simulations

Table 4.1 shows the list of the factors and their levels used for the 2D simulations. An L_{27} array could have been chosen as it can accommodate up to 13 factors at three levels. However, confoundings would have been extensive as nine columns would have been occupied by factors with only four columns left vacant, and it would not have been possible to allocate these nine factors to columns without intricately confounding their effects with interactions. Confoundings are particularly complex with three-level factors, as the effect of each interaction is distributed between two columns. The next orthogonal array for three-level factors is the L_{81} array containing 40 columns, where a more manageable set of confoundings could be defined. Selecting an L_{81} instead of L_{27} increases computational time approximately three-fold due to the number of runs rising from 27 to 81. As the 2D simulations were not computationally expensive, this time increase was considered acceptable. It is noted that the total number of possible combinations of 9 factors at 3 levels is $3^9 = 19683$, so studying this solution space with only 81 simulations was still a very efficient approach.

Table 4.1: *Factors varied, levels used and column of the standard L_{81} array assigned to each factor for the 2D simulations*

Control Factor	Level			Column
	1	2	3	
Bond radius multiplier (–)	0.7	0.8	0.9	1
Bond normal strength ($\mathrm{N\,m^{-2}}$)	1×10^{6}	1.5×10^{6}	2×10^{6}	2
Bond shear strength ($\mathrm{N\,m^{-2}}$)	1×10^{6}	1.5×10^{6}	2×10^{6}	5
Bond normal stiffness ($\mathrm{N\,m^{-3}}$)†	1×10^{11}	1.5×10^{11}	2×10^{11}	14
Bond shear stiffness ($\mathrm{N\,m^{-3}}$)†	1×10^{11}	1.5×10^{11}	2×10^{11}	22
Ball friction (–)	0.4	0.6	0.8	25
Ball normal stiffness ($\mathrm{N\,m^{-1}}$)‡	3×10^{5}	5×10^{5}	7×10^{5}	27
Ball shear stiffness ($\mathrm{N\,m^{-1}}$)‡	3×10^{5}	5×10^{5}	7×10^{5}	35
Random number seed (–)	2000	4000	6000	39

†Bond stiffnesses have dimensions of $^{\text{stress}}/_{\text{displacement}}$.

‡Ball stiffnesses have dimensions of $^{\text{force}}/_{\text{displacement}}$.

The main effects were assigned to the columns of the standard L_{81} array which are listed in Table 4.1. The full L_{81} array is provided in Appendix A on p.214. By reference to the triangular table for the L_{81} array (Table A.8 on p.228), it can be seen that these nine columns were chosen because they were independent of all two-way interactive effects, which were confined to the remaining 31 columns of the array (where they were partially pooled). Therefore, this design allowed all factors to be tested without

confounding. Pools of interactions may also be tested for significance to permit many of those interactions to be eliminated with confidence.

4.4.2 Experimental Design for Three-Dimensional Simulations

An L_{27} array containing 13 columns was used for the 3D simulations. In this case, the computational requirements would not have made an L_{81} design a reasonable choice. However, some insight into the system was gained from the analysis of the 2D results. Two factors whose order of magnitude did not change and which proved to be of little influence in the 2D model were not considered further: the bond radius multiplier and the random number seed. These factors were set at their median values in Table 4.1. One additional factor that needed to be included was the percentage of balls deleted from the lattice. The number of degrees of freedom remaining allowed only two interactive effects to be considered. Thus, the design was developed assuming that all but two interactive effects could be neglected, and factors were allocated to columns to allow these two chosen interactions to be assessed. This was deemed to be appropriate on the basis of the 2D analysis, and the interactive effects selected for consideration were the following:

1. Bond shear strength × bond shear stiffness (Interaction I)
2. Bond shear strength × ball shear stiffness (Interaction II)

Table 4.2 shows the factors and levels used for the 3D simulations, along with the columns of the standard L_{27} array assigned to each factor. The L_{27} array and corresponding triangular table are provided in Appendix A on p.213 and p.226, respectively.

Table 4.2: *Factors varied, levels used and column of the standard L_{27} array assigned to each factor for the 3D simulations*

Control Factors	Levels			Column
	1	2	3	
Bond shear strength ($\mathrm{N\,m^{-2}}$)	1.5×10^5	2×10^5	2.5×10^5	1
Bond shear stiffness ($\mathrm{N\,m^{-3}}$)	3×10^{10}	5×10^{10}	7×10^{10}	2
Ball shear stiffness ($\mathrm{N\,m^{-1}}$)	3×10^5	5×10^5	7×10^5	5
Bond normal strength ($\mathrm{N\,m^{-2}}$)	1.5×10^5	2×10^5	2.5×10^5	8
Ball friction (–)	0.4	0.6	0.8	9
Percentage of balls deleted (%)	0	10	20	10
Bond normal stiffness ($\mathrm{N\,m^{-3}}$)	3×10^{10}	5×10^{10}	7×10^{10}	11
Ball normal stiffness ($\mathrm{N\,m^{-1}}$)	3×10^5	5×10^5	7×10^5	12

Interaction I was contained in columns 3 and 4, and interaction II in columns 6 and 7. The remaining interactions were intricately confounded with factors, and were assumed to be negligible in the data analysis.

4.5 Simulation Responses

The objective of the study was to achieve a controlled mechanical response for the agglomerate as a whole. The mechanics of an agglomerate response under uniaxial compression are often complex and highly non-linear. The force-deflection behaviour may include multiple local maxima, and alternating periods of strain softening and strain hardening. As discussed by Cavarretta (2009), the load deformation response is affected by asperity failure, particle rotation, elastic and plastic response of the solid particle material and gross fragmentation. Therefore, one single response is insufficient to characterise the compression mechanics and in this study, four responses were selected:

1. The normal force on the platens at 10% strain (N)
2. The normal force at the point of failure of the agglomerate (N)
3. The strain at the point of failure of the agglomerate (–)
4. The agglomerate stiffness ($\mathrm{N\,m^{-1}}$)

In many single particle compression tests (either physical tests or simulations), identifying the point of failure for strain-controlled crushing is subjective. However, the results obtained for the 3D simulations in this study were unambiguous. This is illustrated in Figure 4.4, which shows three representative plots of normal force versus displacement for trials 1, 6 and 22 in three dimensions.

The problems associated with determining one unique point of failure from a complex response were discussed in Section 3.1.6 (p.57). The same issue arose with the 2D simulation data. Figure 4.5 shows plots of normal force versus displacement for trials 18, 65 and 75 in two dimensions.

The algorithm which was outlined in Section 3.1.6 was modified for use in this situation. The modified algorithm states that the point of failure is the first point, ordered by increasing strain, which satisfies the following three criteria:

1. The point of failure is a local maximum on a plot of force versus deflection, and has the highest force value within a small (< 2%) strain range surrounding this point.
2. The force at failure must exceed 50% of the maximum force recorded.

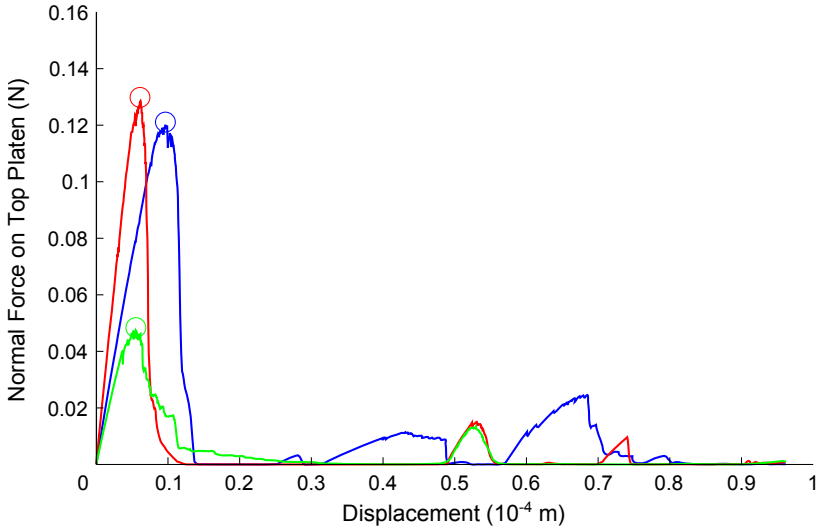

Figure 4.4: *Three plots of normal force (N) versus displacement (10^{-4} m) for three-dimensional agglomerate crushing trials 1, 6 and 22*

3. The difference between the force at failure and the force at the subsequent local minimum, normalised by the force at failure, must be greater than 25%.

This modified algorithm was less generally applicable since the second condition arbitrarily defined the force at failure to be greater than half the maximum force recorded before 20% strain was attained. However, the results obtained were more reliable than the previous algorithm for identifying the points of failure of 2D simulation data. Each agglomerate stiffness was calculated as the slope of the linear region of the force-displacement plot immediately prior to failure, which was found using the same approach as in Section 3.1.6. The circles and dashed lines on Figure 4.5 identify the points of failure and stiffnesses obtained using this approach.

4.6 Analytical Procedure

The data were analysed using STATISTICA (v.7.1, StatSoft, Inc., Tulsa, OK, USA). Firstly, an ANOVA was applied to the raw data obtained for the 2D simulations for each of the four response parameters. Marginal means were calculated and presented graphically; these show the average effect of choosing a particular factor level compared to the global average. In the Taguchi method, estimates for any combination of settings are calculated by addition of the respective marginal means, which implies assuming that all interactions are negligible. In some cases, it is possible to correct for interactions (when the effect of that interaction is confounded neither with any factor nor with other potentially significant interactions). In order to test the predictive ability of this procedure, a validation set was subsequently run by choosing 10 random combinations of levels (other than the 81 already used), and the responses obtained by running DEM

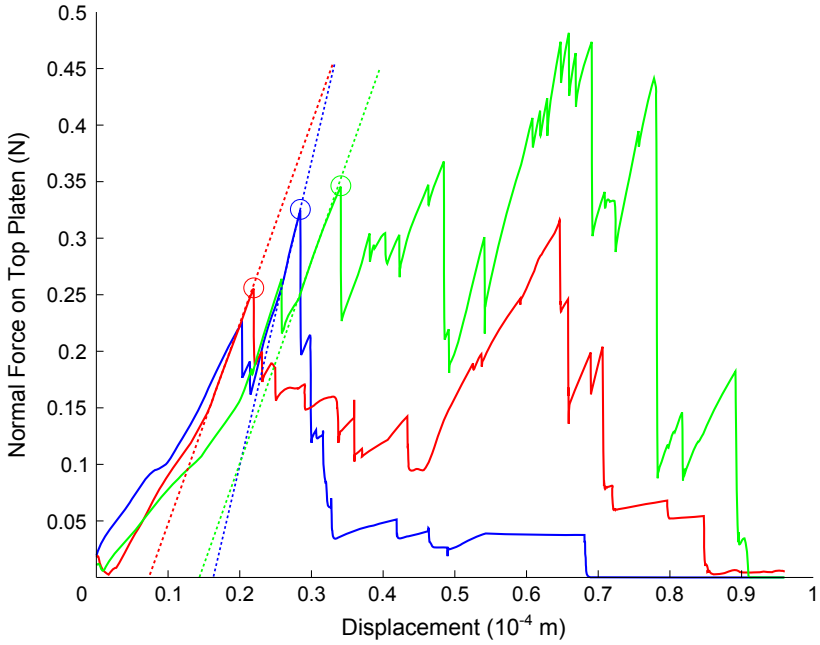

Figure 4.5: *Three plots of normal force (N) versus displacement (10^{-4} m) for two-dimensional agglomerate crushing trials 18, 65 and 75, indicating points of failure of the agglomerates using circles and agglomerate stiffnesses using dashed lines*

simulations using these randomly-chosen levels were compared to those predicted by the marginal means addition.

There were 9 factors in the design and therefore 36 possible two-way interactions $\left[\sum_{i=1}^{n-1} i \text{ where } n \text{ is the number of factors}\right]$. As interactions of three-level factors are distributed between two columns, most of the columns of the L_{81} which were not occupied by factors contained parts of multiple interactions, e.g., column 3 contained parts of the following interactions:

- Bond radius multiplier × bond normal strength
- Bond normal stiffness × bond shear stiffness
- Ball shear stiffness × random number seed

In order to evaluate the potential significance of the interactions in 2D, each was assessed in turn, assuming all others to be negligible. If the added effect of considering an interaction in this test was negligible, then the interaction could be neglected. Otherwise, it could potentially be important, but this was not certain as the effect was confounded with other interactions. In the 3D analysis, all but two interactions were assumed to be negligible. Estimates of the response were corrected for these two interactive effects, and they were also tested for statistical significance and compared with the effects of factors.

4.7 Results and Discussion

4.7.1 Results of Two-Dimensional Simulations

The ANOVA results are shown in Table 4.3. The statistical significance was assessed with the p-value, as described on p.27. As in Section 2.3.1, a significance level of 95% was chosen. To assist visualisation of results, the statistically-significant effects are denoted in bold and with an asterisk. The element denoted as error in the ANOVA table is essentially the error introduced by neglecting all interactions.

Table 4.3: *ANOVA results for the four responses for the 2D simulations. υ is the number of degrees of freedom, SS the sum of squares associated to each element of the table and p the p-value calculated with the respective variances. Statistically-significant effects at a 95% confidence level are denoted in bold and with an asterisk*

Factor	υ	Normal Force at 10% Strain		Normal Force at Point of Failure	
		SS	p	SS	p
Bond radius multiplier	2	0.013	0.473	0.020	0.253
Bond normal strength	2	0.697	**0.000***	0.321	**0.000***
Bond shear strength	2	0.019	0.332	0.087	**0.004***
Bond normal stiffness	2	0.107	**0.003***	0.032	0.108
Bond shear stiffness	2	0.008	0.626	0.008	0.550
Ball friction	2	0.024	0.243	0.008	0.576
Ball normal stiffness	2	0.012	0.506	0.060	**0.018***
Ball shear stiffness	2	0.021	0.284	0.009	0.526
Random number seed	2	0.001	0.962	0.006	0.670
Error	62	0.518		0.435	
Total	80	1.42		0.987	

Factor	υ	Strain at Point of Failure		Agglomerate Stiffness	
		$SS \times 10^4$	p	$SS \times 10^{-7}$	p
Bond radius multiplier	2	1.20	0.815	19.1	0.059
Bond normal strength	2	93.8	**0.000***	18.3	0.066
Bond shear strength	2	25.8	**0.016***	4.48	0.502
Bond normal stiffness	2	42.8	**0.001***	47.2	**0.001***
Bond shear stiffness	2	40.6	**0.002***	14.3	0.116

Continued on page 90

Factor	υ	Strain at Point of Failure		Agglomerate Stiffness	
		$SS \times 10^4$	p	$SS \times 10^{-7}$	p
Ball friction	2	19.4	**0.043***	38.4	**0.004***
Ball normal stiffness	2	9.02	0.223	15.7	0.095
Ball shear stiffness	2	1.66	0.754	3.56	0.577
Random number seed	2	3.27†	0.575	5.89	0.405
Error	62	182		199	
Total	80	419		366	

†Note that this entry is equal to 3.27×10^{-4} to prevent ambiguity.

It is clear that the most important factor in this solution space was the bond normal strength: it had the largest sum of squares (SS) for three of the responses (only not statistically-significant for agglomerate stiffness, although still the fourth more important there). The second more influential parameter was bond normal stiffness, which was not statistically-significant only for normal force at failure (where it was the fourth more influential parameter), and was the most important for agglomerate stiffness (and second most important for the other two responses). Bond shear strength and ball friction were also highly influential parameters as both were statistically-significant at the 95% level for two responses. It was most important to find accurate values for these four parameters within this solution space.

Other influential parameters for certain responses were bond shear stiffness (for strain at failure) and ball normal stiffness (force at failure). Bond radius multiplier, ball shear stiffness and random number seed had no statistically-significant influence on any of the responses, so fixing them at the median value may suffice for calibration. This conclusion assumed negligible interactive effects. The error sums of squares were quite large, which could only have been due to interactive effects being important, as the data were obtained by mathematical simulation and contained no white noise.

To better understand the system, all the interactions were calculated individually (in turn) for each response assuming all others to be negligible, and those that were identified as significant at a 90% confidence level by the respective ANOVA are shown in Table 4.4, along with the sums of squares, p-values and the two columns of the L_{81} that contained the full interaction. Note that 90% confidence for a two-way interaction across two columns was a similar criterion to 95% for an individual factor in one column, as $0.95^2 \approx 0.9$.

Table 4.4: *Two-way interactions, sums of squares, p-values and columns containing those interactions identified as statistically-significant at a 90% level for the 2D simulations*

Interaction	SS	p	Columns
Response: Normal Force at 10% Strain			
Bond normal strength × Bond shear stiffness	0.109	0.007	16, 19
Bond radius multiplier × Bond normal stiffness	0.090	0.023	15, 16
Bond shear strength × Ball friction	0.086	0.030	16, 34
Bond shear strength × Ball shear stiffness	0.069	0.076	17, 26
Response: Normal Force at Point of Failure			
Bond normal stiffness × Ball normal stiffness	0.094	0.006	9, 40
Bond shear strength × Bond shear stiffness	0.090	0.008	31, 40
Bond radius multiplier × Random number seed	0.072	0.030	38, 40
Bond shear strength × Ball shear stiffness	0.068	0.040	17, 26
Bond normal strength × Bond normal stiffness	0.062	0.061	17, 20
Ball friction × Random number seed	0.058	0.078	13, 17
Response: Strain at Point of Failure			
Bond normal stiffness × Ball normal stiffness	2.35×10^{-3}	0.086	9, 40
Bond normal stiffness × Bond shear stiffness	2.33×10^{-3}	0.088	3, 18
Bond radius multiplier × Bond normal strength	2.26×10^{-3}	0.098	3, 4
Response: Agglomerate Stiffness			
Bond radius multiplier × Random number seed	4.44×10^{8}	0.005	38, 40
Bond normal stiffness × Ball normal stiffness	3.61×10^{8}	0.019	9, 40
Bond shear strength × Bond shear stiffness	3.55×10^{8}	0.021	31, 40
Bond shear strength × Random number seed	3.01×10^{8}	0.046	21, 30
Bond normal strength × Ball shear stiffness	2.62×10^{8}	0.081	32, 38
Ball friction × Ball shear stiffness	2.55×10^{8}	0.089	9, 21

For example, for the normal force at 10% strain, all but four of the interactions were shown to be negligible using this procedure. The three interactions with the largest sums of squares had column 16 in common: clearly, this column was associated with a relatively large sum of squares. Therefore, it cannot be said whether only one of these was actually significant and dominant, or if two or even all three were significant. A similar observation could be made regarding column 40 for the normal force at failure and agglomerate stiffness responses.

Figure 4.6 shows the stacked marginal means plots of the data, where the horizontal

dashed limits denote ± two standard errors. For those factors identified as significant in Table 4.3, it is clear that increasing the normal strength of the parallel bonds tended to increase the normal force at 10% strain, while increasing their normal stiffness had the opposite effect. These observations make sense from a mechanical point of view. If the analyst seeks to maximise this force to give stronger agglomerates, this could be achieved by choosing the settings shown in Table 4.5. The response estimated by simple addition of the marginal means (i.e., neglecting all interactive effects) was 0.395 ± 0.0785 N.

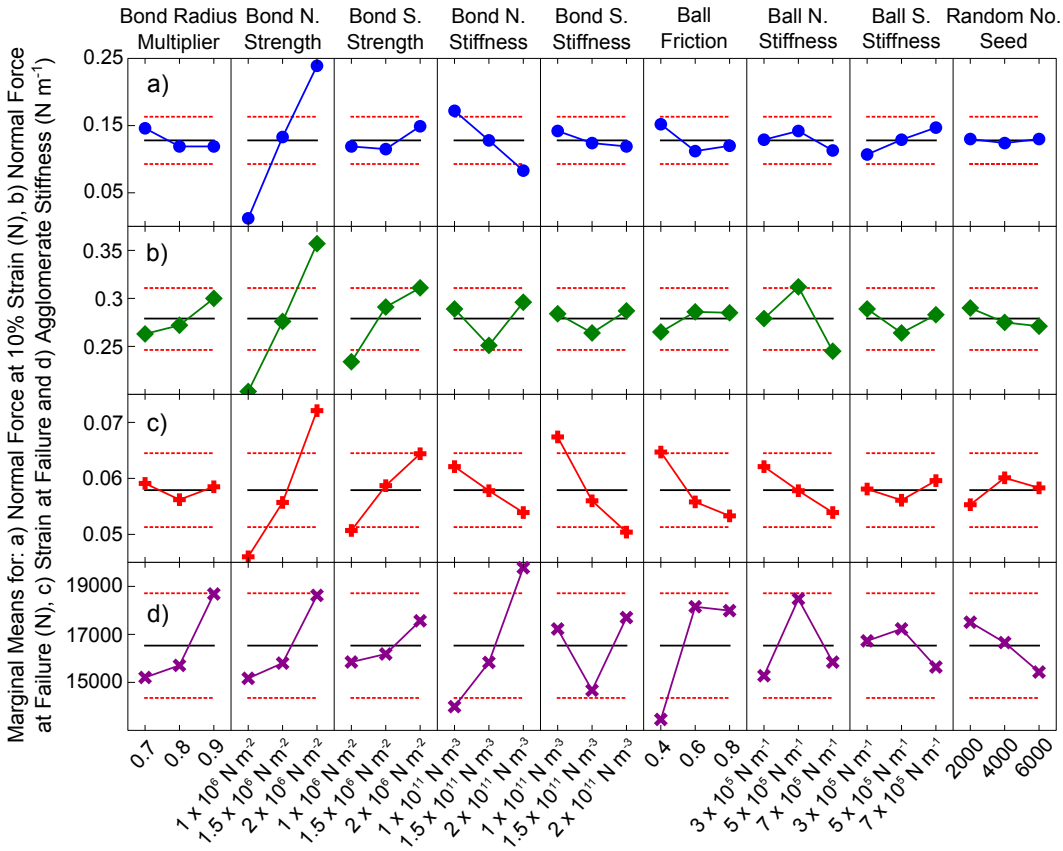

Figure 4.6: *ANOVA marginal means plots for four responses for the 2D simulations: a) normal force on platens at 10% strain (N); b) normal force at failure (N); c) strain at failure and d) agglomerate stiffness ($N m^{-1}$)*

The force at failure increased if higher values of parallel bond normal and shear strength were used, while using an intermediate ball normal stiffness of 5×10^5 $N m^{-1}$ increased this response, i.e., on average, selecting these settings increased the force at which the agglomerate failed under uniaxial compression. The strain at failure may be maximised by choosing high settings for bond normal and shear strength and the lowest settings for ball friction and both bond stiffnesses, within the range tested. The settings for maximisation of agglomerate stiffness were similar: a high value for bond normal stiffness and the intermediate setting for ball friction of 0.6, although there was little difference between the intermediate and high settings of this factor.

Table 4.5: *Factor settings that maximise normal force on the platens at 10% strain for the 2D simulations, with the force estimated by marginal means addition and estimated 95% confidence interval*

Control Factor	Level	Factor Value
Bond radius multiplier	1	0.7
Bond normal strength	3	2×10^6 N m^{-2}
Bond shear strength	3	2×10^6 N m^{-2}
Bond normal stiffness	1	1×10^{11} N m^{-3}
Bond shear stiffness	1	1×10^{11} N m^{-3}
Ball friction	1	0.4
Ball normal stiffness	2	5×10^5 N m^{-1}
Ball shear stiffness	3	7×10^5 N m^{-1}
Random number seed	3	6000
Predicted force at 10% strain		0.3950 N
95% confidence interval		$\pm$ 0.0785 N

To assess the predictive ability of the marginal means addition (i.e., the inaccuracy resulting from neglecting all interactions in the estimation of a specific response), 10 combinations of factor levels, each different from the 81 combinations already used in the design, were selected at random. For each combination, the responses (normal force at 10% strain, normal force at failure, strain at failure and agglomerate stiffness) were found in two ways:

1. By experiment, running a DEM simulation using the appropriate combination of factor levels and obtaining the data as was done for the initial 81 trials.
2. By adding the marginal means for the respective factor settings to the global average for each response.

Figure 4.7 compares the estimates of the marginal means additions with the simulation results. Results were mixed, with certain responses performing better than others. This is not surprising as Table 4.3 shows that neglecting the interactive effects was a major source of error. For the normal force at failure considered in Figure 4.7b, the marginal means estimates over-predicted forces which had very small values, but under-predicted larger forces. A tendency to under-estimate agglomerate stiffness (Figure 4.7d) was also apparent for eight of the combinations tested. It is evident that neglecting all interactive effects would be very limiting. Therefore, the most basic application of the Taguchi method provided some inconclusive results at this stage. It would be necessary to untangle some of the interactions to assess them properly and then apply the Taguchi optimisation procedure for parameter calibration with the appropriate

corrections. This suggests that a two-step procedure may be a better option than larger designs. A two-level design could be used first to eliminate (pools of) interactions that are not significant and then a three-level design may be better defined, even though it may now require fewer runs. While a two-way interaction with two or three levels in the factors are not the same, the reality of most systems is that two levels are often sufficient to reveal the nature of the most common interactions. It is not common that an interaction may prove to be negligible with a two-level design and show relevance with a three-level design.

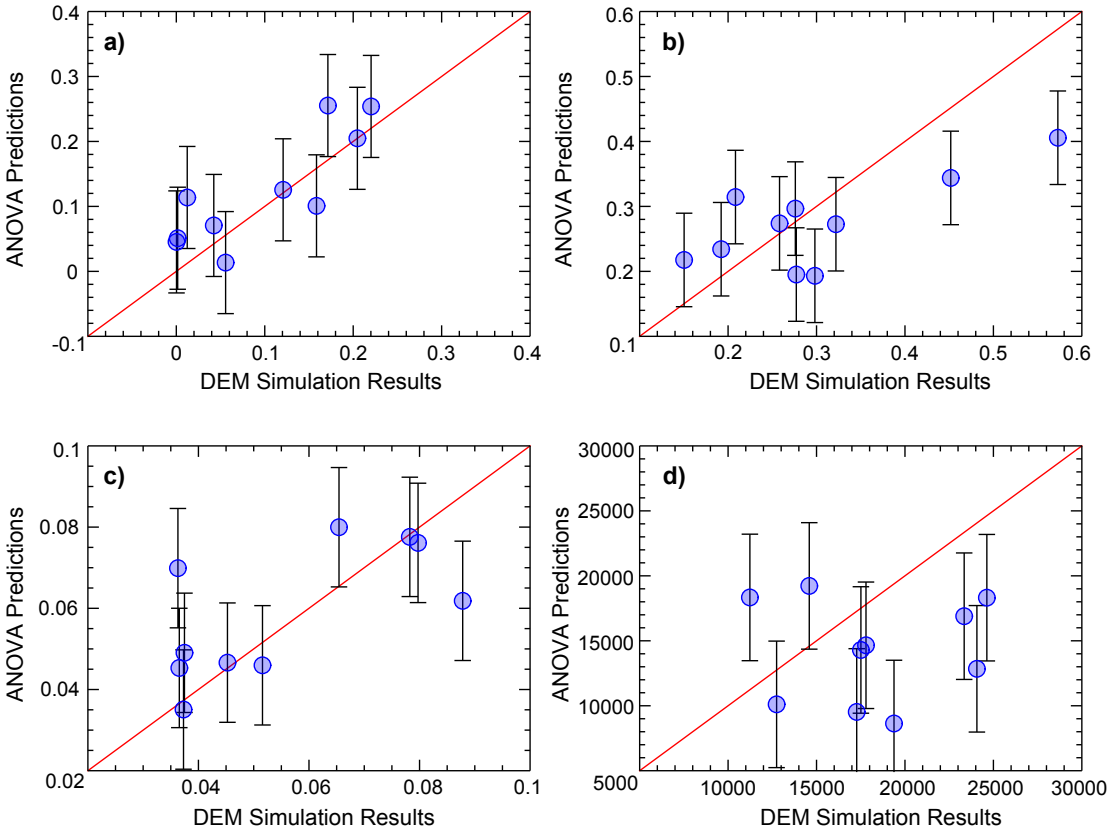

Figure 4.7: *Plots of ANOVA predictions against the corresponding DEM simulation results for 10 randomly-selected combinations of the factor levels for the 2D analysis, where responses a–d are as listed for Figure 4.6 and error bars indicate 95% confidence intervals*

4.7.2 Results of Three-Dimensional Simulations

The same four overall responses were analysed in 3D, i.e., normal force at 10% strain, normal force at failure, strain at failure and agglomerate stiffness. As the 2D results indicated not only many interactions that could be neglected, but also the two factors of least significance, a second design with reduced data requirements could be established (using an L_{27} array). The ANOVA results, which include two interactions that could be assessed fully and independently (once the others had been assumed negligible), are shown in Table 4.6.

Table 4.6: *ANOVA results for the four response parameters for the simulations in 3D. υ is the number of degrees of freedom, SS the sum of squares and p the p-value. Statistically-significant effects at a 95% confidence level are denoted in bold and with an asterisk*

Factor	υ	Normal Force at 10% Strain		Normal Force at Point of Failure	
		$SS \times 10^6$	p	$SS \times 10^4$	p
Bond normal strength	2	19.6†	0.500	33.9	0.099
Bond shear strength	2	18.4	0.517	31.4	0.107
Bond normal stiffness	2	19.3	0.505	3.94	0.487
Bond shear stiffness	2	132	0.130	2.60	0.590
Ball friction	2	8.30	0.703	24.4	0.133
Ball normal stiffness	2	96.1	0.170	1.13	0.768
Ball shear stiffness	2	73.7	0.211	1.55	0.707
Percentage of balls deleted	2	24.8	0.442	709	**0.005***
Interaction I	4	88.8	0.330	8.10	0.532
Interaction II	4	23.1	0.708	1.42	0.925
Error	2	19.7		3.74	
Total	26	524		822	

Factor	υ	Strain at Point of Failure		Agglomerate Stiffness	
		$SS \times 10^6$	p	$SS \times 10^{-7}$	p
Bond normal strength	2	54.7	**0.025***	7.50	0.088
Bond shear strength	2	20.4	0.065	12.0	0.057
Bond normal stiffness	2	170	**0.008***	51.1	**0.014***
Bond shear stiffness	2	26.3	0.051	16.3	**0.042***
Ball friction	2	182	**0.008***	135	**0.005***
Ball normal stiffness	2	1.88	0.430	8.13	0.082
Ball shear stiffness	2	8.45	0.144	5.38	0.118
Percentage of balls deleted	2	17.2	0.076	275	**0.003***
Interaction I	4	14.2	0.173	5.52	0.218
Interaction II	4	12.1	0.199	37.9	**0.037***
Error	2	1.42		0.723	
Total	26	509		555	

† As in Table 4.3, note that this entry is equal to 1.96×10^{-5} in reality.

The results in 3D were comparable to those in 2D, even though different ranges were used in many parameters. However, the most significant parameters were not always the same as in 2D. This is not surprising since an analysis of this type is always relative to the ranges of values used, i.e., to the solution space being scanned. It is also noted that the inclusion of two interactions (each requiring four degrees of freedom) and the more limited number of data naturally resulted in a much larger confidence interval. Therefore, this design did not identify the limit of statistical significance as clearly as the L_{81}. Considering the normal force on the platens at 10% strain, no factor was now statistically-significant in 3D. As this was partially attributable to the low number of degrees of freedom of the error, it was more appropriate to analyse the relative importance of the factors and interactions using their sums of squares. The percentage of balls deleted had the overwhelming influence on force at failure. The three factors that significantly affected the strain at failure were three of the five which were identified as significant in 2D. The percentage of balls deleted significantly influenced the agglomerate stiffness in addition to ball friction and both bond stiffnesses; both bond normal stiffness and ball friction were also significant in 2D. Interaction II, between bond shear strength and ball shear stiffness, was significant at the 95% level for the agglomerate stiffness response. This was particularly interesting since neither factor in the interaction was one of those four identified as significant independently, so the interaction was clearly very important.

It is noted that the relative magnitude of the error was much smaller than in 2D. This could also be quantified by the coefficient of determination (R^2), which is the percentage of the variance of the data explained by the factors and interactions. For the four responses in Table 4.6, R^2 values were 98.1%, 99.8%, 99.9% and 99.9%, respectively. When coefficients of determination were calculated without including both interactions, the results were reduced to 86.5%, 99.2%, 97.2% and 95.9%, respectively. This result confirmed the importance of considering these two interactions.

The stacked marginal means plots are shown for the main effects in Figure 4.8. Force at failure was increased by using 0% ball deletion. The settings to maximise strain at failure were identical to those in 2D for the three factors identified as significant. High settings of bond normal stiffness, bond shear stiffness and ball friction, and low percentage ball deletion maximised agglomerate stiffness. However, this analysis with marginal means alone was no longer complete, as the correction for interactive effects also needed to be taken into consideration. Marginal means plots were drawn for the two interactive effects considered and are shown in Figure 4.9.

As an example, normal force at 10% strain was maximised by choosing a bond shear strength (in green) of $2\times10^5\,\mathrm{N\,m^{-2}}$ for both interactions and the highest settings of bond shear stiffness ($7\times10^{10}\,\mathrm{N\,m^{-3}}$) and ball shear stiffness ($7\times10^5\,\mathrm{N\,m^{-1}}$). Note also that both

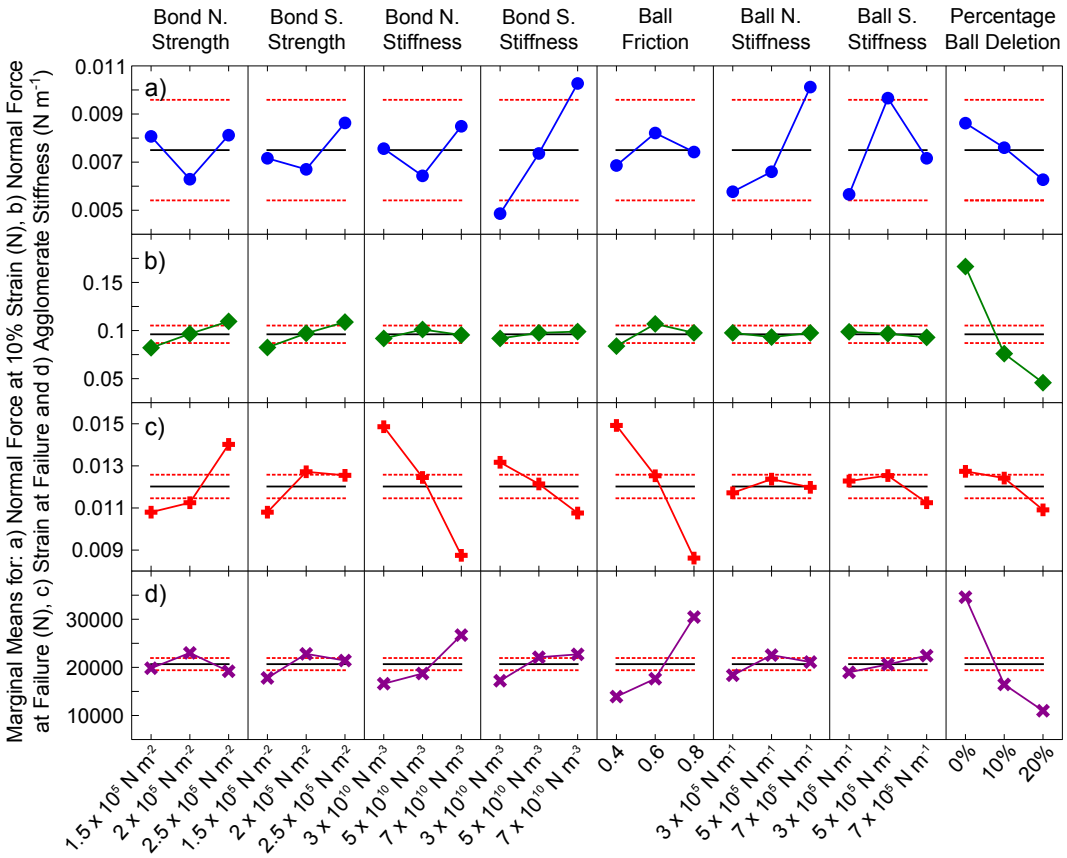

Figure 4.8: *ANOVA marginal means plots for four responses for the 3D simulations: a) normal force on platens at 10% strain (N); b) normal force at failure (N); c) strain at failure and d) agglomerate stiffness ($N m^{-1}$)*

interactive effects were negligible for force at failure, which is unsurprising considering their small SS in Table 4.6. Approximately the same marginal mean was obtained irrespective of the value chosen for bond shear strength. For the single statistically-significant interaction, between bond shear strength and ball shear stiffness for the agglomerate stiffness response, the following may be seen on Figure 4.9:

- Using an intermediate setting of ball shear stiffness (5×10^5 $N m^{-1}$) gave a high marginal mean if bond shear strength was at an extreme setting (1.5×10^5 $N m^{-2}$ or 2.5×10^5 $N m^{-2}$).
- Using an extreme setting of ball shear stiffness (3×10^5 $N m^{-1}$ or 7×10^5 $N m^{-1}$) gave a low marginal mean if bond shear strength was at its minimum setting of 1.5×10^5 $N m^{-2}$.

The predictive ability of marginal means addition was again tested by comparing the results thus estimated with actual simulation results performed for 10 random combinations of settings (other than the 27 already performed). Results are shown in Figure 4.10, both considering and omitting the interactive effects.

Both sets of predictions were very close, and the increase in accuracy obtained by

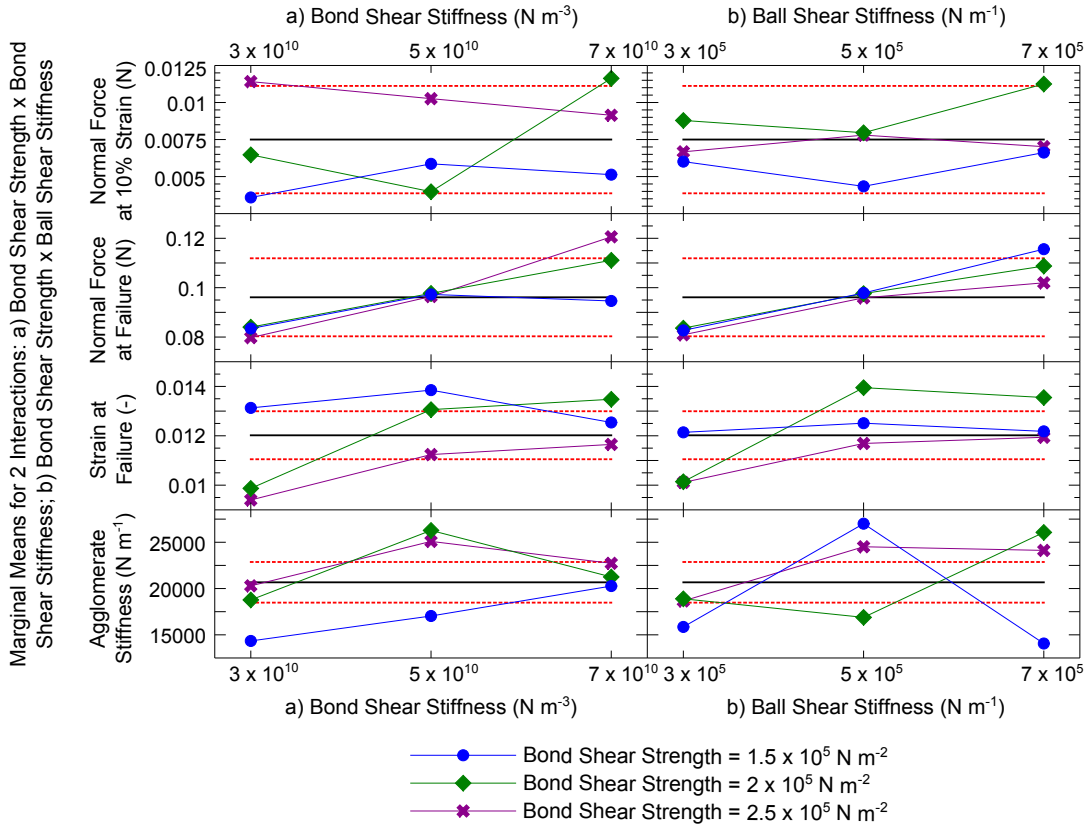

Figure 4.9: *ANOVA marginal means plots for the two interactions considered at three dimensions: a) bond shear strength × bond shear stiffness and b) bond shear strength × ball shear stiffness*

correcting for the interactive effects was quantitatively small. The predictions in 3D were considerably more accurate than those in 2D, with a lower number of anomalous predictions. Predictions were particularly accurate for all normal force at failure points tested (Figure 4.10b) and for low agglomerate stiffnesses (Figure 4.10d). The predictions of normal force at 10% strain were least accurate, which reflected the low R^2 for this response (p.96). The better predictive ability in 3D, in comparison with the 2D case, was due to the smaller proportion of the total sums of squares in the ANOVA table attributed to unexplained variance (error).

4.7.3 Discussion

The results in Sections 4.7.1 and 4.7.2 demonstrate that the application of the Taguchi method is appropriate for DEM calibrations using bonded agglomerates. Good predictive ability was demonstrated when interactions were considered. It is clear that accounting for interactive effects is important; therefore, a two (or more) step approach is preferable to a single (larger) design. This could be a problem with the Taguchi method because it relies on orthogonal arrays with very intricate confoundings between factors and interactions. However, once these are understood they can be tested to

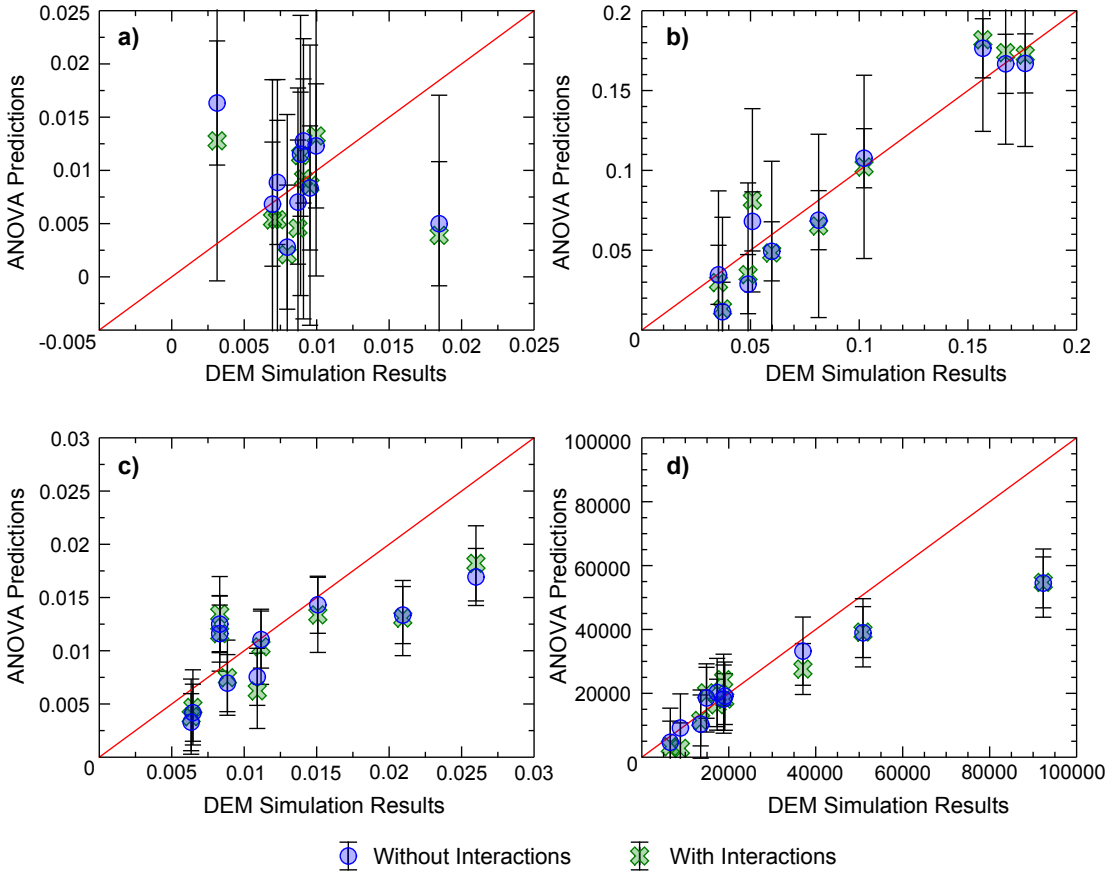

Figure 4.10: *Plots at three dimensions for 10 randomly-selected combinations of factor levels which compare ANOVA predictions, both including interactions (×) and excluding interactions (○), with the corresponding DEM simulation results for the four responses a–d listed for Figure 4.8, where error bars indicate 95% confidence intervals*

some extent, and as few interactions proved to be truly significant, the confoundings were manageable. Since interactions proved to be important, using a "one at a time" approach to parameter tuning is clearly inadequate.

Two additional points must be considered. The first is that the results of this approach are applicable only to combinations of those levels tested. It is neither acceptable in the Taguchi method to predict results by interpolating between levels nor by extrapolating outside of the range of levels tested. For example, strain at failure decreased progressively with increasing ball friction between levels of 0.4 and 0.8. It is not valid to conclude that the result obtained by using a ball friction of 0.5 would lie between the values obtained at friction settings of 0.4 and 0.6; although probable, it is not a certainty. It is also not necessarily true that the strain at failure would decrease further if ball friction is increased to 0.9.

One final point for the analyst to consider is that the Taguchi method makes use of linear statistics. As a consequence, results become more accurate if smaller ranges of levels are used. This has important implications for analysis. If calibration is being

carried out and the researcher does not have reasonable estimates for some parameters, it may be best to consider a multiple step approach to gain increasing insight into the system, which factors are more important and which regions of interest of those factor settings are more promising. Initially, a screening design could be used in which levels of a factor may span several orders of magnitude. These screening designs are often used as a first step where a large number of factors are present, in which case the results are used to justify omitting certain factors to focus on the more influential. Then based on these results, a second finer design could be used with more closely-spaced levels to determine the optimum with a higher level of accuracy.

4.8 Conclusions of Chapter 4

In this chapter, the applicability of the Taguchi method to calibration of discrete element models was demonstrated by considering the calibration of bonded agglomerates in both 2D and 3D. It is clear that the Taguchi approach has many advantages over basic parameter studies which vary only one factor at a time; such calibration approaches remain common and are highly inefficient when compared to an appropriate DOE method. Its main disadvantage is confounding due to the use of orthogonal arrays. However, this can be mitigated by careful allocation of factors to columns of the array to permit the testing of selected interactions, and also by using multiple smaller experimental designs rather than one large design.

The Taguchi method is certainly suitable for DEM calibration of bonded agglomerates, although it is important to identify and include key interactive effects in the analysis to ensure good predictive ability. Close correspondence was obtained between ANOVA predictions of the measured responses and the DEM simulation results in 3D, with all R^2 values exceeding 98%. For the 2D simulations, predictions were made using solely main effects, although some interactions were statistically-significant. As expected, these predictions were considerably poorer than those made in 3D since all interactions were disregarded.

For both two- and three-dimensional simulations, parallel bond normal strength, bond normal stiffness and ball friction all had a statistically-significant effect on strain at failure at a 95% level. Bond normal stiffness and ball friction had a significant effect on agglomerate stiffness. By increasing parallel bond normal stiffness, the agglomerate stiffness was increased and the strain at failure was decreased. Strain at failure may be maximised by choosing a high bond normal strength and low values of ball friction and bond normal stiffness.

5

Discrete Element Modelling of Agglomerates of Infant Formula

As outlined in the introduction to Chapter 3, agglomerates of infant formulae experience many transient contacts, both with other agglomerates and with the inner wall of the pipeline, during pneumatic conveying. The forces experienced by individual agglomerates at any instant are very difficult to quantify experimentally due to their small magnitudes and short durations. As a result, it is seldom possible to conduct a thorough experimental investigation of the response of agglomerates when subjected to such dynamic loads. One method of quantifying the response of agglomerates of infant formulae to loading was discussed in Chapter 3: individual agglomerates were isolated and subjected to mechanical loading using both quasi-static uniaxial compression tests and dynamic drop tests. Data such as forces and strains at failure, agglomerate stiffnesses and coefficients of restitution can be obtained using such methods. However, they do not provide any insight into the evolution of the fabric of the agglomerate (i.e., its internal geometric structure) during loading.

One numerical approach which can capture these fabric changes is coupled CFD-DEM[†] models (e.g., Brosh et al., 2011 (dilute); Han et al., 2003 (dilute); Li et al., 2005 (dense); Sturm et al., 2010 (dense)). The significant computational requirements impose a major restriction on the number of particles which may be simulated. Simplified models are sometimes used to reduce the computation time (e.g., Fraige and Langston, 2006; Sakai and Koshizuka, 2009). Furthermore, disks (2D) or spheres (3D) are often used in simulations of conveying which are not wholly representative of real agglomerates. Using simulated agglomerates which are not geometrically similar to the real, physical agglomerates prevents the researcher from obtaining quantitative data on fabric evolution. However, these models are capable of providing valuable data for the transient

[†]CFD is an abbreviation of "Computational Fluid Dynamics".

forces experienced by agglomerates during conveying, which is a major reason for their application.

A third option is to develop a discrete element model of a single infant formula agglomerate and use this to simulate uniaxial compression or drop tests. DEM was introduced in Section 4.1 (p.74) and has often been used to simulate the uniaxial compression of agglomerates, particularly of soil particles (Cheng et al., 2003; Golchert et al., 2004; Robertson and Bolton, 2001) although other materials have also been simulated (Khanal et al., 2005; Samimi et al., 2005). This approach can provide extremely detailed information about the evolution of the agglomerate fabric over time. Experimental data are required for accurate calibration of the model; in this case, the results of the uniaxial compression experiments presented in Chapter 3 were used. Thus, the primary objectives of this chapter were as follows:

1. To develop a discrete element model for uniaxial compression of infant formula agglomerates
2. To calibrate this model using experimental data so that the agglomerate compression process was accurately simulated
3. To investigate whether this model, calibrated using quasi-static loading data, was also applicable to dynamic loading by simulating impact tests of agglomerates and comparing the results to those obtained by experiment

5.1 Physical Characterisation of the Agglomerates

Since the results obtained for force at failure, strain at failure and agglomerate stiffness were relatively similar for all four formulae tested in Chapter 3 (Table 3.7), the model was developed for only one of these formulae. Infant formula B was selected since its composition in Table 3.1 on p.50 did not contain any extreme values of fat, protein or ash content.

It was necessary to measure those five particular physical characteristics of the agglomerates listed below for input into the discrete element model:

1. Agglomerate length (µm)
2. Agglomerate width (µm)
3. Agglomerate height (µm)
4. Particle diameter (µm)
5. Bond radius multiplier (–)

The agglomerate dimensions were measured as described in Section 5.1.1. The particle diameter and bond radius multiplier are discussed in Section 5.1.2; both of these were found only for infant formula B. Note that it was possible to calculate correlations between pairs of agglomerate physical characteristics, including their lengths or widths, and also between any measurable physical characteristic and agglomerate compression response (force at failure, strain at failure or agglomerate stiffness). These results are shown in Appendix D for information. The experimental impact tests are described in Section 5.1.3. The impact data were required to assess the applicability of the calibrated DEM to dynamic loading, and supplements the experimental drop test data previously discussed in Chapter 3.

5.1.1 Agglomerate Dimensions

The agglomerates were compressed on a glass plate, as discussed in Section 3.1.5 and depicted in Figure 3.5. Each agglomerate could be crudely specified using three dimensions: length and width, measured parallel to the glass plate, and height, which is along the line of motion of the compressing platen. For each infant formula A–D, an average length and width was obtained for the agglomerates using a Malvern PharmaVision 830 instrument (Malvern Instruments Limited, Malvern, Worcestershire, UK). This instrument contains a camera, controlled by means of an actuator, which scans slowly over particles at rest on a glass plate. The particles analysed were artificially illuminated from beneath the plate.

Between 80 and 100 agglomerates of each infant formula were analysed. The instrument's software (v.4.41) saved a *.tif* image of each agglomerate and separately wrote information about the agglomerates scanned to a file, including the required length and width. An example of the software output is shown in Figure 5.1.

The height was found directly from the texture analyser as the distance between the bottom of the platen and the top surface of the glass plate at the instant when the trigger force was reached (labelled as d_o on p.56). The mean dimensions of the infant formula agglomerates are shown in Table 5.1. Note that height was the smallest dimension for all formulae: generally, the most stable orientation for an agglomerate on a flat, horizontal surface is with its two longest dimensions parallel to the surface. Infant formula B, for which the model was developed, had the smallest mean dimensions of all agglomerates, although differences between the formulae were slight.

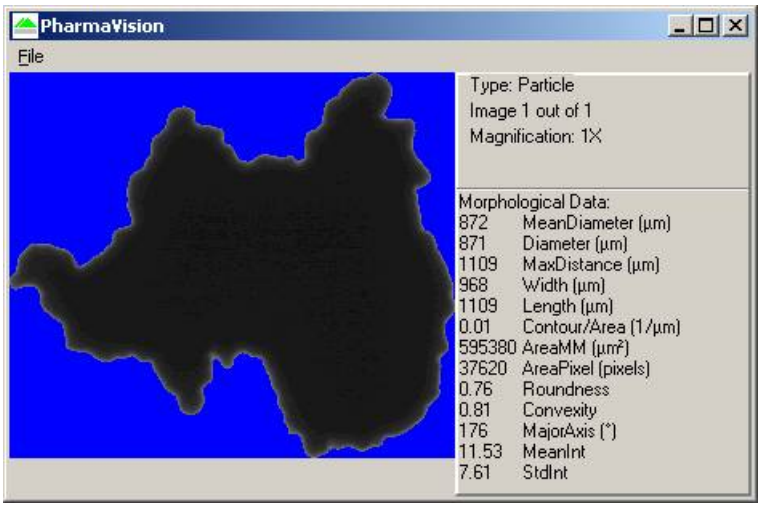

Figure 5.1: *Screenshot showing an example of the output from the Malvern PharmaVision instrument that was used to determine average lengths and widths of the agglomerates*

Table 5.1: *Mean agglomerate dimensions for each infant formula*

Infant Formula	Length (µm)	Width (µm)	Height (µm)
A	1262	946	704
B	1212	937	678
C	1266	963	692
D	1239	946	717

5.1.2 SEM Characterisation of Microstructure

It was assumed that the physical agglomerates were composed of spherical particles of various sizes which were bonded together. Thus, it was necessary to estimate the diameters of the spheres and the sizes of the contact areas between the spheres. The SEM described in Section 1.5.1 (p.14) was used to obtain this data. 37 SEM micrographs of agglomerates of infant formula B in the 710–850 µm size range were obtained. The image analysis software ImageJ (v.1.43u, U.S. National Institutes of Health, Bethesda, MD, USA) was used to measure the approximate diameter of the particles in the agglomerates. The parallel bond radius multipliers were also estimated similarly by dividing the length of the overlap between two particles by the smaller of the particle diameters. All lengths were obtained manually by superimposing straight lines on the image and logging their lengths in a file. The scale bar on each micrograph was used to set the global scale in ImageJ before lengths were measured. This procedure was of limited accuracy, since the diameter of each particle was estimated manually for a circular equivalent projected area. This is shown in Figure 5.2. The two particles which are circled by white dashed lines had diameters of 48.8 µm and 50 µm, while the overlap between the two particles

had a length of 31.6 µm. Thus, the bond radius multiplier was 0.648 $\left(=\frac{31.6}{48.8}\right)$ for this overlap.

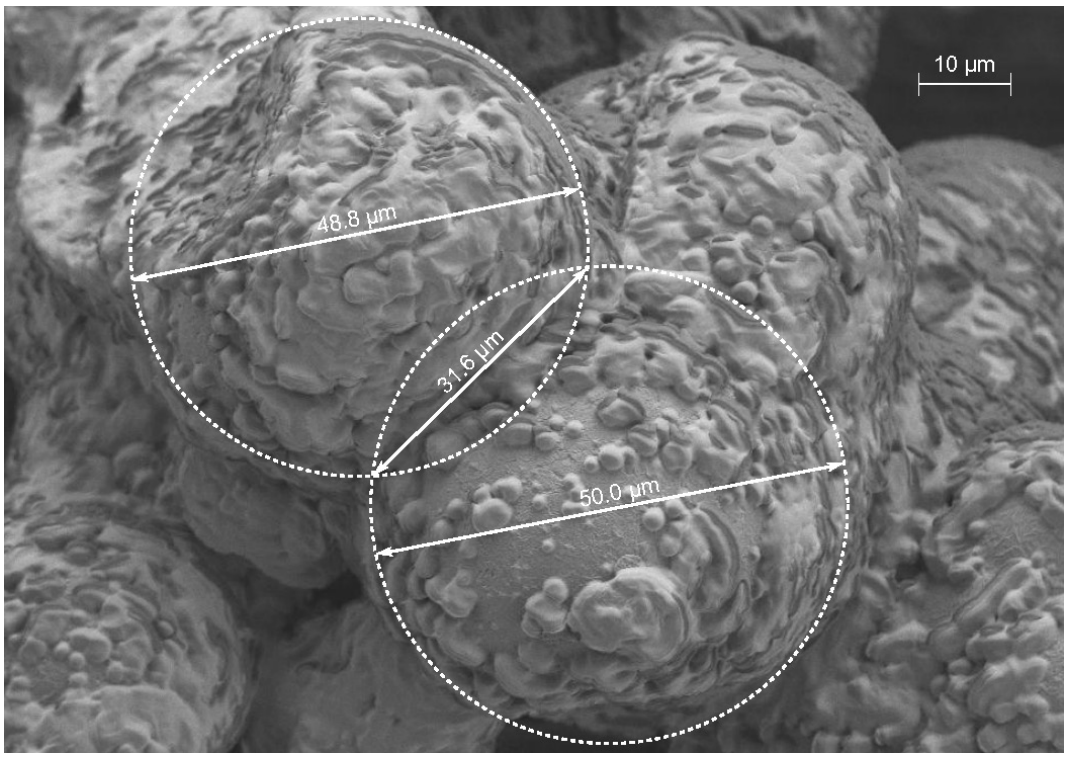

Figure 5.2: *SEM micrograph at 2000X magnification of an agglomerate of infant formula B, which illustrates the methodology used to measure particle diameters and bond radius multipliers*

Lognormal distributions were fitted to the measured particle diameter data in the same manner as described for the compression responses in Section 3.2.2. Figure 5.3 shows the probability histogram and corresponding PDF for the particle diameters recorded for agglomerates of infant formula B.

Basic statistics of the particle diameters and bond radius multipliers are provided in Table 5.2. It can be seen that the distribution in the bond radius multipliers was less marked than the distribution in particle diameters. The maximum ratio between bond radius multipliers was 2.5 $\left(=\frac{0.971}{0.383}\right)$ whereas the equivalent for particle diameters was 8.3 $\left(=\frac{125.39}{15.09}\right)$: almost an order of magnitude difference between extrema. A distribution was not fitted to the bond radius multiplier data as these varied much less than the particle diameter data; instead, the simulations used a fixed value of 0.7 for this parameter. The lognormal distribution fitted to the particle diameter data (in mm) had the parameters listed below, where μ and σ are the mean and standard deviation of the corresponding normal distribution, as returned by the MATLAB function *lognfit*:

- μ = -3.1364 with standard error = 0.0265
- σ = 0.4372 with standard error = 0.0188

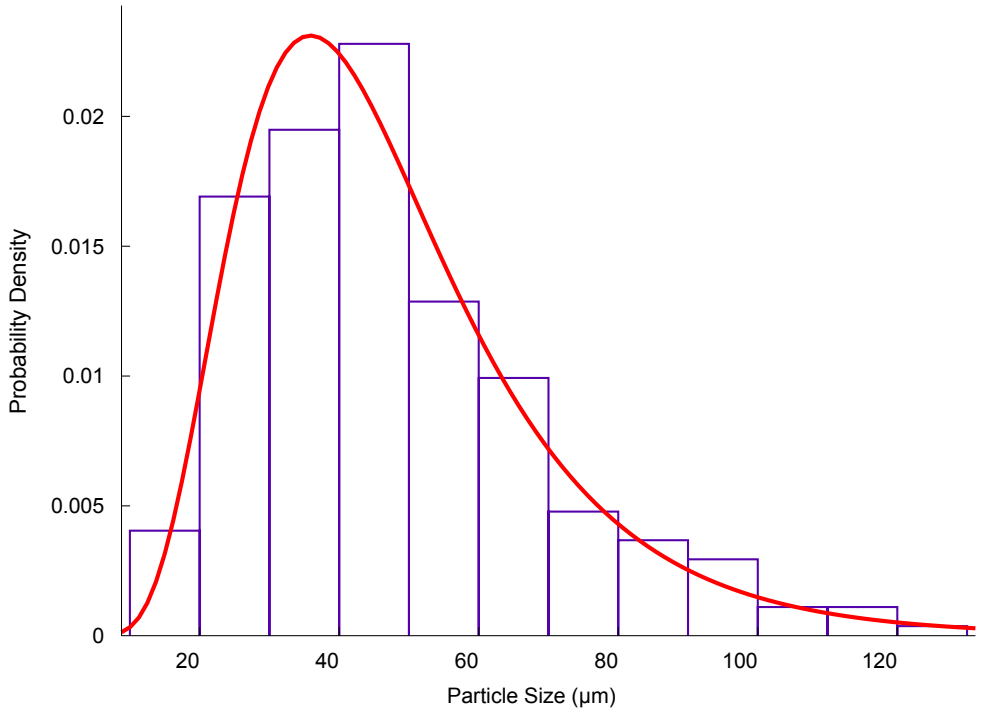

Figure 5.3: *Probability histogram of the particle diameters which comprise the agglomerates of infant formula B, as measured by image analysis of SEM micrographs, compared with the PDF of a fitted lognormal distribution*

Table 5.2: *Means, standard deviations and extreme values of particle diameters and bond radius multipliers, obtained by image analysis of SEM micrographs of agglomerates of infant formula B in the 710–850 μm size range*

	No. of Points	Mean	Std. Dev.	Minimum	Maximum
Particle diameter (μm)	272	47.74	21.26	15.09	125.39
Bond radius multiplier	113	0.711	0.154	0.383	0.971

5.1.3 Experimental Impact Tests using High-Speed Camera

Thirty-five experimental impact tests were conducted using individual agglomerates of infant formula B from the 710–850 μm size range. The camera, operating software and video analysis methods used were identical to those described in Section 3.1.7, except the impacts were recorded at 2000 frames/s and the resolution was halved to 1280×300. The main difference was the method used to accelerate the particles. For the drop tests discussed previously, agglomerates were pushed off a smooth stainless steel platform at an elevation of 450 mm above the target plate so that impact velocities of approximately 1.9 $\mathrm{m\,s^{-1}}$ were attained. These moderate impact velocities did not cause any of the agglomerates tested to fail.

The objective of the impact tests in this chapter was to provide additional experimental data to allow the applicability of the calibrated model to dynamic loading to be evalu-

ated; thus, it was important to use higher velocities for these tests to cause observable damage of the agglomerates. Since the limiting terminal velocity of these agglomerates was low, it was necessary to supply an initial impulse to the agglomerates to reach higher impact velocities. This impulse was supplied using compressed air to propel the agglomerates vertically upwards before they impacted the underside of a smooth stainless steel plate. The pressure of the compressed air was regulated to provide different air velocities, and hence agglomerate impact velocities. The air could be switched between the fully-on and fully-off states almost instantaneously using a pneumatic valve. The internal diameter of the air outlet was 3 mm. A small piece of muslin fabric covered this outlet; this was required to provide a surface upon which the agglomerate could be placed before activating the air supply, yet did not obstruct the flow excessively. The configuration of the air outlet and target plate are shown in Figure 5.4.

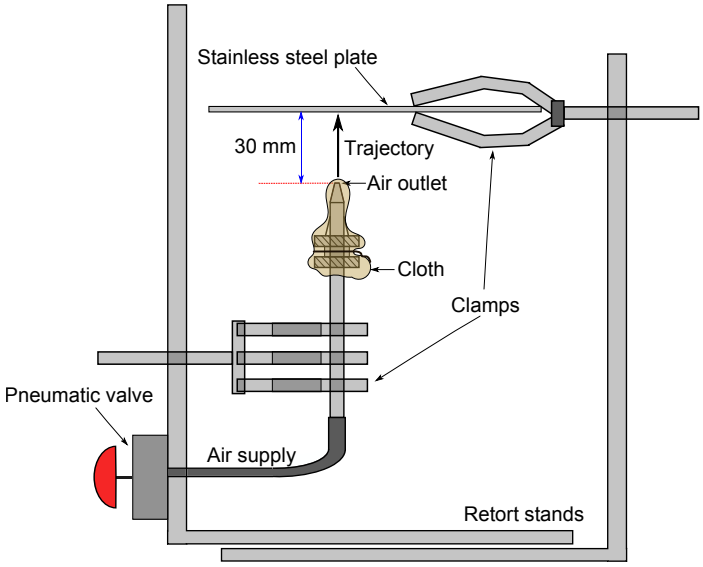

Figure 5.4: *Configuration of the pneumatic apparatus used to obtain high agglomerate impact velocities with the steel target*

As in Section 3.1.7, the video files were analysed using ProAnalyst. For each impact test, only the normal impact velocity and the mode of failure were recorded. There were large variations among the normal impact velocities recorded due to temporal fluctuations in the air pressure and variations in the initial orientations of the agglomerates on the muslin support. The lowest velocity recorded was 6.27 $\mathrm{m\,s^{-1}}$ and the highest was 15.37 $\mathrm{m\,s^{-1}}$; to reduce the variability, all tests for which impact velocities were outside of the range 8–12 $\mathrm{m\,s^{-1}}$ were discarded. This reduced the number of experimental results from 35 to 25. The mean normal impact velocity for these 25 tests was 10.10 $\mathrm{m\,s^{-1}}$ with a standard deviation of 1.31 $\mathrm{m\,s^{-1}}$.

A number of authors have categorised agglomerate failures using terms such as attrition, chipping, disintegration, fracture, fragmentation, shattering or wear (e.g., Ghadiri and Zhang, 2002; Thornton and Liu, 2004). For this work, three unique modes of agglomerate

failure were observed upon analysis of the video footage. Thus, the result of each impact test was assigned to one of the following four categories:

Unbroken The agglomerate was not seen to break. Note that the resolution of the high-speed camera was insufficient to detect damage of an agglomerate unless a breakage event occurred.

Binary fracture The agglomerate broke into two large daughter fragments.

Local disintegration The agglomerate broke into a large number of small fragments at its point of impact with the target plate. However, more than half of the agglomerate remained intact.

Shattering The entire agglomerate disintegrated to leave only a large number of small fragments after impact.

Figure 5.5 shows the percentages of the 25 agglomerates considered in the results which were assigned to each of these four categories. Almost half of the agglomerates shattered upon impact. A small number of the agglomerates did not fail which again demonstrates the wide variations among individual agglomerates for a spray-dried dairy powder.

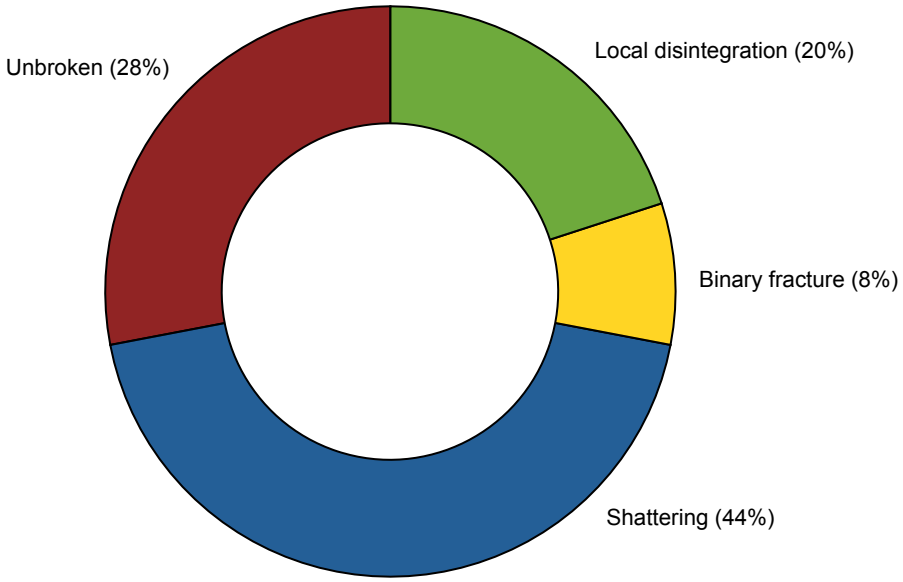

Figure 5.5: *Chart showing the percentages of the agglomerates of infant formula B assigned to each category*

5.2 Discrete Element Modelling of Uniaxial Compression

5.2.1 Agglomerate Structure and Crushing Conditions

The agglomerates required for these simulations were produced using the sequential addition method which was outlined in Section 4.1.4 and described in detail in Appendix C. The diameters of the spheres which comprised the agglomerates were randomly selected from a lognormal distribution using the parameters obtained experimentally for infant formula B in Section 5.1.2. The sphere diameters were restricted to the range 20–125 µm to prevent particles with unrealistic diameters from being generated. Agglomerate dimensions were subject to some variability. However, lengths, widths and heights of the agglomerates were generally within 10% of the values shown for infant formula B in Table 5.1. The mean number of spheres in an agglomerate was 688, with a standard deviation of 107. The sequential addition algorithm yielded agglomerates with low convexities of 0.14 to 0.18; the method used to calculate the convexities of simulated agglomerates and the detailed results are both confined to Appendix E. Figure 5.6 shows an example of an agglomerate generated by this approach, which can be compared to the physical agglomerate of infant formula B shown in Figure 1.2 (p.15).

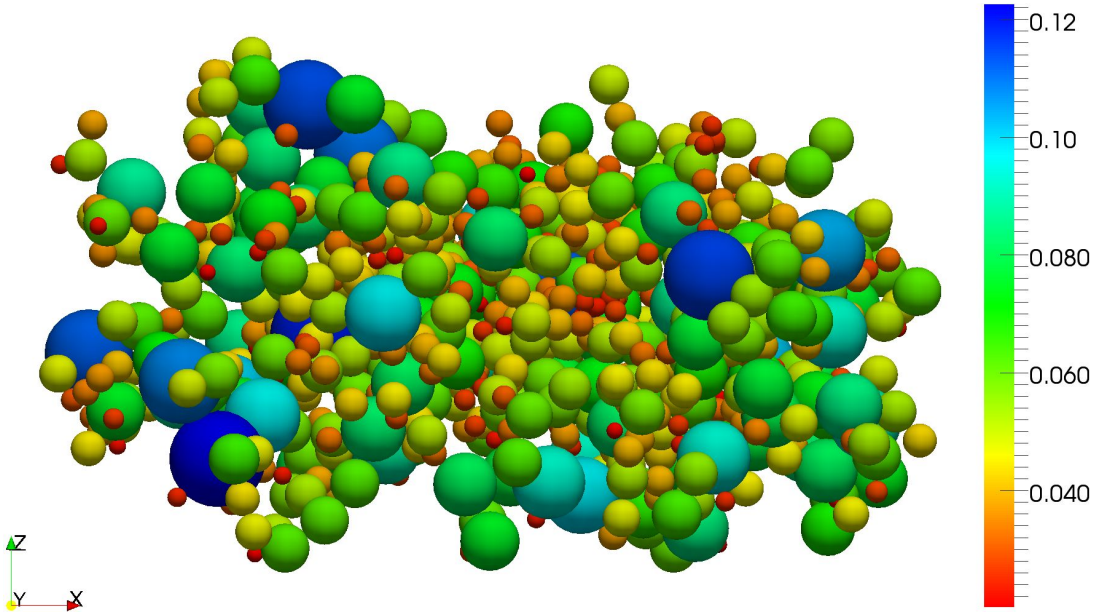

Figure 5.6: *Generated agglomerate containing 765 spheres, which has a length of 1.2202 mm, width of 1.0238 mm and height of 0.7613 mm. The colour bar indicates the size of the spheres in mm*

Each agglomerate was individually compressed between stiff, horizontal, frictionless platens until a strain of 50% was attained. The bottom platen was stationary and the upper platen moved downwards at 0.04 mm s^{-1}. This velocity was low enough to ensure

that quasi-static loading was attained. The initial distance between the platens was equal to the agglomerate height, as for the simulations in Chapter 4.

5.2.2 DEM Calibration

The Taguchi method was used to determine those DEM parameters which could not feasibly be obtained by experiment, e.g., stiffnesses and strengths of parallel bonds. This method was discussed in detail in Chapter 2 and its application to the calibration of discrete element models was illustrated in Chapter 4.

In this case, an initial parameter study was conducted using an L_{18} array which identified the bond strengths and stiffnesses as being particularly influential. Then several sets of simulations were conducted using saturated L_9 arrays (Table 2.1 on p.24). The four available columns were allocated to the parallel bond strengths and stiffnesses, and levels were varied by orders of magnitude. The bond radius multiplier was set to 0.7: approximately equal to the mean recorded in Table 5.2. All of the other parameters were temporarily fixed at reasonable estimates, e.g., ball stiffnesses were set at relatively large values as the bonds were believed to have a much greater influence on the agglomerate compression behaviour. The agglomerate used for all of these simulations was invariant. This reference agglomerate contained 623 spheres: slightly fewer than the average agglomerate to reduce the time required to run each simulation, yet still within the acceptable range for such agglomerates. The emphasis of these simulations was to minimise the differences between three DEM responses (the force at failure, strain at failure and agglomerate stiffness) and the equivalent mean experimental results shown in Table 3.7. Note that these three responses were identified for each simulation using the same algorithm that was used for the uniaxial compression experiments (described in Section 3.1.6 on p.57).

Once these three selected responses showed reasonable agreement, appropriate settings were identified for the remaining parameters using small experimental designs (L_4, L_8 and L_9 arrays), supplemented by a small number of *ad hoc* "trial-and-error" simulations to confirm or disprove certain hypotheses. Multiple agglomerates were introduced at this stage, to ensure that parameters were widely applicable and to mitigate against the chosen reference agglomerate being atypical in some regard. After these simulations were completed, the responses considered corresponded quite well to the experimental means. However, no consideration had yet been given to the shape of the distributions. The only way of checking this was to obtain sufficient data to yield representative distributions of the three responses which necessitated running a larger number of simulations. Twenty simulations were run using identical parameters, each using a

different randomly-generated agglomerate. These parameters are shown as set I in Table 5.3.

The results indicated that the ball friction needed to be increased. A much larger set of 130 simulations were run using these updated parameters, given as set II in Table 5.3. However, the resulting agglomerate stiffnesses were excessively high. This was remedied by reducing the bond stiffnesses by 20% and reducing the ball friction to an intermediate value between 0.6 (used in set I) and 0.7 (used in set II). This resulting set of parameters (III) was the final calibrated set used to obtain the results in Section 5.3. It must be emphasised that the geometric variability of the simulated agglomerates made calibration of the model both difficult and time-consuming. The example given in Appendix F effectively illustrates some of these difficulties.

Table 5.3: *Calibrated parameters used for the DEM simulations, where set III was the final calibrated set used to obtain the results*

Parameter	Setting		
	Set I	Set II	Set III
Ball density ($\mathrm{kg\,m^{-3}}$)†	1×10^{8}	1×10^{8}	1×10^{8}
Ball normal stiffness ($\mathrm{N\,m^{-1}}$)	4×10^{7}	4×10^{7}	4×10^{7}
Ball shear stiffness ($\mathrm{N\,m^{-1}}$)	4×10^{7}	4×10^{7}	4×10^{7}
Ball friction	0.6	0.7	0.65
Bond radius multiplier	0.7	0.7	0.7
Bond normal strength ($\mathrm{N\,m^{-2}}$)	1×10^{9}	1×10^{9}	1×10^{9}
Bond shear strength ($\mathrm{N\,m^{-2}}$)	1×10^{9}	1×10^{9}	1×10^{9}
Bond normal stiffness ($\mathrm{N\,m^{-3}}$)	3×10^{15}	3×10^{15}	2.4×10^{15}
Bond shear stiffness ($\mathrm{N\,m^{-3}}$)	3×10^{15}	3×10^{15}	2.4×10^{15}
PFC damping coefficient	0.3	0.3	0.3
Random number seed	4000	4000	4000

† Note that density scaling was used (see Section 5.2.4).

5.2.3 Model Sensitivity to Small Perturbations

Simulations demonstrated that the model was highly sensitive to small perturbations in the input parameters, i.e., changing one of the parameters in Table 5.3 by a slight amount, e.g., 1%, could cause the responses of the simulations to change completely. However, the initial low-strain behaviour was unaffected by perturbations: the responses were found to deviate only after some strain value which was different for each agglomerate. Figure 5.7 contains subplots for two different agglomerates: each subplot compares the average force on the platens obtained using the bond stiffnesses given in Table 5.3 with

the equivalent responses using stiffness perturbations of ± 1%. Figure 5.8 uses the same agglomerates, but the perturbations were in bond strengths rather than stiffnesses.

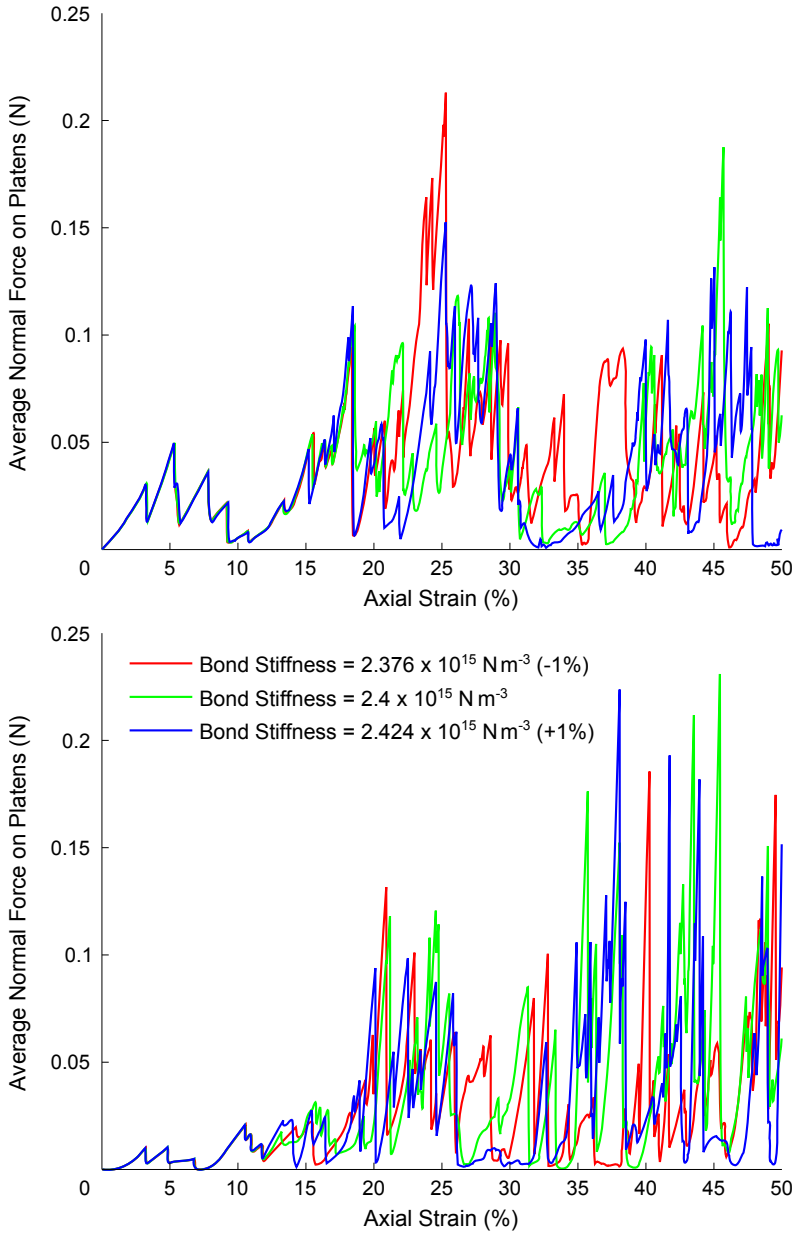

Figure 5.7: *Plots comparing the average normal force exerted on the platens (N) against axial strain (%) for two agglomerates conducted using parallel bond normal and shear stiffnesses of* $2.4 \times 10^{15}\ N m^{-3}$ *and these stiffnesses ± 1% to create a small perturbation in the input*

5.2.4 Density Scaling

These quasi-static simulations of particle compression used density scaling; by increasing the ball density to physically-unrealistic values, the time required to run each simulation was greatly reduced. It was acceptable to increase the density in this manner because no gravitational fields were active in the simulations. This technique has been widely used by other researchers (e.g., Sheng et al., 2004; Sykut et al., 2008;

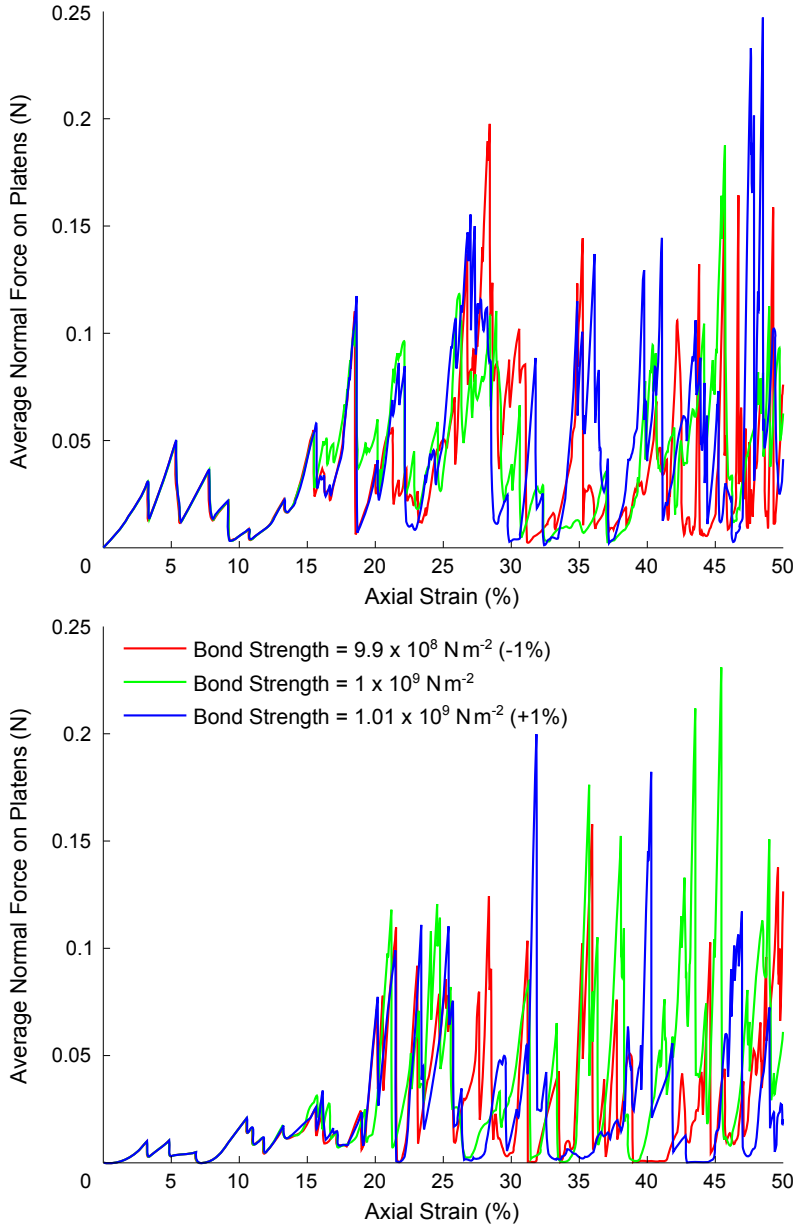

Figure 5.8: *Plots comparing the average normal force exerted on the platens (N) against axial strain (%) for two agglomerates conducted using parallel bond normal and shear strengths of* 1×10^9 *N m*$^{-2}$ *and these strengths* $\pm$ *1% to create a small perturbation in the input*

Thornton, 2000). Without scaling the density, it would not have been feasible to run a statistically-significant number of simulations: using the scaled density, simulation times were typically three days whereas times were greater than four months if realistic ball densities were used (3 GHz Intel Pentium 4). Figure 5.9 illustrates this point using very large perturbations in ball density which differed by orders of magnitude. By comparing this figure to Figures 5.7 and 5.8, it can be seen that very large changes in ball density have no more of an effect than slight perturbations in other simulation parameters.

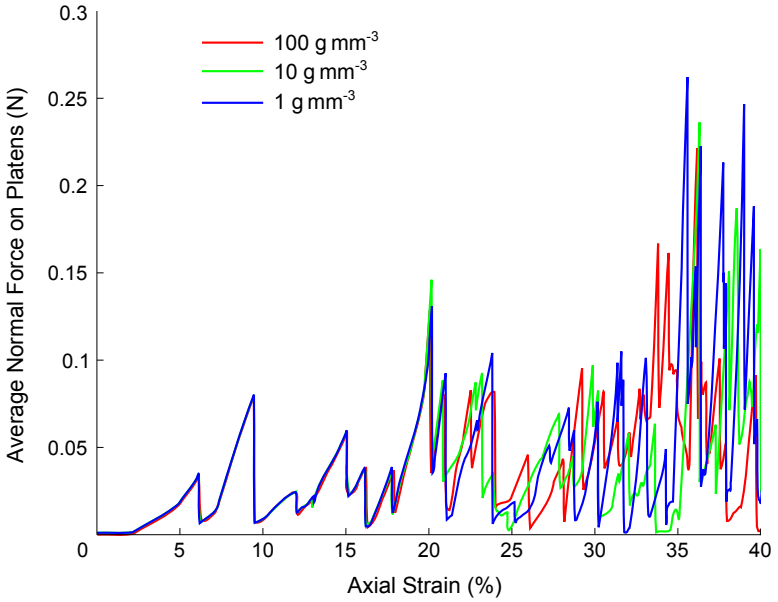

Figure 5.9: *Plots of the average normal force exerted on the platens (N) against axial strain (%) for three simulations conducted using ball densities which varied by orders of magnitude (from 1×10^6 to 1×10^8 kg m^{-3}), where all other parameters were held constant*

5.3 Comparison of DEM and Experimental Results

5.3.1 Probability Histograms and Density Functions

In total, 130 simulations were conducted, of which 116 were deemed to have failed before 50% strain using the criteria in Section 3.1.6. A different randomly-generated agglomerate was used for each of these simulations. Probability histograms of the DEM force at failure, strain at failure and agglomerate stiffness responses are given as Figures 5.10–5.12. As before, the Freedman-Diaconis rule was used to establish the bin widths and locations. The corresponding probability density function for a lognormal distribution is overlaid on each histogram as a solid red line. For ease of comparison, the PDFs of the experimental responses for infant formula B, which were shown previously in Figures 3.14–3.16, are superimposed on the histograms as dashed green lines.

For force at failure, the results corresponded exactly to the experimental results for infant formula B. The results for strain at failure were somewhat skewed compared to the experimental results: for 30% of the simulations, the strains at failure exceeded 25% whereas the same was true for only 14% of the physical agglomerates tested. For stiffness, the PDF of the simulation results exhibited a marked skew towards smaller stiffnesses, yet the distribution was also long-tailed. 59% of the simulations had stiffnesses below 5 kN m^{-1} while 8% of the agglomerates had stiffnesses exceeding 20 kN m^{-1}. Parameters of the lognormal distributions fitted to the DEM data are given in Table 5.4, along with means and standard deviations of the DEM results.

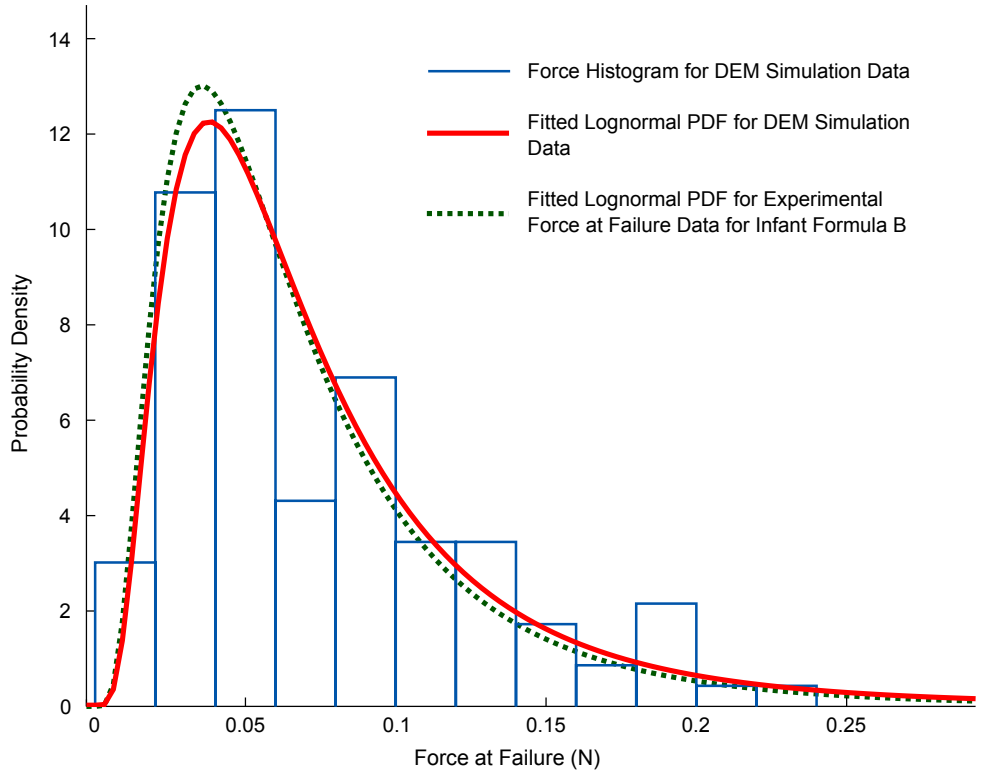

Figure 5.10: *Probability histogram of the DEM force at failure responses (N), with the corresponding PDFs of a fitted lognormal distribution and of the experimental force at failure results for infant formula B shown in red and green respectively for comparison*

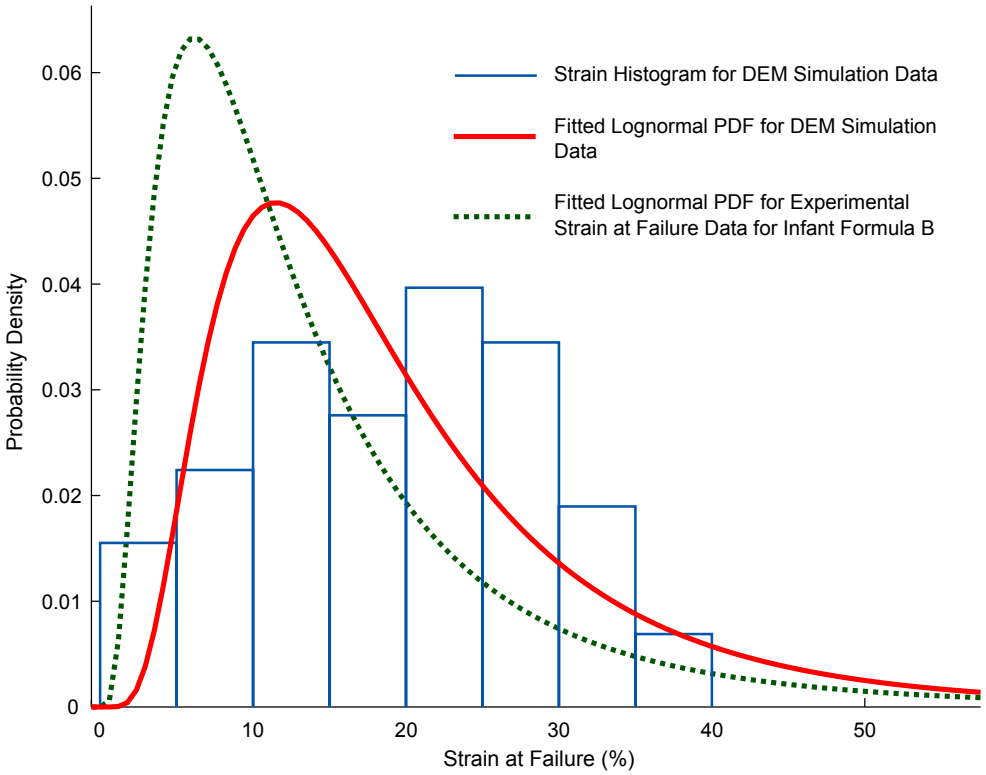

Figure 5.11: *Probability histogram of the DEM strain at failure responses (%), with the corresponding PDFs of a fitted lognormal distribution and of the experimental strain at failure results for infant formula B shown in red and green respectively for comparison*

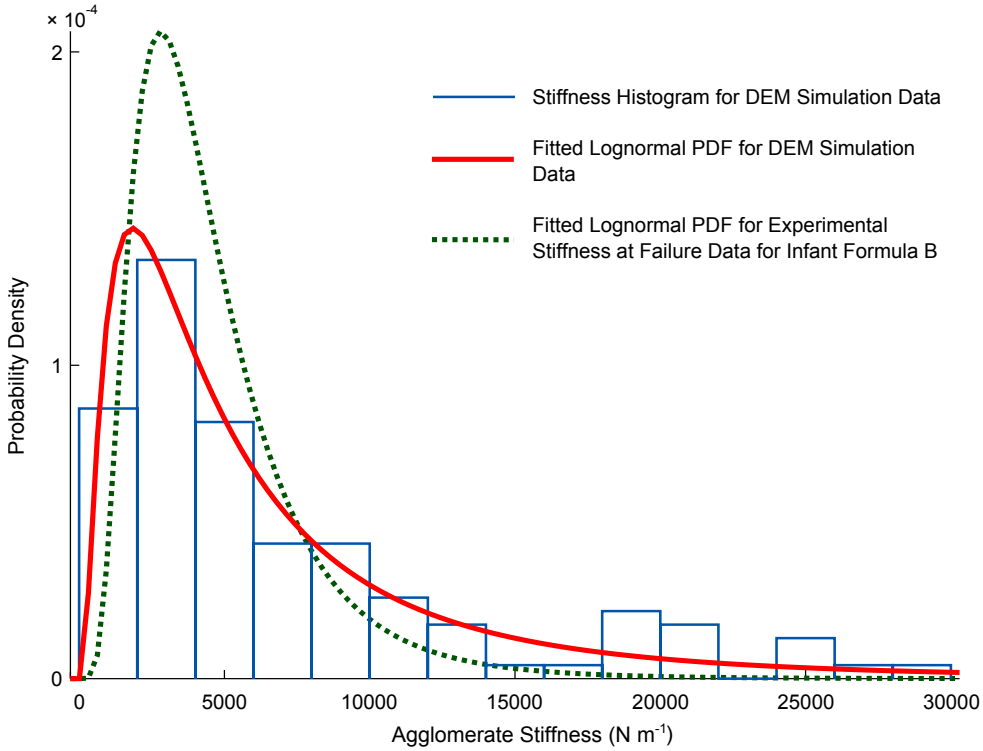

Figure 5.12: *Probability histogram of the DEM agglomerate stiffness responses ($N\,m^{-1}$), with the corresponding PDFs of a fitted lognormal distribution and of the experimental agglomerate stiffness results for infant formula B shown in red and green respectively for comparison*

Table 5.4: *Means and standard deviations of the results obtained for force at failure (N), strain at failure (%) and agglomerate stiffness ($N\,m^{-1}$) for the DEM simulations, and the parameters of the associated fitted lognormal (L/N) distributions*

	Force (N)	Strain (%)	Stiffness ($N\,m^{-1}$)
Mean	0.07487	19.2680	6996.28
Std. Dev.	0.04933	9.0968	6669.12
$\mu^{\dagger}$ (L/N) {Std. Error}	-2.80836 {0.06333}	2.80860 {0.05623}	8.43018 {0.08896}
$\sigma^{\dagger}$ (L/N) {Std. Error}	0.68219 {0.04508}	0.60565 {0.04002}	0.95816 {0.06332}

$^{\dagger}\mu$ and σ are the mean and standard deviation of the corresponding normal distribution.

5.3.2 Correlation Tests of DEM Responses

The existence of correlations between any pair of responses was evaluated for the experimental results in Section 3.2.2. The same was done for the DEM responses: the Spearman R and Kendall τ coefficients are reported in Table 5.5.

Table 5.5: *Spearman R and Kendall τ rank correlations for all combinations of the force at failure, strain at failure and agglomerate stiffness responses obtained for DEM simulations of agglomerate compression*

Correlation	Spearman R		Kendall τ	
	R	p-value	τ	p-value
Force ⟷ Strain	0.2467	0.0076	0.1949	0.0019
Force ⟷ Stiffness	0.7712	0.0000	0.6208	0.0000
Strain ⟷ Stiffness	0.4771	0.0000	0.3258	0.0000

There was a strong positive correlation between force at failure and agglomerate stiffness. Figure 5.13 shows the clear relationship between these responses using a scatter plot. Note however that there were a number of outliers at high force and low stiffness values, without which the correlation coefficients would have been even higher. The correlation between force at failure and agglomerate stiffness was also identified as the strongest for the four formulae tested experimentally and the Spearman R values were similar (Tables 3.9–3.12): for infant formula B, the Spearman R value was 0.7370. There was also a moderate positive correlation between strain at failure and agglomerate stiffness (Spearman R of 0.4771). All of the results in Table 5.5 were statistically-significant at a 99% level.

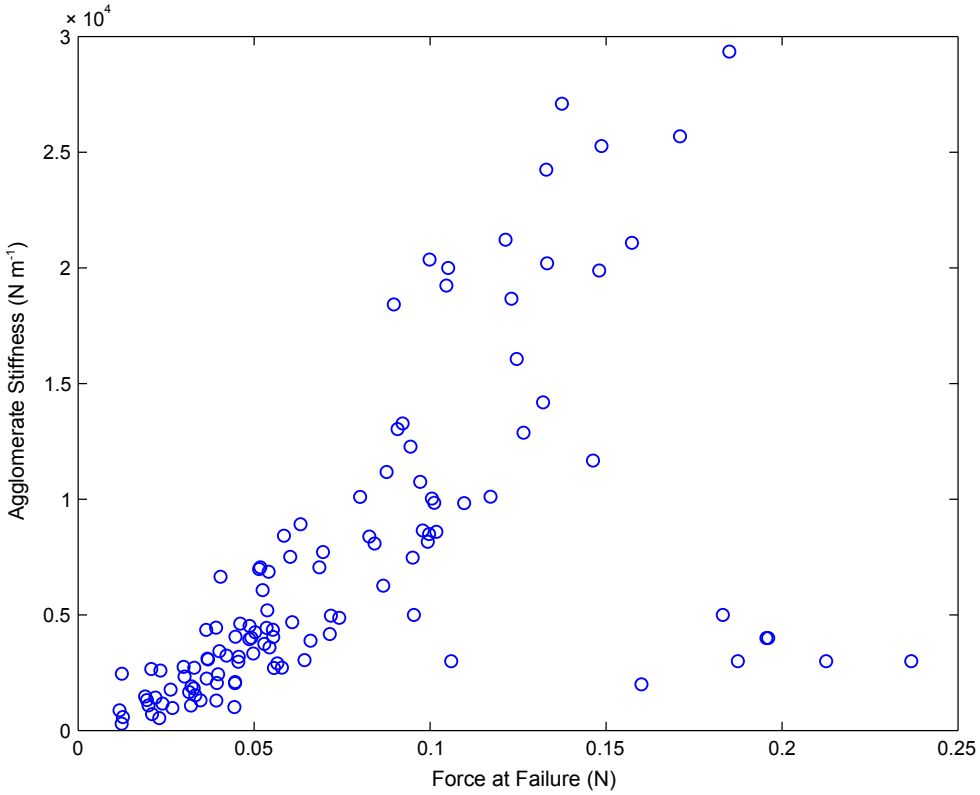

Figure 5.13: *Scatter plot of agglomerate stiffness ($N\,m^{-1}$) against force at failure (N) for the DEM simulation results*

5.3.3 Weibull Analysis

Another useful approach which can be used to compare the experimental results and simulation outputs is to apply Weibull statistics to the data. Eq. 5.1 is the fundamental Weibull equation, in which $P_s(V_o)$ is the probability of survival of a volume V_o of material when exposed to a uniform tensile stress σ, σ_o is the characteristic stress at which 37% $\left(\frac{1}{e}\right)$ of such samples survive and the exponent m is the Weibull modulus (Cheng et al., 2003; McDowell and Amon, 2000):

$$P_s(V_o) = e^{\left[-\left(\frac{\sigma}{\sigma_o}\right)^m\right]} \tag{5.1}$$

McDowell and Amon (2000) modified Eq. 5.1 for the case of agglomerate compression to give Eq. 5.2, in which d is a suitable measure of the agglomerate size and P_s is the survival probability for agglomerates of size d when exposed to a stress σ:

$$P_s(d) = e^{\left[-\left(\frac{\sigma}{\sigma_o}\right)^m\right]} \tag{5.2}$$

For this work, d was specified as the distance between the compression platens at the point of failure of the agglomerate; this is the same definition used by McDowell and Amon (2000), but differs from that of Cheng et al. (2003) who chose d to be the initial separation of the platens before compression. Eq. 5.2 may be rewritten in the form of Eq. 5.3 by applying logarithms:

$$\ln\left[\ln\left(\frac{1}{P_s(d)}\right)\right] = m\ln\left(\frac{\sigma}{\sigma_o}\right) \tag{5.3}$$

σ, the tensile stress at failure, may be found as a function of F, the force at failure, from Eq. 5.4 (Jaeger, 1967; McDowell and Bolton, 1998):

$$\sigma = \frac{F}{d^2} \tag{5.4}$$

The survival probability, P_s, was calculated using the mean rank position approach (e.g., Cheng et al., 2003):

$$P_s(i) = 1 - \frac{i}{n+1} \tag{5.5}$$

n is the total number of data points for σ and i is the index of a particular agglomerate when ordered by increasing σ. Hence, the agglomerate for which $i = 1$ has a survival probability which is close to unity, assuming a reasonable population size, and the lowest σ of all n agglomerates. However, $P_s(n)$ would be close to zero due to the maximum characteristic stress experienced by this agglomerate.

Based on Eq. 5.3, $\ln\left[\ln\left(\frac{1}{P_s(d)}\right)\right]$ was plotted against $\ln(\sigma)$ for each infant formula and a linear regression trendline was fitted to each set of data (Figure 5.14). The slope of each trendline was the Weibull modulus, m, and σ_o was found by taking the exponential

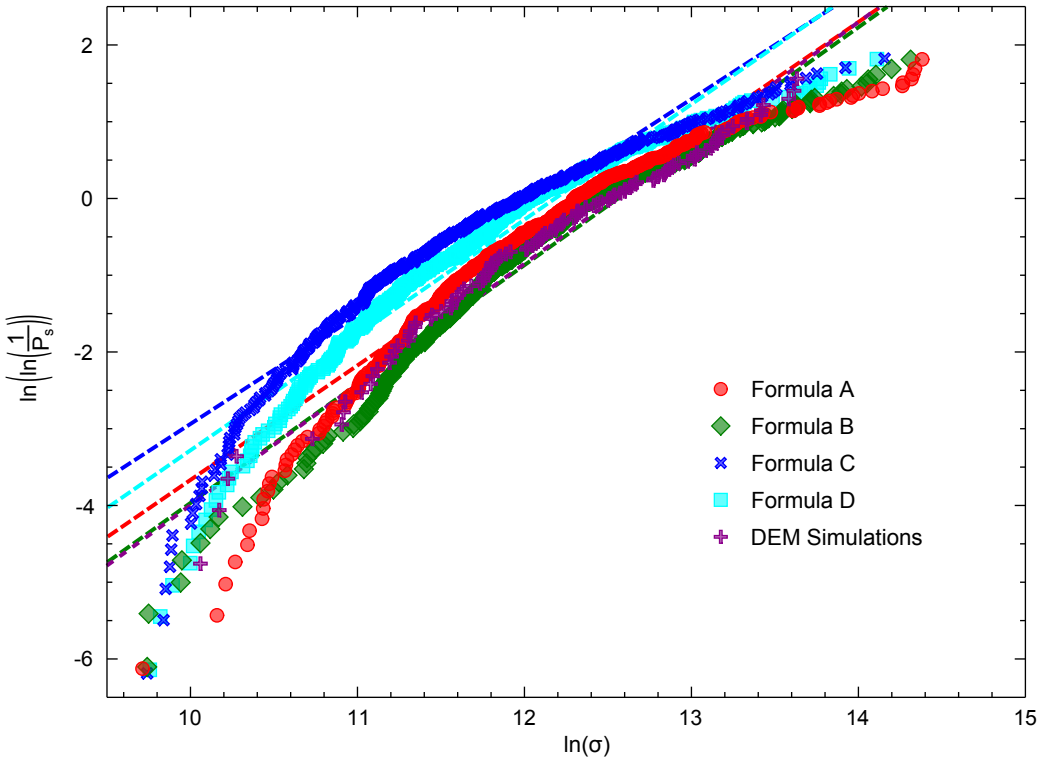

Figure 5.14: *Comparison of Weibull plots for the four formulae tested experimentally and the results of the DEM simulations*

Table 5.6: *Weibull moduli, the characteristic stresses at which 37% of agglomerates survive and coefficients of determination of the linear regressions*

	Infant Formula	Weibull Modulus	37% Characteristic Stress	R^2
		m	σ_o (N m^{-2})	
Experimental	A	1.4123	177364	0.9198
	B	1.4939	256955	0.9195
	C	1.5097	194705	0.9317
	D	1.5502	285941	0.9530
DEM	Simulated	1.4946	280546	0.9749

function of the absolute value of the y-intercept, following division by m. The results obtained for m, σ_o and coefficients of determination of the linear regressions are given in Table 5.6.

The five plots on Figure 5.14 have the same appearance and are closely grouped together. Furthermore, the linear trendlines appear almost parallel, which is unsurprising when the results in Table 5.6 are compared. All of the experimental Weibull moduli lay in a narrow range between 1.412 and 1.550. There was a greater dispersion in the 37% characteristic stresses, from 177.4 kN m^{-2} to 285.9 kN m^{-2}. This behaviour was captured very well by the simulation results: the Weibull modulus of 1.495 was almost identical

to the modulus for infant formula B of 1.494. The 37% characteristic stress for the DEM simulations was within the range of experimental characteristic stresses. All R^2 values were above 0.9 which indicates that these data sets were well described by a linear model.

5.4 Additional DEM Results for Quasi-Static Loading

One of the main benefits of a calibrated discrete element model is that the model is capable of providing insights into the behaviour of the equivalent real system which may not be obtainable by experiment. It was not possible to experimentally verify the results presented in this section; however, the fact that the model captured certain features of the compression response accurately (Sections 5.3.1–5.3.3) and the simulated agglomerates were geometrically similar to real infant formula agglomerates permits us to assume, with a reasonable level of confidence, that these results reflect the behaviour of real agglomerates.

5.4.1 Characterisation of the Mechanical Response using Energy

The results presented in Section 5.3 were in terms of forces and strains, which allowed the simulation results and the data recorded from the texture analyser to be compared easily. It was noted by Rozenblat et al. (2011) that it is generally most straightforward and accurate to represent particle strength in terms of force, although it is also possible to use a function of energy or stress. PFC facilitates the tracking of six energy terms (Itasca Consulting Group, 2008⋆). Three of these were of particular relevance for these quasi-static simulations as others, such as the kinetic energy or body work, were either negligible or not present:

Bond energy The total strain energy of the assembly stored in the parallel bonds

Boundary work The total accumulated work done by the walls on the assembly

Frictional work The total energy dissipated by frictional sliding at all contacts

All figures in this section were plotted for one representative agglomerate, the force-strain behaviour of which was shown previously in Figures 5.7 and 5.8. Figure 5.15 shows the evolution of those three energy terms listed above as the agglomerate is compressed to a strain of 50%. The cumulative lost bond energy and the total energy dissipated due to lost bond energy and friction are also shown for comparison.

The strain energy localised in the parallel bonds remained low (< 1 µJ) as the agglomerate was compressed. The only source of energy input to the system was boundary work, which was approximately equal to the energy dissipated. At any strain, the sum of

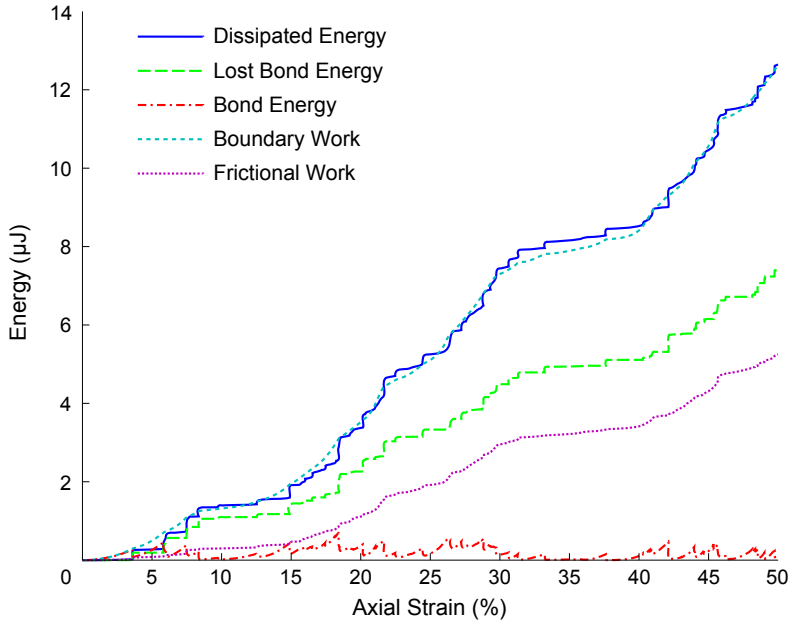

Figure 5.15: *Plots of five energy terms (μJ) against axial strain (%) for uniaxial compression of one representative agglomerate: bond energy, boundary work, frictional work, lost bond energy and total energy dissipated due to friction and lost bond energy*

the dissipated energy and bond energy must be equal to the boundary work; the small disparity in this case was due to the omission of several minor energy terms as mentioned above and the accumulation of floating-point calculation error. More energy was dissipated by lost bond energy than by friction, although both were significant. It was instructive to focus on a restricted region of strain in greater detail; this is shown as Figure 5.16 for which the average normal force on the platens and all three energy terms were normalised by their maximum values.

The trends in bond energy and normal force were very similar: whenever the force on the platens decreased sharply, the strain energy stored in the parallel bonds showed a commensurate decrease. At these points, there was also a corresponding increase in the frictional work, indicating that part of the agglomerate moved relative to another contacting part. Figure 5.17 shows the normal force and bond energy for the entire 50% range of strain, which confirmed that the evolution of bond energy with strain was similar to that of normal force. Figure 5.18 shows that the rate of change of the frictional work was highest where there was a sharp decrease in the normal force. The boundary work increased continuously on Figure 5.15 which demonstrates that the agglomerate always remained in contact with the platens (otherwise, a horizontal region would be observed on the boundary work plot). The rate of change of the boundary work was highest immediately before the local maxima of force or bond energy and was lowest following the points of rapid energy dissipation.

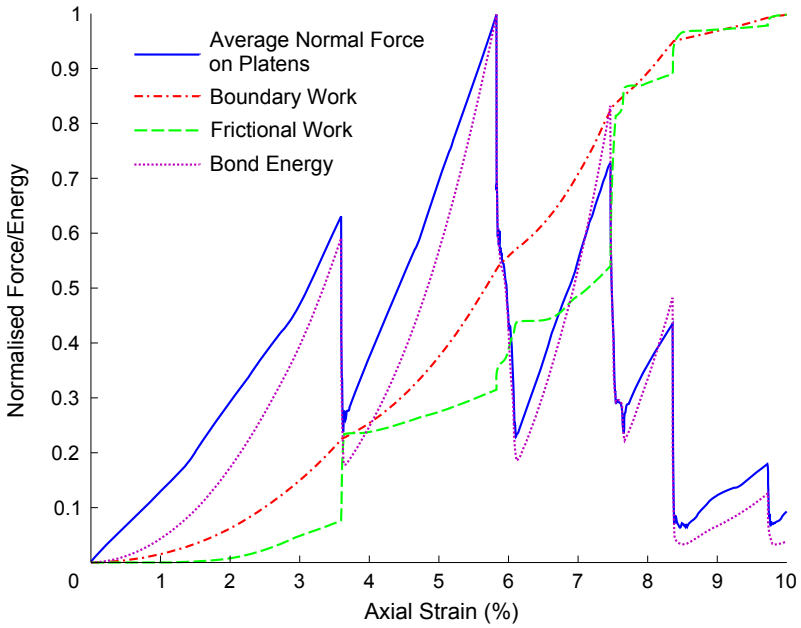

Figure 5.16: *Normalised plots of the average normal force on the platens and three tracked energy components (boundary work, frictional work and bond energy) for the first 10% of axial strain*

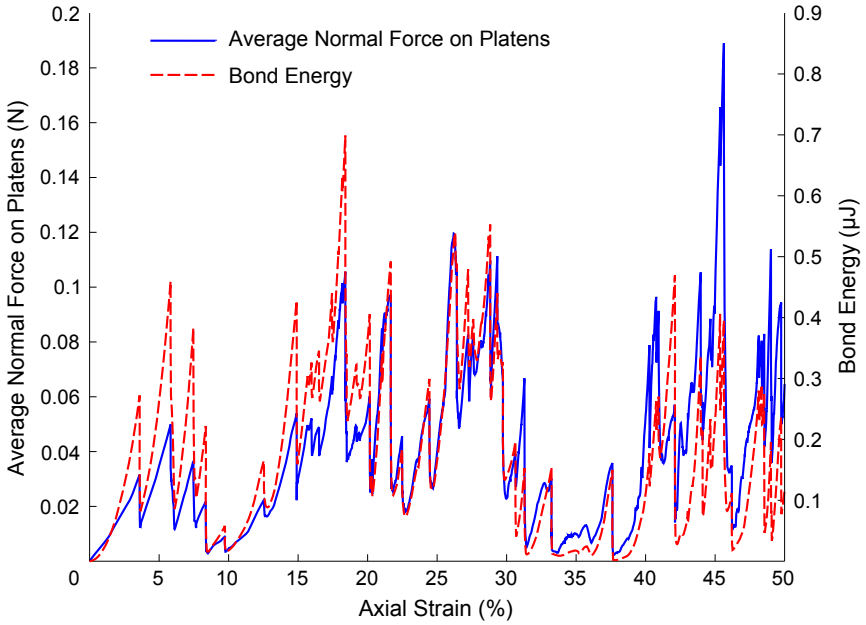

Figure 5.17: *Plots of the average normal force on the platens (N) and bond energy (μJ) against axial strain (%) for uniaxial compression of one representative simulated agglomerate*

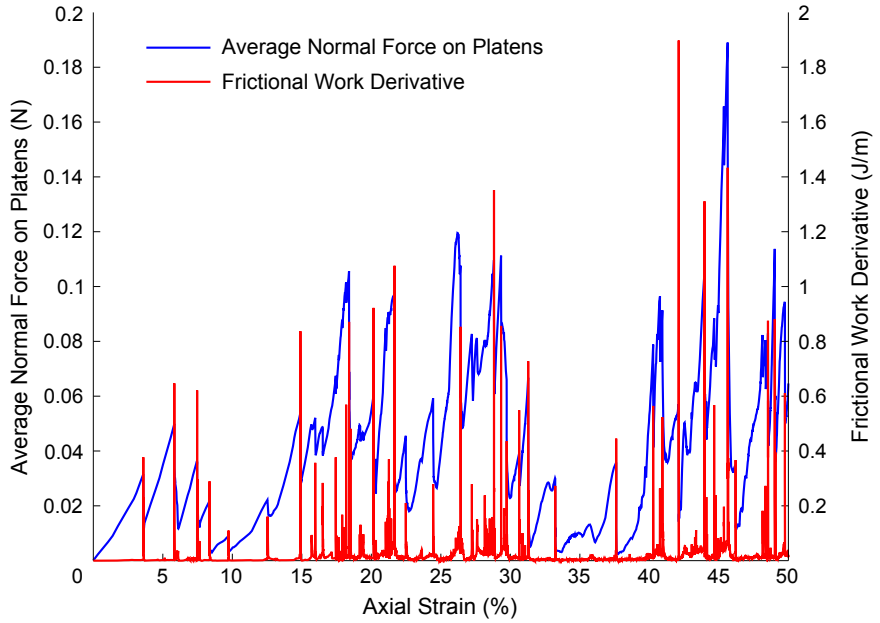

Figure 5.18: *Plots of the average normal force on the platens (N) and the derivative of frictional work (Jm^{-1}) against axial strain (%) for uniaxial compression of one typical agglomerate*

When the rate of energy dissipation due to friction increased rapidly on Figure 5.18, this was caused by relative motion between two contacting parts of the agglomerate. This could potentially be caused by the failure of bonds within the agglomerate, i.e., spheres moving relative to each other at the bond failure location. Alternatively, parts of the agglomerate which were in contact could move relative to each other, with a corresponding increase in frictional work, without bonds failing. This is possible as the bonds were not perfectly rigid and allowed some movement without failure. However, it was most likely that slippage would occur where a bond had been broken during a previous crushing cycle.

Regardless of whether bonds failed or not, the bond energy would still be expected to decrease as the microstructural rearrangement within the agglomerate would relieve some of the stresses which had accumulated. Figure 5.19 plots the number of bonds failed and the derivative of dissipated energy against axial strain. This figure demonstrates that the points at which energy dissipation rates were high coincided with bond breakage events. For example, Figure 5.19 shows that the sharp decrease in force and bond energy (and increase in frictional work) at 3.3% strain on Figure 5.16 was caused by the failure of one parallel bond.

5.4.2 Mode of Failure of the Agglomerates

Figure 5.19 shows that some bonds were failing as the agglomerate was compressed. The total number of bonds which failed could be subdivided by the type of failure, i.e., whether the bond failed as the result of its normal or shear strength being exceeded. In

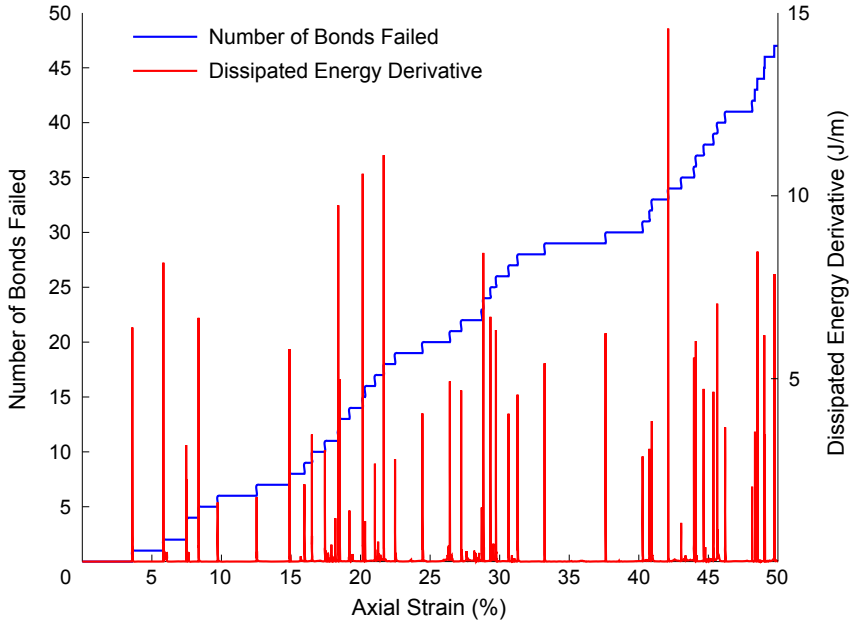

Figure 5.19: *Plots of the number of bonds failed and the derivative of dissipated energy (Jm^{-1}) against axial strain (%) for uniaxial compression of one representative simulated agglomerate*

fact, very few of the bonds which failed (< 2%) were caused by excessive shear stresses being generated; for example, none of the 47 bonds that had failed by 50% strain for the agglomerate in Figure 5.19 were shear failures. The percentages of bonds which failed were plotted against axial strain in Figure 5.20 for 20 randomly-selected agglomerates subjected to quasi-static uniaxial compression.

This progressive parallel bond breakage with increasing axial strain caused the agglomerate to break into multiple daughter agglomerates. The total number of agglomerate fragments and the number of spheres contained in each fragment were recorded at each 0.5% increment of strain for each simulation. Figure 5.21 shows the data for one representative agglomerate. For example, the total of 739 spheres was partitioned into six daughter agglomerates by 10% strain; these contained 493, 96, 90, 46, 10 and 4 spheres when ordered by size. The same procedure was applied to the other 130 agglomerates tested. At each strain increment, Figure 5.22 shows the median number of daughter fragments present and the median number of spheres in the largest remaining fragment (the largest fragment was shown as a blue area at the bottom of Figure 5.21).

One important result of this work was that relatively few bonds were required to fail to cause resulting failure of the agglomerate. This is emphasised by Figure 5.23, which shows how the percentages of bonds that failed changed around the point of failure. Each agglomerate is represented by two connected points: one at 5% of strain before the point of failure and the other at 5% of strain after the point of failure[†], e.g., if an

[†]In cases where the point of failure was ≥ 45% strain, the second point was taken at 50% strain.

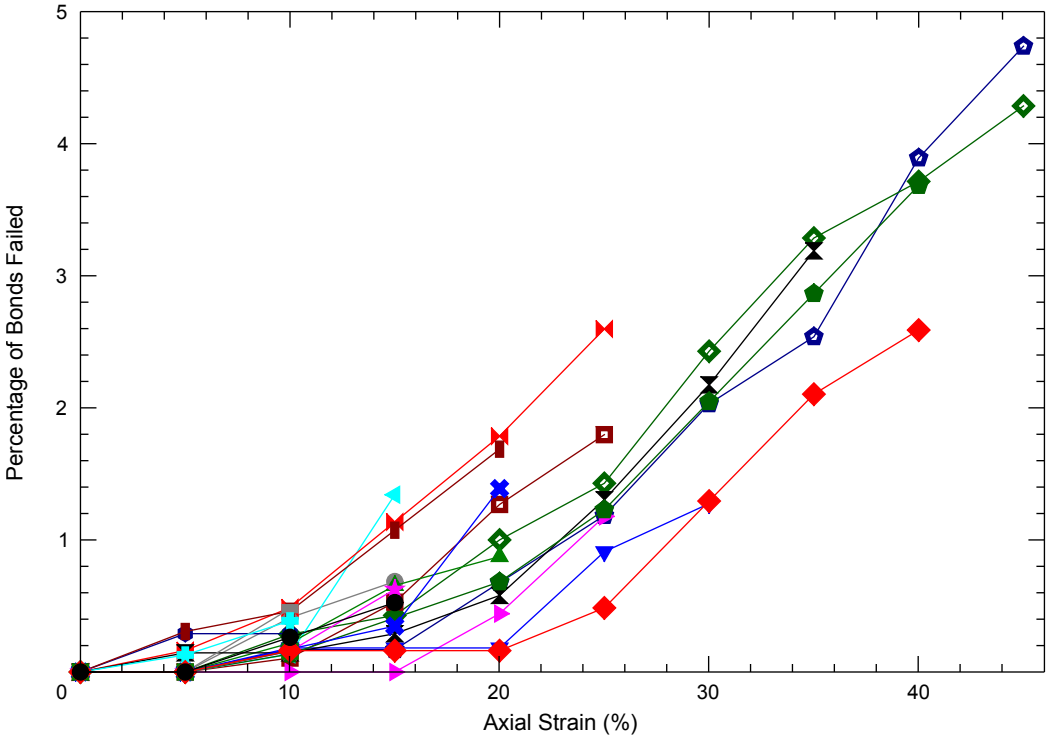

Figure 5.20: *Plots of percentage of bonds failed against axial strain (%) for uniaxial compression of 20 randomly-selected agglomerates, using discrete data points at 5% increments of strain up to the point of failure of each agglomerate*

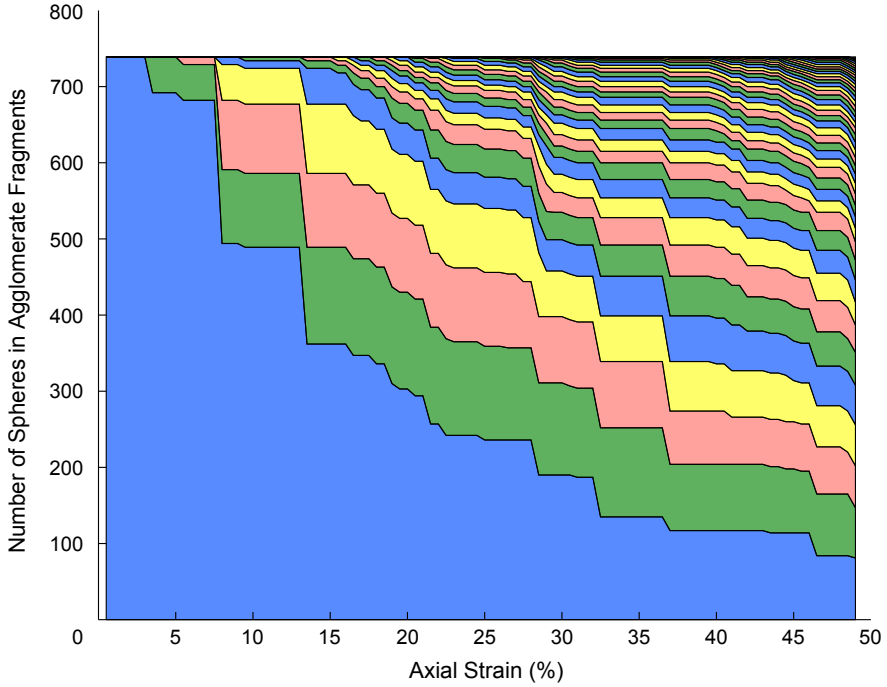

Figure 5.21: *Plot showing the number of spheres contained in each daughter agglomerate for uniaxial compression of one representative agglomerate*

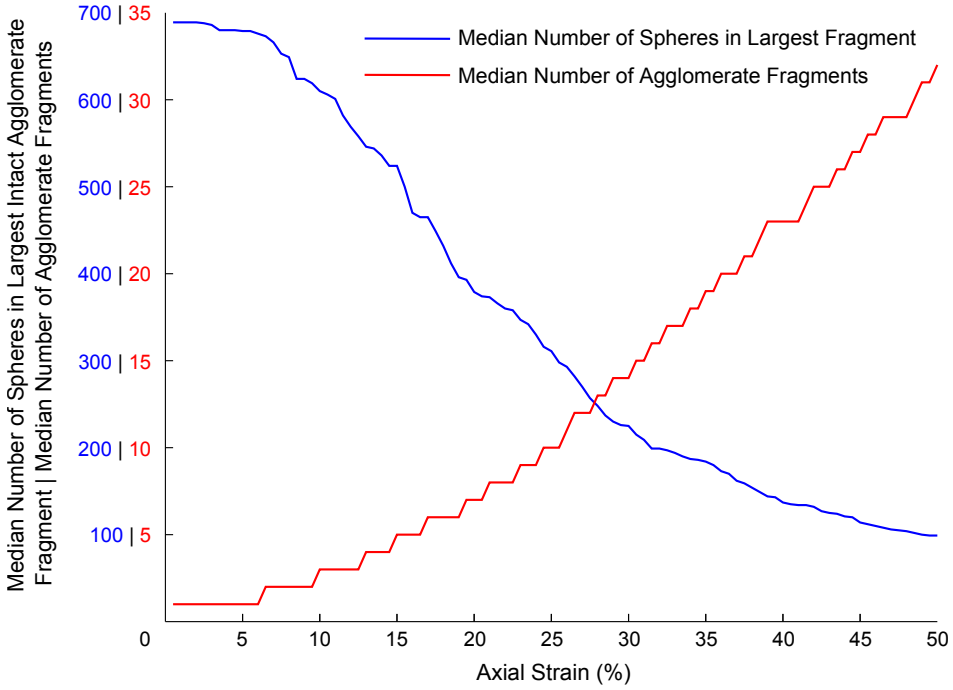

Figure 5.22: *Plot showing the median number of spheres remaining in the largest intact agglomerate fragment (axis: $0 \rightarrow 700$) and the median number of agglomerate fragments (axis: $0 \rightarrow 35$) against axial strain (%) for all 130 agglomerates tested*

agglomerate failed at a strain of 20%, these two points would be at strains of 15% and 25%.

Therefore, it is important to have an understanding not only of the number of bonds that fail, but also of where those bonds are located in the agglomerate. Pages 128–132 show two views of the representative agglomerate depicted by Figure 5.21 at each of the following axial strains: 5%, 10%, 20%, 30% and 40%. The first of these figures shows the arrangement of the spheres within the agglomerate, in which the colour of each daughter fragment is related to the number of spheres it contains. The second figure is a visualisation of the parallel bonds within the agglomerate, both intact and failed. The diameters of the lines connecting the centrepoints of the bonded spheres vary as a function of the maximum normal stress acting on the periphery of each bond. These bond networks were both highly complex and difficult to analyse.

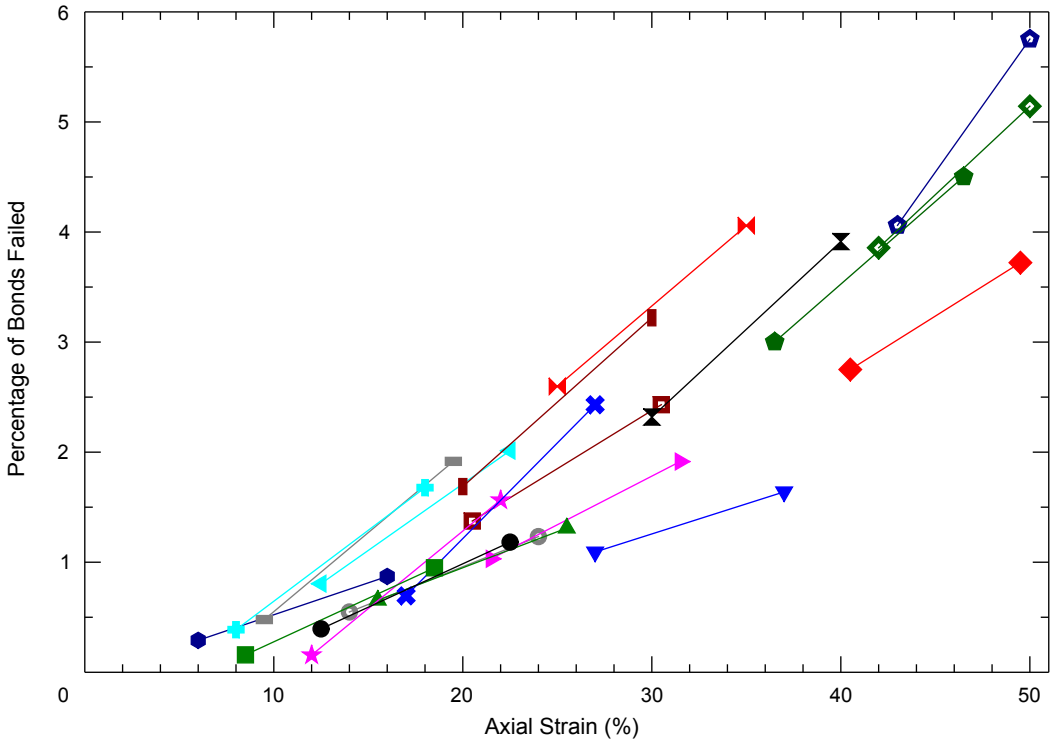

Figure 5.23: *Plots of percentage of bonds failed against axial strain (%) for uniaxial compression of 20 randomly-selected agglomerates, showing two data points for each agglomerate: one at 5% of strain before and the other 5% after the point of failure*

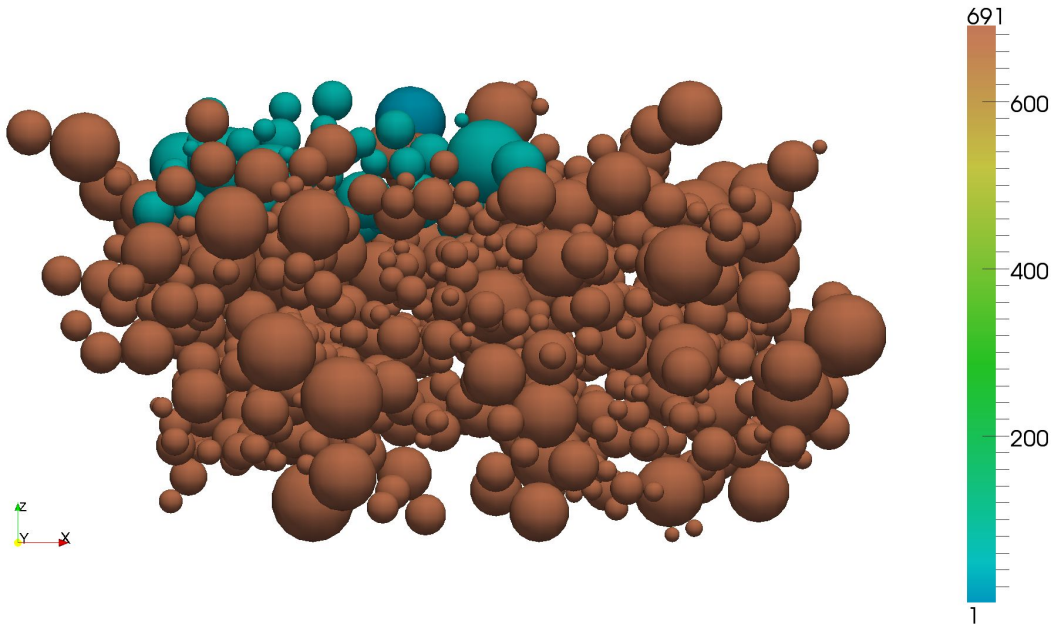

Figure 5.24: *Visualisation of a representative agglomerate at an axial strain of 5%, in which the colour bar indicates the number of spheres contained in each fragment of the agglomerate*

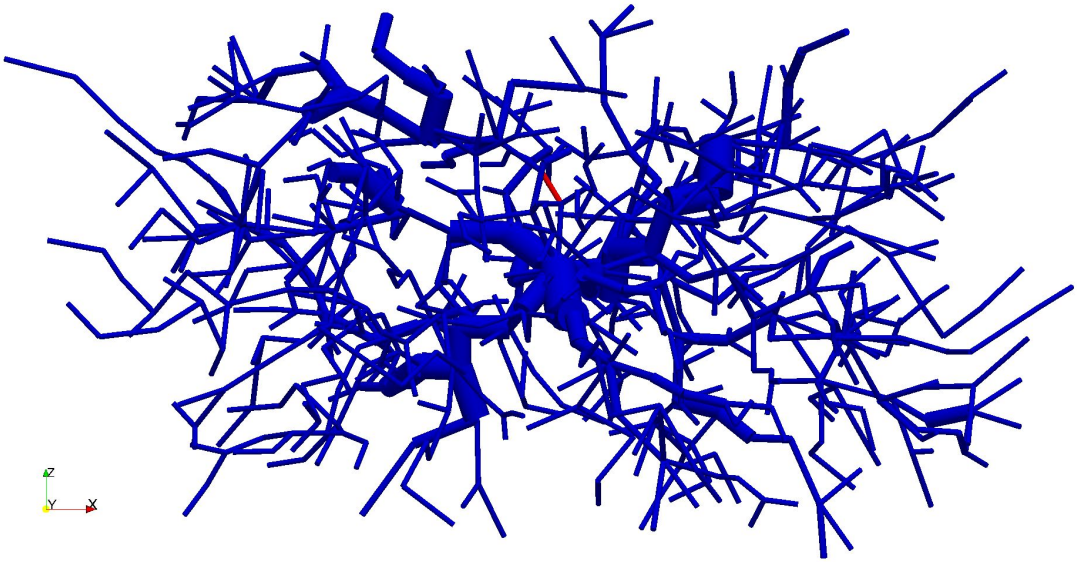

Figure 5.25: *Visualisation of the parallel bonds within a representative agglomerate at an axial strain of 5%, in which the maximum normal stress acting on each intact bond (—) was indicated by the diameter of the bond and failed bonds (—) were assigned a nominal diameter*

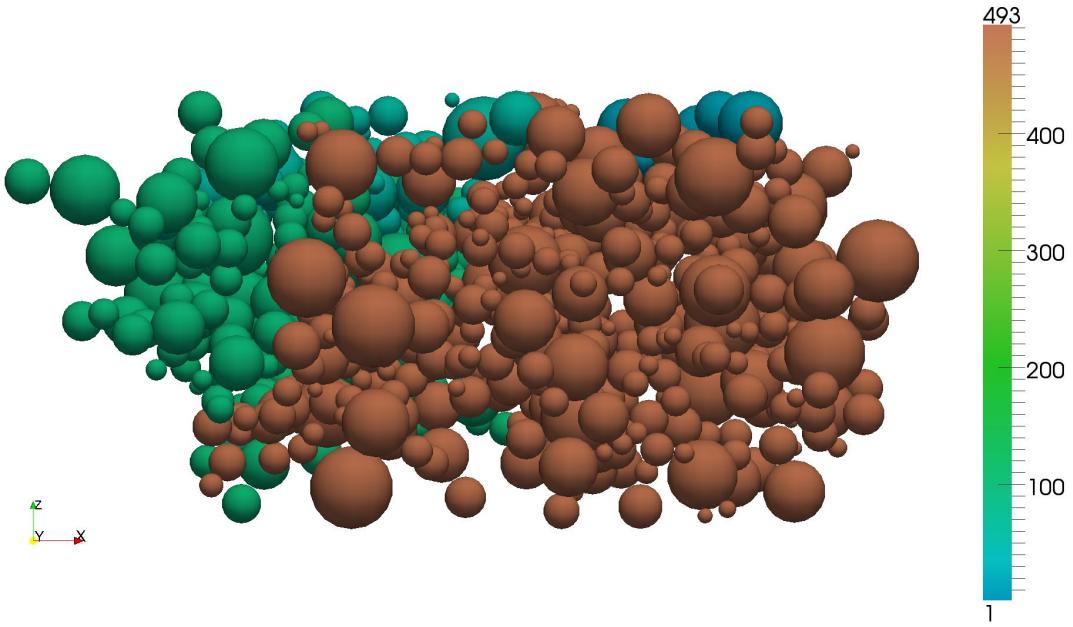

Figure 5.26: *Visualisation of a representative agglomerate at an axial strain of 10%, in which the colour bar indicates the number of spheres contained in each fragment of the agglomerate*

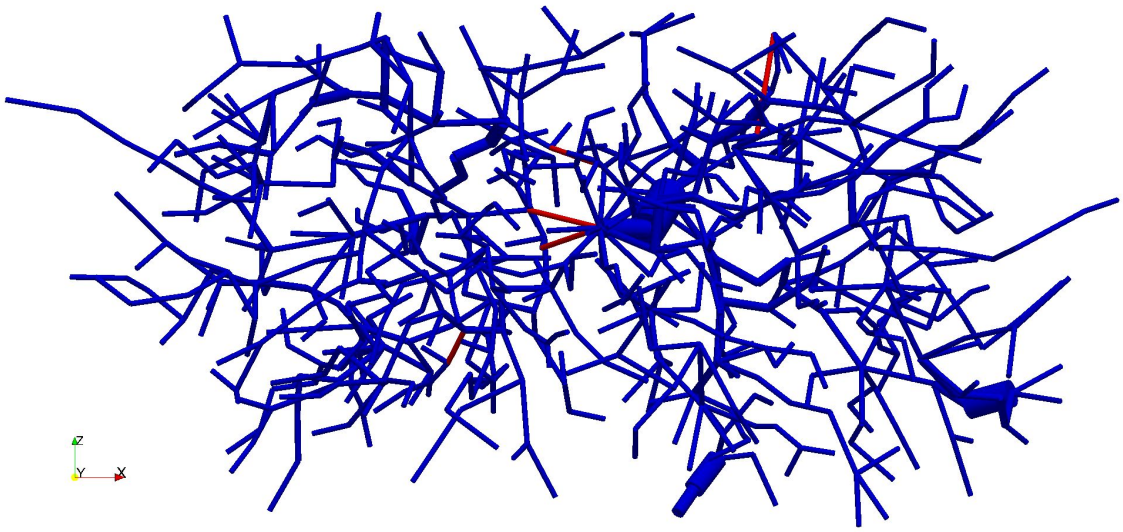

Figure 5.27: *Visualisation of the parallel bonds within a representative agglomerate at an axial strain of 10%, in which the maximum normal stress acting on each intact bond (—) was indicated by the diameter of the bond and failed bonds (—) were assigned a nominal diameter*

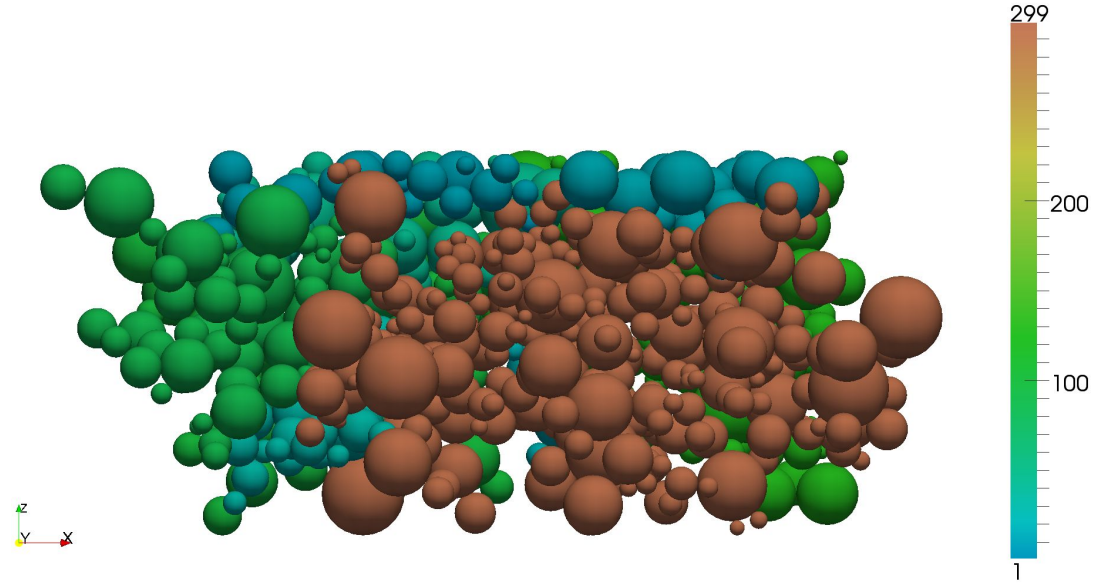

Figure 5.28: *Visualisation of a representative agglomerate at an axial strain of 20%, in which the colour bar indicates the number of spheres contained in each fragment of the agglomerate*

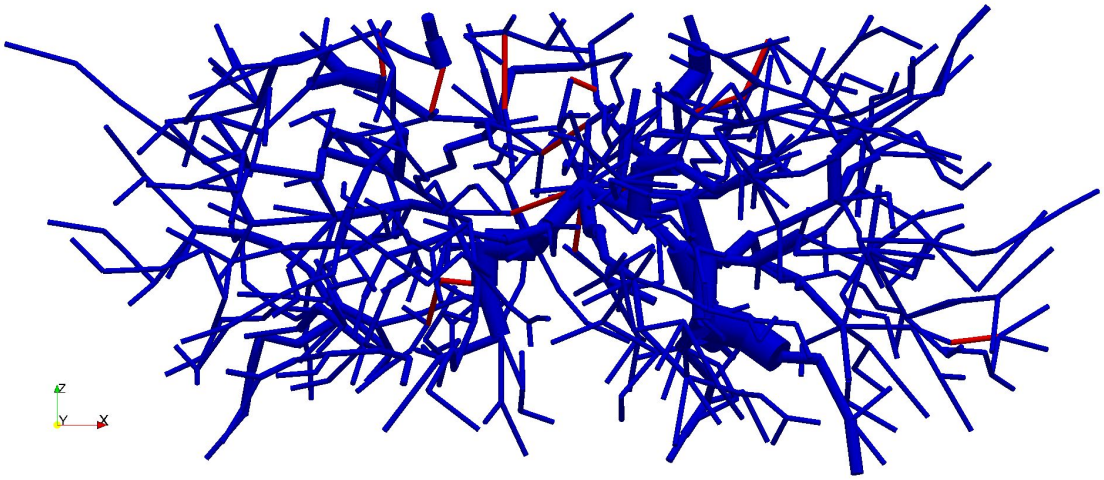

Figure 5.29: *Visualisation of the parallel bonds within a representative agglomerate at an axial strain of 20%, in which the maximum normal stress acting on each intact bond (—) was indicated by the diameter of the bond and failed bonds (—) were assigned a nominal diameter*

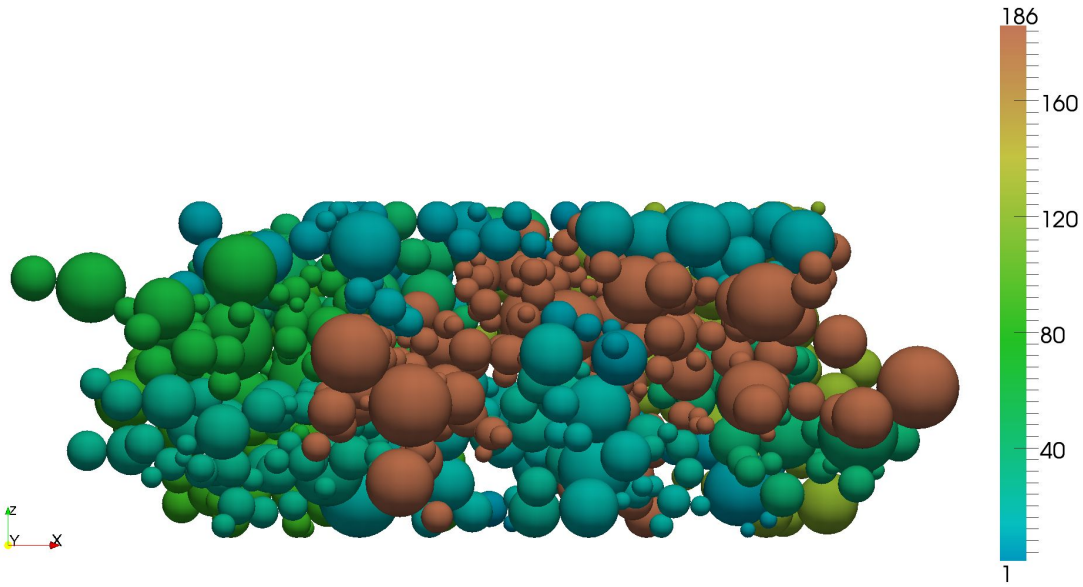

Figure 5.30: *Visualisation of a representative agglomerate at an axial strain of 30%, in which the colour bar indicates the number of spheres contained in each fragment of the agglomerate*

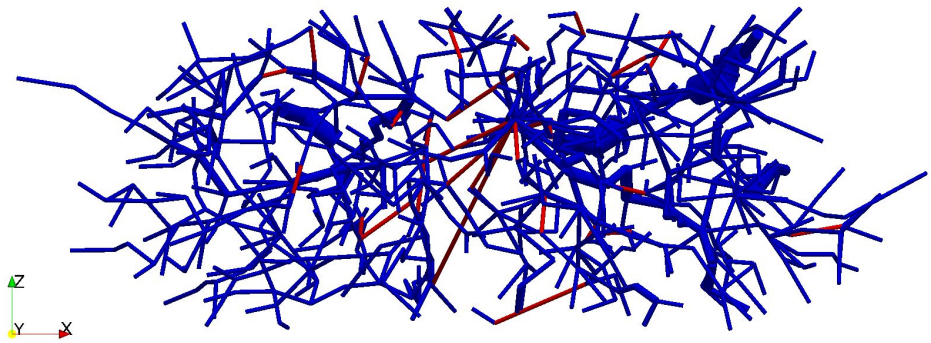

Figure 5.31: *Visualisation of the parallel bonds within a representative agglomerate at an axial strain of 30%, in which the maximum normal stress acting on each intact bond (—) was indicated by the diameter of the bond and failed bonds (—) were assigned a nominal diameter*

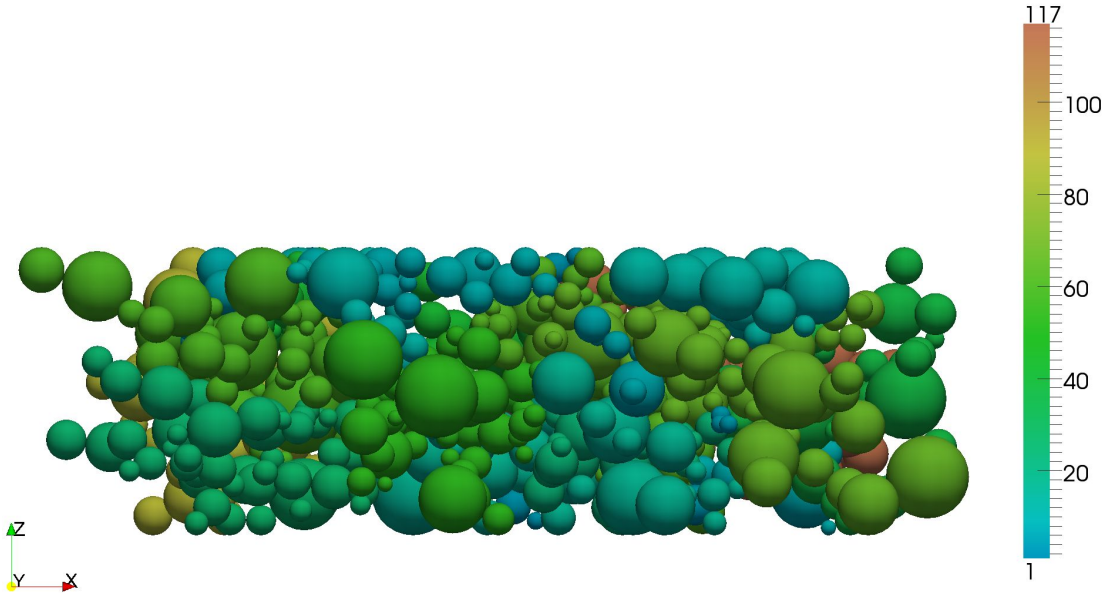

Figure 5.32: *Visualisation of a representative agglomerate at an axial strain of 40%, in which the colour bar indicates the number of spheres contained in each fragment of the agglomerate*

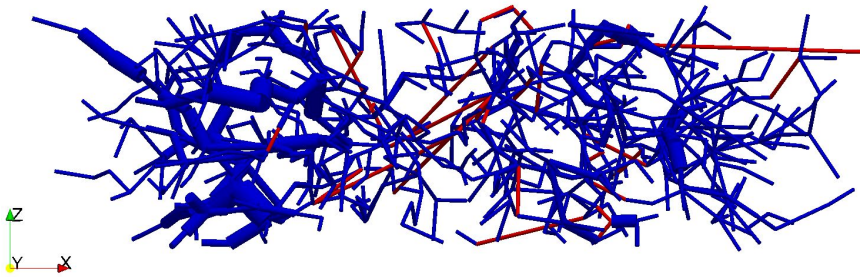

Figure 5.33: *Visualisation of the parallel bonds within a representative agglomerate at an axial strain of 40%, in which the maximum normal stress acting on each intact bond (—) was indicated by the diameter of the bond and failed bonds (—) were assigned a nominal diameter*

The dissipation of energy due to friction demonstrated that parts of the agglomerate were in relative motion. This was quantified by measuring the volumetric strains within the agglomerate during the uniaxial compression process. The agglomerate was divided into tetrahedral regions by generating a Delaunay tessellation of the three-dimensional sphere centrepoint data in MATLAB. This particular tessellation, or triangulation, is the most commonly used in scientific computing. The volume of any tetrahedron before compression was denoted as V_o while the volume at any subsequent stage of the compression process was V_t. The volumetric strain may be calculated from Eq. 5.6:

$$\text{Volumetric strain} = \frac{V_t - V_o}{V_o} \tag{5.6}$$

Figure 5.34 compares the volumetric strains calculated at three axial strains for the representative agglomerate used previously, showing the results for one plane which passes through the centrepoint of the agglomerate. The average volumetric strain increased progressively with axial strain. Note that one sphere had become separated

from the main agglomerate at an axial strain of 40% (Figure 5.34c), which corresponds to the long failed bond (in red) on the right of Figure 5.33.

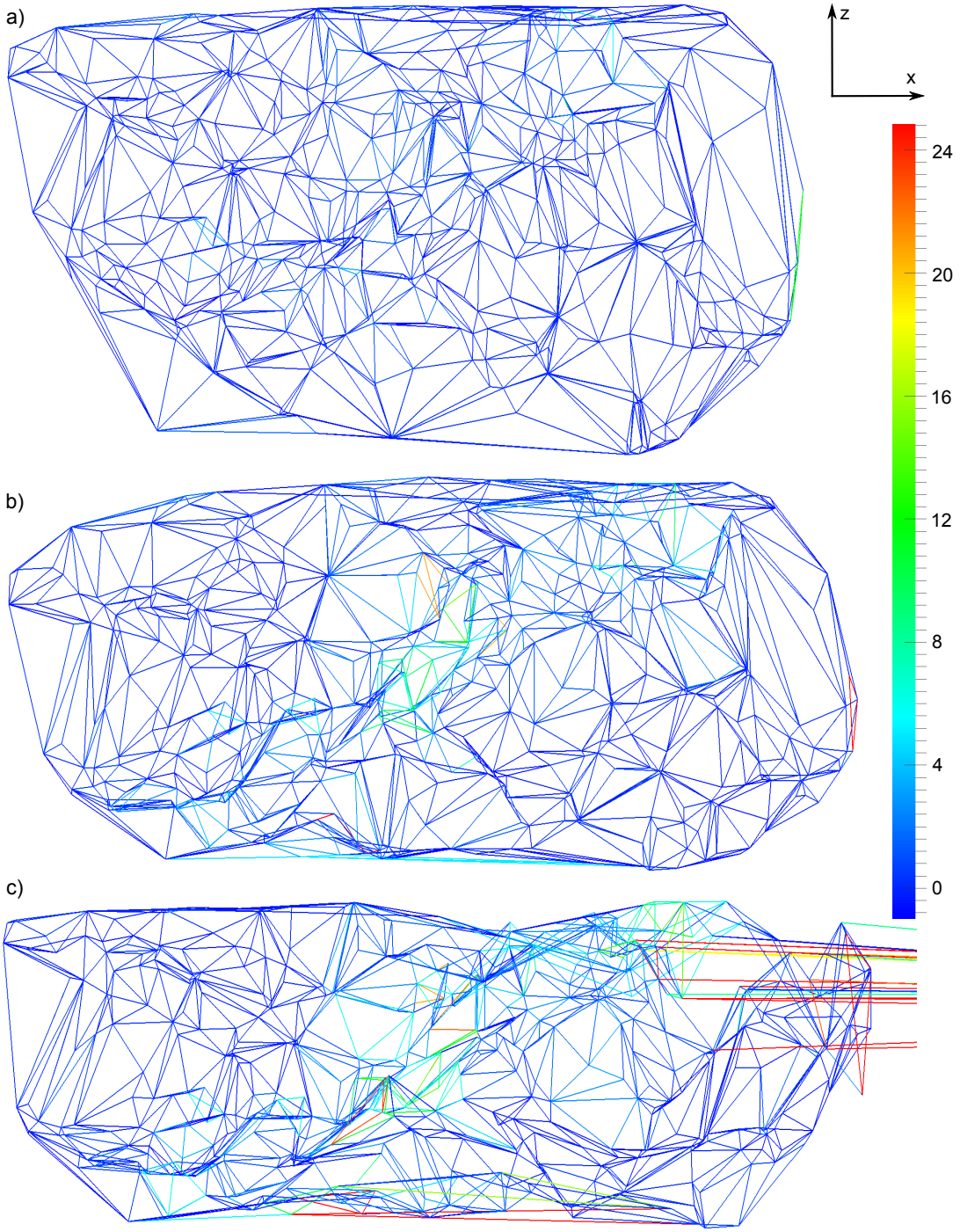

Figure 5.34: *Visualisation of the fabric changes within an agglomerate subjected to uniaxial compression at axial strains of a) 20%, b) 30% and c) 40%, where the colour bar denotes volumetric strain*

Although Figure 5.34 conveys a lot of information, it can be difficult to interpret the fabric changes which occur as an agglomerate is loaded. It is also possible to apply a statistical approach to fabric analysis (O'Sullivan, 2011, §10.6) which generally requires

calculation of the second-order fabric tensor for contact orientations. This is shown as Eq. 5.7 in three dimensions, where N_c is the number of contacts in the agglomerate and (n_x^c, n_y^c, n_z^c) is a unit vector describing the normal orientation of contact c.

$$\begin{pmatrix} \Phi_{xx} & \Phi_{xy} & \Phi_{xz} \\ \Phi_{yx} & \Phi_{yy} & \Phi_{yz} \\ \Phi_{zx} & \Phi_{zy} & \Phi_{zz} \end{pmatrix} = \frac{1}{N_c} \begin{pmatrix} \sum_{c=1}^{N_c} n_x^c n_x^c & \sum_{c=1}^{N_c} n_x^c n_y^c & \sum_{c=1}^{N_c} n_x^c n_z^c \\ \sum_{c=1}^{N_c} n_y^c n_x^c & \sum_{c=1}^{N_c} n_y^c n_y^c & \sum_{c=1}^{N_c} n_y^c n_z^c \\ \sum_{c=1}^{N_c} n_z^c n_x^c & \sum_{c=1}^{N_c} n_z^c n_y^c & \sum_{c=1}^{N_c} n_z^c n_z^c \end{pmatrix} \tag{5.7}$$

This tensor is symmetric (e.g., $\Phi_{xy} = \Phi_{yx}$) and its trace ($\Phi_{xx} + \Phi_{yy} + \Phi_{zz}$) is equal to 1 (O'Sullivan, 2011). The eigenvalues and eigenvectors of the fabric tensor may be calculated at multiple increments of strain. The former are denoted as Φ_1, Φ_2 and Φ_3 in order of decreasing magnitude; thus, Φ_1 and Φ_3 are the magnitudes of the major and minor fabric, respectively, which can be used to quantify the magnitude of the anisotropy within the system. The simplest approach is simply to find the difference between the major and minor fabric, a quantity which increases with anisotropy. Figure 5.35 shows these results for the representative agglomerate used previously.

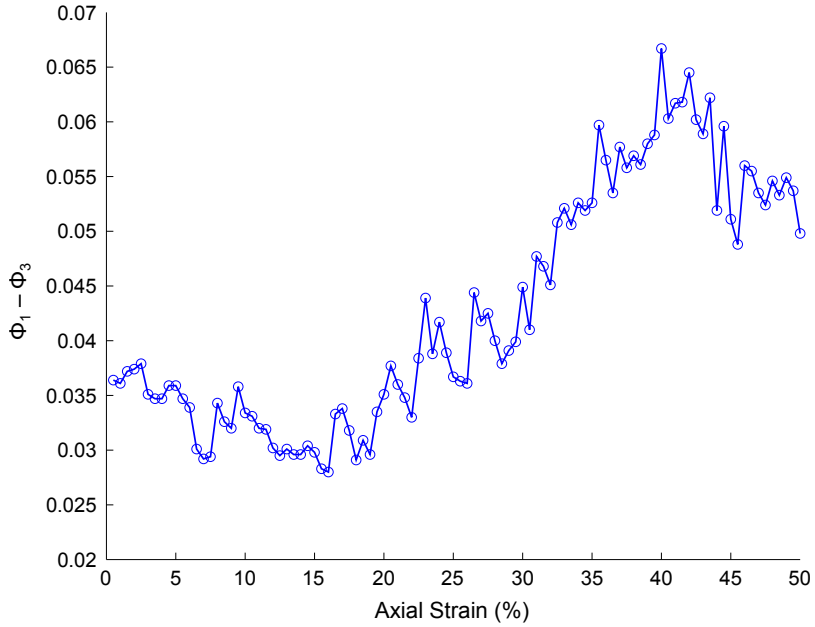

Figure 5.35: *Plot showing the difference between the major and minor fabric against percentage axial strain for a representative agglomerate subjected to quasi-static uniaxial compression*

The difference between Φ_1 and Φ_3 was low at the initiation of crushing, and approximately doubled nearing 50% strain indicating increased anisotropy. The orientation of the principal fabric could be found as the angle between the eigenvector corresponding to the major fabric eigenvalue (Φ_1) and the unit vector in the vertical direction. These results are shown for the same agglomerate in Figure 5.36.

The major fabric was initially in the horizontal plane and deviated from this as the agglomerate was compressed. The orientation of the major fabric to the vertical reached a minimum of 62° at an axial strain of 40%.

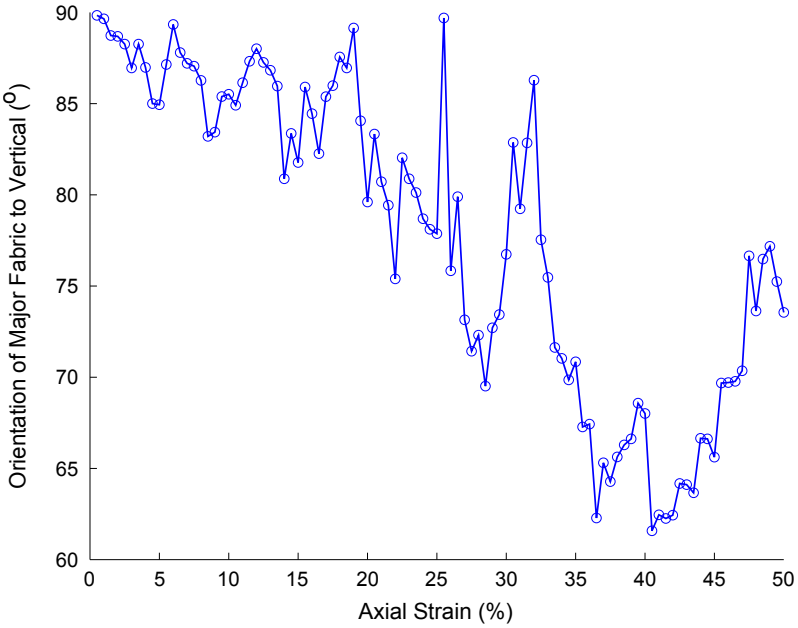

Figure 5.36: *Plot showing the orientation of the major fabric to the vertical (°) against percentage axial strain for the typical agglomerate compressed in Figure 5.35*

5.5 DEM Simulations of Dynamic Loading

While the calibrated model gives good results for quasi-static loading, it is interesting to assess whether or not it can also be applied effectively to dynamic loading. Two additional sets of simulations were conducted using the final set of calibrated parameters shown in Table 5.3 (except ball density). Each set consisted of 20 simulations and were conducted similarly: a stiff, horizontal, frictionless platen was placed beneath each simulated agglomerate and an initial normal velocity was assigned to the agglomerate to cause a collision with the platen. The initial distance between the lowest point of the agglomerate and the upper surface of the platen was set at 5% of the agglomerate height for computational efficiency.

One key difference between these dynamic simulations and the quasi-static simulations was that density scaling was not used. The forces induced by the relative motion of spheres would be excessively high unless the density was reduced to a physically realistic value. The ball density was set at 1100 $\mathrm{kg\,m^{-3}}$: approximately equal to the particle density of infant formula as measured by nitrogen pycnometry (Section 2.2.3 on p.32). The differences between both sets of dynamic simulations were as follows:

1. One set simulated the drop tests in Section 3.1.7. The impact velocity was set at 1.9 $\mathrm{m\,s^{-1}}$ and gravity was active. This allowed coefficients of restitution to be evaluated and compared with those obtained by experiment.

2. The other set simulated the impact tests in Section 5.1.3, and thus used an impact velocity of 10.1 $\mathrm{m\,s^{-1}}$. Gravity was not active for these simulations.

It should be noted that the algorithm given in Section 3.1.6 for determining the points at which agglomerates failed could not be applied to the results of these dynamic simulations for several reasons:

- The deformations of the unconfined agglomerates were low, even for the impact tests at 10.1 $\mathrm{m\,s^{-1}}$. The strain was defined as the absolute difference between the initial agglomerate height before impact and the height thereafter divided by the initial height, where height was measured in the direction normal to the platen. The highest strain attained during any of these dynamic simulations was 8.5%. Therefore, the third criterion, that "the maximum force attained in a 10% strain range following the point of failure must be less than the force at failure", was inapplicable.
- It is often the case that the forces at which materials fail depend upon the rate of loading. The numerical values in the algorithm were selected for quasi-static loading and would need to be modified to choose the point of failure reliably for dynamic loading.
- The strain did not increase monotonically, instead increasing to a maximum and then decreasing. This required a more sophisticated MATLAB algorithm than the one described in Section 3.1.6.

The drop tests at 1.9 $\mathrm{m\,s^{-1}}$ and impact tests at 10.1 $\mathrm{m\,s^{-1}}$ are discussed separately in Sections 5.5.1 and 5.5.2, respectively.

5.5.1 Drop Tests at 1.9 $\mathrm{m\,s^{-1}}$

The results of the experimental drop tests were given in Section 3.2.3, and none of the agglomerates were seen to fail in these tests. Similarly, none of the parallel bonds, and hence none of the agglomerates, failed during any of the 20 drop test simulations conducted. The highest force exerted on the stiff platen during any simulation was 0.0801 N, which was close to the mean force at failure for quasi-static loading of 0.0749 N (Table 5.4 on p.116). There was a significant decrease from this maximum force to the second-highest force of 0.0599 N, and only three of the 20 simulated agglomerates had maximum forces which exceeded 0.03 N. Figure 5.37 shows three representative plots of force versus time for these agglomerates.

The coefficient of restitution was calculated for each simulation as the absolute value of the maximum normal velocity in the upward direction divided by the maximum normal velocity in the downward direction. The velocity of the agglomerate was taken as the unweighted arithmetic mean of the velocities of each of the spheres comprising

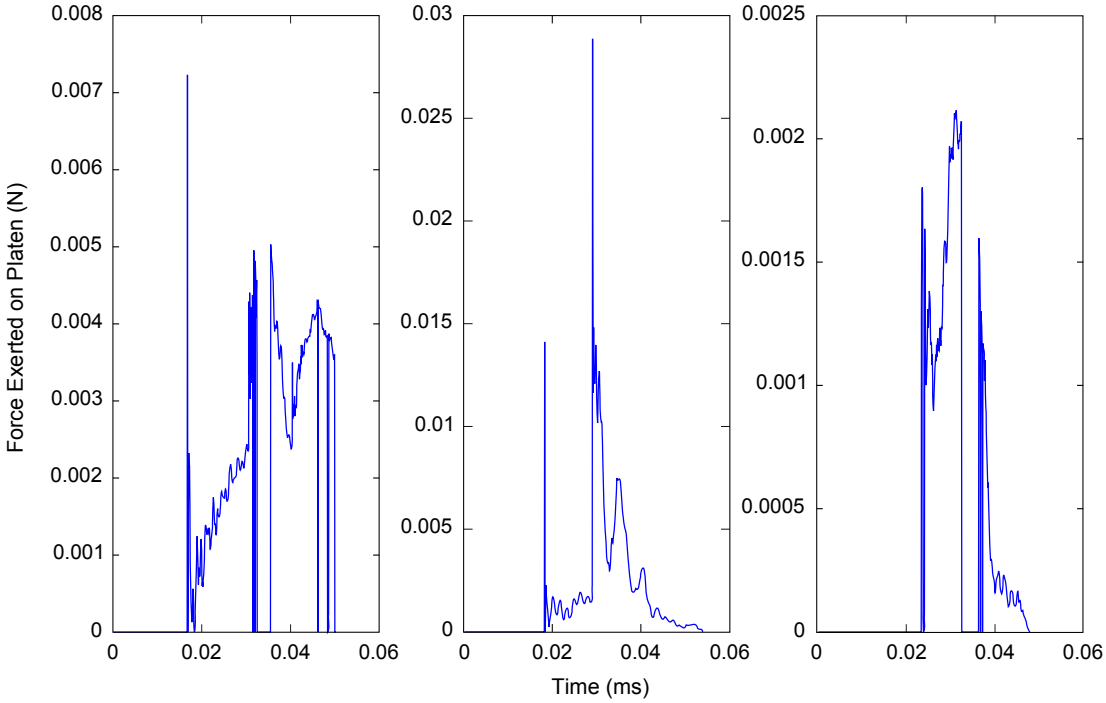

Figure 5.37: *Three plots of force exerted on the target platen (N) against time (ms) for simulated drop tests of agglomerates of infant formula at 1.9 ms^{-1}*

the agglomerate. Infant formula B had a mean coefficient of restitution of 0.3258 (Table 3.13), while the mean for the simulated agglomerates was considerably lower at 0.0954.

Thus, a higher proportion of the incident energy was absorbed by the simulated agglomerates, on average, than by the physical agglomerates. The local damping coefficient, previously mentioned in Section 4.3.1, was set at 0.3 for these simulations. It was hypothesised that the coefficients of restitution of the simulated agglomerates would increase, and thus become closer to the experimental results, if the damping were reduced. This was tested by running the same 20 simulations using damping coefficients of 0 and 0.15. Reducing the damping coefficient to 0.15 had a small effect: the mean coefficient of restitution increased to 0.1298. However, eliminating the damping completely had a huge effect: the coefficient of restitution increased to 0.5826 without a corresponding increase in the standard deviation. Figure 5.38 shows the cumulative distributions in coefficients of restitution, while Table 5.7 gives basic statistics of the data obtained.

Three energy terms which were not significant for the quasi-static tests needed to be considered for the dynamic tests:

Body work The total accumulated work done by all body forces on the assembly, i.e., gravity for the drop tests

Kinetic energy The kinetic energy of all particles in the assembly

Strain energy The total strain energy of the assembly stored at all contacts

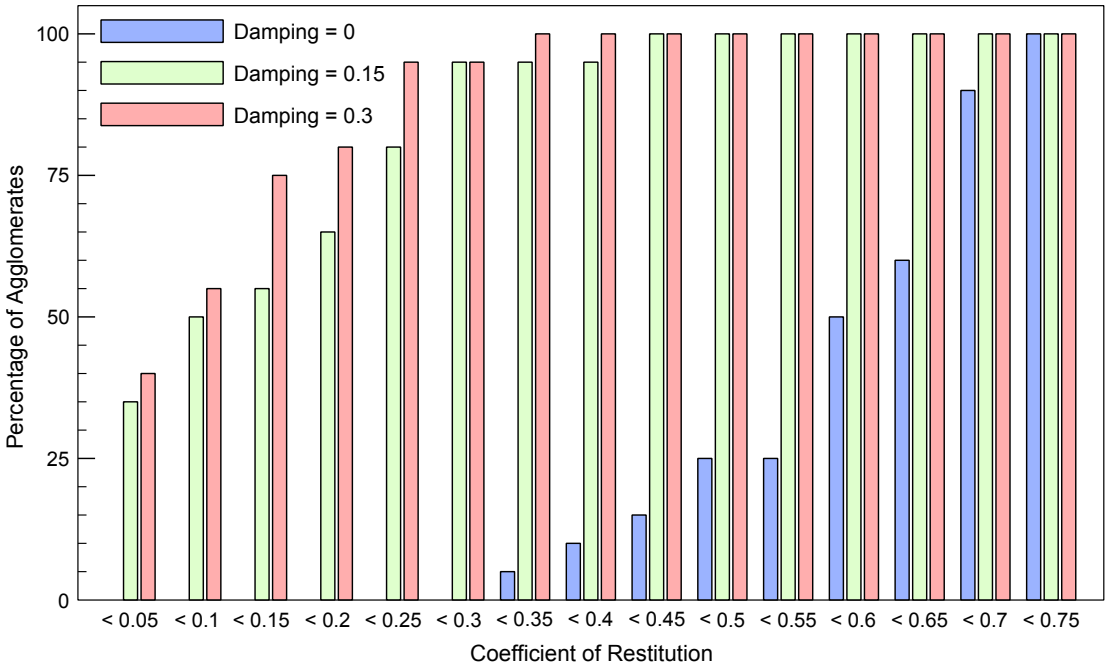

Figure 5.38: *Bar charts showing the percentage of the agglomerates tested using local damping coefficients of 0, 0.15 and 0.3 which had coefficients of restitution less than the values given on the x-axis*

Table 5.7: *Basic statistics comparing the coefficient of restitution data for drop tests conducted using sets of 20 agglomerates having three different local damping coefficients: 0, 0.15 and 0.3*

Damping	Coefficient of Restitution			
	Mean	Std. Dev.	Minimum	Maximum
0	0.5826	0.1149	0.3310	0.7301
0.15	0.1298	0.1203	0.0030	0.4009
0.3	0.0954	0.0903	0.0002	0.3085

Note that Figures 5.39, 5.40, 5.42 and 5.43 in this section were plotted for one representative agglomerate which had a coefficient of restitution of 0.117. The first of these shows the evolution of the kinetic and bond energies over time for this agglomerate.

The kinetic energy of the agglomerate increased slowly before impact due to the effect of gravity, reaching a maximum of 0.1596 µJ. This impact energy was very low compared to those recorded during the quasi-static crushing simulations (Figure 5.15). The bond energy was almost zero before impact occurred at 16.7 µs. The remaining four energy terms recorded (strain energy, body work, boundary work and frictional work) were small compared to the kinetic and bond energies, and are shown in Figure 5.40.

The increase in frictional work over time demonstrates that some energy was dissipated by frictional sliding, although this was a minor contributor to the total energy dissipated. The boundary work was rounded to zero at each time step in the computations (<

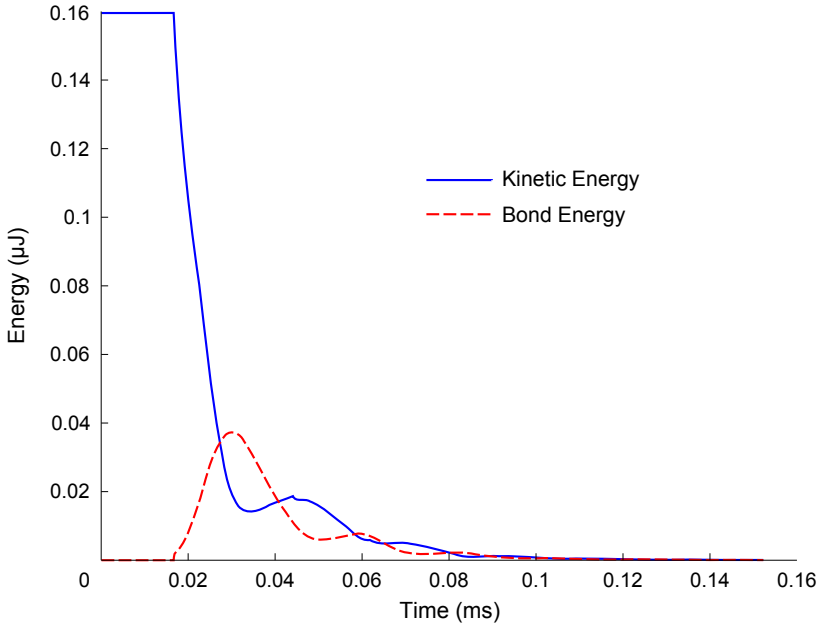

Figure 5.39: *Plots of the kinetic and bond energies (both in μJ) against time (ms) for a simulated drop test of one representative agglomerate*

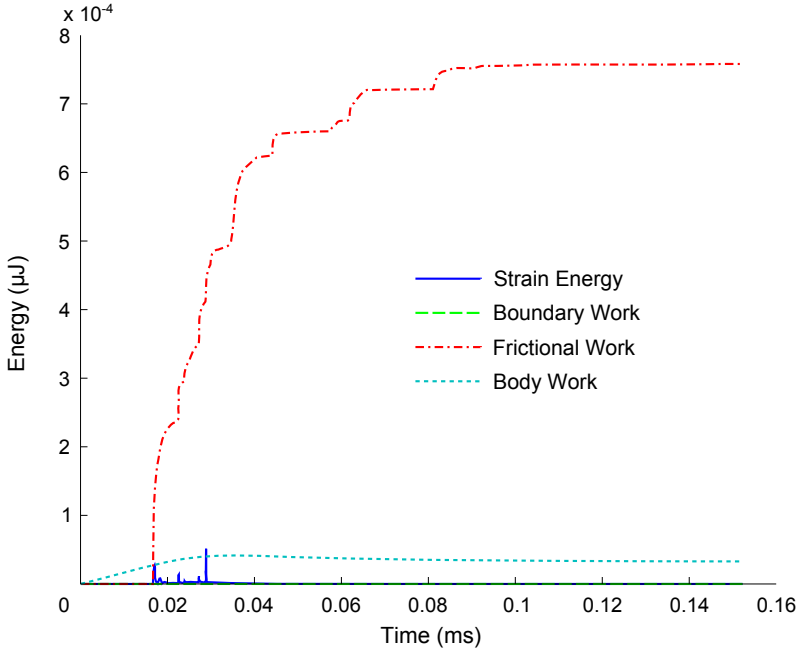

Figure 5.40: *Plots of the strain energy, boundary work, frictional work and body work (all in μJ) against time (ms) for a simulated drop test of one representative agglomerate*

0.1 fJ), which indicates that the platen experienced no deformation when impacted by the simulated agglomerate. The total bond energy dissipated during the simulation was 0.0405 μJ: approximately 1/4 of the kinetic energy possessed by the agglomerate before impact. Thus, most of the incident kinetic energy was dissipated by damping. Damping clearly had an important role in these drop test simulations, which explains why eliminating local damping had such a marked effect on the coefficient of restitution.

Figure 5.41 shows the evolution of three key energy terms when the simulation shown in Figures 5.39 and 5.40 was rerun using a local damping coefficient of zero.

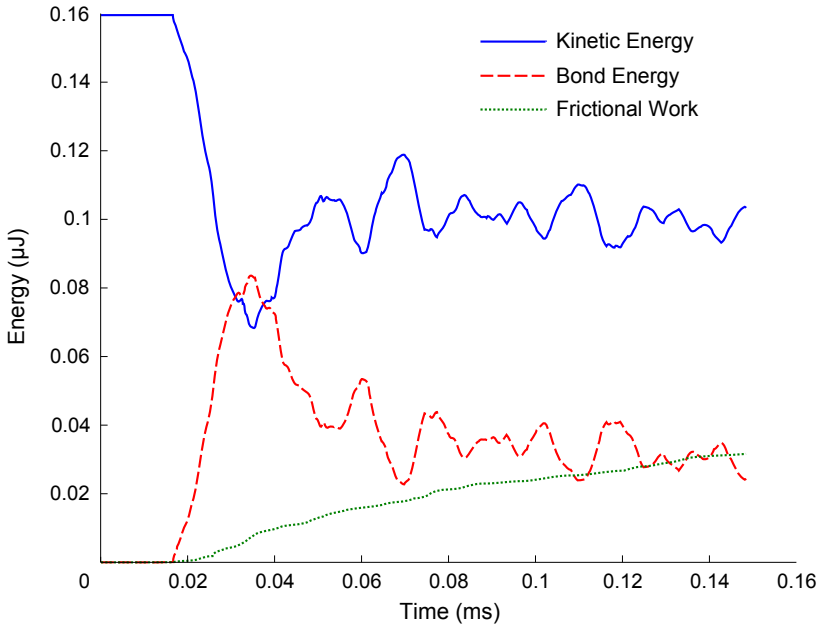

Figure 5.41: *Plots of the kinetic energy, bond energy and frictional work (all in μJ) against time (ms) for a simulated drop test of one representative agglomerate where the local damping coefficient was set at zero*

The kinetic energy of the agglomerate remained above 0.06 μJ throughout the simulation. The primary mechanism for energy dissipation was friction, which became much more significant in the absence of damping. The lack of damping also caused the bond energy to attain values which were more than twice the maximum when damping was active (0.084 μJ compared to 0.037 μJ). Figure 5.42 compares the force exerted on the platen when damping was active with plots of three energy terms: the kinetic energy, bond energy and frictional work. The maximum force (equal to 0.057 N) was attained after a time of 28.9 μs, which corresponds to the peak of bond energy. This is similar to the results in Section 5.4.1 in which the bond energy and normal force on the platens showed a close correspondence.

Figure 5.43 shows the parallel bonds within the agglomerate when the force was highest. The maximum normal stress attained (425 $\mathrm{MN\,m^{-2}}$) was less than half the bond normal strength of 1 $\mathrm{GN\,m^{-2}}$. The corresponding maximum shear stress at this time was considerably lower, at only 241 $\mathrm{MN\,m^{-2}}$. It was interesting to observe how the stresses were distributed within the agglomerate. Strong force chains radiated outwards from the point of contact between the agglomerate and the platen; however, most of the agglomerate remained relatively unstressed.

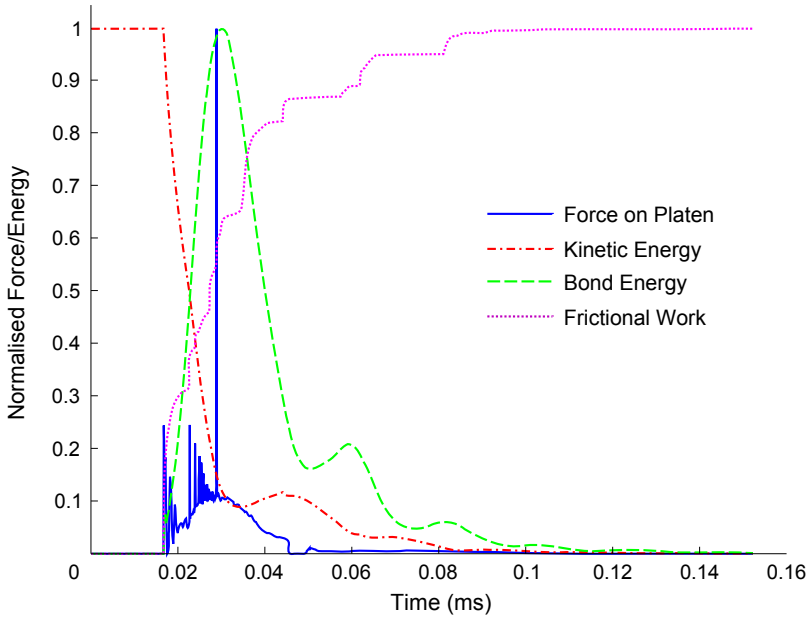

Figure 5.42: *Normalised plots of the force exerted on the platen and three tracked energy components (kinetic energy, bond energy and frictional work) against time (ms) for a simulated drop test of one representative agglomerate*

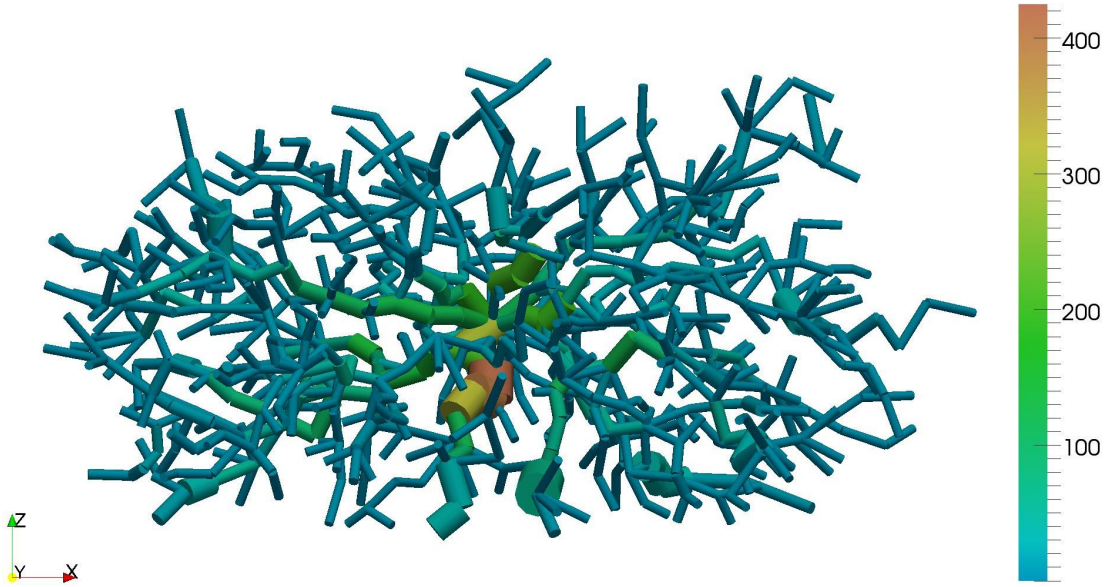

Figure 5.43: *Visualisation of the parallel bonds within a representative agglomerate when the force exerted on the platen was at its maximum value. The maximum normal stress acting on the periphery of each bond was indicated both by the diameter of the bond and by the colour bar (in $MN\,m^{-2}$)*

5.5.2 Impact Tests at 10.1 $m\,s^{-1}$

By increasing the impact velocity to approximately 10.1 $m\,s^{-1}$, 72% of the agglomerates tested experimentally were seen to fail. It was not possible to apply the algorithm to determine failure (as discussed on p.136); instead, the number of daughter fragments and the number of spheres contained in each fragment were recorded during the

simulations. Each agglomerate was assigned to one of the four categories defined in Section 5.1.3 using the following criteria:

Unbroken Agglomerates were deemed to be unbroken following the impact test if more than 95% of the spheres remained in one intact agglomerate.

Binary fracture Two large daughter fragments were produced, each containing more than 40% of the total number of spheres.

Local disintegration One large daughter fragment was produced, containing more than 50% of the total number of spheres, and none of the other fragments contained more than 10% of the spheres.

Shattering No daughter fragment remained which contained more than 20% of the spheres.

A number of the simulated agglomerates failed in a similar manner, but could not be allocated to one of these four categories. Therefore, a fifth category was defined:

Fragmentation One large daughter fragment was produced, containing more than 40% of the total number of spheres, while at least one of the other fragments contained more than 10% of the spheres.

Figure 5.44 shows the percentages of the 20 simulated agglomerates which were assigned to each of these five categories. By comparing these data with the experimental results in Figure 5.5, it can be seen that a higher proportion of the simulated agglomerates failed: 85% compared with 72%. The most marked difference was in the mode of failure. None of the simulated agglomerates failed by binary fracture or shattering, while the latter was the most common mode of failure for the physical agglomerates. The majority of the simulated agglomerates (55%) failed by local disintegration; this represented an increase of 175% compared to the experimental results. At least one parallel bond failed in each of the 20 agglomerates simulated, while a maximum of seven bonds failed (median of three). Therefore, the percentages of bonds which failed were relatively low: the mean was 0.501% with a standard deviation of 0.195%.

Figure 5.45 shows plots of force against time for three simulated impact tests. The highest force exerted on the platen during any of the simulations was 0.8203 N, while the mean and standard deviation of the 20 maxima were 0.2511 N and 0.2175 N, respectively. This mean was more than three times greater than the mean force at failure for quasi-static loading given in Table 5.4.

The body work was zero as gravity was not active for the impact simulations. As for the drop test results, the strain energy was negligible for all simulations and the boundary work was rounded to zero at each time step, indicating that no deformation of the platen occurred. One representative agglomerate was selected and used for Figures

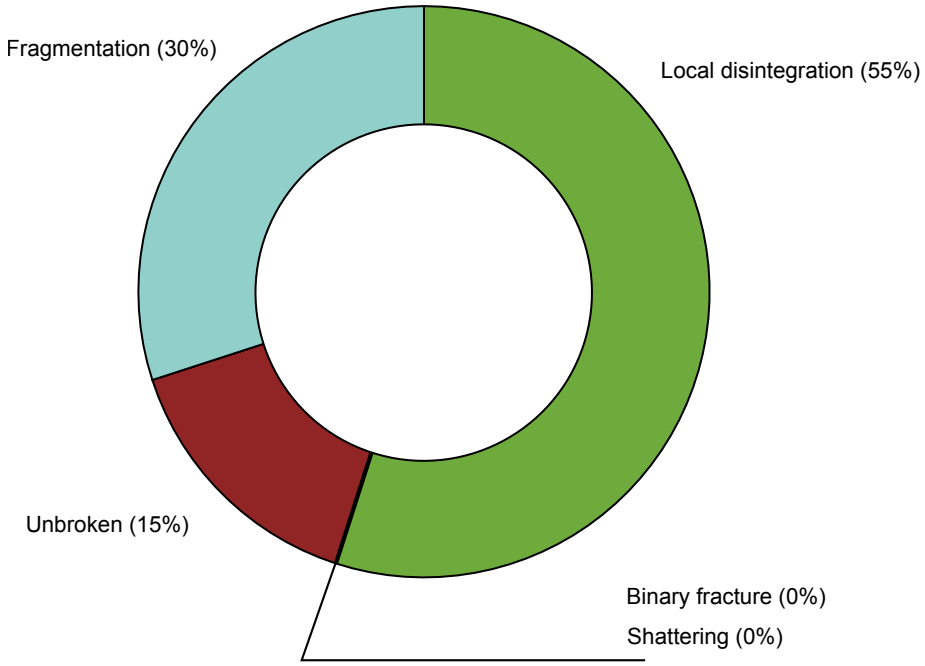

Figure 5.44: *Chart showing the percentages of the agglomerates assigned to each failure category for simulated impact tests at 10.1 ms^{-1}*

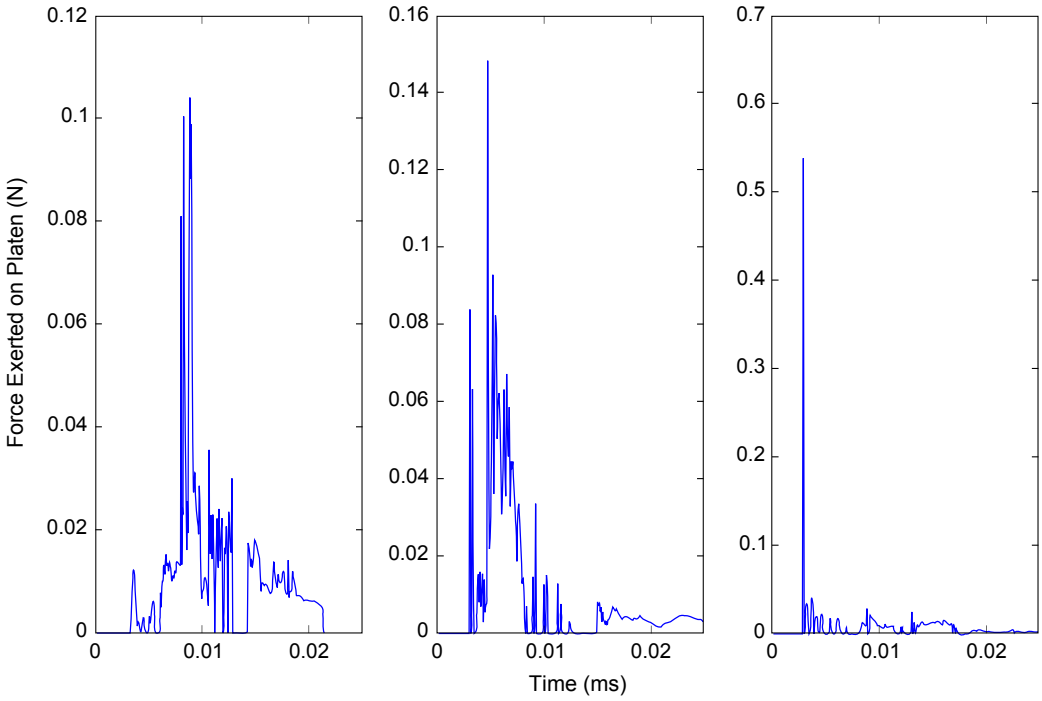

Figure 5.45: *Three plots of force exerted on the target platen (N) against time (ms) for simulated impact tests of agglomerates of infant formula at 10.1 ms^{-1}*

5.46–5.48. Four bonds failed in this chosen agglomerate which was assigned to the local disintegration category. Figure 5.46 shows the evolution of the three most significant energy terms over time: the kinetic energy, bond energy and frictional work.

The kinetic energy was constant at 3.603 µJ before impact occurred at 3.2 µs. This incident kinetic energy was almost 23 times larger than that for the drop test at 1.9 ms^{-1},

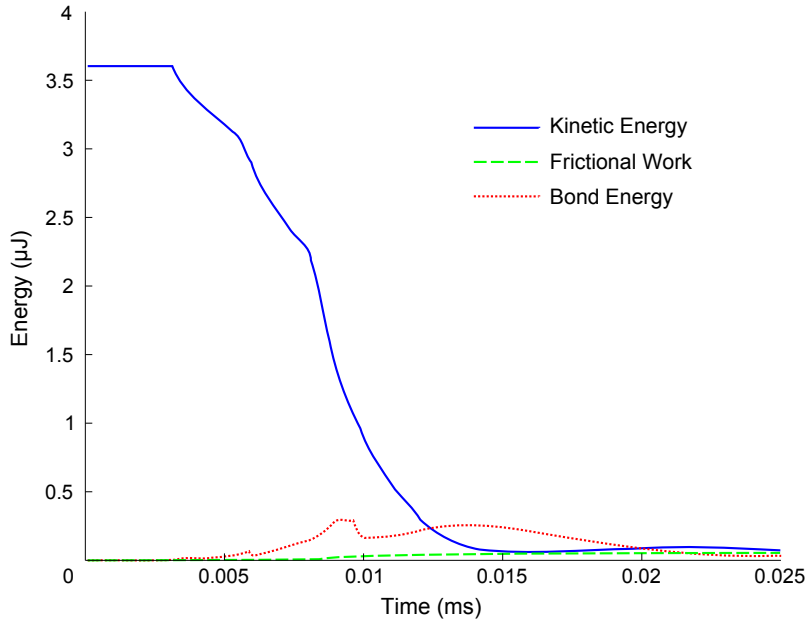

Figure 5.46: *Plots of the kinetic energy, bond energy and frictional work (all in μJ) against time (ms) for a simulated impact test of one representative agglomerate at 10.1 ms^{-1}*

which reflects the quadratic relationship between kinetic energy and speed. The energy dissipated by friction was low: 0.054 μJ by the end of the simulation. This was smaller than the residual kinetic energy at the end of the simulation of 0.061 μJ. The total bond energy dissipated was 0.406 μJ; thus, more than 85% of the incident kinetic energy was dissipated by damping. Figure 5.47 compares the force exerted on the platen with plots of three key energy terms. The maximum force (0.104 N) was attained after 8.9 μs. This coincided with the maximum bond energy, an observation that was also made for Figure 5.42.

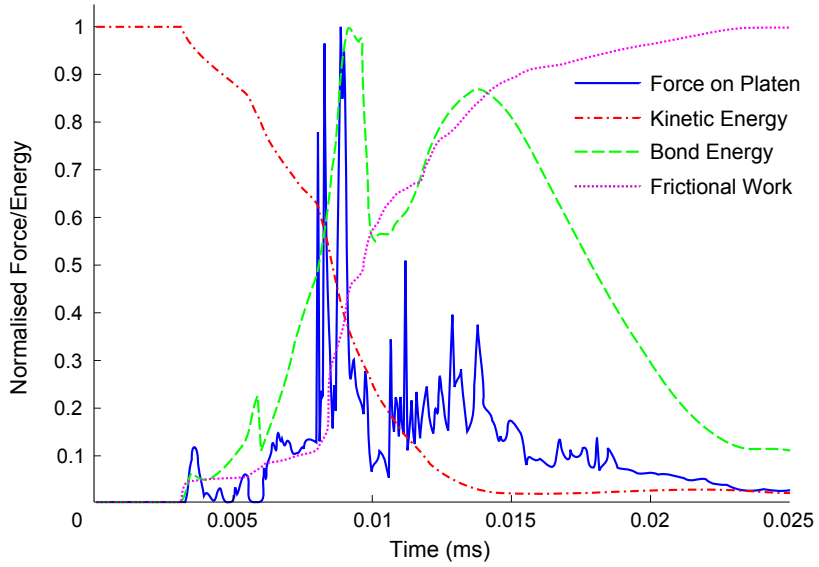

Figure 5.47: *Normalised plots of the force exerted on the platen and three tracked energy components (kinetic energy, bond energy and frictional work) against time (ms) for a simulated impact test of one representative agglomerate*

Figure 5.48 plots the number of bonds failed and the derivative of bond energy against axial strain. On each occasion when a bond failed, a local maximum was seen in the rate of change of the bond energy. Figure 5.49 compares the volumetric strains in a representative agglomerate at times of 0.014 ms and 0.025 ms. As for Figure 5.34, this figure illustrates the strains for one plane which passes through the centrepoint of the agglomerate. For all of the agglomerates tested, the highest volumetric strain within the agglomerate increased from zero to a maximum value when the bond energy was high (Figure 5.49a). The highest volumetric strain decreased progressively nearing the end of the simulation (Figure 5.49b), indicating that the accumulated bond energy was being relieved and strains were being recovered.

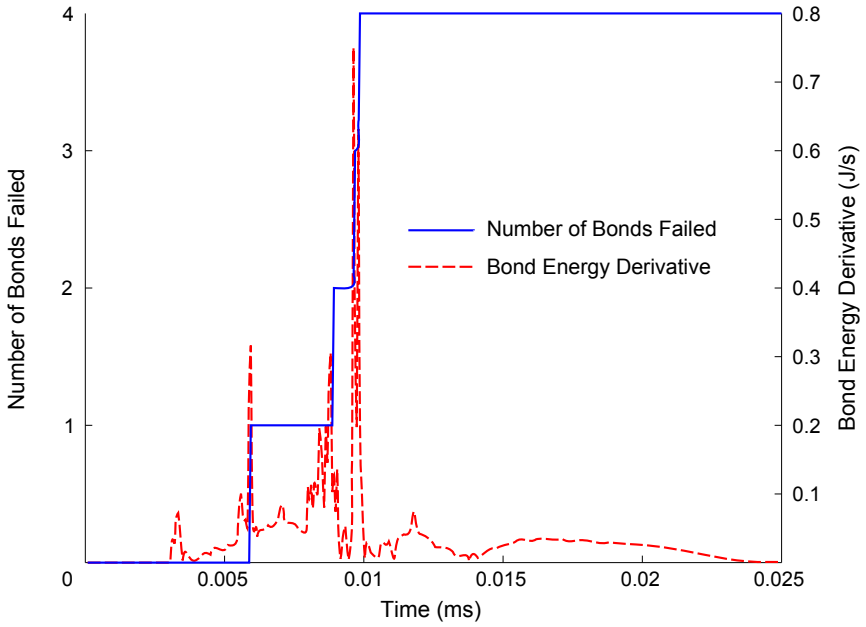

Figure 5.48: *Plots of the number of bonds failed and the derivative of bond energy (Js^{-1}) against time (ms) for an impact test at 10.1 ms^{-1}*

5.5.3 Assessment of Applicability

The discrete element model was originally developed for quasi-static compression of agglomerates. Despite this, it generally captured the failure of agglomerates during dynamic loading quite well. For the drop tests at 1.9 ms^{-1}, none of the agglomerates tested experimentally failed, while none of the parallel bonds (and hence none of the agglomerates) failed during the analogous simulations. When coefficients of restitution were compared for the drop tests, those obtained from the simulation data were considerably lower than the experimental results (means of 0.0954 and 0.3258, respectively) using a damping coefficient of 0.3. Most of the incident kinetic energy of the agglomerates was dissipated by damping; thus, reducing the damping coefficient caused the mean coefficient of restitution to increase. There was an optimum damping coefficient

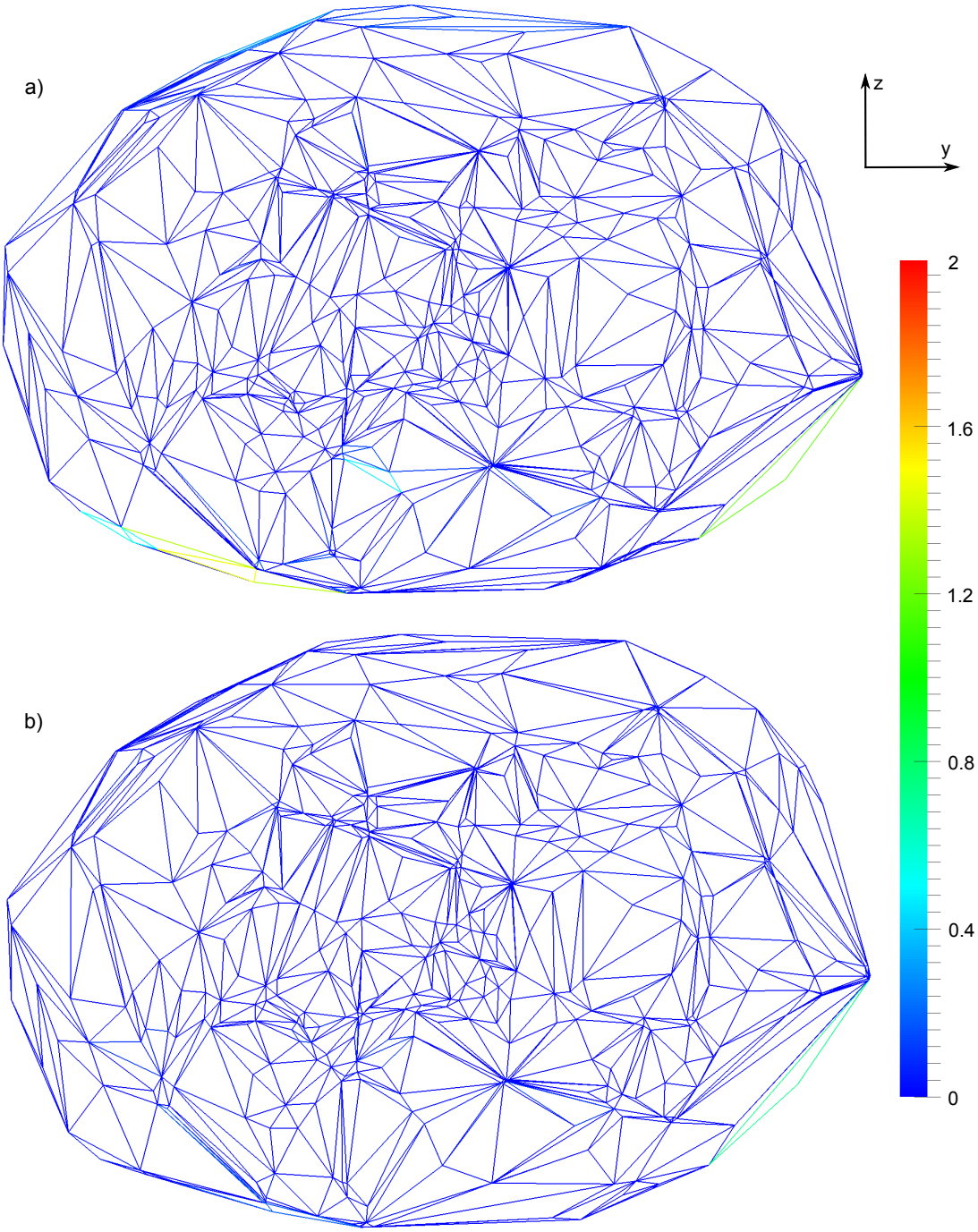

Figure 5.49: *Comparison of the fabric changes that occurred during the impact test of a representative agglomerate at 10.1 ms^{-1} at times of a) 0.014 ms and b) 0.025 ms, in which the colour bar denotes volumetric strain*

(approximately 0.1) at which the experimental and simulated coefficients of restitution were equivalent. This demonstrates that it is necessary to supplement the experimental quasi-static data with some dynamic results to ascertain the most appropriate value for the damping coefficient. Local damping in PFC is not a physically-measurable parameter so it must be calibrated with experimental data. However, the robustness of values thus obtained must be considered: while the damping parameter should be

appropriate for simulations which replicate the experimental conditions, there is no guarantee that it would be suitable for other boundary conditions.

For impact tests at 10.1 $\mathrm{m\,s^{-1}}$, 72% of the physical agglomerates were seen to fail upon analysis of high-speed camera footage, while 85% of the simulated agglomerates were adjudged to have failed when subjected to similar loading conditions. This correspondence was quite good, and it is possible that it might have improved if more data had been available, both for the experimental trials and simulations. The greatest difference was in the mode of failure: most of the simulated agglomerates failed by local disintegration and none shattered, whereas 44% of the physical agglomerates shattered upon impact. Overall the model gave a reasonable description of the experimental results for dynamic loading, despite being developed for quasi-static loading and therefore being far outside its range of applicability.

5.6 Conclusions of Chapter 5

In this chapter, a discrete element model was developed for quasi-static, uniaxial compression of individual infant formula agglomerates and calibrated using the experimental data reported for infant formula B in Chapter 3. It was necessary for the simulated agglomerates to capture the large variability apparent in the natural agglomerates which made the calibration process difficult. The final calibrated parameters included ball and parallel bond stiffnesses of 4×10^7 $\mathrm{N\,m^{-1}}$ and 2.4×10^{15} $\mathrm{N\,m^{-3}}$ respectively and parallel bond strengths of 1×10^9 $\mathrm{N\,m^{-2}}$. The mean force at failure, strain at failure and agglomerate stiffness were 0.075 N, 19.27% and 6996 $\mathrm{N\,m^{-1}}$, respectively, while the corresponding means obtained by experiment for the physical agglomerates of infant formula B were 0.071 N, 14.41% and 4648 $\mathrm{N\,m^{-1}}$. When lognormal distributions were fitted to the experimental and DEM results and their probability density functions were compared, the results for force were very close. The DEM results were skewed towards larger strains at failure and smaller stiffnesses compared to the experimental results, although still gave a good representation of the experimental data.

It was shown that the force at failure and agglomerate stiffness had a strong positive correlation (Spearman R > 0.75), which was also present in the experimental data for infant formula B. Furthermore, when Weibull statistics were applied, the Weibull moduli for the simulation results (1.4946) and the experimental data (1.4939) were almost identical. An analysis of the key energy terms during the simulations shows that the trends in the bond energy and the normal force exerted on the platens were very similar, and bond breakage events coincided with large energy dissipation rates.

This discrete element model was also applied to dynamic loading tests conducted

at two velocities: 1.9 ms^{-1} and 10.1 ms^{-1}. Results for the lower velocity case were generally good, although coefficients of restitution were lower than those obtained experimentally using a damping coefficient of 0.3. Most of the incident kinetic energy of the agglomerate was dissipated by damping; hence, the mean coefficient of restitution of the simulated agglomerates was shown to increase if a lower value was selected for the local damping coefficient. This coefficient could be obtained only by calibration, which requires experimental data for dynamic loading. For the higher velocity case, 85% of the simulated agglomerates were deemed to have failed, despite low percentages of bonds failing (mean of 0.501%). 72% of the physical agglomerates failed: a close correspondence. The main difference was in the mode of failure: none of the simulated agglomerates shattered while 44% of the physical agglomerates shattered upon impact. Even though this calibrated DEM was not developed for dynamic loading applications, the model still gave adequate results for such applications.

6

Probabilistic Modelling of Pneumatic Conveying

The DEM developed in Chapter 5 for quasi-static loading of an individual agglomerate gave extremely detailed information about the stresses generated and the evolution of the microstructure of an agglomerate during mechanical loading. The computational requirements were quite significant, even though only single agglomerates were simulated. Typically, pneumatic conveying of powders involves the transport of very large numbers of particles concurrently. For example, if particles are assumed to be perfect, monosized spheres of diameter 1 mm, one plug of length 300 mm and diameter 50 mm would contain more than 500,000 particles, given a packing efficiency of 50%: sufficiently many particles to make DEM simulations difficult, even if spheres are used to represent the particles.

Rather than using DEM, a macro-scale probabilistic model of dilute phase conveying was developed in this chapter to provide data for the distribution in maximum impact forces for collisions of particles and to stochastically quantify the percentage of particles which break due to this loading. The model pneumatic conveying system consisted of a long, straight horizontal pipe section terminated by one 90° bend. Particles in a conveying system break as a result of collisions, either with each other or with the inner walls of the conveyor. The former condition requires particles to be transported at different velocities; otherwise, particles would move on parallel paths at identical speeds and collisions would not be possible. There are a number of reasons why particles may be transported at different velocities at any specific cross-section of the pipeline, including the following:

1. Larger, heavier particles require longer times and distances than finer particles to reach any attainable velocity.

2. The existence of a velocity profile causes those particles which are near the cen-

treline of the pipe to have preferentially higher velocities than those close to the pipe wall.

3. There are random temporal components in both the air and particle velocities.
4. Particles follow different curvilinear trajectories around bends depending on their masses.

These inter-particle collisions are likely to make a negligible contribution to particle breakage: the relative velocities between particles are small compared to their absolute velocities and thus, the normal impact velocities at the pipe bend are considerably greater than the relative velocities between agglomerates. Since fatigue of particles is not considered (Section 6.1.1), any particle that would have broken due to collisions with other particles would certainly have broken at the subsequent bend. It would also be very difficult to incorporate inter-particle collisions caused by differences between curvilinear trajectories of particles around bends into such a probabilistic model. Therefore, inter-particle collisions are not considered explicitly as a cause of particle breakage in the model, although their effect on the impact velocities of the particles with the pipe bend is included.

The research detailed in this chapter had two primary objectives. The first was to present a general approach to the prediction of particle breakage in a pneumatic conveying system, focusing on the integration of particle motion and the corresponding structural response. The second objective was to demonstrate a novel probabilistic approach for representing the many uncertainties and complexities in real systems. It should be noted that the results obtained using this model could not be validated experimentally.

6.1 Model Development

One of the main advantages of the model presented in this chapter is that it is composed of a number of sub-models, any of which may be substituted by a reasonable alternative without having to develop an entirely new model. These sub-models are discussed individually in Sections 6.1.2–6.1.12. Much of the detailed mathematical development is confined to Appendix G, and references are made to this appendix throughout Section 6.1.

6.1.1 Assumptions

The model outlined in this chapter was predicated on a number of assumptions. For convenience, the main assumptions made are listed below, and are referred to through-

out the remainder of Section 6.1. Some of these assumptions are verified mathematically in Section 6.3.5.

i The particles are rigid, monosized spheres: assuming a monodispersed flow is commonplace in such models (Eskin et al., 2004).

ii The particle diameter is small compared to the pipe diameter.

iii Particles are treated as point masses from a kinetic perspective and no rotational effects are included. Magnus and Saffman forces are neglected since both are negligible when the particles being conveyed are relatively large, typically > 100 µm (Eskin et al., 2007). The Basset force is also not considered as it is negligible compared to the drag force for particles which are much denser than the conveying fluid (Elghobashi and Truesdell, 1992).

iv The mass flow ratio is low.

v The particles are uniformly distributed over the pipe cross-section, a common assumption (e.g., Eskin et al., 2007).

vi The tendency of fine particles which are suspended in the air flow to be swept around the bend by the motion of the air without contacting the bend wall is ignored.

vii The air velocity has a high magnitude, ensuring that particles remain in suspension, i.e., homogeneous flow rather than degeneration to dune flow (Wen and Simons, 1959).

viii Each particle collides with the bend exactly once (Chapelle et al., 2004⋆).

ix The effect of fatigue loading on particles is not considered (Chapelle et al., 2004⋆).

x The fluid velocity is invariant in the axial direction in the straight length of pipeline.

xi The radial and tangential components of air velocity are not modelled explicitly.

xii Entry length effects are ignored for both the air and particulate fractions conveyed.

xiii Inter-particle collisions are not considered explicitly as a mechanism for particle breakage.

xiv All collisions are elastic; the coefficient of restitution is 1 (or very close to 1). This assumption was also made by Louge et al. (1991).

xv Only the normal component of wall impact velocity contributes to the breakage force. Frye and Peukert (2002) and Kalman (2000) both state that the normal component of stress is the primary contributor to particle damage.

xvi The particles are moving in straight lines at the bend; the possibility of curvilinear motion due to the changed fluid flow pattern in this region is not examined.

xvii The bend geometry is defined by only a single, rather than a double, curvature.

xviii Fluctuations in the particle velocity due to fluid turbulence are not considered.

6.1.2 Statistics of Fluid Velocity

Several assumptions were made regarding the air velocity in the conveying system, including vii, x and xi. For the system under consideration, the Reynolds number of the air flow is large and the flow is considered to be turbulent. Such flows may be characterised by the empirical $^1/_7{}^{\text{th}}$ power law velocity profile, which relates the fluid velocity, u_f, to the maximum velocity along the centreline, u_m, at a radial distance of r from the centreline of a pipe of internal radius R. This velocity profile is given as Eq. 6.1 (Fox et al., 2010, p.324), while Figure 6.1 schematically illustrates the velocity profile across a pipeline.

$$u_f = u_m \left(1 - \frac{r}{R}\right)^{\frac{1}{n}} \tag{6.1}$$

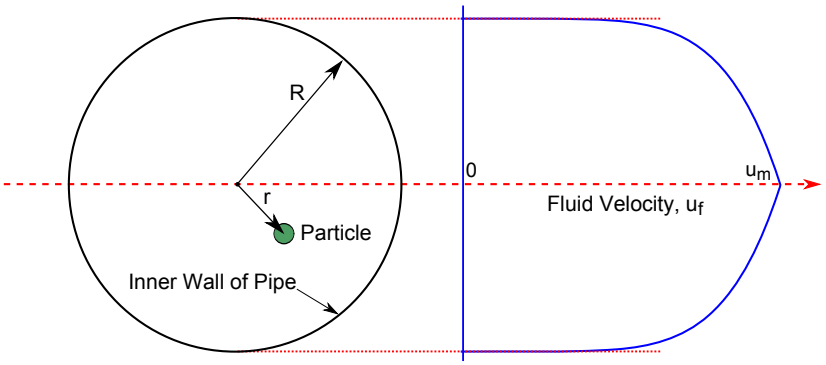

Figure 6.1: *Illustration showing the turbulent velocity profile in a pipeline*

It should be noted that the effect of the particles on the air flow was neglected, which can be justified by assumption iv, i.e., a low mass flow ratio. As the mass flow ratio decreases towards zero, the effect of conveyed solids on the air flow is progressively reduced. The parameter n is a function of Reynolds number which can be approximated by Eq. 6.2. Note that the velocity profile in Figure 6.1 used $n = 6$, corresponding to a Reynolds number of 15,000–25,000 (exactly 19,669).

$$n = 1.77 \log_{10} Re - 1.6 \tag{6.2}$$

The probability density function (PDF) of fluid velocity, $P(u_f)$, was found as Eq. 6.3 (derivation in Section G.1):

$$P(u_f) = \frac{2n({u_f}^n - {u_m}^n)}{{u_f}^{1-n}\,{u_m}^{2n}} \qquad 0 \leq u_f \leq u_m \tag{6.3}$$

The zeroth moment of this expression for $P(u_f)$ is equal to unity, i.e., $\int_{u_m}^{0} P(u_f)\,du_f = 1$, thus showing that Eq. 6.3 satisfies the basic requirement of a valid PDF. The first moment of $P(u_f)$ about zero gives the mean fluid velocity, μ_{uf}, while the second moment of $P(u_f)$ about its mean value yields the variance in fluid velocity, σ^2_{uf}. Expressions for both of these quantities are given as Eqs. 6.4 and 6.5 respectively, while derivations are provided in Sections G.2 and G.3.

$$\mu_{uf} = \int_0^{u_m} P(u_f)\,u_f\,du_f = \frac{2n^2}{(n+1)(2n+1)}u_m \tag{6.4}$$

$$\sigma^2_{uf} = \int_0^{u_m} P(u_f)(u_f-\mu_{uf})^2\,du_f = \frac{n^2(5n+1)}{(n+1)^2(n+2)(2n+1)^2}{u_m}^2 \tag{6.5}$$

Figure 6.2 shows the PDFs of fluid velocity for three different values of n. The PDFs deviate more from normality as n is increased, and there is a marked skew when n has a realistic value of 6. The mean and variance in fluid velocity are defined solely by the centreline velocity, u_m, and the power law exponent, n. For $n = 6$, the average fluid velocity is just under 80% of u_m and the standard deviation in fluid velocity is around 13% of u_m.

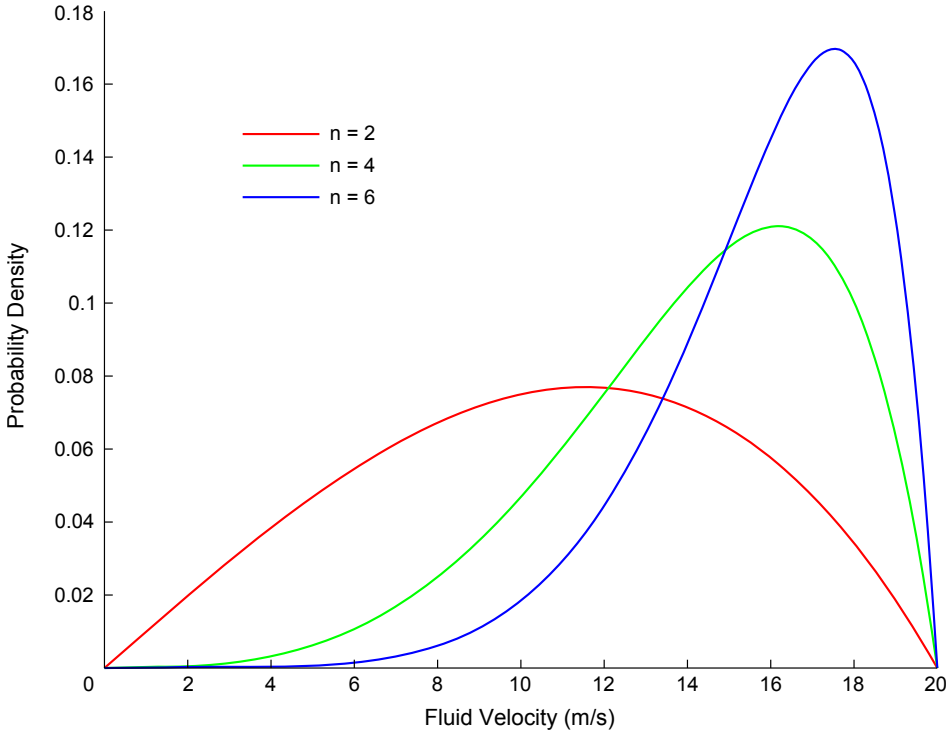

Figure 6.2: *Probability density functions of fluid velocity for $u_m = 20\ ms^{-1}$ and n values of 2, 4 and 6*

6.1.3 Statistics of Effective (Particle-Averaged) Fluid Velocity

The variation of fluid velocity with radial displacement from the centreline was quantified in Section 6.1.2. The steady-state velocity of a particle at any radial location within

the pipe is determined by the local velocity of the fluid at that point. If the dimensions of the particles being conveyed are infinitesimal compared to the pipe radius, the statistics of particle velocity would correspond exactly to those of fluid velocity. However, larger particles occupy a greater fraction of the pipe cross-section and thus experience a gradient in velocity acting on the cross-section of the particle normal to the axial fluid flow (as shown in Figure 6.1). As an example, consider an extremely large particle with a diameter slightly larger than the pipe radius in contact with the pipe wall. The fluid velocity at the point of contact with the wall is zero, while the point on the surface of the particle lying on the pipe centreline would be subjected to a fluid velocity of u_m. Therefore, the average fluid velocity acting on this particle would be some value between these two extremes. The effective fluid velocity acting on a particle, u_e, is the average spatial fluid velocity acting on the particle projected area (i.e., the cross-sectional area normal to the axial fluid velocity). The existence of a velocity distribution across the surface of a particle would cause rotation of the particle in reality. However, rotational effects are disregarded in this model (assumption ii). For a spherical particle of radius r_p with its centre a distance r from the centreline of the pipe, u_e is approximated by Eq. 6.7, which is derived in Section G.4:

$$u_e(r) = \int_{r-r_p}^{r+r_p} \frac{u_m \left(1-\frac{r}{R}\right)^{\frac{1}{n}} \cdot 2\pi r \, dr}{\pi \left[(r+r_p)^2-(r-r_p)^2\right]} \qquad 0 \le r \le R-r_p \tag{6.6}$$

$$= \frac{u_m}{2\left(1+\frac{1}{n}\right)\frac{r_p}{R}} \left[\left(1+\frac{r_p}{R}-\frac{r}{R}\right)^{\frac{n+1}{n}} - \left(1-\frac{r_p}{R}-\frac{r}{R}\right)^{\frac{n+1}{n}}\right] \tag{6.7}$$

The validity of Eq. 6.7 depends on assumption ii, i.e., that $\frac{r_p}{R}$ is small. A more precise equation for u_e was derived in Section G.4 which requires numerical solution (Eq. G.14). Figure 6.3 compares the results of Eqs. 6.7 and G.14 using typical values of the parameters: $\frac{r_p}{R} = 0.01$, $u_m = 20\ \mathrm{m\,s^{-1}}$ and $n = 6$.

Since both equations give identical results, u_e was defined by Eq. 6.7 for this model. It was shown in Section G.6 that Eq. 6.7 satisfies the required limiting condition that as particle radius tends towards zero, the effective fluid velocity becomes equal to the fluid velocity, i.e.:

$$\lim_{r_p \to 0} u_e = u_f \tag{6.8}$$

In theory, the PDF of u_e could be obtained in a similar manner to that of u_f, and this could be used to calculate the mean and variance of u_e. However, a closed-form analytical expression for $P(u_e)$ could not be obtained in terms of u_e, although an expression could be derived for $P(u_e)$ in terms of u_f as shown in Eq. 6.9 (Section G.5):

$$P(u_e) = \frac{4r_p({u_m}^n - {u_f}^n)R^{\frac{1}{n}-1}}{{u_m}^n \left[\left(R{u_f}^n - r_p{u_m}^n\right)^{\frac{1}{n}} - \left(R{u_f}^n + r_p{u_m}^n\right)^{\frac{1}{n}}\right]} \tag{6.9}$$

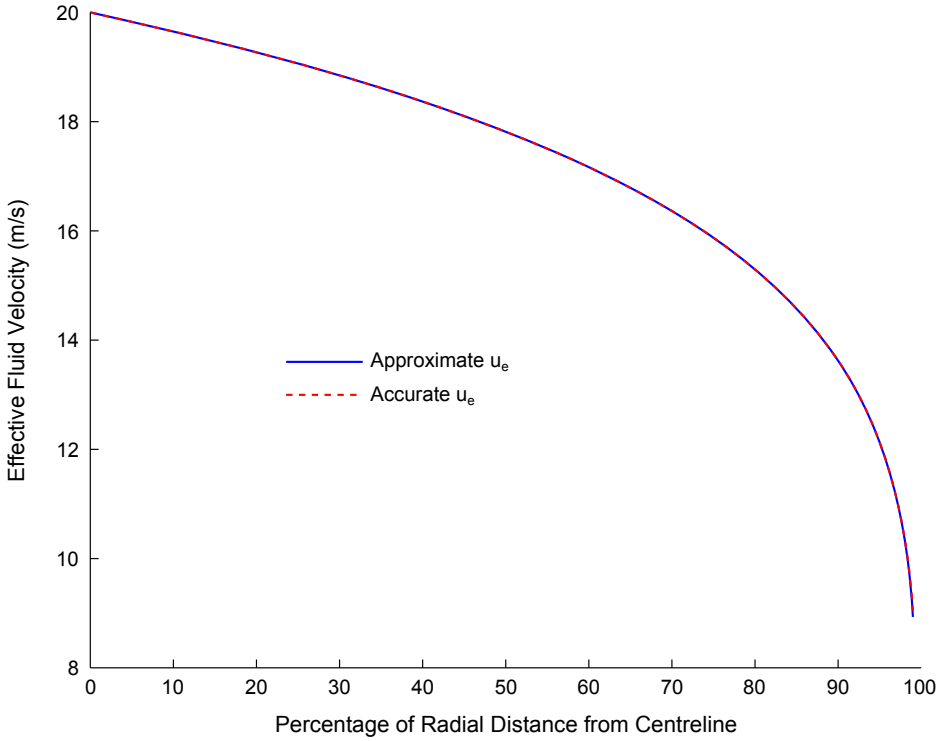

Figure 6.3: *Comparison of the approximation of u_e given by Eq. 6.7 with the more theoretically-precise expression for u_e given by Eq. G.14*

For physically-realistic ranges of n and $\frac{r_p}{R}$, $P(u_e) \approxeq P(u_f)$. Figure 6.4 shows that the correspondence between both functions is closest when n is large and $\frac{r_p}{R}$ is small. Hence, the mean and variance of u_e are taken to be the same as those of u_f for the remainder of Chapter 6.

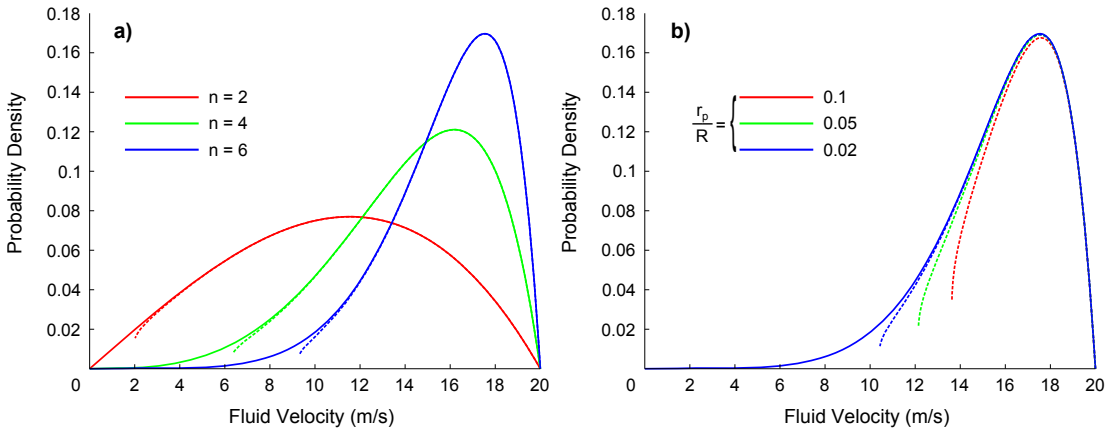

Figure 6.4: *Comparison of $P(u_f)$ [—] and $P(u_e)$ [- - -] for $u_m = 20\ ms^{-1}$: a) uses a constant $\frac{r_p}{R}$ of 0.01 and n values of 2, 4 and 6, while b) uses a constant n of 6 and $\frac{r_p}{R}$ values of 0.02, 0.05 and 0.1*

The main difference between the two PDFs is in the prediction of extreme values, particularly as $r \to R$ where $P(u_e)$ is not defined for $r > R - r_p$. Considering the fluid velocity, its maximum value of u_m is attained at the pipe centreline and its minimum value is zero at the wall. For effective fluid velocity, the corresponding statistics are

given by Eqs. 6.10 and 6.11:

$$\text{Minimum } u_e = \frac{2^{\frac{1}{n}} u_m}{\left(1+\frac{1}{n}\right)} \left(\frac{r_p}{R}\right)^{\frac{1}{n}} \tag{6.10}$$

$$\text{Maximum } u_e = \frac{u_m}{2\left(1+\frac{1}{n}\right)\frac{r_p}{R}} \left[\left(1+\frac{r_p}{R}\right)^{1+\frac{1}{n}} - \left(1-\frac{r_p}{R}\right)^{1+\frac{1}{n}}\right] \tag{6.11}$$

Note again that in the limit as $r_p \to 0$, both of these equations predict the same extreme values as for fluid velocity. The effective fluid velocity field has lower radial gradients than the corresponding fluid velocity field.

6.1.4 Particle Velocity

The motion of the fluid in the axial direction causes the particles to be transported accordingly in the same direction. The primary force acting on any particle in the horizontal, straight section of the conveying system is the drag force arising from its motion through the fluid. It should be noted that the acceleration of the particle from its initial velocity up to its asymptotic velocity (where particle velocity equals u_e) is neglected (assumption xii), which was one of the assumptions verified in Section 6.3.5.

The effective fluid velocity acting on any particle fluctuates over time for reasons explained in Section 6.1.5. If the magnitudes of these fluctuations are low (i.e., if the standard deviation of u_e is relatively small), the instantaneous relative velocity between the fluid and particle is also low. Thus, the particle Reynolds number, Re_p, is low according to Eq. 6.12, where u_p is the particle velocity and ν is the kinematic viscosity of air:

$$Re_p = \frac{2|u_p - u_e| r_p}{\nu} \tag{6.12}$$

In that case, the drag force for a spherical particle of radius r_p immersed in a fluid of density ρ would be described by Eq. 6.13, where c_D is the drag coefficient. Note that assumption iv (low mass flow ratio) is important to ensure the applicability of this equation, which was developed for single, non-interacting spheres.

$$F_D = -c_D \pi r_p^2 \frac{\rho}{2}(u_p - u_e) \tag{6.13}$$

The governing differential equation for particle motion in the axial direction would therefore be given by Eq. 6.14, where m is the mass of the particle and p is its inertial rate constant, i.e., $p = \frac{c_D \pi r_p^2 \rho}{2m}$.

$$\begin{aligned} F_D &= m\frac{du_p}{dt} \\ \frac{du_p}{dt} &= -p(u_p - u_e) \end{aligned} \tag{6.14}$$

Eq. 6.14 is valid only in the Stokes' law regime, in which $Re_p \lessapprox 2$. Simulations demonstrated that generally $Re_p \not< 2$. More generally, F_D is directly proportional to the square of the relative velocity between the particle and the fluid and the equations can be rewritten:

$$F_D = -c_D \pi r_p^2 \frac{\rho}{2}(u_p - u_e)|u_p - u_e| \tag{6.15}$$

$$\frac{du_p}{dt} = -p(u_p - u_e)|u_p - u_e| \tag{6.16}$$

p may be replaced in Eq. 6.16 by introducing the effective inertial rate constant of the particle, $p_e = p|u_p - u_e|$:

$$\frac{du_p}{dt} = -p_e(u_p - u_e) \tag{6.17}$$

p_e is related to p by Eq. 6.18:

$$p_e = p|u_p - u_e| = \frac{c_D \pi r_p^2 \rho}{2m}|u_p - u_e| \tag{6.18}$$

c_D is a function of the particle Reynolds number. One commonly-used expression which relates c_D and Re_p was provided by Clift and Gauvin (1970):

$$c_D = \frac{24}{Re_p}\left(1 + 0.15 Re_p^{0.687}\right) + \frac{0.42}{1 + 42500 Re_p^{-1.16}} \tag{6.19}$$

Eq. 6.19 is valid for all $Re_p < 10^5$. An approximation for c_D which is sometimes applied is Eq. 6.20:

$$c_D \approxeq \frac{10}{\sqrt{Re_p}} \tag{6.20}$$

Eqs. 6.19 and 6.20 compare well for particle Reynolds numbers between 1 and 500, as shown by Figure 6.5. Thus, Eq. 6.18 could be rewritten as Eq. 6.21:

$$\begin{aligned} p_e &= \frac{c_D \pi r_p^2 \rho}{2m}|u_p - u_e| \qquad (6.18)\\ &= \frac{10 \pi r_p^2 \rho}{2m\sqrt{Re_p}}|u_p - u_e| \\ &= \frac{5 \pi r_p^2 \rho \sqrt{\nu}}{m\sqrt{2|u_p - u_e| r_p}}|u_p - u_e| \\ p_e &= \frac{5 \pi r_p^{1.5} \rho}{m}\sqrt{\frac{\nu|u_p - u_e|}{2}} \qquad (6.21) \end{aligned}$$

6.1.5 Effective Fluid Velocity as a Random Process

The effective fluid velocity, u_e, was quantified in Section 6.1.3; this is the fluid velocity averaged over the projected area of the particle at its particular radial location in the pipe. u_e determines the particle velocity at that location. Up to this point in the

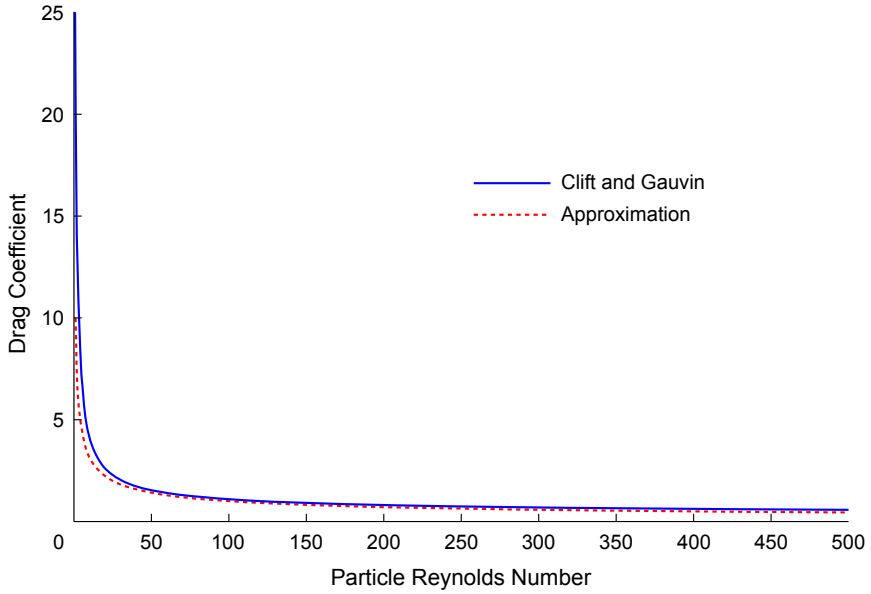

Figure 6.5: *Comparison of the drag coefficients predicted by Eqs. 6.19 and 6.20 for* $1 \leq Re_p \leq 500$

model development, it has been assumed that the particles move solely along straight, horizontal paths within the pipe, i.e., each particle moves in the axial direction at a fixed radial distance from the centreline. Thus, effective fluid velocity acting on the particle was a time-invariant random variable. This is quite unrealistic since all conveyed particles have some radial component of motion in reality. There are a number of physical effects which could cause this motion, including:

- The random temporal variation in fluid velocity as a result of turbulence
- Oblique inter-particle collisions
- The effect of gravity on the particles
- The real complexity of the interaction between the particle and the fluid

The average velocity of a particle in the radial direction is generally much lower than its average velocity in the axial direction (e.g., Zhang et al., 2007). The existence of this radial component of motion means that particles are subjected to time-varying effective fluid velocities (and hence drag forces) in the axial direction as they move through the radially-varying fluid velocity field. The actual motion of the population of particles in the radial direction is complex and random. However, ***on average*** the particles are taken to move in the radial direction with some characteristic velocity, u_ϕ. It is important to note that the actual radial motion of any particular particle is not captured by this approach; only the overall average effect, hence assumption xi (radial and tangential components of air velocity are not modelled explicitly). Figure 6.6 compares the hypothetical evolution of the fluid velocity and the effective fluid velocity as a particle moves randomly in the radial direction.

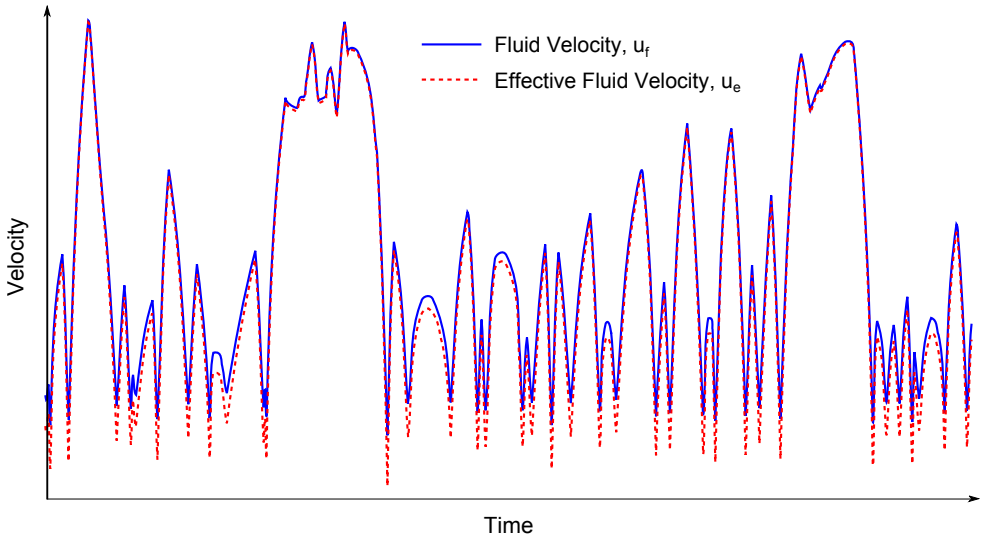

Figure 6.6: *Illustration showing u_f and u_e for the hypothetical radial motion of a particle in a cross-section of the pipe*

Thus, u_e can be described as a time-varying random process for any given particle having a random component of motion in the radial direction. As the origin of the random process results from the motion of the particle, the process must display autocorrelation, i.e., the magnitudes of u_e experienced by the particle at any two times measured in quick succession should be related. The level of autocorrelation is sensitive to the magnitude of u_ϕ; where u_ϕ is low, the level of autocorrelation should be high and *vice versa*. In the limit as u_ϕ tends towards zero, values of u_e are perfectly correlated as was the case for a time-invariant random variable. Conversely, u_e approximates a white-noise process as u_ϕ tends towards infinity. For simplicity and considerations of physical reasonableness, the autocorrelation function for the random process is defined as a first-order autoregressive process:

$$R_{ue}(\tau) = e^{-\phi\tau} \tag{6.22}$$

In this equation, ϕ is the autocorrelation parameter of the random process and τ is the separation time, i.e., the time interval between successive samples. ϕ determines the rate at which the correlation decays: as ϕ increases, the random process is characterised by more rapidly unpredictable fluctuations. The inverse of the autocorrelation parameter is known as the correlation (or decorrelation) time constant, τ_c. Eq. 6.22 implies that the degree of correlation between successive sampled values of u_e falls monotonically with increasing separation time between the samples. In cases where $\tau < \tau_c$, values of u_e are strongly correlated.

The magnitude of the autocorrelation parameter, ϕ, should be informed by the magnitude of the characteristic radial velocity, u_ϕ. The simplest functional relationship is given as Eq. 6.23, in which R_ϕ is a characteristic dimension that depends on how u_ϕ is

selected.

$$\phi = \frac{u_\phi}{R_\phi} \tag{6.23}$$

This function is clearly a suitable descriptor of ϕ at its limits:

- As the characteristic radial velocity of the particle, u_ϕ, tends towards zero, $\phi \to 0$ and $R_{ue}(\tau) \to 1$, i.e., a perfect correlation.
- As $u_\phi \to \infty$, $\phi \to \infty$ and $R_{ue}(\tau) \to 0$ irrespective of the separation time, τ, i.e., no correlation.

In summary, the effective fluid velocity, u_e was treated as a first-order, autoregressive process which had a mean of μ_{uf} given by Eq. 6.4, a variance of σ^2_{uf} given by Eq. 6.5, a PDF given by Eq. 6.9 and an autocorrelation function given by Eq. 6.22. To generate realisations of u_e, the effective fluid velocity at any time $t + \Delta t$ could be related to u_e at time t by Eq. 6.24:

$$u_e(t + \Delta t) = \mu_{ue} + \rho_{ue}[u_e(t) - \mu_{ue}] + z_t \tag{6.24}$$

The ρ_{ue} term in this recursion scheme is a function of the time increment, Δt, and the correlation time, τ_c:

$$\rho_{ue} = e^{-\frac{\Delta t}{\tau_c}} = e^{-\phi \Delta t} \tag{6.25}$$

z_t is a random term with a mean of zero and a variance of $(1 - \rho^2_{ue})\sigma^2_{ue}$.

6.1.6 Statistics of Particle Velocity

For a conveying system where the particles have no radial motion, the statistics of particle axial velocity are those of effective fluid velocity (or for sufficiently small particles those of fluid velocity itself). u_e is a random variable (Eq. 6.24); therefore, the particle velocity is likewise a random variable. In practice, the randomness in the axial velocity of any particle arises because of its radial component of motion within the pipe: particles are subjected to a high effective fluid velocity close to the centreline, which reduces towards zero as the particle approaches the pipe wall. It is equivalent to fix the radial positions of the particles, so that they move only in horizontal, mutually-parallel lines, and then subject each particle to a time-varying effective fluid velocity. Analytical estimates for the mean and variance in the particle (axial) velocity as a result of this approach could be obtained only by an approximate analysis for which one additional assumption was required: u_e was treated as normally-distributed although its actual PDF (Eq. 6.9) was only approximately Gaussian.

Eq. 6.17 is a stochastic differential equation because u_e contains a time-varying random component (Eq. 6.24). A solution of a stochastic differential equation with a similar form was presented by Nicolaï et al. (2007), and their solution was adapted for this problem

to find the mean and variance in particle velocity. Note that an outline derivation of Eq^{s}. 6.26 and 6.27 is given in Section G.7. The asymptotic value of the mean particle velocity in the axial direction is equal to the mean effective fluid velocity:

$$\mu_{up} = \mu_{ue} \tag{6.26}$$

However, the variance of particle velocity also has a dependence on time:

$$\sigma^2_{up} = \frac{p_e}{p_e+\phi}\sigma^2_{ue} + \frac{p_e}{p_e-\phi}\sigma^2_{ue}e^{-2p_e t} - \frac{2p_e^2}{(p_e+\phi)(p_e-\phi)}\sigma^2_{ue}e^{-(p_e+\phi)t} \tag{6.27}$$

For long times, i.e., $t \gg \frac{1}{2p_e}$ and $t \gg \frac{1}{p_e+\phi}$, Eq. 6.27 reaches the steady-state value given by Eq. 6.28:

$$\sigma^2_{up} = \frac{1}{1+\frac{\phi}{p_e}}\sigma^2_{ue} \qquad t \gg \frac{1}{2p_e}; t \gg \frac{1}{p_e+\phi} \tag{6.28}$$

Eq^{s}. 6.26 and 6.28 imply that the particle velocity in the axial direction becomes a stationary random process after some time has elapsed. Eq. 6.28 shows that the magnitude of the dispersion in particle velocity is lower than the dispersion in effective fluid velocity, and the difference depends on the relative magnitudes of p_e and ϕ. Given a relatively large and heavy particle with a correspondingly low effective inertial rate constant and with a fluid velocity field characterised by high-frequency fluctuations (i.e., large ϕ), then σ^2_{up} would be much lower than σ^2_{ue} reflecting the fact that the particle is physically unable to follow the rapid disturbances. However, the variance in particle velocity would almost equal that of fluid velocity in the opposite situation for a small, light particle (large p_e) in a velocity field which varies gradually (small ϕ). Finally, it should be noted that Eq^{s}. 6.26 and 6.28 could be considered only as estimates of particle velocity statistics. Their suitability was assessed by numerical calculations presented in Section 6.3.1.

6.1.7 Autocorrelation Parameter of Effective Fluid Velocity

Several equations presented in Sections 6.1.5 and 6.1.6 contained the autocorrelation parameter, ϕ. It was necessary to identify a justifiable basis for determining the magnitude of ϕ which reflected the physical causes of random particle motion in the radial direction. This required determining suitable values for u_ϕ and R_ϕ to use in Eq. 6.23. Two different reasons for radial particle motion are the following:

1. Inter-particle collisions cause the trajectories of the conveyed particles to deviate from axial motion. This is applicable if the mass flow ratio is sufficiently high to ensure a high number of inter-particle collisions (notwithstanding assumption iv).

2. If the mass flow ratio is very low, inter-particle collisions are unlikely. The force of gravity may then be the main factor capable of supplying the radial component of motion to the particles. Note that gravity was not included in Eq. 6.16 as the particles are assumed to remain in suspension at all times (assumption vii) and lift forces, which are not explicitly modelled (assumption iii), would be active to partially balance the gravitational force. However, the gravitational force may be used to provide an estimate for ϕ.

Both are discussed individually below and were computed numerically in Section 6.2.2. It should be noted that these methods provided only estimates of ϕ; if detailed experiments show that the actual value of ϕ differs considerably from these approximations, the disparity would have little effect on the calculated results. Of course, there are other reasons why particles may move in the radial direction, including fluid turbulence, which are not considered below.

Inter-Particle Collision Mechanism

By making assumptions i and xiv (i.e., particles are rigid, monosized elastic spheres), it may also be assumed that collisions that occur cause an exchange of radial velocity between particles, and the particle velocity within any cross-sectional plane of the pipeline corresponds to a discrete white-noise process with no correlation between the velocities before and after any collision. The mean free path between collisions, λ, is approximated by Eq. 6.29, where n_{pv} is the number of particles per unit volume in the pipe (Present, 1958, p.32; Serway, 1996, p.605).

$$\lambda = \frac{1}{4\sqrt{2}\pi {r_p}^2 n_{pv}} \tag{6.29}$$

The smaller is the distance travelled by a particle between successive collisions, the lower is the change in the effective fluid velocity acting on it over the corresponding time. Of course, the change in u_e is also sensitive to the component of this distance in the radial direction and the local spatial gradient in u_e. Nonetheless, the magnitude of the mean free path, λ, compared to the pipe radius, R, can be used as a measure of the change in the magnitude of the effective fluid velocity acting on the particle. According to this approach, the characteristic radial distance, R_ϕ, is equal to the inter-collision mean free path, λ. Hence, the corresponding time for any particle to travel along its mean free path can act as a useful measure of correlation in the system; this time is termed t_ϕ. For any time less than t_ϕ, successive values of u_f or u_e are strongly correlated. Conversely, this correlation is low if times are greater than t_ϕ. t_ϕ is equivalent to the correlation time constant (τ_c) which was introduced in Section 6.1.5. The reciprocal of t_ϕ is the collision frequency, f_c, which is related to ϕ by Eq. 6.30. $\overline{u}$ is the average speed of a

particle (Serway, 1996, p.605).

$$\phi = f_c = 4\sqrt{2}\pi {r_p}^2 n_{pv} \overline{u} \tag{6.30}$$

One approach which may be applied to find an estimate of u_ϕ was to use the concept of granular temperature, which is discussed more thoroughly by Goldhirsch (2008). Granular temperature is similar to gas temperature, although particles are macroscopic entities rather than infinitesimal gas molecules. It is a measure of the dispersion in particle velocity and has units of $m^2 s^{-2}$. The granular temperature, Θ, can be related to the average collision velocity between particles, $\overline{u}_c$, by Eq. 6.31 (Gidaspow, 1994):

$$\overline{u}_c = \frac{3}{2}\sqrt{\pi\Theta} \tag{6.31}$$

The characteristic radial velocity, u_ϕ, is taken to equal $\overline{u}_c$ for the inter-particle collision mechanism.

Gravitational Mechanism

For the gravitational mechanism, it is assumed that a particle which is initially at rest falls vertically under gravity to collide with the inner wall of the pipe, and would then rebound without a loss of energy (elastic spheres). An estimate for R_ϕ could be obtained as the average height through which a particle would fall if placed randomly in the pipe cross-section. u_ϕ is taken to be the average vertical velocity of a particle falling through this distance.

The vertical velocity of a particle falling from rest under gravity and retarded by fluid drag (u_v) is given by Eq. 6.32, where u_t is the terminal velocity of the particle.

$$u_v = u_t \tanh\left(\frac{g\,t}{u_t}\right) \tag{6.32}$$

u_t may be calculated by equating the drag and buoyancy forces (acting upwards) to the weight of the particle (of density ρ_p) to give Eq. 6.33. Note that u_e in Eq. 6.15 for calculating the drag force is zero for a static fluid.

$$u_t = \sqrt{\frac{8 r_p\, g(\rho_p - \rho)}{3 c_D \rho}} \tag{6.33}$$

c_D may be calculated using Eq. 6.19, for which Re_p is a function of u_t, thus requiring Eq. 6.33 to be solved iteratively. Assuming that particles are uniformly distributed over the cross-section of the pipe (assumption v), the average height that a particle falls through is given by Eq. 6.34:

$$\mu_h = \frac{8(R - r_p)}{3\pi} \tag{6.34}$$

μ_h is taken as R_ϕ. As mentioned above, the corresponding characteristic radial velocity, u_ϕ, is the average vertical velocity of a particle falling through this distance. This was derived as Eq. 6.35 in Section G.8.

$$u_\phi = \frac{2}{\pi(R-r_p)^2}\int_{x=0}^{x=R-r_p}\int_{H=0}^{H=2\sqrt{(R-r_p)^2-x^2}} \frac{gH}{u_t \operatorname{arccosh}\left(e^{\frac{gH}{u_t{}^2}}\right)}\,dH\,dx \tag{6.35}$$

6.1.8 Inter-Particle Collision Velocity Statistics

Although the effect of collisions were not considered as a mechanism for particle breakage (assumption xiii), it was important to estimate the mean inter-particle collision velocity in order to justify this assumption. A theoretical estimate for the mean inter-particle collision velocity can be obtained only if the distribution in particle velocity is known. It is also necessary to have data regarding the homogeneity and isotropy of the velocity field. However, estimates of the relative magnitude of the mean collision velocity can still be calculated in the absence of such information. One possibility is to consider particle velocity to be normally distributed and the relative velocity for a single pair-wise collision to be described by the absolute magnitude of this distribution. In this case, the mean value for collision velocity is given by Eq. 6.36:

$$\mu_{uc} = \frac{2}{\sqrt{\pi}}\sigma_{up} = 1.128\sigma_{up} \tag{6.36}$$

Alternatively, the mean collision velocity can be obtained by considering the granular temperature of the mixture, in which case the result is given by Eq. 6.37:

$$\mu_{uc} = \frac{\sqrt{3\pi}}{2}\sigma_{up} = 1.535\sigma_{up} \tag{6.37}$$

Although Eq[s]. 6.36 and 6.37 were derived from different theoretical bases, both indicate that the average inter-particle collision velocity is of the same order of magnitude as the standard deviation in particle velocity.

6.1.9 Pipe Bend Collision Velocity Statistics

At the end of the straight section of pipe, the particles collide with the inner wall of the single 90° bend in the system. A number of simplifying assumptions are made in the development of this sub-model, specifically assumptions vi, viii and xvi, i.e., all particles travel in straight lines at the bend with no curvilinear motion caused by the changed fluid flow and collide once with the bend wall. Since the radial component of air velocity is disregarded, its effect on the impact velocity of the particle was also not considered. The assumption that particles travel in straight lines in the bend requires a minimum particle size to ensure validity. Furthermore, the pipe wall at the bend has

a double curvature in reality, i.e., is curved in two orthogonal directions. Therefore, the impact angle for any real particle collision depends on its vertical and horizontal position in the pipe cross-section at the moment of impact. This makes any probabilistic analysis of impact velocity statistics very cumbersome. Assumption xvii was made which resulted in a considerable simplification: the impact angle depends solely on the vertical location of a particle in the pipe at the point of impact†. The normal impact velocity at the bend, u_n, is given by Eq. 6.38, in which u_p is the axial velocity of the particle at impact and θ is the impact angle.

$$u_n = u_p \sin\theta \tag{6.38}$$

Distributions exist in both the particle velocity, u_p, and the impact angle, θ. Both can be considered to be represented by random variables (since u_p is being examined at a particular moment in time). This makes Eq. 6.38 deceptively complicated: it is non-linear due to the presence of a product and a sine function. However, the mean and variance of u_n could be estimated by the method of statistical differentials, having knowledge of the mean and variance of both input random variables. The mean normal impact velocity is given by Eq. 6.39:

$$\mu_{un} \approxeq \mu_{up} \sin\mu_\theta \tag{6.39}$$

In contrast to inter-particle collisions where the mean collision velocity was proportional to the standard deviation in particle velocity (Section 6.1.8), the mean normal collision velocity between the particles and wall of the pipe bend is proportional to the mean particle velocity, μ_{up}. As the mean particle velocity is typically an order of magnitude greater than the standard deviation in particle velocity, it is clear that collisions with the bend wall are the dominant cause of particle breakage. The variance of normal impact velocity is given by Eq. 6.40, in which the partial derivatives are evaluated at the mean values of the input variables and $\rho_{u_p,\theta}$ is the cross-correlation coefficient of particle velocity and impact angle.

$$\sigma^2_{un} \approxeq \left(\frac{\partial u_n}{\partial u_p}\right)^2_n \sigma^2_{up} + 2\rho_{u_p,\theta}\frac{\partial u_n}{\partial u_p}\frac{\partial u_n}{\partial \theta}\sigma_{up}\sigma_\theta + \left(\frac{\partial u_n}{\partial \theta}\right)^2_n \sigma^2_\theta \tag{6.40}$$

It is necessary to take into consideration the dependence of particle velocity, u_p, and impact angle, θ. If the particles have no radial motion, then the velocity of any particle is determined by its radial distance from the pipe centreline. The impact angle is also sensitive to radial location, which means that u_p and θ are dependent random variables. However, the degree of dependence between these variables depends on the level of autocorrelation in the effective fluid velocity, u_e, which was quantified by ϕ

†The terminal bend was curved upwards out of the plane of the horizontal pipe section, as shown on Figure 6.7 (p.166).

(Eq. 6.23). If u_ϕ is low, the particles move in almost straight lines (with a large degree of autocorrelation in particle velocity) and there is a significant dependence between u_p and θ. As u_ϕ increases, the particle velocity becomes more random with respect to time and the connection between particle velocity and impact angle becomes weaker (increased ϕ and decreased R_{ue}). If it is assumed that u_ϕ is sufficiently high to ensure a negligible correlation between u_p and θ, $\rho_{u_p,\theta} \approxeq 0$ and hence the variance in impact velocity is given by Eq. 6.41:

$$\sigma_{un}^2 \approxeq \sin^2 \mu_\theta \cdot \sigma_{up}^2 + \mu_{up}^2 \cos^2 \mu_\theta \cdot \sigma_\theta^2 \tag{6.41}$$

Eq^{s}. 6.39 and 6.41 allow estimates of the mean and variance of normal impact velocity to be calculated given the corresponding statistics for particle velocity and impact angle. Expressions for the mean and variance of particle velocity are available (Eq^{s}. 6.26 and 6.28), while expressions for the corresponding statistics for the impact angle are developed in Section 6.1.10.

6.1.10 Impact Angle Statistics

The 90° bend at the end of the modelled conveying system is defined by the mean bend radius, R_b. The geometry of the bend is shown in Figure 6.7. The impact angle, θ, is related to the vertical displacement from the centre of the cross-section, y, by Eq. 6.42.

$$\theta(y) = \arccos\left[\frac{1 - \frac{y}{R_b}}{1 + \frac{R - r_p}{R_b}}\right] \tag{6.42}$$

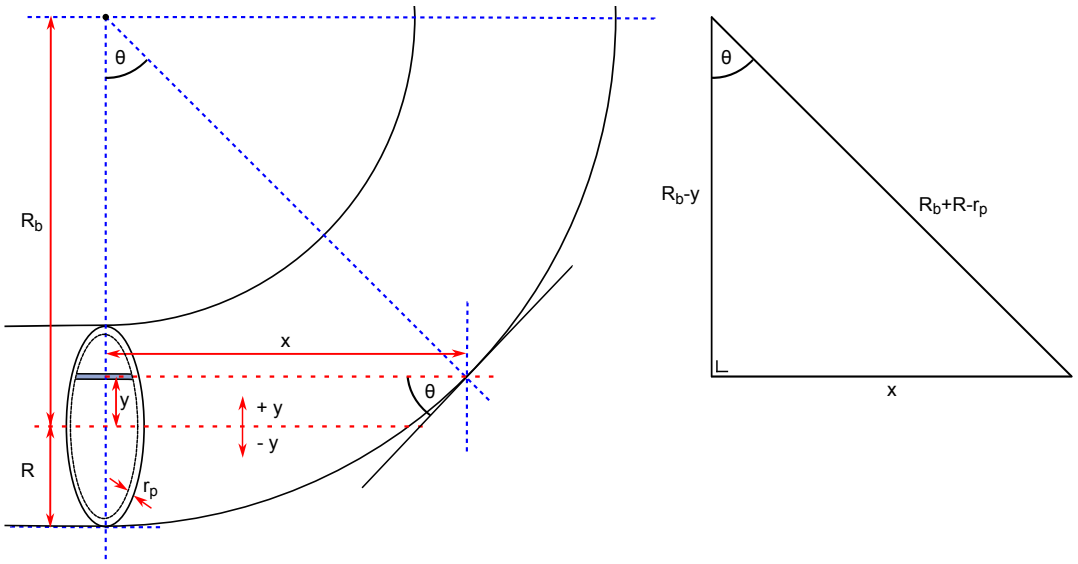

Figure 6.7: *Geometry used to derive the trigonometric relationship between θ and y given as Eq. 6.42*

As $y \rightarrow -(R-r_p)$, $\theta \rightarrow 0$ while the maximum impact angle, θ_{max}, is attained at the top of the pipe, i.e., where $y = R - r_p$. The impact angle corresponding to motion along the pipe centreline (where $y = 0$) is designated as the centreline impact angle, θ_c. The magnitudes of θ_c and θ_{max} are given by Eqs. 6.43 and 6.44, respectively:

$$\theta_c = \arccos\left[\frac{1}{1+\frac{R-r_p}{R_b}}\right] \tag{6.43}$$

$$\theta_{max} = \arccos\left[\frac{1-\frac{R-r_p}{R_b}}{1+\frac{R-r_p}{R_b}}\right] \tag{6.44}$$

The probability density function of impact angle, $P(\theta)$, was found as Eq. 6.45 (the derivation is confined to Section G.9):

$$P(\theta) = \frac{2\sin\theta}{\pi(R-r_p)^2}\sqrt{\Big(R-r_p-R_b+(R_b+R-r_p)\cos\theta\Big)(1-\cos\theta)}(R_b+R-r_p)^{\frac{3}{2}} \quad 0 \leq \theta \leq \theta_{max} \tag{6.45}$$

Figure 6.8 illustrates the nature of this PDF for a range of $\frac{R_b}{R}$ values.

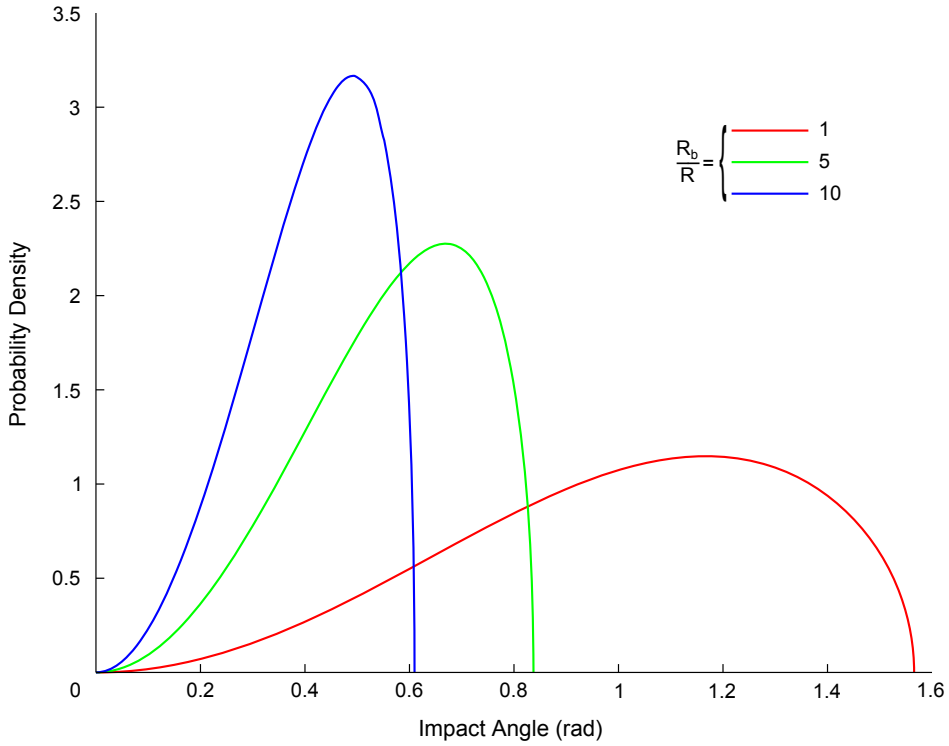

Figure 6.8: *Probability density functions of impact angle for a constant $\frac{r_p}{R}$ of 0.01 and $\frac{R_b}{R}$ values of 1, 5 and 10*

It is not possible to obtain analytical expressions for the mean and variance of impact angle. However, it can be shown numerically that the mean impact angle, μ_θ, is fractionally less than the centreline impact angle, θ_c, and the standard deviation of impact

angle, σ_θ, is 0.29 times this mean, i.e.:

$$\mu_\theta = 0.965\theta_c \tag{6.46}$$

$$\sigma_\theta = 0.29\mu_\theta \tag{6.47}$$

These results are almost independent of $\frac{R_b}{R}$. Figure 6.9 compares the mean impact angle obtained using Eq. 6.46 with the values obtained by numerically integrating $P(\theta)\cdot\theta$ between the limits 0 and θ_{max} using Mathematica (v.8, Wolfram Research, Inc., Champaign, IL, USA). It is clear that the agreement between both plots is almost perfect across a wide range of $\frac{R_b}{R}$ values.

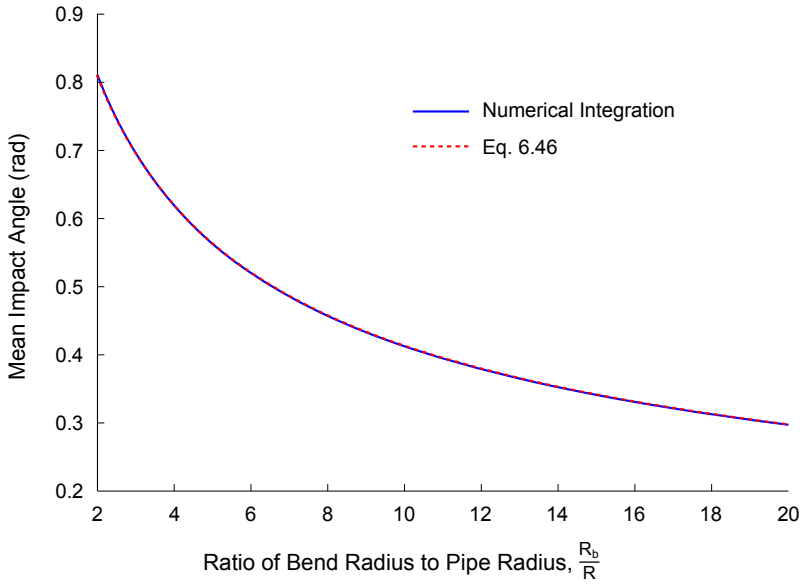

Figure 6.9: *Variation of the mean impact angle (rad) obtained both by numerical integration and using Eq. 6.46, with the ratio of bend radius to pipe radius, $\frac{R_b}{R}$*

A similar comparison was made for the standard deviations in Figure 6.10, where the variance was obtained by numerically integrating $P(\theta)\cdot(\theta-\mu_\theta)^2$, taking μ_θ from Eq. 6.46. The correspondence is not as close as in Figure 6.9, but the maximum error remains small: 4.4% when $\frac{R_b}{R}$ is 2. Since bend radii are generally much greater than the pipe radius in pneumatic conveying systems, the error for a realistic $\frac{R_b}{R}$ ratio would be < 1%.

6.1.11 Particle Impact Force Statistics

A structural model of the particle is necessary to relate the impact velocity to the corresponding impact force. There are many continuous contact dynamic models in literature which relate force and deformation for particle impacts; these are comprehensively surveyed by Gilardi and Sharf (2002). Such models often insert some combination of conceptual springs and dashpots at the contact points. The springs provide the required

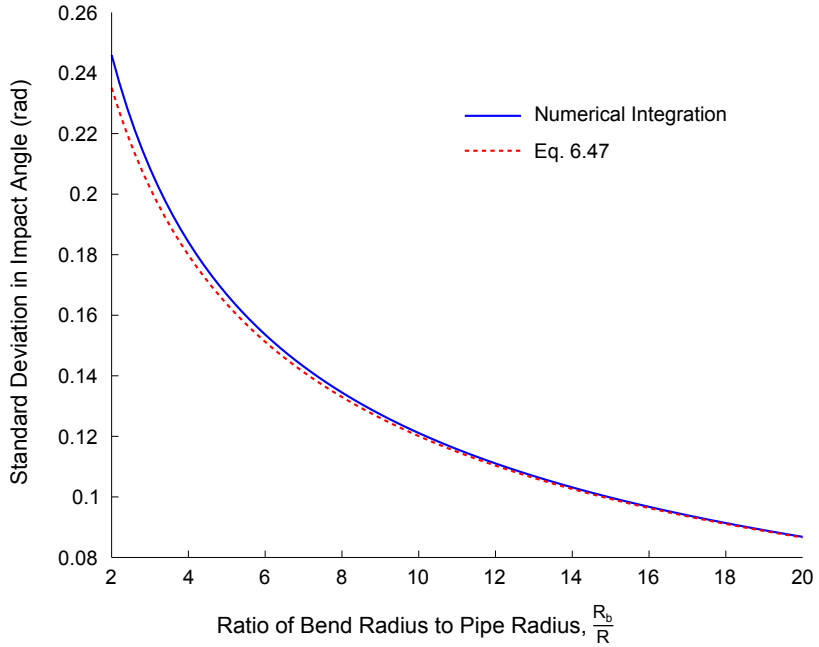

Figure 6.10: *Variation of the standard deviation in impact angle (rad) obtained both by numerical integration and using Eq. 6.47, with the ratio of bend radius to pipe radius,* $\frac{R_b}{R}$

elastic behaviour while the dashpots dissipate energy. The Kelvin-Voigt model was selected for this work. Marhefka and Orin (1996) highlight some of the deficiencies of this model, including discontinuous contact forces at the beginning of the impact. However, it has the major advantage of simplicity: a linear spring (with stiffness k) and a dashpot (with damping coefficient c) are inserted at each contact. The governing differential equation is Eq. 6.48:

$$mx''(t)+cx'(t)+kx(t)=0 \tag{6.48}$$

Each impact is modelled as an impulse, P, which is the product of particle mass, m, and normal impact velocity, u_n (from Eq. 6.38). The deflection of the particle during the impact is given by Eq. 6.49 for underdamped conditions, where ζ is the dimensionless damping factor, ω_d is the damped natural frequency and ω_n is the natural frequency (see Section G.10 for details).

$$x(t)=\frac{u_n}{\omega_d}e^{-\zeta\omega_n t}\sin(\omega_d t) \tag{6.49}$$

The corresponding force on the particle, $F(t)$, was obtained by multiplying the second derivative of Eq. 6.49 with respect to time by the particle mass:

$$F(t)=m\,u_n e^{-\zeta\omega_n t}\left[\left(\frac{\zeta^2\omega_n^2}{\omega_d}-\omega_d\right)\sin(\omega_d t)-2\zeta\omega_n\cos(\omega_d t)\right] \tag{6.50}$$

It was not possible to find an analytical expression which relates $F(t)$ and u_n, although the maximum contact force tends towards $\sqrt{km}\,u_n$ as $c\to 0$. k and c could be found by knowing the coefficient of restitution of the particles, ε, and the contact time, t_c, at any

impact velocity. Eq$^{\underline{s}}$. 6.51 and 6.52 are the relevant expressions which were derived in Section G.10.

$$c = -\frac{2m \ln \varepsilon}{t_c} \tag{6.51}$$

$$k = \frac{m}{t_c^2}(\ln^2 \varepsilon + \pi^2) \tag{6.52}$$

6.1.12 Particle Strength Statistics

A criterion is necessary to determine whether or not the force that any particle experiences in an impact with the pipe bend is sufficient to cause breakage. As the results of the particle crushing experiments in Chapter 3 demonstrated, there are major differences between the strengths of individual infant formula agglomerates. The Weibull PDF is often used to model the variability in particle strength; this approach was used previously in Section 5.3.3 on p.118. The key equation for Weibull analysis is Eq. 5.3:

$$\ln\left[\ln\left(\frac{1}{P_s(d)}\right)\right] = m \ln\left(\frac{\sigma}{\sigma_o}\right) \tag{5.3}$$

Thus, two parameters are required: the Weibull modulus, m, and the characteristic stress at which 37% of agglomerates survive, σ_o. The methodology used to obtain these parameters is described in Section 6.2.3.

6.2 Materials and Methods

In order to be able to apply the model, many physical parameters needed to be specified, both for the infant formula and for the conveying system. These are discussed in Sections 6.2.1–6.2.3. while the computational methodology used to conduct the Monte Carlo simulations is outlined in Section 6.2.4.

6.2.1 Model Infant Formula Particles

Although the particles were assumed *a priori* to be spherical, their other physical properties for use in the model were informed by experimental data for the physical infant formula agglomerates. The volume mean diameter, or D[4,3], was found to be 312 µm for the infant formula used in Chapter 2; thus, 150 µm was used as r_p in this model. The bulk and particle densities of this formula were measured as 462 kg m^{-3} and 1107 kg m^{-3}, respectively. Since the model particles are solid spheres, their density would be expected

to lie between these two densities[†]. The packing density of the monosized spheres was assumed to be 60% (the upper limit of 74.05% for close-packing was mentioned in Section 4.1.4 on p.79). Therefore, the density of the model particles was approximated as 770 $\mathrm{kg\,m^{-3}}$ $\left(=\frac{462}{0.6}\right)$. Once the radius and density of the particles were known, the mass of each particle could be calculated: $m = 770(4/3)\pi(150\times10^{-6})^3 = 1.09\times10^{-8}$ kg.

Two other parameters were required for input into the Kelvin-Voigt model, in addition to the particle mass: k and c. These could be found using Eqs. 6.51 and 6.52, provided that ε and t_c were known. A range of drop tests were described in Chapter 3 using agglomerates of four infant formulae. These drop tests were restricted to agglomerates in the 710–850 µm size range: somewhat larger than the particle diameter of 300 µm used for this model. Nonetheless, the mean coefficient of restitution in Table 3.13 of 0.2883 was a reasonable estimate for ε. A value of 3 µs was obtained for t_c using the calibrated DEM which was developed in Chapter 5. The local damping coefficient was set at 0.1 for these DEM simulations using agglomerates which had diameters of approximately 300 µm and impact velocities of 1.9 $\mathrm{m\,s^{-1}}$. This mean contact time is much shorter than the high-speed camera is capable of measuring at an acceptable resolution. Thus, c, k, ζ, ω_d and ω_n were calculated and are given in Table 6.1. Note that the behaviour was underdamped ($\zeta < 1$), and so all of the equations in Sections 6.1.11 and G.10 are valid.

Table 6.1: *Quantities calculated for the Kelvin-Voigt model from m, ε and t_c*

	Equation	Value
c	6.51	9.026×10^{-3} $\mathrm{kg\,s^{-1}}$
k	6.52	13,808 $\mathrm{kg\,s^{-2}}$
ζ	G.30	0.3681
ω_d	G.32	1.047×10^{6} $\mathrm{s^{-1}}$
ω_n	G.29	1.126×10^{6} $\mathrm{s^{-1}}$

The data in Table 6.1 may be used to plot the relationship between the maximum impact force and the normal impact velocity, u_n. This plot is shown as Figure 6.11 and is linear, since Eq. 6.50 indicates that $F(t) \propto u_n$.

[†]When calculating the bulk density, the volume includes the voids between agglomerates. Therefore, the densities of the agglomerates, and of the spheres representing the agglomerates, must be higher than the bulk density as the packing efficiency of spheres is less than 100%. The particle density includes the solid fraction of the agglomerates only. The idealised spheres represent not only the solid fraction of the real agglomerates, but also the pores and hollows within the agglomerates that are accessible to nitrogen. Therefore, the density of the spheres must be less than the particle density of infant formula.

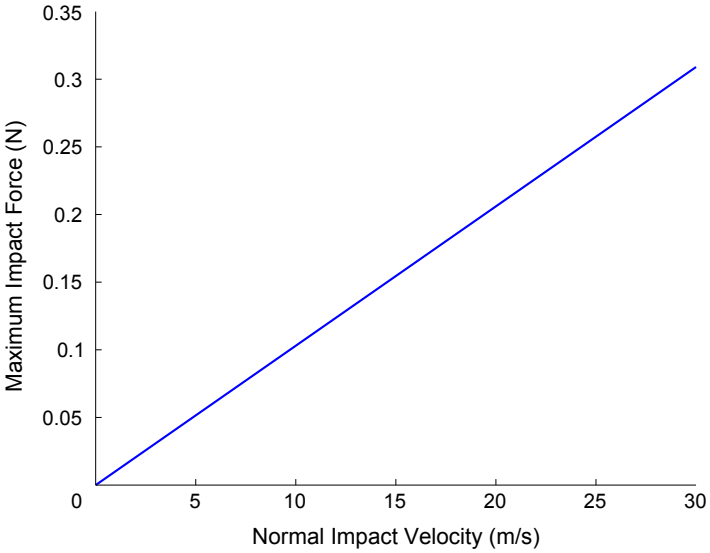

Figure 6.11: *Plot of the maximum impact force (N) against normal impact velocity ($m\,s^{-1}$) for the data given in Table 6.1, showing the linear relationship required by Eq. 6.50*

6.2.2 Conveying System Geometry and Flow Conditions

The basic geometry of the conveying system was already described in this chapter as a long, straight, horizontal pipe section with a 90° bend at its end. It was not important to maintain geometric similarity with the experimental system used in Chapter 2 as the outputs of the probabilistic model could not feasibly be compared to experimental results obtained previously; therefore, the modelled conveying system was selected for simplicity. A 20 m pipe length was used for calculating the model results. The pipe radius was chosen as 50 mm, as typical diameters of industrial pneumatic conveying systems used for the transport of infant formula are around 100 mm. The ratio $\frac{r_p}{R}$ was therefore fixed at 0.003. The radius of the bend, R_b, was selected as 800 mm: industrial systems often use long, sweeping bends, and the 16:1 ratio of R_b:R was the same as for the lab-scale rig used in Chapter 3. The impact angle along the pipe centreline, θ_c, and the maximum impact angle, θ_{max}, were calculated as 0.345 rad (19.75°) and 0.490 rad (28.07°) respectively from Eqs. 6.43 and 6.44. The variation of θ with y is shown in Figure 6.12.

The maximum (centreline) fluid velocity, denoted by u_m in the model, was selected as 20 $m\,s^{-1}$; this velocity is typical for dilute phase conveying and considerably exceeds the saltation velocity for infant formula, which was necessary to satisfy assumption vii. The mass flow ratio is an important parameter which is calculated as the mass of solids per unit mass of conveying air. There is a large range in mass flow ratios used for dilute phase conveying, as discussed in Section 1.4.2. Klinzing (2001⋆) states that mass flow ratios of around 1 are often used, while Marcus et al. (1990) indicate that ratios below 15 would be reasonable for dilute phase transport. Two different values were

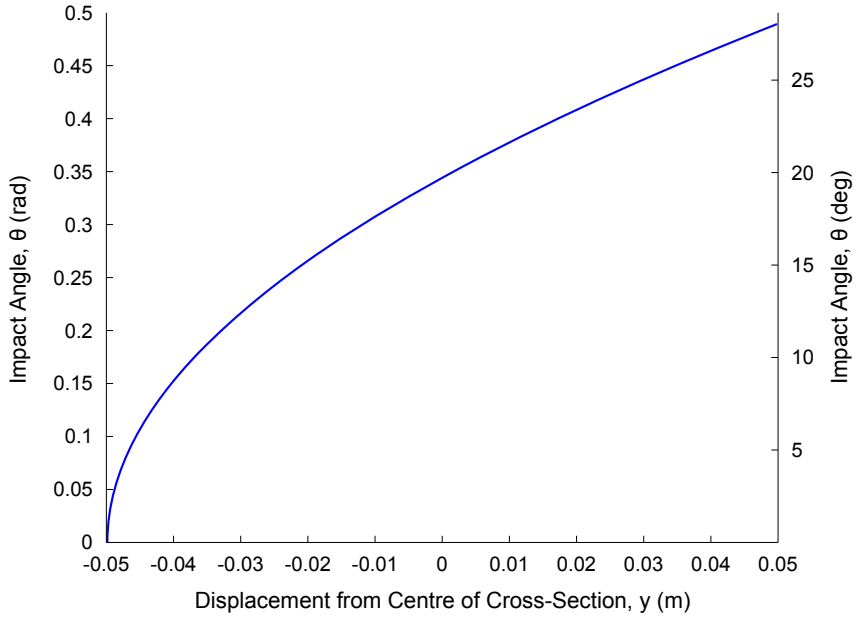

Figure 6.12: *Plot showing the non-linear variation of impact angle with displacement from the centre of the pipe cross-section (m)*

used in the model: 1 and 10. By knowing the density of air, the particle density, the mass of each particle and the mass flow ratio, n_{pv} was calculated as shown in Eq. 6.53. Note that the conveying air was assumed to be at 20°C; at this temperature and at standard atmospheric pressure, the kinematic viscosity and density of dry air were 1.506×10^{-5} $m^2 s^{-1}$ and 1.206 $kg m^{-3}$, respectively (Rogers and Mayhew, 1995, p.16).

$$n_{pv} = \begin{cases} \dfrac{\frac{1}{1.09 \times 10^{-8}}}{\frac{1}{770} + \frac{1}{1.206}} = 1.11 \times 10^{8}\ m^{-3} & \text{if mass flow ratio} = 1 \\ \dfrac{\frac{10}{1.09 \times 10^{-8}}}{\frac{10}{770} + \frac{1}{1.206}} = 1.09 \times 10^{9}\ m^{-3} & \text{if mass flow ratio} = 10 \end{cases} \tag{6.53}$$

The pipe Reynolds number, n, and the mean air velocity (μ_{uf}) were calculated iteratively since all three were related. Re was found as the product of μ_{uf} and the pipe diameter divided by the kinematic viscosity of air, n is the function of Re given by Eq. 6.2 and μ_{uf} is the function of n and u_m given by Eq. 6.4. These three quantities were found to equal 1.09×10^5, 7.32 and 16.47 $m s^{-1}$, respectively. The large magnitude of Re confirms that it was acceptable to describe the radial variation of fluid velocity using the $1/7^{th}$ power law velocity profile.

Two causes of particle motion in the radial direction were discussed in Section 6.1.7. Since the gravitational mechanism was applicable only at low mass flow ratios, it was used only where the mass flow ratio was 1. Conversely, the inter-particle collision mechanism was applied only for a mass flow ratio of 10. Where inter-particle collisions were the main cause, the mean free path between collisions, λ, was calculated using

Eq. 6.29:

$$\lambda = \frac{1}{4\sqrt{2}\pi {r_p}^2 n_{pv}} = 2.3 \text{ mm} \tag{6.29}$$

The characteristic radial distance, R_ϕ, was equal to λ for this approach. The characteristic radial velocity, u_ϕ, required estimates of the granular temperature. There is a lack of reliable data in the literature for granular temperatures for pneumatic conveying; in the absence of suitable estimates, the granular temperature for this conveying scenario was assumed to be 0.01 $m^2 s^{-2}$. This is close to the maximum granular temperature of 0.009 $m^2 s^{-2}$ obtained by Rajniak et al. (2009) for a Wurster type fluidised bed granulator. For this value of Θ, $\overline{u}_c$ was calculated as 0.266 $m s^{-1}$ from Eq. 6.31, which was taken as u_ϕ for the inter-particle collision mechanism. This gave a value of 116 s^{-1} for ϕ.

Alternatively, gravity might act as the main cause of particle motion in the radial direction. Where this was the case, the average height that the particles fall through, μ_h, was calculated as 42.3 mm from Eq. 6.34. R_ϕ was taken to equal μ_h for this mechanism. u_ϕ was calculated by numerically integrating Eq. 6.35 in Mathematica. This integration required the terminal velocity of the particle, u_t, which was found as 0.97 $m s^{-1}$ from Eq. 6.33. Thus, u_ϕ was 0.39 $m s^{-1}$ and ϕ was equal to 9.24 s^{-1} for the gravitational mechanism.

6.2.3 Determination of Weibull Parameters

The calibrated DEM which was developed in Chapter 5 was used to obtain both of the required Weibull parameters. It has already been demonstrated that this model gives acceptable results for dynamic loading, despite being developed for quasi-static compression of agglomerates. Therefore, it could be applied to this dynamic loading situation with some assurance of obtaining a reasonable result. One hundred dynamic DEM simulations were run in total. These were similar to the impact simulations described in Section 5.5.2, with two important differences:

- The agglomerates used were smaller, having a diameter of approximately 300 µm. The mean number of spheres in an agglomerate was 46, with a standard deviation of 11.
- The impact velocity was 20 $m s^{-1}$ rather than 10.1 $m s^{-1}$.

Failure of these agglomerates was determined using the criterion defined in Section 5.5.2, i.e., an agglomerate was deemed to have failed during the simulation if fewer than 95% of the spheres remained in one intact entity. Exactly half of the simulated agglomerates failed according to this criterion. The force at failure for the Weibull analysis was taken to be the maximum force attained prior to agglomerate failure,

while the required measure of agglomerate size, d, was the height of the agglomerate (measured perpendicularly to the platen) before impact.

As before, $\ln\left[\ln\left(\frac{1}{P_s(d)}\right)\right]$ was plotted against $\ln(\sigma)$ and a linear regression trendline was fitted. This is shown in Figure 6.13. The Weibull modulus, m, was equal to 1.7936 and σ_o was 8.711×10^6 N m^{-2}. R^2 of the linear regression was extremely high: 0.9804. Rather than using nominal stresses at failure, it was also possible to determine Weibull parameters directly using the forces at failure (i.e., without division by d^2). In that case, m was equal to 1.7180 and the 37% characteristic force, F_o, was 1.336 N.

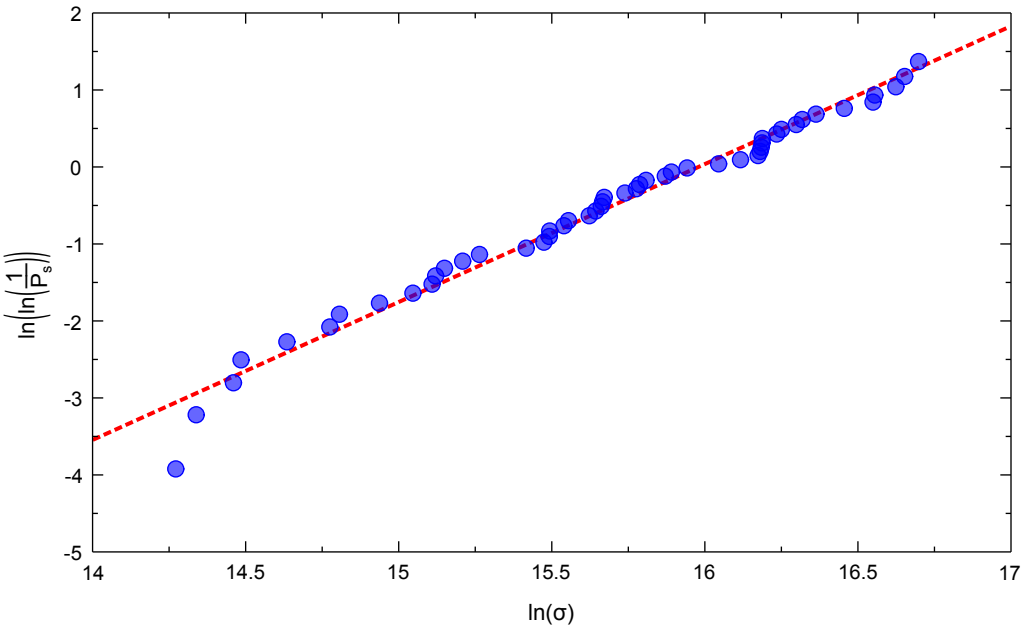

Figure 6.13: *Weibull plot for the 50 simulated agglomerates which failed when subjected to impact loading at 20 ms^{-1}*

The probability density functions thus obtained are shown in Figure 6.14 in terms of both stress and force.

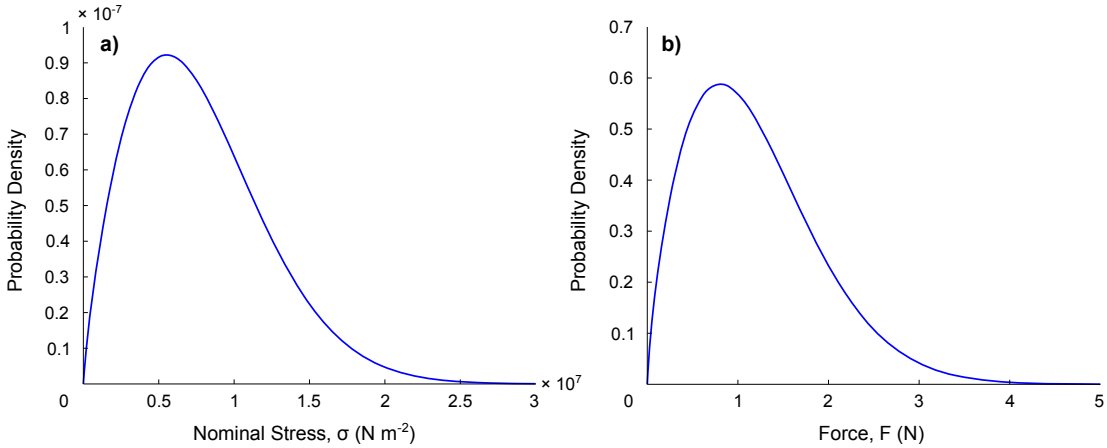

Figure 6.14: *Probability density functions of the Weibull distributions in a) σ and b) F for the parameters determined in Section 6.2.3*

6.2.4 Monte Carlo Approach for Model Application

Monte Carlo simulation was selected as the most suitable probabilistic approach for validating the theoretical predictive equations developed for this model. Instead of representing each input parameter by a single number, certain model inputs are sampled from probability distributions which characterise the variability in those parameters (Cronin and Gleeson, 2007). It is necessary to conduct sufficient simulations to ensure statistical significance of the model outputs; in this case, 5,000 simulations were conducted for each value of ϕ to properly account for the input variability. The algorithm is outlined below and was implemented using MATLAB. Note that the time step chosen for these simulations, Δt, was fixed at 0.1 ms.

1. For each simulation, the position of the particle was selected randomly. The position is defined by the Cartesian coordinates of the centrepoint of the particle, i.e., x and y. Two variates were randomly selected from the uniform distribution on the interval [0,1]: γ_1 and γ_2. x, y and the radial distance, r, were then calculated from Eqs. 6.54–6.56:

$$x = \gamma_1 (R - r_p) \cos(2\pi\gamma_2) \tag{6.54}$$

$$y = \gamma_1 (R - r_p) \sin(2\pi\gamma_2) \tag{6.55}$$

$$r = \sqrt{x^2 + y^2} \tag{6.56}$$

2. u_f, μ_{uf} (= μ_{ue}) and σ_{uf} (= σ_{ue}) were calculated using Eqs. 6.1, 6.4 and 6.5, respectively.

3. u_e and u_p were calculated at each incremental time step (Δt) using Eqs. 6.24 and 6.17, respectively.

$$u_p(t + \Delta t) = u_p(t) - p_e[u_p(t) - u_e(t)]\Delta t \tag{6.17}$$

The particle Reynolds number and effective inertial rate constant were recalculated for each time step using Eqs. 6.12 and 6.21, respectively, since the relative velocity between the fluid and particle changed continuously. The axial displacement along the pipeline, x_p, was also found at each time step using Eq. 6.57. x_p and t were initialised at 0 at the start of the simulation, while u_e and u_p were both initialised at u_f.

$$x_p(t + \Delta t) = x_p(t) + \frac{1}{2}\left[u_p(t) + u_p(t + \Delta t)\right]\Delta t \tag{6.57}$$

x_p was used as a termination condition for this time-stepping algorithm, i.e., the algorithm was completed when $x_p(t + \Delta t)$ became greater than the pipe length. u_e, u_p, x_p, t, p_e and Re_p were all stored in a data matrix for subsequent use.

4. The impact angle, θ, was calculated for each simulation using Eq. 6.42. The normal impact velocity, u_n, was found using Eq. 6.38, noting that the particle velocity in this equation was the final value recorded for u_p. Basic statistics were calculated for u_e and u_p: means, standard deviations and extreme values. σ^2_{up} was calculated using Eq. 6.28 for comparison, taking p_e to be the mean of the relevant column in the matrix.

5. The maximum absolute impact force was found using Eq. 6.58, which is a simplified form of Eq. 6.50.

$$|F(t)|\Big|_{\max} = 0.0103 u_n \tag{6.58}$$

   This was divided by the square of the particle diameter, d^2, to obtain the nominal σ required for the Weibull determination of breakage (Eq. 5.4), where d was fixed at 0.3 mm. The probability of survival of the particle, P_s, was found using Eq. 5.2.

6. Whether or not the particle failed was determined by randomly selecting another variate from the uniform distribution on the interval [0,1], γ_3. If $\gamma_3 \geq P_s$, the particle was deemed to have failed, otherwise, it survived the loading. For example, if P_s was found to be 0.95 and γ_3 was randomly generated as 0.37, the particle would be judged to survive the loading. However, if γ_3 was instead 0.96, the particle would be deemed to have failed. All of the relevant data were appended to a text file for subsequent analysis, the variables were cleared from memory and the algorithm recommenced.

6.3 Results and Discussion

6.3.1 Effective Fluid and Particle Velocities

Figures 6.15 and 6.16 show three realisations of u_e and u_p against distance along the pipeline where ϕ was 116 s^{-1} and 9.24 s^{-1}, respectively. By comparing these two figures, it can be seen that increasing ϕ had the effect of increasing the frequency of the fluctuations in the effective fluid velocity, and hence in the particle velocity.

Table 6.2 presents basic statistics of u_p which were calculated using two methods:

1. By determining the statistics for 5,000 Monte Carlo simulations conducted at ϕ values of 9.24 s^{-1} and 116 s^{-1}
2. Using the theoretical equations for μ_{up} and σ_{up} presented in Section 6.1.6

Note that each of the statistics in Table 6.2 which were obtained from the Monte Carlo simulations is the mean of the corresponding values recorded, e.g., the mean of the

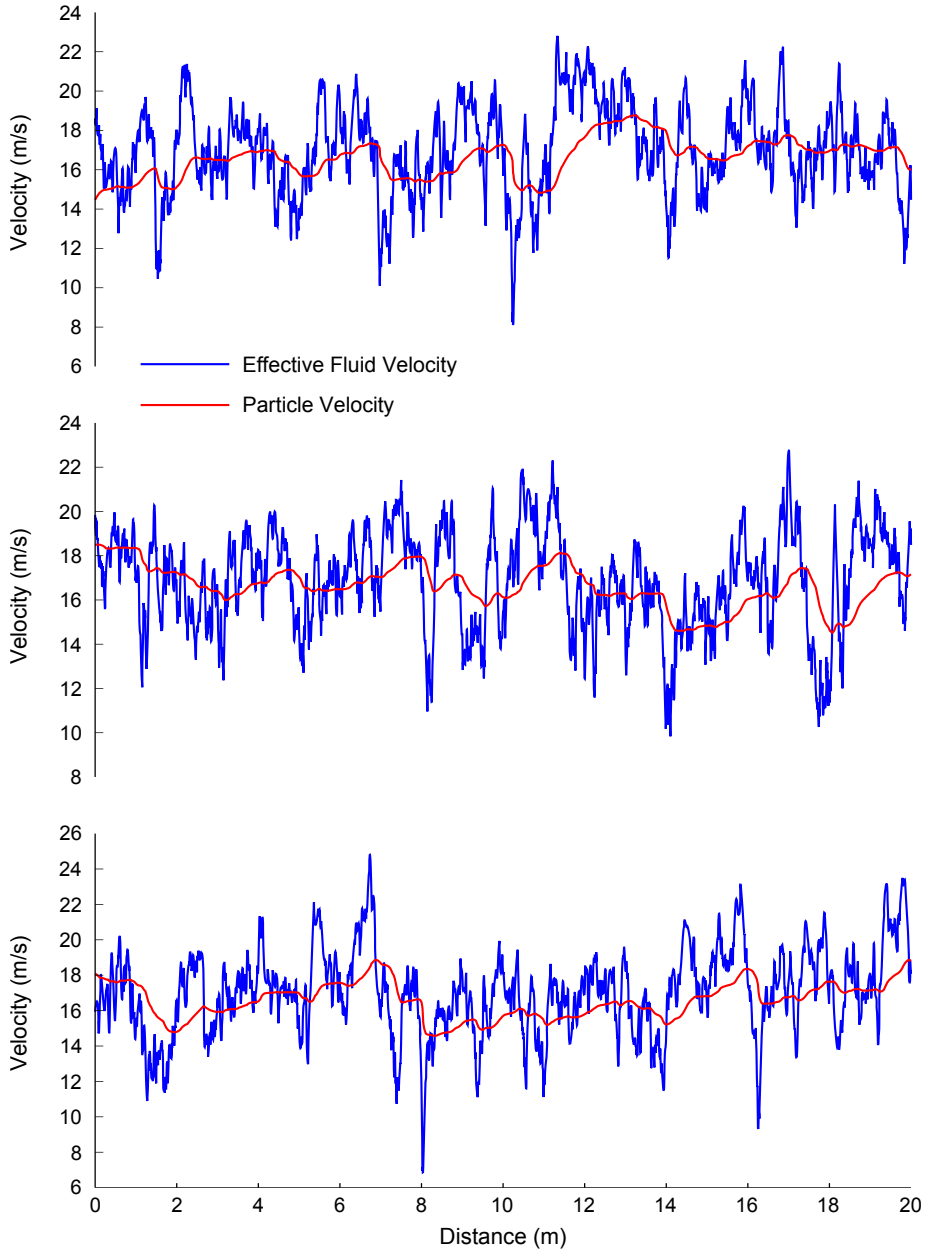

Figure 6.15: *Three representative realisations of the effective fluid velocity and particle velocity (both in ms^{-1}) against distance along the pipeline (m) for $\phi = 116\ s^{-1}$*

minimum values recorded for u_p was 13.941 ms^{-1} when $\phi = 9.24\ s^{-1}$, which was considerably different from the global minimum for all of these simulations: 9.033 ms^{-1}.

Changing the autocorrelation parameter had a negligible effect on the means of u_p. However, there were marked differences in the other statistics. Increasing ϕ caused the fluid velocity field to fluctuate more quickly, and the particle was not capable of following the rapid disturbances: this effect was expected from the discussion of Eq. 6.28 in Section 6.1.6. The same effect can also be seen when the extreme values are compared: the range of u_p was smaller when ϕ was 116 s^{-1} (3.943 ms^{-1}) than when ϕ was 9.24 s^{-1} (5.301 ms^{-1}).

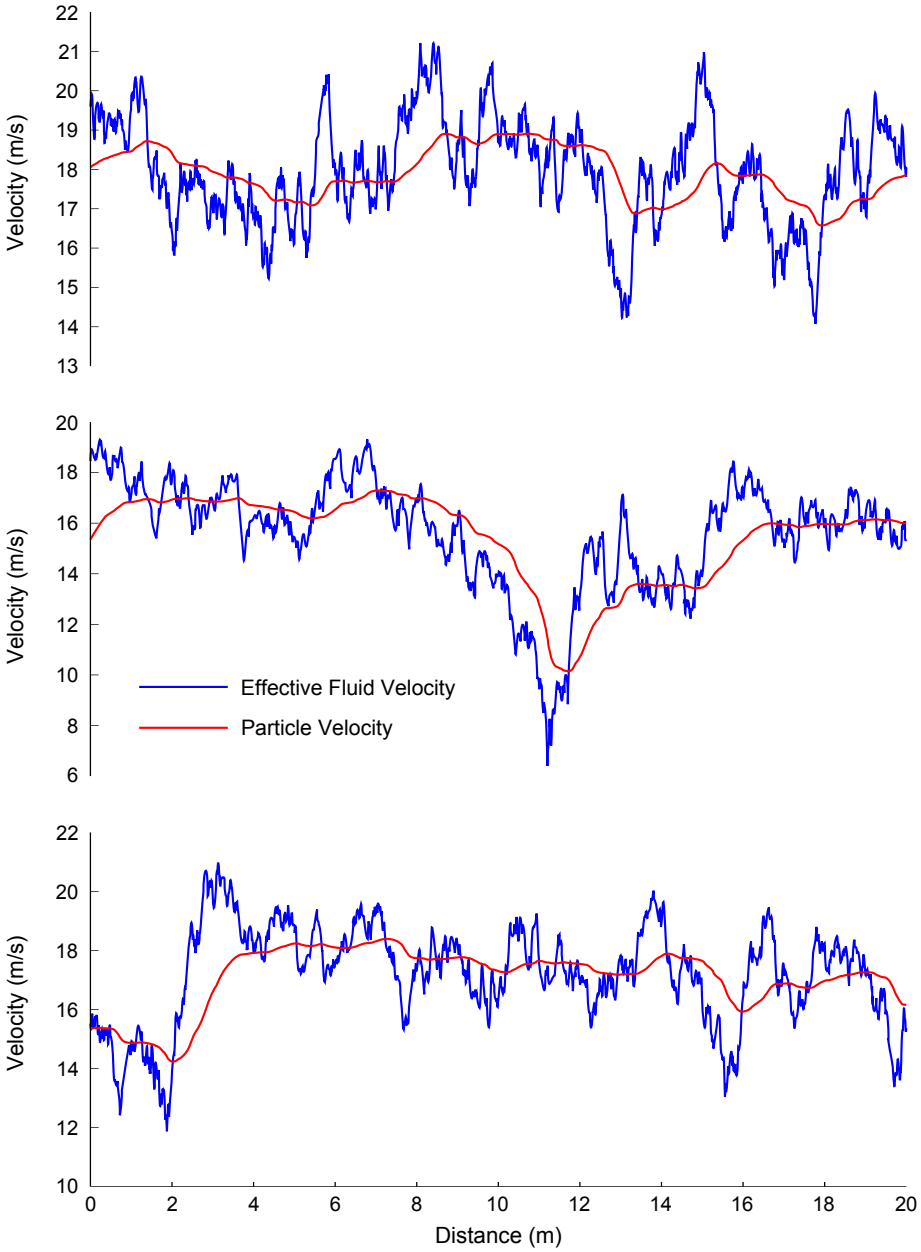

Figure 6.16: *Three representative realisations of the effective fluid velocity and particle velocity (both in ms^{-1}) against distance along the pipeline (m) for $\phi = 9.24\ s^{-1}$*

Eqs. 6.26 and 6.28 were given in Section 6.1.6 for the mean and variance of particle velocity, respectively. The former is equal to μ_{ue}, which is given by Eq. 6.4 as a function of only two parameters: n and u_m. The value of μ_{up} calculated using this equation, 16.471 ms^{-1}, was very close to the simulation values: the magnitudes of the differences are less than 1% for both ϕ values when compared to the equivalent Monte Carlo simulation means. However, the standard deviations do not compare as well, with differences from the equivalent Monte Carlo simulation standard deviations of 13% and -17% for ϕ values of 9.24 s^{-1} and 116 s^{-1}, respectively. Eq. 6.28 assumes that $t \gg \frac{1}{2p_e}$ and $t \gg \frac{1}{p_e+\phi}$. Since the mean values of p_e were > 7 for all simulations (average of 9.75),

Table 6.2: *Means, standard deviations and extreme values of the particle velocity (ms^{-1}), averaged over the 5,000 simulations conducted at each value of ϕ, compared to the means and standard deviations calculated using theoretical predictive equations*

	ϕ (s^{-1})	u_p ($m s^{-1}$)			
		Mean	Std. Dev.	Minimum	Maximum
Simulations	9.24	16.592	1.399	13.941	19.242
	116	16.493	0.788	14.580	18.523
Equations	9.24	16.471	1.583	—	—
	116	16.471	0.655	—	—

and the conveying time exceeded 1 s, both of these conditions were comfortably met. Two alternative reasons were identified for the disparity between standard deviations:

1. The modelled conveying system had a length of 20 m. This was insufficient for σ_{ue} to reach the theoretical value of 2.260 $m s^{-1}$ from Eq. 6.5 when ϕ was 9.24 s^{-1} (the average σ_{ue} for these simulations was 2.030 $m s^{-1}$). Since Eq. 6.28 contains σ_{ue}^2, σ_{up}^2 showed a corresponding deviation.
2. Even as the pipe length tends towards infinity, a difference remains between simulated and theoretical σ_{up} values. This difference $\lessapprox$ 30% for typical values of ϕ between 1 and 150. The reason for this has not been established definitively, but it is hypothesised that it may be due to the assumption that $P(u_e)$ is normally distributed, which was clearly not the case (Figure 6.4 on p.155).

The development of Eqs. 6.26 and 6.28 incorporated an effective inertial rate constant, p_e, to ensure that the expressions were valid outside of the Stokes' law regime in which $Re_p \lessapprox 2$. Figure 6.17 plots the particle Reynolds number against distance along the pipeline. Clearly, Re_p fluctuated greatly and values were almost always greater than 2. The mean particle Reynolds numbers for all 5,000 Monte Carlo simulations were 24.1 (ϕ of 9.24 s^{-1}) and 34.2 (ϕ of 116 s^{-1}), while the average maximum values from all simulations were 91.4 and 149.3, respectively.

The variation of p_e with ϕ is small, which is unsurprising since the only non-constant term in Eq. 6.21 is $\sqrt{|u_p - u_e|}$. The mean value of p_e was 8.9 s^{-1} when ϕ had a value of 9.24 s^{-1} in the simulations, which increased to 10.6 s^{-1} when ϕ was 116 s^{-1}. Taking an average p_e of 9.8 s^{-1} and σ_{ue} to be at its theoretical value of 2.26 $m s^{-1}$, Figure 6.18 plots σ_{up}^2 against ϕ using Eq. 6.28.

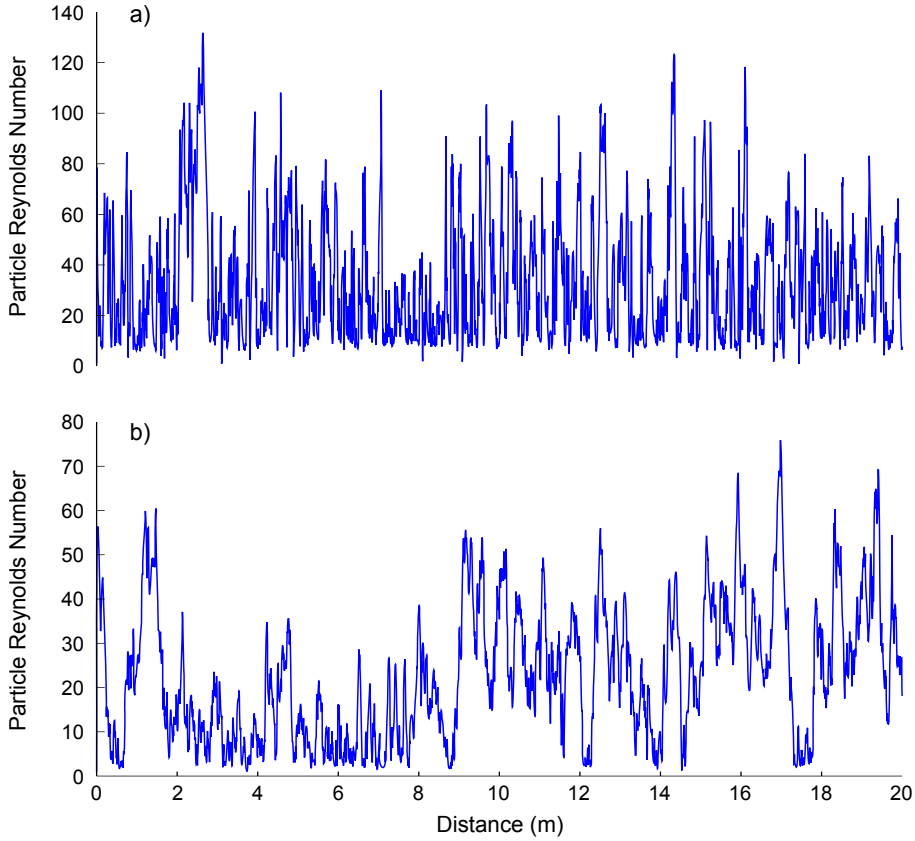

Figure 6.17: *Plots of the particle Reynolds number against distance along the pipeline (m) for ϕ values of a) 116 s^{-1} and b) 9.24 s^{-1}*

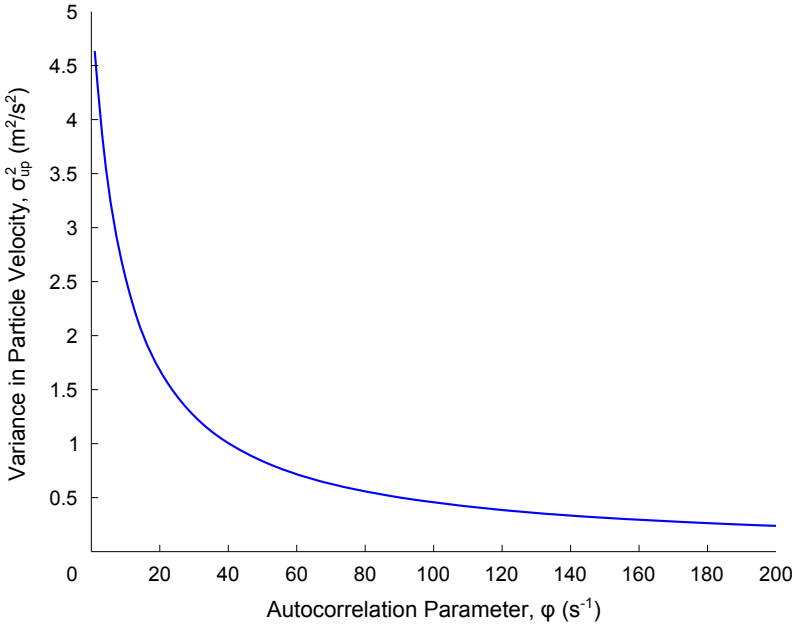

Figure 6.18: *Plot of the variance in particle velocity ($m^2\,s^{-2}$) against ϕ (s^{-1})*

6.3.2 Impact Angles and Normal Impact Velocities

Basic statistics of the angle of impact with the 90° pipe bend, θ, are given in Table 6.3. As for u_p in Table 6.2, means and standard deviations could be calculated from the

simulation data and compared with those obtained from theoretical equations (Eq^{s}. 6.46 and 6.47). The autocorrelation parameter had no influence on any of the simulation statistics, while the maximum impact angles almost reached the theoretical θ_{max} of 0.490 rad.

Table 6.3: *Means, standard deviations and extreme values of the impact angle, averaged over the 5,000 simulations conducted at each value of ϕ, compared to the means and standard deviations calculated using theoretical predictive equations*

	ϕ (s^{-1})	θ (rad {°})			
		Mean	Std. Dev.	Minimum	Maximum
Simulations	9.24	0.335 {19.17}	0.078 {4.49}	0.025 {1.43}	0.488 {27.96}
	116	0.333 {19.10}	0.079 {4.53}	0.022 {1.26}	0.488 {27.96}
Equations	9.24	0.333 {19.08}	0.097 {5.53}	—	—
	116	0.333 {19.08}	0.097 {5.53}	—	—

The means compared extremely well. However, the standard deviations obtained from the simulations and predictive equations differed considerably: by 24% (ϕ of 9.24 s^{-1}) and 22% (ϕ of 116 s^{-1}), relative to the Monte Carlo simulation results. The formula always over-predicted the actual standard deviations that occurred in the simulations. The analogous statistics for the normal impact velocity, u_n, are given in Table 6.4, for which Eq^{s}. 6.39 and 6.41 were the theoretical equations. Note that the required values of μ_{up} and σ_{up} were taken as the simulation results in Table 6.2, while μ_θ and σ_θ were taken from Table 6.3.

Table 6.4: *Means, standard deviations and extreme values of the normal impact velocity (ms^{-1}), averaged over the 5,000 simulations conducted at each value of ϕ, compared to the means and standard deviations calculated using theoretical predictive equations*

	ϕ (s^{-1})	u_n ($m\,s^{-1}$)			
		Mean	Std. Dev.	Minimum	Maximum
Simulations	9.24	5.446	1.369	0.373	9.710
	116	5.383	1.270	0.335	8.361
Equations	9.24	5.455	1.306	—	—
	116	5.391	1.258	—	—

The normal components of impact velocity had an average of around 5.4 $m\,s^{-1}$, and thus were more than three times smaller than the mean particle velocities. Of course, this observation was caused by the selection of a long bend radius of 0.8 m, and choosing progressively smaller bend radii would cause the ratio of u_n:u_p to increase asymptot-

ically towards 1. The means and standard deviations in Table 6.4 showed excellent agreement, particularly considering that Eq^{s}. 6.39 and 6.41 were approximations obtained by the method of statistical differentials, and thus would be expected to contain some error. The cross-correlation coefficient of particle velocity and impact angle, $\rho_{u_p,\theta}$, was calculated to assess the validity of omitting the partial derivative terms from Eq. 6.40. $\rho_{u_p,\theta}$ was equal to -0.005 or 0.021 when ϕ was 9.24 s^{-1} or 116 s^{-1}, respectively. The magnitudes of both are negligible, confirming that it was acceptable to omit the partial derivative terms in Eq. 6.41. This equation was the sum of two distinct terms, one proportional to the variance in particle velocity and the other proportional to the variance in impact angle. Their relative importance is quantified in Table 6.5.

Table 6.5: *Contributions made by each term of Eq. 6.41 to the variance in normal impact velocity, σ^2_{un}*

ϕ (s^{-1})	Percentage	
	$\sin^2\mu_\theta \cdot \sigma^2_{up}$	$\mu^2_{up}\cos^2\mu_\theta \cdot \sigma^2_\theta$
9.24	12.4	87.6
116	4.2	95.8

The term containing σ^2_θ makes the dominant contribution to σ^2_{un} for both values of ϕ tested, and its relative importance became more marked as ϕ increased. Thus, if it is desirable to minimise the variance in normal impact velocity, it may be more effective to optimise the design of the pipe bend rather than to minimise the variance in particle velocity.

6.3.3 Impact Forces and Agglomerate Breakage Statistics

Statistics of the maximum impact forces are provided in Table 6.6. Since neither θ nor u_n were significantly affected by ϕ, the same was true for $|F(t)|\big|_{\max}$ and P_s. Thus, the statistics were combined for the simulations conducted at both ϕ values to yield one set of 10,000 simulations. The mean and standard deviation of the maximum impact force could be predicted using Eq. 6.58, i.e., the mean is $0.0103\mu_{un}$ and the standard deviation is $0.0103\sigma_{un}$. μ_{un} and σ_{un} were both taken as the average of the simulation statistics in Table 6.4.

The means and standard deviations calculated using both methods were identical. The MATLAB function *wblfit* was used to fit a Weibull distribution to the simulation data for $|F(t)|\big|_{\max}$. The parameters of the PDF (Eq. 3.4) are given below, while the PDF is graphed on Figure 6.19.

Table 6.6: *Means, standard deviations and extreme values of the maximum impact forces (N), averaged over 10,000 simulations, compared to the means and standard deviations calculated using theoretical predictive equations*

	Mean	Std. Dev.	Minimum	Maximum
Simulations	0.056	0.014	0.003	0.100
Equations	0.056	0.014	—	—

- a, the scale parameter, was equal to 0.0609 (95% confidence interval: 0.0606 → 0.0611)
- b, the shape parameter, was equal to 4.7657 (95% confidence interval: 4.6928 → 4.8398)

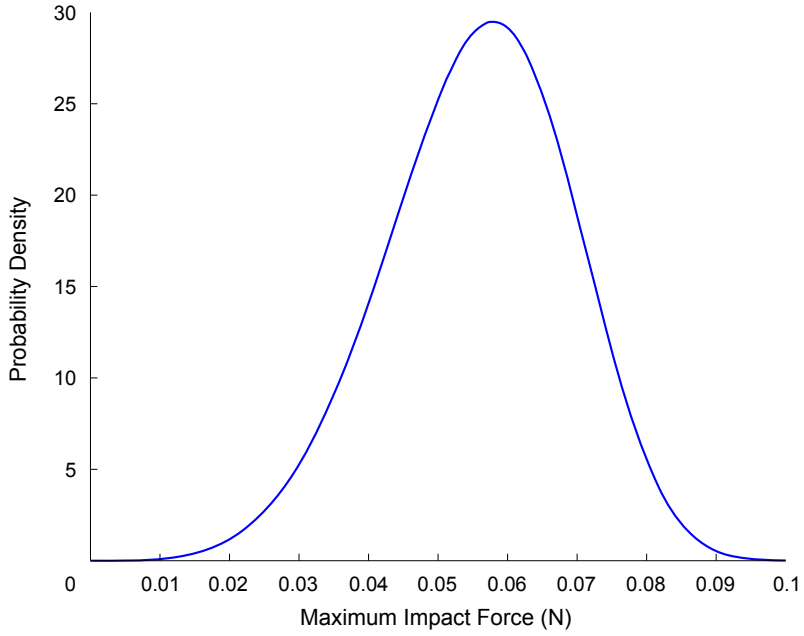

Figure 6.19: *Probability density function of the Weibull distribution fitted to the simulation data for* $|F(t)|\Big|_{max}$

The mean of this Weibull distribution was 0.056 and its standard deviation was 0.013, both of which show excellent agreement with the statistics given in Table 6.6. Table 6.7 contains the statistics for the probability of survival of agglomerates when subjected to this loading. An equation was derived for the mean of P_s, μ_{Ps}, by comparing the Weibull PDFs for force at failure of the particles and the maximum impact forces in the conveying system: Figures 6.14b and 6.19, respectively. The force at which these PDFs intersected was termed F^*, which is shown on Figure 6.20[†].

F^* was found to equal 0.093 N for these simulations. The probability that a particle survives the loading could therefore be approximated by the Weibull cumulative density

[†]Note that both PDFs were truncated on Figure 6.20 so that F^* could be seen clearly.

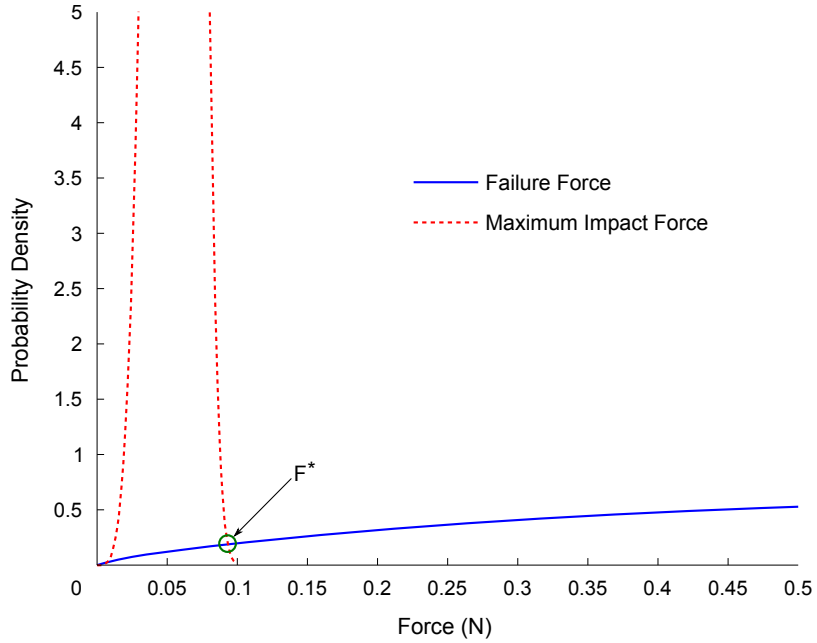

Figure 6.20: *Identification of F*: the point of intersection of the Weibull PDFs for force at failure and for the maximum impact forces in the conveying system*

function given as Eq. 6.59.

$$\mu_{Ps} = e^{\left[-\left(\frac{F^*}{F_o}\right)^m\right]} \tag{6.59}$$

F_o and m in Eq. 6.59 are the parameters given for the Weibull PDF of forces in Section 6.2.3 (equal to 1.336 N and 1.718, respectively).

Table 6.7: *Means, standard deviations and extreme values of the probability of survival, averaged over 10,000 simulations, compared to the mean calculated using Eq. 6.59*

	Mean	Std. Dev.	Minimum	Maximum
Simulations	0.991	0.004	0.975	1.000
Equations	0.990	—	—	—

Both results for μ_{Ps} showed excellent agreement. Only 0.9% of the particles failed when subjected to this loading. The proportion of the agglomerates which fail would be expected to increase as u_m increases. This is demonstrated by Figure 6.21, which shows that the mean probability of survival of an agglomerate decreases with increasing u_m. The data for this figure were obtained by running 500 Monte Carlo simulations at each value of u_m.

6.3.4 Advantage of Theoretical Predictive Equations

Throughout Sections 6.3.1–6.3.3, means and standard deviations have been presented that were obtained from two sources: the Monte Carlo simulations and the theoretical

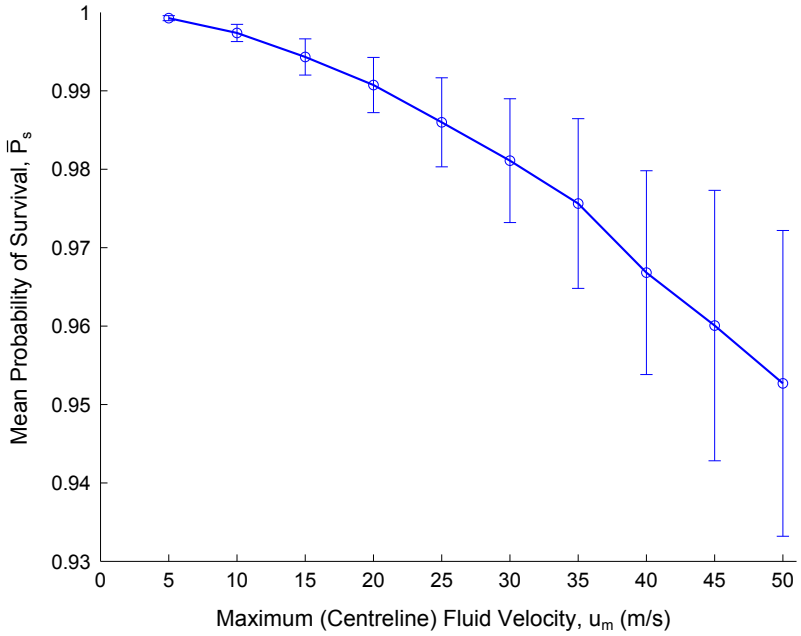

Figure 6.21: *Plot of the mean probability of survival of an agglomerate against the maximum (centreline) air velocity (ms^{-1}), where the error bars indicate ± one standard deviation of P_s*

equations that were provided in Section 6.1. Generally, both approaches have shown good agreement, particularly for the mean statistics. The main advantage of these equations is that they provide insights into the conveying process that could not be attained by simulation. If any parameter is changed, the simulations would need to be rerun to quantify its effect, whereas the equations allow for immediate prediction of the resulting effect without the requirement to conduct simulations. Some of the insights gained are presented below:

- The mean particle velocity always coincides with the mean (effective) fluid velocity given sufficiently long conveying times (Eq. 6.26). Thus, it is affected only by n and u_m. Since n varies little for realistic ranges of conveying conditions, μ_{up} is approximately $0.8u_m$.
- The variance in particle velocity is proportional to, and always less than, the variance in (effective) fluid velocity (Eq. 6.28), which is in turn proportional to u_m^2 (Eq. 6.5). Hence, σ_{up} is approximately proportional to u_m. σ_{up}^2 can be reduced by either increasing ϕ or reducing p_e (e.g., by conveying particles of larger diameter).
- μ_θ and σ_θ depend only on the centreline impact angle, θ_c, and hence are affected only by the geometry of the pipe bend (Eqs. 6.46 and 6.47). Both of these equations have very low sensitivity to the ratio of bend radius to pipe radius, $\frac{R_b}{R}$.
- The mean normal impact velocity is directly proportional to the mean particle velocity (Eq. 6.39). Table 6.5 shows that the variance in normal impact velocity is mainly affected by the variance in impact angle rather than the variance in particle

velocity (Eq. 6.41). Therefore, σ_{un} is nearly proportional to both μ_{up} and σ_θ for realistic ranges of ϕ.

- By using the Kelvin-Voigt dynamic model, the mean and standard deviation of the maximum impact force are directly proportional to the equivalent statistics for the normal impact velocity (Eq. 6.58).

6.3.5 Verification of Key Model Assumptions

xii: Neglecting the Acceleration Period for Particles in the Conveying System

Several simulations were conducted in which the initial velocity of the particle was zero. Figure 6.22 shows the evolution of particle velocity with axial displacement along the pipeline for one such representative simulation.

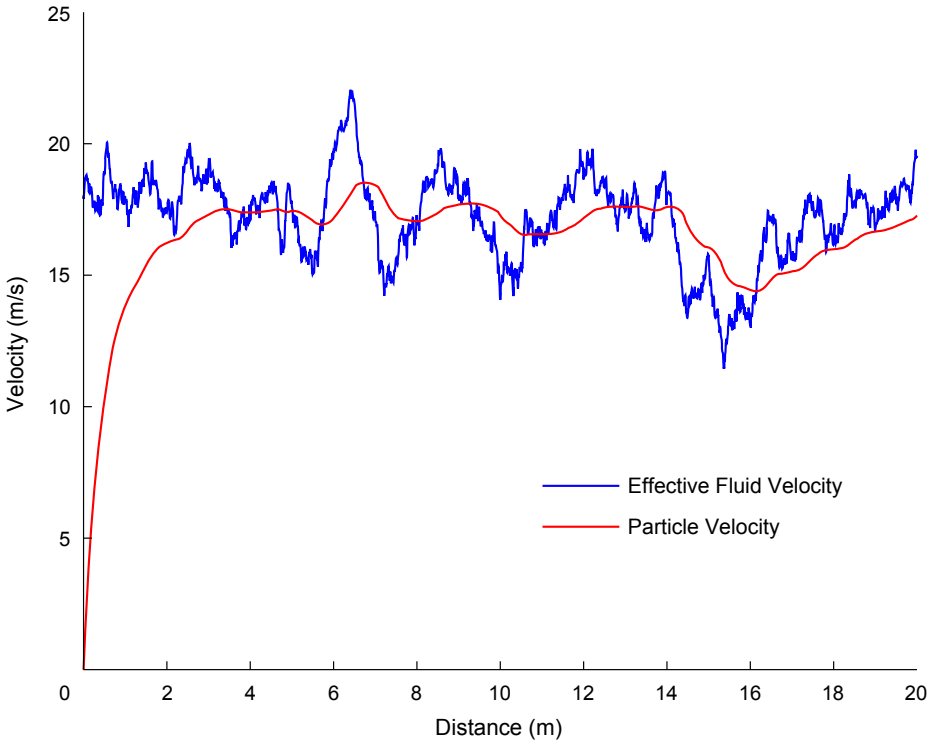

Figure 6.22: *Plot of the particle velocity and effective fluid velocity (both in $m s^{-1}$) against distance (m) for a representative conveying simulation in which the particle was initially at rest*

μ_{ue} was 16.47 $m s^{-1}$ for this simulation. The particle attained this velocity after 0.132 s by which time it had travelled 2.38 m. Since the pipe length is 20 m, the acceleration phase of the particle from rest up to the mean effective fluid velocity was completed within the first 12% of the conveying system. Thus, it was acceptable to neglect this initial phase of the simulations.

xiii: Inter-Particle Collisions Not Considered Explicitly as a Mechanism for Particle Breakage

The mean inter-particle collision velocity was calculated using Eq^{s}. 6.36 and 6.37 to be 1.579 ms^{-1} or 2.147 ms^{-1}, respectively, taking σ_{up} as 1.399 ms^{-1} from Table 6.2. These estimates of μ_{uc} were much less than 1/2 of the mean normal impact velocities at the pipe bend in Table 6.4, and since fatigue of the particles was not considered (assumption ix), assumption xiii was acceptable.

xviii: Not Considering Fluctuations in the Particle Velocity due to Fluid Turbulence

Assume that turbulence effects are present in the fluid flow which are characterised by a turbulence intensity of 10%, i.e., $\sigma_{ut} = 0.1\mu_{uf}$, where σ^2_{ut} is the variance in fluid velocity due to turbulence. Therefore σ_{ut} is 1.647 ms^{-1}, since μ_{uf} = 16.471 ms^{-1} from Eq. 6.4. Oesterle and Petitjean (1993) present Eq. 6.60 which relates σ^2_{ut} to the corresponding variance in particle velocity, σ^2_{up}.

$$\sigma^2_{up} = \frac{\int_0^\infty S_p(\omega)\,d\omega}{\int_0^\infty S_f(\omega)\,d\omega}\sigma^2_{ut} \tag{6.60}$$

In this equation, ω represents the frequency, while $S_f(\omega)$ and $S_p(\omega)$ are the fluid turbulence energy spectrum and particle energy spectrum, respectively. These spectra can be obtained from Eq^{s}. 6.61 and 6.62.

$$S_f(\omega) = \frac{4T}{1+T^2\omega^2} \tag{6.61}$$

$$S_p(\omega) = \frac{S_f(\omega)}{1+t^{*2}\omega^2} \tag{6.62}$$

T is the integral time scale and t^* is the particle relaxation time. The former can be approximated by Eq. 6.63 while the latter is defined by Eq. 6.64 (Louge et al., 1991).

$$T \approx 0.1\frac{R}{u_f} \tag{6.63}$$

$$t^* = \frac{8\rho_p r_p}{3c_D\rho(u_f - u_p)} \tag{6.64}$$

Taking u_f in Eq. 6.63 to be the mean fluid velocity, T was evaluated as 0.3 ms. The drag coefficient in Eq. 6.64 was replaced by Eq. 6.20 and the slip velocity between the fluid and particle was assumed to be 1 ms^{-1}, which is physically realistic. Thus, t^* was calculated as 0.114 s.

Since $T > 0$, both of the integrals in Eq. 6.60 can be solved to yield the following results:

$$\int_0^\infty S_f(\omega)\,d\omega = 2\pi$$

$$\int_0^\infty S_p(\omega)\,d\omega = \frac{2\pi T}{T+t^*}$$

Thus, Eq. 6.60 simplifies to Eq. 6.65:

$$\sigma_{up}^2 = \frac{T}{T + t^*}\sigma_{ut}^2 \tag{6.65}$$

σ_{up}^2 was evaluated as 0.0072 $m^2 s^{-2}$. This variance in particle velocity, which is solely attributable to fluid turbulence, is less than 2% of the smallest simulation value of σ_{up}^2 caused by radial motion of the particle in Table 6.2.

Oesterle and Petitjean (1993) also give the heuristic that fluctuations in particle velocity due to turbulence are small if $\frac{u_f t^*}{R} \gg 1$. This statistic was evaluated as 37.5, taking $u_f = \mu_{uf}$ as was done for Eq. 6.63. This heuristic and the negligible magnitude of σ_{up}^2 caused by fluid turbulence both confirm that assumption xviii was acceptable.

6.4 Conclusions of Chapter 6

A macro-scale probabilistic model of dilute phase pneumatic transport was developed in this chapter to predict the percentage of agglomerates which break when conveyed under specified conditions. Most of the assumptions made in the model development were realistic. However, a small number were not and were made to simplify the model (e.g., assuming a monodispersed flow). This model was very straightforward compared to some alternative approaches, yet provided much quantitative data for analysis. In addition to its ease of implementation, the model also had the benefit of a modular structure, i.e., any of the sub-models comprising the overall model could easily be substituted by a reasonable alternative without necessarily compromising the functionality of the model as a whole.

For infant formula agglomerates with typical dimensions, the fluid velocity and effective (particle-averaged) fluid velocity were almost identical. Slightly less than 1% of the infant formula agglomerates failed when conveyed through a simple system containing one 90° bend (radius of 0.8 m) at a maximum superficial velocity of 20 $m s^{-1}$. The speed at which the agglomerates moved in the radial direction, and hence the autocorrelation parameter, did not influence the probability of survival of the agglomerates conveyed. The cross-correlation coefficients between particle velocity and impact angle were negligible. The mean inter-particle collision velocity was much lower than the normal impact velocity at the pipe bend, thus justifying the assumption to neglect inter-particle collisions as a mechanism for particle breakage.

7

Closing Discussion and Final Conclusions

In this chapter, the results presented in the preceding chapters are discussed further, with particular reference to the three objectives defined in Section 1.7 (p.18), and the main conclusions of the research are stated. The first of these objectives was to establish relationships between the geometry and operating conditions of a pneumatic conveying system, and the corresponding changes in bulk properties of infant formulae when conveyed through the system. Chapter 2 addressed this objective by conducting a reasonably comprehensive study of the effect of changing seven selected pneumatic conveying parameters on four key quality characteristics of infant formulae: bulk density, D[4,3], particle density and wettability. This approach worked well, although it had some limitations. It would be extremely time-consuming and difficult from a practical standpoint to investigate all of the parameters which could potentially affect the properties of the conveyed product; those which were not considered in this research included the surface finish of the inner wall of the pipeline, the diameter of the pipeline and the temperature of the conveying air. Bend angles other than 90° and the use of inclined sections were also not considered. One limitation of the pneumatic conveying rig used was the tendency of the single plugs of infant formula used for dense phase conveying to disintegrate rapidly during transport through the system. Industrial systems convey multiple plugs, separated by cushions of air, which would be somewhat less prone to disintegration. However, the sophisticated apparatus required to convey multiple plugs in this manner were unavailable in this lab-scale rig.

It was found that the mode of conveying (dilute or dense phase) and the air velocity were the most influential parameters by a wide margin, although the latter was significant only for dilute phase conveying. The importance of these two parameters was not surprising as many researchers had found similar results (e.g., Kalman and Goder, 1998). What was more interesting to note was the comparative unimportance of the other factors considered, including the bend radii, the vertical conveying length and

the number of rig passes: as long as the conveying velocity was selected to ensure dense phase conveying, attrition was low regardless of the settings chosen for the other factors. Conveying velocities which are used industrially for infant formula transport are usually close to the minimum required to ensure reliable flow, so there might appear to be little potential to reduce the velocity below the values currently used if this was desired. However, a number of systems based on supplementary air injection have been developed with the aim of ensuring reliable flow at extremely low velocities. These include the Gattys, Fluidstat/Turboflow and Takt-Schub systems (Marcus et al., 1990, §7.6.6).

The second objective, to identify which infant formula components have the largest effect on attrition when conveyed, was addressed by Chapter 3. It was found that the percentage of protein in the formulae was the most influential compositional factor: formulae containing high levels of protein had the highest bulk densities before pneumatic conveying. Since bulk density increased with breakage and their densities were quite high initially, these high-protein formulae showed less variation of bulk density when conveyed. This is beneficial for manufacturers as small variations between key quality characteristics of the powders before and after conveying make the process easier to control and reduce the risk of batches failing to comply with specifications. There is usually limited scope to change the composition of an infant formula to reduce attrition when the powder is conveyed. However, by having advance knowledge of the predisposition of low-protein formulae to break significantly, manufacturers may be able to take additional precautions when batches of these formulae are being produced, e.g., use the spray dryers which are closest to the can filling lines.

It was necessary to develop mathematical models at two scales to fulfil the third objective: one a detailed micro-scale model to assess breakage of individual agglomerates when subjected to mechanical loading and one a macro-scale probabilistic model of a simple pneumatic conveying system. Discrete element modelling was used for the former, for which it was necessary to obtain experimental data for quasi-static uniaxial compression of single agglomerates to calibrate the model. The model was calibrated using a novel approach based on Taguchi methods, which was illustrated in Chapter 4. This DEM, which was discussed in detail in Chapter 5, gave a good description of key mechanical responses for quasi-static loading and also gave acceptable results when applied to two dynamic loading situations. One important general finding of this chapter was that while it was important to track the number of bonds which failed during a simulation, it was even more crucial to understand where those bonds were located in the agglomerate and the effect the bond failures had on the structure of the agglomerate. For example, if a hypothetical agglomerate is loaded so that 20% of the bonds fail, yet all of these bond failures occur at the periphery of the agglomerate, its structure may not be significantly affected. Only 1% of the bonds may fail if the agglomerate is loaded in a different

manner. However, this may cause the agglomerate to split into several large fragments if these bonds are located at key points in the structure. The latter is a much more significant alteration of the agglomerate's structure, but the implications could not be known by simply comparing the numbers of failed bonds.

The discrete element model that was developed for a single agglomerate was very complex, consisting of approximately 700 spheres with a lognormal distribution of diameters and linked by parallel bonds. A completely different philosophy was used when developing the probabilistic model described in Chapter 6. Many simplifying assumptions were made: the geometry of the agglomerates was not considered explicitly and they were treated as monosized spheres, or as point masses from a kinetic perspective; the radial and tangential components of air velocity were disregarded; and the particles were assumed to be uniformly distributed over the cross-sectional area. The applications for such a model are, of course, quite different to the detailed DEM. It provides no information about the microstructural fabric changes that occur within the agglomerates, instead giving statistics of the distribution in impact force and the percentage of the particles which fail due to this loading. One major advantage of this model was that it was composed of a series of smaller sub-models. This means that if a researcher intends to apply this probabilistic approach, they can easily simplify some of the sub-models if those effects are deemed unimportant, or incorporate more sophisticated sub-models if effects are thought to be highly significant, without having to develop the entire model again. Thus, the probabilistic model can be regarded as a number of interacting components, any of which could be replaced by a reasonable alternative without creating difficulties for the functionality of the model as a whole.

Ideally, the DEM and the probabilistic model could be combined by replacing the idealised spheres of the probabilistic model with the calibrated agglomerates from the detailed DEM. The computational requirements for simulating a large population of agglomerates makes this approach infeasible at present. However, it may become feasible in the near future due to constant advances in computational power (Koh and Magee, 2006; Nagy et al., 2010). Until this occurs, the compromise which is often made is to progressively reduce the detail as the number of particles to be simulated increases.

The main conclusions of the work described in this thesis are given below; more detailed conclusions are provided at the end of each chapter:

- Mode of conveying and air velocity had a statistically-significant effect on bulk density at a 95% level, while the former was also significant for D[4,3] (95%) and for wettability (90%). A polynomial model was used to show that air velocity was significant only for dilute phase conveying, and not for dense phase. The changes in quality characteristics of infant formulae caused by pneumatic transport should

be minimal, irrespective of the settings chosen for the other conveying parameters, provided that the air velocity is selected to ensure dense phase conveying.

- When individual agglomerates of infant formula were subjected to quasi-static uniaxial compression, both the force at failure and stiffness of the agglomerates, which were strongly correlated, increased with the protein to fat ratio while the opposite trend was seen for strain at failure. Those formulae which had the highest forces at failure were also least susceptible to attrition when pneumatically conveyed. Bulk densities of the four infant formulae tested were directly related to the percentage of protein in the compositions, while the percentage surface free fat increased with the fat content of the formulae.
- It was demonstrated that simple "one factor at a time" parameter studies were severely flawed for calibration of discrete element models of bonded agglomerates. The Taguchi method was applied and shown to be suitable for such calibrations, although it is important to be aware of potential confoundings when assigning the factors to columns and to include significant interactive effects in the analysis.
- A DEM was developed and calibrated for quasi-static, uniaxial compression of individual agglomerates of one typical infant formula. Although the model was difficult to calibrate because of the necessity to capture the variability of the physical agglomerates, the selected responses (force and strain at failure, and agglomerate stiffness) generally compared well for the physical and simulated agglomerates, as did Weibull statistics of failure. Force at failure and agglomerate stiffness were strongly correlated, which was also the case for the agglomerates tested experimentally. When the applicability of the DEM to dynamic loading was evaluated, the model was found to give relatively good results, although it was important to select an appropriate value for the local damping coefficient.
- A novel probabilistic model was developed for pneumatic conveying of particles. This model was capable of providing insights into the effect of changing parameters of the conveying process without the requirement to conduct experimental trials or simulations. A major advantage of this model was its modular structure, which permitted parts of the model to either be simplified or else replaced with more sophisticated alternatives without affecting the functionality of the model as a whole.

References[†]

Aarseth, K.A., 2004. Attrition of feed pellets during pneumatic conveying: the influence of velocity and bend radius. *Biosystems Engineering*, **89**(2): 197–213.

Abbott Ireland. Abbott Ireland Nutritional Division, Cootehill. http://www.abbott.ie/locations-aindcootehill.

Adams, M.J., Mullier, M.A., and Seville, J.P.K., 1994. Agglomerate strength measurement using a uniaxial confined compression test. *Powder Technology*, **78**(1): 5–13.

Advertising Standards Authority, 2010. ASA Adjudication on John Wyeth & Brother Ltd. http://www.asa.org.uk/Complaints-and-ASA-action/Adjudications/2010/3/John-Wyeth--Brother-Ltd/TF_ADJ_48288.aspx.

Agarwal, V.K., Mills, D., and Mason, J.S., 1985. Some aspects of bend erosion in pneumatic conveying system pipelines. *Bulk Solids Handling*, **5**(5): 1085–1090.

Al-Raoush, R. and Alsaleh, M., 2007. Simulation of random packing of polydisperse particles. *Powder Technology*, **176**(1): 44–55.

Antonyuk, S., Tomas, J., Heinrich, S., and Mörl, L., 2005. Breakage behaviour of spherical granulates by compression. *Chemical Engineering Science*, **60**(14): 4031–4044.

Asaf, Z., Rubinstein, D., and Shmulevich, I., 2006. Evaluation of link-track performances using DEM. *Journal of Terramechanics*, **43**(2): 141–161.

Barletta, B.J. and Barbosa-Cánovas, G.V., 1993. Fractal Analysis to Characterize Ruggedness Changes in Tapped Agglomerated Food Powders. *Journal of Food Science*, **58**(5): 1030–1035.

Barrett, A.H. and Peleg, M., 1995. Applications of Fractal Analysis to Food Structure. *Lebensmittel-Wissenschaft und-Technologie*, **28**(6): 553–563.

Bawden, T., 2009. Pfizer to merge with Wyeth in $68bn deal. *Times Online*, 26th January 2009. http://www.thetimes.co.uk/tto/health/article2171332.ece.

Bayer Healthcare. Our Range. http://www.novalac.com.au/our-range.asp.

[†]References to online sources were verified at the time of submission. Note that it is inevitable that some of these will become invalid over time; there is little that can be done to prevent this.

Belheine, N., Plassiard, J.P., Donzé, F.V., Darve, F., and Seridi, A., 2009. Numerical simulation of drained triaxial test using 3D discrete element modeling. *Computers and Geotechnics*, **36**(1–2): 320–331.

Benkovic, M. and Bauman, I., 2009. Flow properties of commercial infant formula powders. *World Academy of Science, Engineering and Technology*, **54**: 495–499.

Bika, D.G., Gentzler, M., and Michaels, J.N., 2001. Mechanical properties of agglomerates. *Powder Technology*, **117**(1–2): 98–112.

Bobet, A., Fakhimi, A., Johnson, S., Morris, J., Tonon, F., and Yeung, M.R., 2009. Numerical models in discontinuous media: Review of advances for rock mechanics applications. *Journal of Geotechnical and Geoenvironmental Engineering*, **135**(11): 1547–1561.

Box, G.E.P., Bisgaard, S., and Fung, C.A., 1988. An explanation and critique of Taguchi's contributions to quality engineering. *Quality and Reliability Engineering International*, **4**(2): 123–131.

Brosh, T., Kalman, H., and Levy, A., 2011. DEM simulation of particle attrition in dilute-phase pneumatic conveying. *Granular Matter*, **13**(2): 175–181.

Cavarretta, I., 2009. *The Influence of Particle Characteristics on the Engineering Behaviour of Granular Materials*. Ph.D. thesis, Imperial College London.

Chapelle, P., Abou-Chakra, H., Christakis, N., Bridle, I., Patel, M.K., Baxter, J., Tuzun, U., and Cross, M., 2004. Numerical predictions of particle degradation in industrial-scale pneumatic conveyors. *Powder Technology*, **143–144**: 321–330.

Chapelle, P., Christakis, N., Abou-Chakra, H., Bridle, I., Bradley, M.S.A., Patel, M.K., and Cross, M., 2004. Computational model for prediction of particle degradation during dilute phase pneumatic conveying: modelling of dilute phase pneumatic conveying. *Advanced Powder Technology*, **15**(1): 31–49.

Chareyre, B. and Villard, P., 2002. Discrete element modeling of curved geosynthetic anchorages with known macro-properties. In: H. Konietzky (Ed.) *Numerical Modeling in Micromechanics via Particle Methods*, pp. 197–204. Balkema, Lisse.

Cheng, Y.P., Nakata, Y., and Bolton, M.D., 2003. Discrete element simulation of crushable soil. *Géotechnique*, **53**(7): 633–641.

Clift, R. and Gauvin, W.H., 1970. The motion of particles in turbulent gas streams. *Proceedings of Chemeca '70*, **1**: 14–28.

Codex Alimentarius, 2007. Codex Alimentarius official standard 72, Standard for infant formula and formulas for special medical purposes intended for infants, Rev.1. http://www.codexalimentarius.net/download/standards/288/CXS_072e.pdf.

Coetzee, C.J. and Els, D.N.J., 2009. Calibration of discrete element parameters and the modelling of silo discharge and bucket filling. *Computers and Electronics in Agriculture*, **65**(2): 198–212.

Coop, M.R., Sorensen, K.K., Bodas Freitas, T., and Georgoutsos, G., 2004. Particle breakage during shearing of a carbonate sand. *Géotechnique*, **54**(3): 157–163.

Cronin, K. and Gleeson, J.P., 2007. Chapter 16: Monte Carlo Simulation. In: S.S. Sablani, M.S. Rahman, A.K. Datta, and A.S. Mujumdar (Eds.) *Handbook of Food and Bioprocess Modeling Techniques*, pp. 501–531. CRC Press, Florida, 1st ed.

Cundall, P.A., 2001. A discontinuous future for numerical modelling in geomechanics? *Geotechnical Engineering*, **149**(1): 41–47.

Cundall, P.A. and Hart, R.D., 2004. Numerical modelling of discontinua. *Engineering Computations*, **9**(2): 101–113.

Cundall, P.A. and Strack, O.D.L., 1979. A discrete numerical model for granular assemblies. *Géotechnique*, **29**(1): 47–65.

D'Addetta, G.A., Kun, F., and Ramm, E., 2002. On the application of a discrete model to the fracture process of cohesive granular materials. *Granular Matter*, **4**(2): 77–90.

Deng, T., Chaudhry, A.R., Patel, M., Hutchings, I., and Bradley, M.S.A., 2005. Effect of particle concentration on erosion rate of mild steel bends in a pneumatic conveyor. *Wear*, **258**(1–4): 480–487.

Dept. of Agriculture, Fisheries and Food, 2010. Irish Food Processing Sector. http://www.agriculture.gov.ie/media/migration/agri-foodindustry/foodharvest2020/foodharvest2020/2020strategy/2020FoodProcessingSector.doc.

Devaux, M.F., Taralova, I., Levy-Vehel, J., Bonnin, E., Thibault, J.F., and Guillon, F., 2006. Contribution of image analysis to the description of enzymatic degradation kinetics for a particulate food material. *Journal of Food Engineering*, **77**(4): 1096–1107.

Di Renzo, A. and Di Maio, F.P., 2004. Comparison of contact-force models for the simulation of collisions in DEM-based granular flow codes. *Chemical Engineering Science*, **59**(3): 525–541.

Doležalová, M., Czene, P., and Havel, F., 2002. Micromechanical modeling of stress path effects using PFC2D code. In: H. Konietzky (Ed.) *Numerical Modeling in Micromechanics via Particle Methods*, pp. 173–182. Balkema, Lisse.

Donohue, S., O'Sullivan, C., and Long, M., 2009. Particle breakage during cyclic triaxial loading of a carbonate sand. *Géotechnique*, **59**(5): 477–482.

Donzé, F.V., Richefeu, V., and Magnier, S.A., 2008. Advances in Discrete Element

Method Applied to Soil, Rock and Concrete Mechanics. http://xa.yimg.com/kq/groups/2670907/1137192241/name/Donze_ppr.pdf.

Elghobashi, S. and Truesdell, G.C., 1992. Direct simulation of particle dispersion in a decaying isotropic turbulence. *Journal of Fluid Mechanics*, **242**: 655–700.

Entremont Alliance. Nutribio. http://www.entremont-alliance.com/the_group/subsidiaries/nutribio/.

Eskin, D., Leonenko, Y., and Vinogradov, O., 2004. Engineering model of dilute pneumatic conveying. *Journal of Engineering Mechanics*, **130**(7): 794–799.

Eskin, D., Leonenko, Y., and Vinogradov, O., 2007. An engineering model of dilute polydisperse pneumatic conveying. *Chemical Engineering and Processing*, **46**(3): 247–256.

European Commission, December 2006. Commission Directive 2006/141/EC of 22 December 2006 on infant formulae and follow-on formulae and amending Directive 1999/21/EC Text with EEA relevance. *Official Journal of the European Union*, **L401**: 1–33. http://eur-lex.europa.eu/LexUriServ/LexUriServ.do?uri=OJ:L:2006:401:0001:0033:EN:PDF.

European Commission Food and Veterinary Office, 2007. Final report of a mission carried out in Ireland from 10 to 14 September 2007 in order to evaluate the official controls over the production and placing on the market of infant formulae, follow-on formulae and baby foods, including the supply chain. Inspection Number: 2007–7148. http://ec.europa.eu/food/fvo/act_getPDF.cfm?PDF_ID=6682.

European Communities (Infant Formulae and Follow-On Formulae) (Amendment) Regulations, 2009. http://www.dohc.ie/legislation/statutory_instruments/pdf/si20090209.pdf.

European Communities (Infant Formulae and Follow-On Formulae) Regulations, 2007. http://www.dohc.ie/legislation/statutory_instruments/pdf/si20070852.pdf.

FAO/WHO Food Standards Codex Alimentarius, 2010. http://www.codexalimentarius.net/web/index_en.jsp.

Favier, J., Curry, D., and LaRoche, R., April 2010. Calibration of DEM material models to approximate bulk particle characteristics. *6th World Congress on Particle Technology*, Nuremberg, Germany.

Favier, J.F., Abbaspour-Fard, M.H., Kremmer, M., and Raji, A.O., 1999. Shape representation of axi-symmetrical, non-spherical particles in discrete element simulation using multi-element model particles. *Engineering Computations*, **16**(4): 467–480.

Feng, Y.T., Han, K., and Owen, D.R.J., 2003. Filling domains with disks: an advancing front approach. *International Journal for Numerical Methods in Engineering*, **56**(5): 699–713.

Feng, Z., Zuo, M.J., and Chu, F., 2010. Application of regularization dimension to gear damage assessment. *Mechanical Systems and Signal Processing*, **24**(4): 1081–1098.

Fitzpatrick, J.J., Barry, K., Cerqueira, P.S.M., Iqbal, T., O'Neill, J., and Roos, Y.H., 2007. Effect of composition and storage conditions on the flowability of dairy powders. *International Dairy Journal*, **17**(4): 383–392.

Food and Drink Industry Ireland, 2011. Food Industry in Ireland → Sector Profile. http://www.fdii.ie/Sectors/FDII/FDII.nsf/vPages/Food_Industry_in_Ireland~sector-profile.

Foroutan-pour, K., Dutilleul, P., and Smith, D.L., 1999. Advances in the implementation of the box-counting method of fractal dimension estimation. *Applied Mathematics and Computation*, **105**(2–3): 195–210.

Fox, P.F. and McSweeney, P.L.H., 1998. *Dairy Chemistry and Biochemistry*. Kluwer Academic/Plenum Publishers, New York, 1st ed.

Fox, P.F. and McSweeney, P.L.H. (Eds.), 2003. *Advanced dairy chemistry: Proteins, Part B*, vol. 1. Kluwer Academic/Plenum Publishers, New York, 3rd ed.

Fox, R.W., Pritchard, P.J., and McDonald, A.T., 2010. *Introduction to Fluid Mechanics*. John Wiley & Sons, New Jersey, 7th ed.

Fraige, F.Y. and Langston, P.A., 2006. Horizontal pneumatic conveying: a 3d distinct element model. *Granular Matter*, **8**(2): 67–80.

Frye, L. and Peukert, W., 2002. Attrition of bulk solids in pneumatic conveying: mechanisms and material properties. *Particulate Science and Technology*, **20**(4): 267–282.

GEA Niro, 2005. GEA Niro Method No. A 10 a: Surface free fat of powder. http://www.niro.com/niro/cmsdoc.nsf/WebDoc/ndkw6u9c45.

GEA Niro, 2006. GEA Niro Method No. A 2 a: Powder bulk density. http://www.niro.com/niro/cmsdoc.nsf/WebDoc/ndkw6u9atz.

GEA Niro, 2009. GEA Niro Method No. A 5 b: Wettability IDF method. http://www.niro.com/niro/cmsdoc.nsf/WebDoc/ndkw6u9bd3.

Ghaboussi, J. and Barbosa, R., 1990. Three-dimensional discrete element method for granular materials. *International Journal for Numerical and Analytical Methods in Geomechanics*, **14**(7): 451–472.

Ghadiri, M., Moreno-Atanasio, R., Hassanpour, A., and Antony, S.J., 2007. Chapter 19: Analysis of Agglomerate Breakage. In: A.D. Salman, M. Ghadiri, and M.J. Hounslow

(Eds.) *Particle Breakage*, vol. 12 of *Handbook of Powder Technology*, pp. 837–872. Elsevier Science B.V., Amsterdam, 1st ed.

Ghadiri, M. and Zhang, Z., 2002. Impact attrition of particulate solids. Part 1: A theoretical model of chipping. *Chemical Engineering Science*, **57**(17): 3659–3669.

Gidaspow, D., 1994. *Multiphase Flow and Fluidization: Continuum and Kinetic Theory Descriptions*. Academic Press, Boston.

Gilardi, G. and Sharf, I., 2002. Literature survey of contact dynamics modelling. *Mechanism and Machine Theory*, **37**(10): 1213–1239.

Global Industry Analysts, Inc. Report, 2010. Global Baby Foods and Infant Formula Market to Reach US$23.8 Billion by 2015, According to New Report by Global Industry Analysts, Inc. http://www.prweb.com/releases/baby_foods_market/infant_formula_market/prweb4123354.htm.

Golchert, D., Moreno, R., Ghadiri, M., and Litster, J., 2004. Effect of granule morphology on breakage behaviour during compression. *Powder Technology*, **143–144**(4): 84–96.

Goldhirsch, I., 2008. Introduction to granular temperature. *Powder Technology*, **182**(2): 130–136.

Guo, M.R., Hendricks, G.M., and Kindstedt, P.S., 1998. Component Distribution and Interactions in Powdered Infant Formula. *International Dairy Journal*, **8**(4): 333–339.

Guo, M.R., Hendricks, G.M., Kindstedt, P.S., Flynn, A., and Fox, P.F., 1996. Nitrogen and mineral distribution in infant formulae. *International Dairy Journal*, **6**(10): 963–979.

Han, T., Levy, A., and Kalman, H., 2003. DEM simulation for attrition of salt during dilute-phase pneumatic conveying. *Powder Technology*, **129**(1–3): 92–100.

Hardin, B.O., 1985. Crushing of soil particles. *Journal of Geotechnical Engineering*, **111**(10): 1177–1192.

Harireche, O. and McDowell, G.R., 2003. Discrete element modelling of cyclic loading of crushable aggregates. *Granular Matter*, **5**(3): 147–151.

Hart, R., Cundall, P.A., and Lemos, J., 1988. Formulation of a three-dimensional distinct element model – Part II. Mechanical calculations for motion and interaction of a system composed of many polyhedral blocks. *International Journal of Rock Mechanics and Mining Sciences & Geomechanics Abstracts*, **25**(3): 117–125.

Harzer, G., Haug, M., and Bindels, J.G., 1986. Biochemistry of human milk in early lactation. *Zeitschrift für Ernährungswissenschaft*, **25**(2): 77–90.

Hausner, H., 1967. Friction conditions in a mass of metal powder. *International Journal of Powder Metallurgy*, **3**(4): 7–13.

Heine, W.E., Klein, P.D., and Reeds, P.J., 1991. The importance of α-lactalbumin in infant nutrition. *The Journal of Nutrition*, **121**(3): 277–283.

Hogekamp, S. and Schubert, H., 2003. Rehydration of food powders. *Food Science and Technology International*, **9**(3): 223–235.

Hong, J. and Tomita, Y., 1995. Analysis of high density gas-solids stratified pipe flow. *International Journal of Multiphase Flow*, **21**(4): 649–665.

Hosseininia, E.S. and Mirghasemi, A.A., 2006. Numerical simulation of breakage of two-dimensional polygon-shaped particles using discrete element method. *Powder Technology*, **166**(2): 100–112.

Hou, T.H., Su, C.H., and Liu, W.L., 2007. Parameters optimization of a nano-particle wet milling process using the Taguchi method, response surface method and genetic algorithm. *Powder Technology*, **173**(3): 153–162.

Infant Formula Australia, 2009. Products and Services – Infant Formula Australia. http://babymilkaustralia.com/products.php.

International Dairy Federation, 1979. International IDF Standard 87, Instant dried milk - Determination of the dispersibility & wettability.

Issa, J.A. and Nelson, R.B., 1993. Numerical analysis of micromechanical behaviour of granular materials. *Engineering Computations*, **9**(2): 211–223.

Itasca Consulting Group, 2008. *PFC2D: Particle Flow Code in Two Dimensions*. Minneapolis, Minnesota, 4th ed.

Itasca Consulting Group, 2008. *PFC3D: Particle Flow Code in Three Dimensions*. Minneapolis, Minnesota, 4th ed.

Jaeger, J.C., 1967. Failure of rocks under tensile conditions. *International Journal of Rock Mechanics and Mining Sciences & Geomechanics Abstracts*, **4**(2): 219–227.

Jenness, R., 1979. The composition of human milk. *Seminars in Perinatology*, **3**(3): 225–239.

Jensen, R.P., Bosscher, P.J., Plesha, M.E., and Edil, T.B., 1999. DEM simulation of granular media-structure interface: effects of surface roughness and particle shape. *International Journal for Numerical and Analytical Methods in Geomechanics*, **23**(6): 531–547.

Johnstone, M. and Ooi, J., April 2010. Calibration of DEM models using rotating drum and confined compression measurements. *6th World Congress on Particle Technology*, Nuremberg, Germany.

Jones, P.J. and Leung, L.S., 1978. A Comparison of Correlations for Saltation Velocity in

Horizontal Pneumatic Conveying. *Industrial and Engineering Chemistry Process Design and Development*, **17**(4): 571–575.

Kafui, K.D. and Thornton, C., 2000. Numerical simulations of impact breakage of a spherical crystalline agglomerate. *Powder Technology*, **109**(1–3): 113–132.

Kalman, H., 1999. Attrition control by pneumatic conveying. *Powder Technology*, **104**(3): 214–220.

Kalman, H., 2000. Attrition of powders and granules at various bends during pneumatic conveying. *Powder Technology*, **112**(3): 244–250.

Kalman, H. and Goder, D., 1998. Design criteria for particle attrition. *Advanced Powder Technology*, **9**(2): 153–167.

Karperien, A., 2007. FracLac Guide. http://rsbweb.nih.gov/ij/plugins/fraclac/FLHelp/Introduction.htm.

Kendall, K.J., 1988. Agglomerate strength. *Powder Metallurgy*, **31**(1): 28–31.

Khanal, M., Schubert, W., and Tomas, J., 2005. DEM simulation of diametrical compression test on particle compounds. *Granular Matter*, **7**(2–3): 83–90.

Khanal, M., Schubert, W., and Tomas, J., 2008. Compression and impact loading experiments of high strength spherical composites. *International Journal of Mineral Processing*, **86**(1–4): 104–113.

Kim, S.J., Kim, K.S., and Jang, H., 2003. Optimization of manufacturing parameters for a brake lining using Taguchi method. *Journal of Materials Processing Technology*, **136**(1–3): 202–208.

Klinzing, G.E., 2001. Dense phase (plug) conveying – observations and projections. In: A. Levy and H. Kalman (Eds.) *Handbook of Conveying and Handling of Particulate Solids*, vol. 10 of *Handbook of Powder Technology*, pp. 329–341. Elsevier Science B.V., Amsterdam, 1st ed.

Klinzing, G.E., 2001. Pneumatic conveying: transport solutions, pitfalls and measurements. In: A. Levy and H. Kalman (Eds.) *Handbook of Conveying and Handling of Particulate Solids*, vol. 10 of *Handbook of Powder Technology*, pp. 291–301. Elsevier Science B.V., Amsterdam, 1st ed.

Koh, H. and Magee, C.L., 2006. A functional approach for studying technological progress: Application to information technology. *Technological Forecasting & Social Change*, **73**(9): 1061–1083.

Konami, M., Tanaka, S., and Matsumoto, K., 2002. Attrition of granules during repeated pneumatic transport. *Powder Technology*, **125**(1): 82–88.

Kwak, B.M., Lee, J.E., Ahn, J.H., and Jeon, T.H., 2009. Laser diffraction particle sizing by wet dispersion method for spray-dried infant formula. *Journal of Food Engineering*, **92**(3): 324–330.

Laing, I.A., 2002. Hypernatraemic dehydration in newborn infants. *Acta Pharmacologica Sinica*, **23**(Supp.): 48–51.

Laouar, S. and Molodtsof, Y., 1998. Experimental characterization of the pressure drop in dense phase pneumatic transport at very low velocity. *Powder Technology*, **95**(2): 165–173.

Li, J., Webb, C., Pandiella, S.S., Campbell, G.M., Dyakowski, T., and McGlinchey, D., 2005. Solids deposition in low-velocity slug flow pneumatic conveying. *Chemical Engineering and Processing*, **44**(2): 167–173.

Lian, G., Thornton, C., and Adams, M.J., 1998. Discrete particle simulation of agglomerate impact coalescence. *Chemical Engineering Science*, **53**(19): 3381–3391.

Lien, E.L., 2003. Infant formulas with increased concentrations of α-lactalbumin. *American Journal of Clinical Nutrition*, **77**(6): 1555S–1558S.

Lin, X. and Ng, T.T., 1997. A three-dimensional discrete element model using arrays of ellipsoids. *Géotechnique*, **47**(2): 319–329.

Lönnerdal, B., 1986. Effects of maternal dietary intake on human milk composition. *The Journal of Nutrition*, **116**(4): 499–513.

Louge, M.Y., Mastorakos, E., and Jenkins, J.T., 1991. The role of particle collisions in pneumatic transport. *Journal of Fluid Mechanics*, **231**: 345–359.

Lucas, A., Lockton, S., and Davies, P.S.W., 1991. Milk for babies and children. *British Medical Journal*, **302**(6772): 350–351.

Lucas, A., Lockton, S., and Davies, P.S.W., 1992. Randomised trial of a ready-to-feed compared with powdered formula. *Archives of Disease in Childhood*, **67**(7): 935–939.

Maghsoodloo, S., Ozdemir, G., Jordan, V., and Huang, C.H., 2004. Strengths and limitations of Taguchi's contributions to quality, manufacturing, and process engineering. *Journal of Manufacturing Systems*, **23**(2): 73–126.

Mahapatra, S.S., Patnaik, A., and Satapathy, A., 2008. Taguchi method applied to parametric appraisal of erosion behavior of GF-reinforced polyester composites. *Wear*, **265**(1–2): 214–222.

Malave-Lopez, J. and Peleg, M., 1986. Mechanical attrition rate measurements in agglomerated instant coffee. *Journal of Food Science*, **51**(3): 687–690.

Malvern Instruments Ltd., 2004. *PharmaVision 830 System Manager's Manual*. Malvern, Worcestershire. Version 1.1.

Mandelbrot, B., 1982. *The Fractal Geometry of Nature*. W.H. Freeman & Co., San Francisco, 1st ed.

Marcus, R.D., Leung, L.S., Klinzing, G.E., and Rizk, F., 1990. *Pneumatic conveying of solids: a theoretical and practical approach*. Chapman and Hall, London, 1st ed.

Marhefka, D.W. and Orin, D.E., 1996. Simulation of contact using a nonlinear damping model. *Robotics and Automation*, pp. 1662–1668. Proceedings of the IEEE International Conference on Robotics and Automation (22nd–28th Apr.), Minneapolis, Minnesota.

Martin, A. and Sorkin, A.R., 2007. Nestlé Agrees to Buy Gerber From Novartis. *The New York Times*, 13th April 2007. http://www.nytimes.com/2007/04/13/business/worldbusiness/13gerber-web.html.

Mason, J.S. and Smith, B.V., 1972. The erosion of bends by pneumatically conveyed suspensions of abrasive particles. *Powder Technology*, **6**(6): 323–335.

Mayo Clinic, 2010. Infant formula: Your questions answered. http://www.mayoclinic.com/health/infant-formula/PR00058.

McDowell, G.R. and Amon, A., 2000. The application of Weibull statistics to the fracture of soil particles. *Soils and Foundations*, **40**(5): 133–141.

McDowell, G.R. and Bolton, M.D., 1998. On the micromechanics of crushable aggregates. *Géotechnique*, **48**(5): 667–679.

McDowell, G.R. and Harireche, O., 2002. Discrete element modelling of yielding and normal compression of sand. *Géotechnique*, **52**(4): 299–304.

Michelson, M. and Stevenson, R., 2007. Danone offers $17 bln for food firm Numico. *Reuters*, 9th July 2007. http://www.reuters.com/article/idUSWEB467920070709.

Mills, D. and Mason, J.S., 1981. Conveying velocity effects in bend erosion. *Journal of Pipelines*, **1**(1): 69–81.

Mindlin, R.D. and Deresiewicz, H., 1953. Elastic spheres in contact under varying oblique forces. *Journal of Applied Mechanics*, **20**(9): 327–344.

Molerus, O., 1996. Overview: Pneumatic transport of solids. *Powder Technology*, **88**(3): 309–321.

Montgomery, D.C., 2009. *Design and Analysis of Experiments [International Student Version]*. John Wiley & Sons, New York, 7th ed.

Moreno-Atanasio, R. and Ghadiri, M., 2006. Mechanistic analysis and computer simula-

tion of impact breakage of agglomerates: Effect of surface energy. *Chemical Engineering Science*, **61**(8): 2476–2481.

Nagy, B., Farmer, J.D., Trancik, J.E., and Gonzales, J.P., 2010. Superexponential long-term trends in information technology. http://santafe.edu/media/workingpapers/10-11-030.pdf.

National Dairy Council, 2008. Dairy: Food for Life. A strategy to promote Irish milk & dairy products 2008– 2012. http://www.ndc.ie/docs/NDCstrategyreporExsummary.pdf.

Ng, T.T., 2004. Shear strength of assemblies of ellipsoidal particles. *Géotechnique*, **54**(10): 659–669.

Nicholson, A., 2009. Nutrition for infant and toddler development. *Irish Medical News*, Monday 30th November 2009. http://www.imn.ie/clinical/clinical-review/51-nutrition-for-infant-and-toddler-development.

Nicolaï, B.M., Scheerlinck, N., and Hertog, M.L.A.T.M., 2007. Chapter 8: Probabilistic Modeling. In: S.S. Sablani, M.S. Rahman, A.K. Datta, and A.S. Mujumdar (Eds.) *Handbook of Food and Bioprocess Modeling Techniques*, pp. 265–289. CRC Press, Florida, 1st ed.

Ning, Z., Boerefijn, R., Ghadiri, M., and Thornton, C., 1997. Distinct element simulation of impact breakage of lactose agglomerates. *Advanced Powder Technology*, **8**(1): 15–37.

Nolan, G.T. and Kavanagh, P.E., 1992. Computer simulation of random packing of hard spheres. *Powder Technology*, **72**(2): 149–155.

Noonan, L., 2010. Agri-business plan to put it at centre of economic recovery. *Irish Independent*, Friday 22nd Jan. 2010. http://www.independent.ie/business/irish/agribusiness-plan-to-put-it-at-centre-of-economic-recovery-2026536.html.

Norton-Smith, D., 2008. A Guide to Infant Formula. Which Preparation is Best For Your Baby? http://www.suite101.com/content/a-guide-to-infant-formula-a48908.

Nussinovitch, A., Corradini, M.G., Normand, M.D., and Peleg, M., 2000. Effect of sucrose on the mechanical and acoustic properties of freeze-dried agar, κ-carrageenan and gellan gels. *Journal of Texture Studies*, **31**(2): 205–223.

Nutri Seven Pty. Ltd., 2010. Nutri Seven OEM Infant Formula Stage 1. http://nutriseven.com.au/stage1.html.

Nutricia, 2011. About Nutricia. http://www.nutricia.ie/about.

Oates, R.K., 1973. Infant-feeding Practices. *British Medical Journal*, **2**(5869): 762–764.

Oesterle, B. and Petitjean, A., 1993. Simulation of particle-to-particle interactions in gas solid flows. *International Journal of Multiphase Flow*, **19**(1): 199–211.

Oktem, H., Erzurumlu, T., and Uzman, I., 2007. Application of Taguchi optimization technique in determining plastic injection molding process parameters for a thin-shell part. *Materials and Design*, **28**(4): 1271–1278.

Oliveira, V., Prell, M., Smallwood, D., and Frazão, E., 2001. Infant Formula Prices and Availability: Final Report to Congress. Document E-FAN-02-001; Economic Research Service of the United States Dept. of Agriculture. http://www.ers.usda.gov/publications/efan02001/efan02001.pdf.

Ortega-Rivas, E., 2009. Bulk Properties of Food Particulate Materials: An Appraisal of their Characterisation and Relevance in Processing. *Food and Bioprocess Technology*, **2**(1): 28–44.

O'Sullivan, C., October 2008. Particle-Based Discrete Element Modelling: A Geomechanics Overview. *12th International Conference of International Association for Computer Methods and Advances in Geomechanics*, Goa, India.

O'Sullivan, C., 2011. *Particulate Discrete Element Modelling*. Taylor & Francis, Oxford, 1st ed.

Ozbay, E., Oztas, A., Baykasoglu, A., and Ozbebek, H., 2009. Investigating mix proportions of high strength self compacting concrete by using Taguchi method. *Construction and Building Materials*, **23**(2): 694–702.

Pasricha, S., Frost, and Sullivan, 2009. Safe Milk for Infants. http://www.asiafoodjournal.com/article-6464-safemilkforinfants-Asia.html.

PBM International Ltd., 2011. Product Line. http://www.pbminternational.com/product.aspx.

Peleg, M., 1977. Flowability of food powders and methods for its evaluation: a review. *Journal of Food Process Engineering*, **1**(4): 303–328.

Peleg, M., 1993. Fractals and Foods. *Critical Reviews in Food Science and Nutrition*, **33**(2): 149–165.

Peleg, M., February 2003. The mechanical properties of brittle, cellular and particulated foods. *3rd International Symposium on Food Rheology and Structure*, Zürich, Switzerland.

Peleg, M. and McClements, J., 1997. Measures of line jaggedness and their use in foods textural evaluation. *Critical Reviews in Food Science and Nutrition*, **37**(6): 491–518.

Pfizer Ireland, 2011. Business Operations. http://www.pfizer.ie/operations.cfm.

Písecký, J., 1997. *Handbook of Milk Powder Manufacture*. Niro A/S, Copenhagen.

Potyondy, D.O. and Cundall, P.A., 2004. A bonded-particle model for rock. *International Journal of Rock Mechanics and Mining Sciences*, **41**(8): 1329–1364.

PR Newswire, 2010. Perrigo Closes Acquisition of Infant Formula Manufacturer PBM Holdings. *PR Newswire*, 3rd May 2010. http://www.prnewswire.com/news-releases/perrigo-closes-acquisition-of-infant-formula-manufacturer-pbm-holdings-92658629.html.

Present, R.D., 1958. *Kinetic theory of gases*. International Series in Pure and Applied Physics, McGraw-Hill, New York.

Rajniak, P., Dhanasekharan, K., Sinka, C., MacPhail, N., and Chern, R., 2008. Modeling and measurement of granule attrition during pneumatic conveying in a laboratory scale system. *Powder Technology*, **185**(3): 202–210.

Rajniak, P., Stepanek, F., K. Dhanasekharan and, R.F., Mancinelli, C., and Chern, R.T., 2009. A combined experimental and computational study of wet granulation in a Wurster fluid bed granulator. *Powder Technology*, **189**(2): 190–201.

Renfrew, M.J., Ansell, P., and Macleod, K.L., 2003. Formula feed preparation: helping reduce the risks; a systematic review. *Archives of Disease in Childhood*, **88**(10): 855–858.

Robertson, D. and Bolton, M.D., May 2001. DEM simulations of crushable grains and soils. *4th International Conference on Micromechanics of Granular Media, Powders and Grains*, Sendai, Japan.

Rogers, G.F.C. and Mayhew, Y.R., 1995. *Thermodynamic and Transport Properties of Fluids*. Blackwell Publishing Ltd., Oxford, 5th ed.

Ross, P.J., 1988. *Taguchi techniques for quality engineering: loss function, orthogonal experiments, parameter and tolerance design*. McGraw-Hill, New York, 1st ed.

Rozenblat, Y., Portnikov, D., Levy, A., Kalman, H., Aman, S., and Tomas, J., 2011. Strength distribution of particles under compression. *Powder Technology*, **208**(1): 215–224.

Rudloff, S. and Kunz, C., 1997. Protein and nonprotein nitrogen components in human milk, bovine milk, and infant formula: quantitative and qualitative aspects in infant nutrition. *Journal of Pediatric Gastroenterology and Nutrition*, **24**(3): 328–344.

Rumpf, H., 1962. The strength of granules and agglomerates. In: W.A. Knepper (Ed.) *Agglomeration*, pp. 379–418. Wiley-Interscience, New York.

Russ, J.C., 1994. *Fractal Surfaces*. Plenum Press, New York, 1st ed.

Ryan, R., 2010. More than 2,500 agricultural science students to get farm talks. *Irish Examiner*, Wednesday 24th Feb. 2010. http://www.examiner.ie/business/more-than-2500-agricultural-science-students-to-get-farm-talks-112966.html.

Sakai, M. and Koshizuka, S., 2009. Large-scale discrete element modeling in pneumatic conveying. *Chemical Engineering Science*, **64**(3): 533–539.

Salman, A.D., Hounslow, M.J., and Verba, A., 2002. Particle fragmentation in dilute phase pneumatic conveying. *Powder Technology*, **126**(2): 109–115.

Samimi, A., Ghadiri, M., Boerefijn, R., Groot, A., and Kohlus, R., 2003. Effect of structural characteristics on impact breakage of agglomerates. *Powder Technology*, **130**(1–3): 428–435.

Samimi, A., Hassanpour, A., and Ghadiri, M., 2005. Single and bulk compressions of soft granules: Experimental study and DEM evaluation. *Chemical Engineering Science*, **60**(14): 3993–4004.

Samimi, A., Moreno, R., and Ghadiri, M., 2004. Analysis of impact damage of agglomerates: effect of impact angle. *Powder Technology*, **143–144**: 97–109.

Sanganwar, G.P. and Gupta, R.B., 2008. Enhancement of Shelf Life and Handling Properties of Drug Nanoparticles: Nanoscale Mixing of Itraconazole with Silica. *Industrial & Engineering Chemistry Research*, **47**(14): 4717–4725.

Santiso, E. and Muller, E.A., 2002. Dense packing of binary and polydisperse hard spheres. *Molecular Physics*, **100**(15): 2461–2469.

Schulze, D., 2008. *Powders and Bulk Solids. Behaviour, Characterisation, Storage and Flow*. Springer-Verlag, Berlin, 1st ed.

Schwager, T., 2007. Coefficient of restitution for viscoelastic discs. *Physical Review E*, **75**(5): 051305.

Schwager, T. and Pöschel, T., 2007. Coefficient of restitution and linear-dashpot model revisited. *Granular Matter*, **9**(6): 465–469.

Serway, R.A., 1996. *Physics for Scientists and Engineers with Modern Physics*. Saunders College Publishing, Philadelphia, 4th ed.

Sheng, Y., Lawrence, C.J., and Briscoe, B.J., 2004. Numerical studies of uniaxial powder compaction process by 3D DEM. *Engineering Computations*, **21**(2–4): 304–317.

SMA Nutrition, 2011. SMA Core Range. http://www.smanutrition.co.uk/sma-products-258.aspx.

Song, Y., Turton, R., and Kayihan, F., 2006. Contact detection algorithms for DEM simulations of tablet-shaped particles. *Powder Technology*, **161**(1): 32–40.

Sørensen, I., Jørgensen, E., and Westergaard, V., 1992. Production of powdered baby foods. *Scandinavian Dairy Information*, **6**(4): 44–47.

Sturm, M., Wirtz, S., Scherer, V., and Denecke, J., 2010. Coupled DEM-CFD simulation of pneumatically conveyed granular media. *Chemical Engineering & Technology*, **33**(7): 1184–1192.

Subero, J. and Ghadiri, M., 2001. Breakage patterns of agglomerates. *Powder Technology*, **120**(3): 232–243.

Sykut, J., Molenda, M., and Horabik, J., 2008. DEM simulation of the packing structure and wall load in a 2-dimensional silo. *Granular Matter*, **10**(4): 273–278.

Taguchi, G., 1987. *System of experimental design: engineering methods to optimize quality and minimize costs*, vol. 1–2. UNIPUB/Kraus International Publications, New York.

Taguchi, G., Konishi, S., and Wu, Y., 1992. *Taguchi methods: research and development*, vol. 1 of *Quality Engineering Series*. American Supplier Institute Inc., Michigan.

TA.HD*plus* Texture Analyzer, 2011. TA.HD*plus* Texture Analyzer. http://www.texturetechnologies.com/texture-analyzers/TA-HDPlus-texture-analyzer.php.

Taylor, T., 1998. Specific energy consumption and particle attrition in pneumatic conveying. *Powder Technology*, **95**(1): 1–6.

The Infant Formula and Follow-on Formula (England) Regulations, 2007. http://www.legislation.gov.uk/uksi/2007/3521/pdfs/uksi_20073521_en.pdf.

Thornton, C., 2000. Numerical simulations of deviatoric shear deformation of granular media. *Géotechnique*, **50**(1): 43–53.

Thornton, C., Ciomocos, M.T., and Adams, M.J., 1999. Numerical simulations of agglomerate impact breakage. *Powder Technology*, **105**(1): 74–82.

Thornton, C., Ciomocos, M.T., and Adams, M.J., 2004. Numerical simulations of diametrical compression tests on agglomerates. *Powder Technology*, **140**(3): 258–267.

Thornton, C. and Liu, L., 2004. How do agglomerates break? *Powder Technology*, **143–144**: 110–116.

Ting, J.M., Khwaja, M., Meachum, L.R., and Rowell, J.D., 1993. An ellipse-based discrete element model for granular materials. *International Journal for Numerical and Analytical Methods in Geomechanics*, **17**(9): 603–623.

Ubic Consulting, 2010. Ingredients for the World Infant Formula Market. http://www.ubic-consulting.com/template/fs/documents/Nutraceuticals/Ingredients-in-the-world-infant-formula-market.pdf.

United Pharmaceuticals, 2010. Infant nutrition. http://www.unitedpharmaceuticals.fr/httpdocs/htmlAnglais/infantNutrition.html.

U.S. Food and Drug Administration, 2003. Powdered Infant Formula: An Overview of Manufacturing Processes. http://www.fda.gov/OHRMS/DOCKETS/AC/03/briefing/3939b1_tab4b.htm.

U.S. Food and Drug Administration, 2010. Federal Food, Drug, and Cosmetic Act, Sec. 412. [21 USC §350a] Requirements for Infant Formulas. http://www.fda.gov/RegulatoryInformation/Legislation/FederalFoodDrugandCosmeticActFDCAct/default.htm.

Visscher, W.M. and Bolsterli, M., 1972. Random packing of equal and unequal spheres in two and three dimensions. *Nature*, **239**: 504–507.

Walstra, P., Geurts, T.J., Noomen, A., Jellema, A., and van Boekel, M.A.J.S., 1999. *Dairy technology: principles of milk properties and processes*. Marcel Dekker Inc., New York.

Wen, C.Y. and Simons, H.P., 1959. Flow characteristics in horizontal fluidized solids transport. *AIChE Journal*, **5**(2): 263–267.

West, A.R., 1999. *Basic solid state chemistry*. John Wiley & Sons, Chichester, 2nd ed.

Wong, N.P., Jenness, R., Keeney, M., and Marth, E.H., 1988. *Fundamentals of Dairy Chemistry*. Van Nostrand Reinhold Co., New York, 3rd ed.

Wu, K.L., Yan, B.H., Huang, F.Y., and Chen, S.C., 2005. Improvement of surface finish on SKD steel using electro-discharge machining with aluminum and surfactant added dielectric. *International Journal of Machine Tools & Manufacture*, **45**(10): 1195–1201.

Wypych, P.W. and Arnold, P.C., 1993. Minimizing wear and particle damage in pneumatic conveying. *Powder Handling and Processing*, **5**(2): 129–134.

Yan, G., Yu, H., and McDowell, G., 2009. Simulation of granular material behaviour using DEM. *Procedia Earth and Planetary Science*, **1**(1): 598–605.

Yan, H. and Barbosa-Cánovas, G.V., 2000. Attrition evaluation for selected agglomerated food powders: The effect of agglomerate size and water activity. *Journal of Food Process Engineering*, **24**(1): 37–49.

Yanko, E.G., 2007. Hygienic engineering of transfer systems for dry particulate materials. *Trends in Food Science & Technology*, **18**(12): 626–631.

Yoon, J., 2007. Application of experimental design and optimization to PFC model calibration in uniaxial compression simulation. *International Journal of Rock Mechanics and Mining Sciences*, **44**(6): 871–889.

Zhang, D. and Whiten, W.J., 1996. The calculation of contact forces between particles using spring and damping models. *Powder Technology*, **88**(1): 59–64.

Zhang, Y., Lim, E.W.C., and Wang, C.H., 2007. Pneumatic transport of granular materials in an inclined conveying pipe: comparison of computational fluid dynamics–discrete element method (CFD-DEM), electrical capacitance tomography (ECT), and particle image velocimetry (PIV) results. *Industrial & Engineering Chemistry Research*, **46**(19): 6066–6083.

Zhang, Z. and Ghadiri, M., 2002. Impact attrition of particulate solids. Part 2: Experimental work. *Chemical Engineering Science*, **57**(17): 3671–3686.

Zhu, H.P., Zhou, Z.Y., Yang, R.Y., and Yu, A.B., 2007. Discrete particle simulation of particulate systems: Theoretical developments. *Chemical Engineering Science*, **62**(13): 3378–3396.

A

Orthogonal Arrays and Triangular Tables

This appendix contains the orthogonal arrays for all the Taguchi experimental designs used in this thesis (Section A.1). Since these arrays are commonly used, they are also provided in numerous literature sources (e.g., Taguchi, 1987, App.11) and in statistical software packages. Triangular tables are provided in Section A.2; these identify the columns (for interactions between two-level factors) or pairs of columns (for interactions between three-level factors) which contain all first-order interactions. Note that a triangular table is not available for the L_{18} array that was used for the conveying experiments in Chapter 2 since, as mentioned in Section 2.2.2, all interactions except one (between the two-level factor in column 1 and the three-level factor in column 2) are partially confounded with the remaining columns in the array.

A.1 Orthogonal Arrays

In the orthogonal arrays below, the numbers 1, 2 and 3 represent factor levels, with 1 being the lowest setting of any factor.

Table A.1: *Standard form of the L_8 orthogonal array*

Row	Column						
	1	2	3	4	5	6	7
1	1	1	1	1	1	1	1
2	1	1	1	2	2	2	2
3	1	2	2	1	1	2	2
4	1	2	2	2	2	1	1

Continued on page 212

Row	Column						
	1	2	3	4	5	6	7
5	2	1	2	1	2	1	2
6	2	1	2	2	1	2	1
7	2	2	1	1	2	2	1
8	2	2	1	2	1	1	2

Table A.2: *Standard form of the L_{18} orthogonal array*[‡]

Row	Column							
	1	2	3	4	5	6	7	8
1	1	1	1	1	1	1	1	1
2	1	1	2	2	2	2	2	2
3	1	1	3	3	3	3	3	3
4	1	2	1	1	2	2	3	3
5	1	2	2	2	3	3	1	1
6	1	2	3	3	1	1	2	2
7	1	3	1	2	1	3	2	3
8	1	3	2	3	2	1	3	1
9	1	3	3	1	3	2	1	2
10	2	1	1	3	3	2	2	1
11	2	1	2	1	1	3	3	2
12	2	1	3	2	2	1	1	3
13	2	2	1	2	3	1	3	2
14	2	2	2	3	1	2	1	3
15	2	2	3	1	2	3	2	1
16	2	3	1	3	2	3	1	2
17	2	3	2	1	3	1	2	3
18	2	3	3	2	1	2	3	1

[‡]This is notable for being a mixed-level array, which was originally derived from a Plackett-Burman design (Box et al., 1988).

Table A.3: *Standard form of the L_{27} orthogonal array*

Row	Column												
	1	2	3	4	5	6	7	8	9	10	11	12	13
1	1	1	1	1	1	1	1	1	1	1	1	1	1
2	1	1	1	1	2	2	2	2	2	2	2	2	2
3	1	1	1	1	3	3	3	3	3	3	3	3	3
4	1	2	2	2	1	1	1	2	2	2	3	3	3
5	1	2	2	2	2	2	2	3	3	3	1	1	1
6	1	2	2	2	3	3	3	1	1	1	2	2	2
7	1	3	3	3	1	1	1	3	3	3	2	2	2
8	1	3	3	3	2	2	2	1	1	1	3	3	3
9	1	3	3	3	3	3	3	2	2	2	1	1	1
10	2	1	2	3	1	2	3	1	2	3	1	2	3
11	2	1	2	3	2	3	1	2	3	1	2	3	1
12	2	1	2	3	3	1	2	3	1	2	3	1	2
13	2	2	3	1	1	2	3	2	3	1	3	1	2
14	2	2	3	1	2	3	1	3	1	2	1	2	3
15	2	2	3	1	3	1	2	1	2	3	2	3	1
16	2	3	1	2	1	2	3	3	1	2	2	3	1
17	2	3	1	2	2	3	1	1	2	3	3	1	2
18	2	3	1	2	3	1	2	2	3	1	1	2	3
19	3	1	3	2	1	3	2	1	3	2	1	3	2
20	3	1	3	2	2	1	3	2	1	3	2	1	3
21	3	1	3	2	3	2	1	3	2	1	3	2	1
22	3	2	1	3	1	3	2	2	1	3	3	2	1
23	3	2	1	3	2	1	3	3	2	1	1	3	2
24	3	2	1	3	3	2	1	1	3	2	2	1	3
25	3	3	2	1	1	3	2	3	2	1	2	1	3
26	3	3	2	1	2	1	3	1	3	2	3	2	1
27	3	3	2	1	3	2	1	2	1	3	1	3	2

Table A.4: *Standard form of the L_{81} orthogonal array*

Row	Column																								
	1	2	3	4	5	6	7	8	9	10	11	12	13	14	15	16	17	18	19	20	21	22	23	24	25
1	1	1	1	1	1	1	1	1	1	1	1	1	1	1	1	1	1	1	1	1	1	1	1	1	1
2	1	1	1	1	1	1	1	1	1	1	1	1	1	2	2	2	2	2	2	2	2	2	2	2	2
3	1	1	1	1	1	1	1	1	1	1	1	1	1	3	3	3	3	3	3	3	3	3	3	3	3
4	1	1	1	1	2	2	2	2	2	2	2	2	2	1	1	1	1	1	1	1	1	1	2	2	2
5	1	1	1	1	2	2	2	2	2	2	2	2	2	2	2	2	2	2	2	2	2	2	3	3	3
6	1	1	1	1	2	2	2	2	2	2	2	2	2	3	3	3	3	3	3	3	3	3	1	1	1
7	1	1	1	1	3	3	3	3	3	3	3	3	3	1	1	1	1	1	1	1	1	1	3	3	3

Row	Column														
	26	27	28	29	30	31	32	33	34	35	36	37	38	39	40
1	1	1	1	1	1	1	1	1	1	1	1	1	1	1	1
2	2	2	2	2	2	2	2	2	2	2	2	2	2	2	2
3	3	3	3	3	3	3	3	3	3	3	3	3	3	3	3
4	2	2	2	2	2	2	3	3	3	3	3	3	3	3	3
5	3	3	3	3	3	3	1	1	1	1	1	1	1	1	1
6	1	1	1	1	1	1	2	2	2	2	2	2	2	2	2
7	3	3	3	3	3	3	2	2	2	2	2	2	2	2	2

Continued on page 215

Table A.4 continued from page 214

Row	Column																								
	1	2	3	4	5	6	7	8	9	10	11	12	13	14	15	16	17	18	19	20	21	22	23	24	25
8	1	1	1	1	3	3	3	3	3	3	3	3	3	2	2	2	2	2	2	2	2	2	1	1	1
9	1	1	1	1	3	3	3	3	3	3	3	3	3	3	3	3	3	3	3	3	3	3	2	2	2
10	1	2	2	2	1	1	1	2	2	2	3	3	3	1	1	1	2	2	2	3	3	3	1	1	1
11	1	2	2	2	1	1	1	2	2	2	3	3	3	2	2	2	3	3	3	1	1	1	2	2	2
12	1	2	2	2	1	1	1	2	2	2	3	3	3	3	3	3	1	1	1	2	2	2	3	3	3
13	1	2	2	2	2	2	2	3	3	3	1	1	1	1	1	1	2	2	2	3	3	3	2	2	2
14	1	2	2	2	2	2	2	3	3	3	1	1	1	2	2	2	3	3	3	1	1	1	3	3	3

Row	Column														
	26	27	28	29	30	31	32	33	34	35	36	37	38	39	40
8	1	1	1	1	1	1	3	3	3	3	3	3	3	3	3
9	2	2	2	2	2	2	1	1	1	1	1	1	1	1	1
10	2	2	2	3	3	3	1	1	1	2	2	2	3	3	3
11	3	3	3	1	1	1	2	2	2	3	3	3	1	1	1
12	1	1	1	2	2	2	3	3	3	1	1	1	2	2	2
13	3	3	3	1	1	1	3	3	3	1	1	1	2	2	2
14	1	1	1	2	2	2	1	1	1	2	2	2	3	3	3

Continued on page 216

Table A.4 continued from page 215

Row	Column																								
	1	2	3	4	5	6	7	8	9	10	11	12	13	14	15	16	17	18	19	20	21	22	23	24	25
15	1	2	2	2	2	2	2	3	3	3	1	1	1	3	3	3	1	1	1	2	2	2	1	1	1
16	1	2	2	2	3	3	3	1	1	1	2	2	2	1	1	1	2	2	2	3	3	3	3	3	3
17	1	2	2	2	3	3	3	1	1	1	2	2	2	2	2	2	3	3	3	1	1	1	1	1	1
18	1	2	2	2	3	3	3	1	1	1	2	2	2	3	3	3	1	1	1	2	2	2	2	2	2
19	1	3	3	3	1	1	1	3	3	3	2	2	2	1	1	1	3	3	3	2	2	2	1	1	1
20	1	3	3	3	1	1	1	3	3	3	2	2	2	2	2	2	1	1	1	3	3	3	2	2	2
21	1	3	3	3	1	1	1	3	3	3	2	2	2	3	3	3	2	2	2	1	1	1	3	3	3

Row	Column														
	26	27	28	29	30	31	32	33	34	35	36	37	38	39	40
15	2	2	2	3	3	3	2	2	2	3	3	3	1	1	1
16	1	1	1	2	2	2	2	2	2	3	3	3	1	1	1
17	2	2	2	3	3	3	3	3	3	1	1	1	2	2	2
18	3	3	3	1	1	1	1	1	1	2	2	2	3	3	3
19	3	3	3	2	2	2	1	1	1	3	3	3	2	2	2
20	1	1	1	3	3	3	2	2	2	1	1	1	3	3	3
21	2	2	2	1	1	1	3	3	3	2	2	2	1	1	1

Continued on page 217

Table A.4 continued from page 216

Row	Column																								
	1	2	3	4	5	6	7	8	9	10	11	12	13	14	15	16	17	18	19	20	21	22	23	24	25
22	1	3	3	3	2	2	2	1	1	1	3	3	3	1	1	1	3	3	3	2	2	2	2	2	2
23	1	3	3	3	2	2	2	1	1	1	3	3	3	2	2	2	1	1	1	3	3	3	3	3	3
24	1	3	3	3	2	2	2	1	1	1	3	3	3	3	3	3	2	2	2	1	1	1	1	1	1
25	1	3	3	3	3	3	3	2	2	2	1	1	1	1	1	1	3	3	3	2	2	2	3	3	3
26	1	3	3	3	3	3	3	2	2	2	1	1	1	2	2	2	1	1	1	3	3	3	1	1	1
27	1	3	3	3	3	3	3	2	2	2	1	1	1	3	3	3	2	2	2	1	1	1	2	2	2
28	2	1	2	3	1	2	3	1	2	3	1	2	3	1	2	3	1	2	3	1	2	3	1	2	3

Row	Column														
	26	27	28	29	30	31	32	33	34	35	36	37	38	39	40
22	1	1	1	3	3	3	3	3	3	2	2	2	1	1	1
23	2	2	2	1	1	1	1	1	1	3	3	3	2	2	2
24	3	3	3	2	2	2	2	2	2	1	1	1	3	3	3
25	2	2	2	1	1	1	2	2	2	1	1	1	3	3	3
26	3	3	3	2	2	2	3	3	3	2	2	2	1	1	1
27	1	1	1	3	3	3	1	1	1	3	3	3	2	2	2
28	1	2	3	1	2	3	1	2	3	1	2	3	1	2	3

Continued on page 218

Table A.4 continued from page 217

Row	Column																								
	1	2	3	4	5	6	7	8	9	10	11	12	13	14	15	16	17	18	19	20	21	22	23	24	25
29	2	1	2	3	1	2	3	1	2	3	1	2	3	2	3	1	2	3	1	2	3	1	2	3	1
30	2	1	2	3	1	2	3	1	2	3	1	2	3	3	1	2	3	1	2	3	1	2	3	1	2
31	2	1	2	3	2	3	1	2	3	1	2	3	1	1	2	3	1	2	3	1	2	3	2	3	1
32	2	1	2	3	2	3	1	2	3	1	2	3	1	2	3	1	2	3	1	2	3	1	3	1	2
33	2	1	2	3	2	3	1	2	3	1	2	3	1	3	1	2	3	1	2	3	1	2	1	2	3
34	2	1	2	3	3	1	2	3	1	2	3	1	2	1	2	3	1	2	3	1	2	3	3	1	2
35	2	1	2	3	3	1	2	3	1	2	3	1	2	2	3	1	2	3	1	2	3	1	1	2	3

Row	Column														
	26	27	28	29	30	31	32	33	34	35	36	37	38	39	40
29	2	3	1	2	3	1	2	3	1	2	3	1	2	3	1
30	3	1	2	3	1	2	3	1	2	3	1	2	3	1	2
31	2	3	1	2	3	1	3	1	2	3	1	2	3	1	2
32	3	1	2	3	1	2	1	2	3	1	2	3	1	2	3
33	1	2	3	1	2	3	2	3	1	2	3	1	2	3	1
34	3	1	2	3	1	2	2	3	1	2	3	1	2	3	1
35	1	2	3	1	2	3	3	1	2	3	1	2	3	1	2

Continued on page 219

Table A.4 continued from page 218

Row	Column																								
	1	2	3	4	5	6	7	8	9	10	11	12	13	14	15	16	17	18	19	20	21	22	23	24	25
36	2	1	2	3	3	1	2	3	1	2	3	1	2	3	1	2	3	1	2	3	1	2	2	3	1
37	2	2	3	1	1	2	3	2	3	1	3	1	2	1	2	3	2	3	1	3	1	2	1	2	3
38	2	2	3	1	1	2	3	2	3	1	3	1	2	2	3	1	3	1	2	1	2	3	2	3	1
39	2	2	3	1	1	2	3	2	3	1	3	1	2	3	1	2	1	2	3	2	3	1	3	1	2
40	2	2	3	1	2	3	1	3	1	2	1	2	3	1	2	3	2	3	1	3	1	2	2	3	1
41	2	2	3	1	2	3	1	3	1	2	1	2	3	2	3	1	3	1	2	1	2	3	3	1	2
42	2	2	3	1	2	3	1	3	1	2	1	2	3	3	1	2	1	2	3	2	3	1	1	2	3

Row	Column														
	26	27	28	29	30	31	32	33	34	35	36	37	38	39	40
36	2	3	1	2	3	1	1	2	3	1	2	3	1	2	3
37	2	3	1	3	1	2	1	2	3	2	3	1	3	1	2
38	3	1	2	1	2	3	2	3	1	3	1	2	1	2	3
39	1	2	3	2	3	1	3	1	2	1	2	3	2	3	1
40	3	1	2	1	2	3	3	1	2	1	2	3	2	3	1
41	1	2	3	2	3	1	1	2	3	2	3	1	3	1	2
42	2	3	1	3	1	2	2	3	1	3	1	2	1	2	3

Continued on page 220

Table A.4 continued from page 219

Row	Column																								
	1	2	3	4	5	6	7	8	9	10	11	12	13	14	15	16	17	18	19	20	21	22	23	24	25
43	2	2	3	1	3	1	2	1	2	3	2	3	1	1	2	3	2	3	1	3	1	2	3	1	2
44	2	2	3	1	3	1	2	1	2	3	2	3	1	2	3	1	3	1	2	1	2	3	1	2	3
45	2	2	3	1	3	1	2	1	2	3	2	3	1	3	1	2	1	2	3	2	3	1	2	3	1
46	2	3	1	2	1	2	3	3	1	2	2	3	1	1	2	3	3	1	2	2	3	1	1	2	3
47	2	3	1	2	1	2	3	3	1	2	2	3	1	2	3	1	1	2	3	3	1	2	2	3	1
48	2	3	1	2	1	2	3	3	1	2	2	3	1	3	1	2	2	3	1	1	2	3	3	1	2
49	2	3	1	2	2	3	1	1	2	3	3	1	2	1	2	3	3	1	2	2	3	1	2	3	1

Row	Column														
	26	27	28	29	30	31	32	33	34	35	36	37	38	39	40
43	1	2	3	2	3	1	2	3	1	3	1	2	1	2	3
44	2	3	1	3	1	2	3	1	2	1	2	3	2	3	1
45	3	1	2	1	2	3	1	2	3	2	3	1	3	1	2
46	3	1	2	2	3	1	1	2	3	3	1	2	2	3	1
47	1	2	3	3	1	2	2	3	1	1	2	3	3	1	2
48	2	3	1	1	2	3	3	1	2	2	3	1	1	2	3
49	1	2	3	3	1	2	3	1	2	2	3	1	1	2	3

Continued on page 221

Table A.4 continued from page 220

Row	Column																								
	1	2	3	4	5	6	7	8	9	10	11	12	13	14	15	16	17	18	19	20	21	22	23	24	25
50	2	3	1	2	2	3	1	1	2	3	3	1	2	2	3	1	1	2	3	3	1	2	3	1	2
51	2	3	1	2	2	3	1	1	2	3	3	1	2	3	1	2	2	3	1	1	2	3	1	2	3
52	2	3	1	2	3	1	2	2	3	1	1	2	3	1	2	3	3	1	2	2	3	1	3	1	2
53	2	3	1	2	3	1	2	2	3	1	1	2	3	2	3	1	1	2	3	3	1	2	1	2	3
54	2	3	1	2	3	1	2	2	3	1	1	2	3	3	1	2	2	3	1	1	2	3	2	3	1
55	3	1	3	2	1	3	2	1	3	2	1	3	2	1	3	2	1	3	2	1	3	2	1	3	2
56	3	1	3	2	1	3	2	1	3	2	1	3	2	2	1	3	2	1	3	2	1	3	2	1	3

Row	Column														
	26	27	28	29	30	31	32	33	34	35	36	37	38	39	40
50	2	3	1	1	2	3	1	2	3	3	1	2	2	3	1
51	3	1	2	2	3	1	2	3	1	1	2	3	3	1	2
52	2	3	1	1	2	3	2	3	1	1	2	3	3	1	2
53	3	1	2	2	3	1	3	1	2	2	3	1	1	2	3
54	1	2	3	3	1	2	1	2	3	3	1	2	2	3	1
55	1	3	2	1	3	2	1	3	2	1	3	2	1	3	2
56	2	1	3	2	1	3	2	1	3	2	1	3	2	1	3

Continued on page 222

Table A.4 continued from page 221

Row	Column																								
	1	2	3	4	5	6	7	8	9	10	11	12	13	14	15	16	17	18	19	20	21	22	23	24	25
57	3	1	3	2	1	3	2	1	3	2	1	3	2	3	2	1	3	2	1	3	2	1	3	2	1
58	3	1	3	2	2	1	3	2	1	3	2	1	3	1	3	2	1	3	2	1	3	2	2	1	3
59	3	1	3	2	2	1	3	2	1	3	2	1	3	2	1	3	2	1	3	2	1	3	3	2	1
60	3	1	3	2	2	1	3	2	1	3	2	1	3	3	2	1	3	2	1	3	2	1	1	3	2
61	3	1	3	2	3	2	1	3	2	1	3	2	1	1	3	2	1	3	2	1	3	2	3	2	1
62	3	1	3	2	3	2	1	3	2	1	3	2	1	2	1	3	2	1	3	2	1	3	1	3	2
63	3	1	3	2	3	2	1	3	2	1	3	2	1	3	2	1	3	2	1	3	2	1	2	1	3

Row	Column														
	26	27	28	29	30	31	32	33	34	35	36	37	38	39	40
57	3	2	1	3	2	1	3	2	1	3	2	1	3	2	1
58	2	1	3	2	1	3	3	2	1	3	2	1	3	2	1
59	3	2	1	3	2	1	1	3	2	1	3	2	1	3	2
60	1	3	2	1	3	2	2	1	3	2	1	3	2	1	3
61	3	2	1	3	2	1	2	1	3	2	1	3	2	1	3
62	1	3	2	1	3	2	3	2	1	3	2	1	3	2	1
63	2	1	3	2	1	3	1	3	2	1	3	2	1	3	2

Continued on page 223

Table A.4 continued from page 222

Row	Column																								
	1	2	3	4	5	6	7	8	9	10	11	12	13	14	15	16	17	18	19	20	21	22	23	24	25
64	3	2	1	3	1	3	2	2	1	3	3	2	1	1	3	2	2	1	3	3	2	1	1	3	2
65	3	2	1	3	1	3	2	2	1	3	3	2	1	2	1	3	3	2	1	1	3	2	2	1	3
66	3	2	1	3	1	3	2	2	1	3	3	2	1	3	2	1	1	3	2	2	1	3	3	2	1
67	3	2	1	3	2	1	3	3	2	1	1	3	2	1	3	2	2	1	3	3	2	1	2	1	3
68	3	2	1	3	2	1	3	3	2	1	1	3	2	2	1	3	3	2	1	1	3	2	3	2	1
69	3	2	1	3	2	1	3	3	2	1	1	3	2	3	2	1	1	3	2	2	1	3	1	3	2
70	3	2	1	3	3	2	1	1	3	2	2	1	3	1	3	2	2	1	3	3	2	1	3	2	1

Row	Column														
	26	27	28	29	30	31	32	33	34	35	36	37	38	39	40
64	2	1	3	3	2	1	1	3	2	2	1	3	3	2	1
65	3	2	1	1	3	2	2	1	3	3	2	1	1	3	2
66	1	3	2	2	1	3	3	2	1	1	3	2	2	1	3
67	3	2	1	1	3	2	3	2	1	1	3	2	2	1	3
68	1	3	2	2	1	3	1	3	2	2	1	3	3	2	1
69	2	1	3	3	2	1	2	1	3	3	2	1	1	3	2
70	1	3	2	2	1	3	2	1	3	3	2	1	1	3	2

Continued on page 224

Table A.4 continued from page 223

Row	Column																								
	1	2	3	4	5	6	7	8	9	10	11	12	13	14	15	16	17	18	19	20	21	22	23	24	25
71	3	2	1	3	3	2	1	1	3	2	2	1	3	2	1	3	3	2	1	1	3	2	1	3	2
72	3	2	1	3	3	2	1	1	3	2	2	1	3	3	2	1	1	3	2	2	1	3	2	1	3
73	3	3	2	1	1	3	2	3	2	1	2	1	3	1	3	2	3	2	1	2	1	3	1	3	2
74	3	3	2	1	1	3	2	3	2	1	2	1	3	2	1	3	1	3	2	3	2	1	2	1	3
75	3	3	2	1	1	3	2	3	2	1	2	1	3	3	2	1	2	1	3	1	3	2	3	2	1
76	3	3	2	1	2	1	3	1	3	2	3	2	1	1	3	2	3	2	1	2	1	3	2	1	3
77	3	3	2	1	2	1	3	1	3	2	3	2	1	2	1	3	1	3	2	3	2	1	3	2	1

Row	Column														
	26	27	28	29	30	31	32	33	34	35	36	37	38	39	40
71	2	1	3	3	2	1	3	2	1	1	3	2	2	1	3
72	3	2	1	1	3	2	1	3	2	2	1	3	3	2	1
73	3	2	1	2	1	3	1	3	2	3	2	1	2	1	3
74	1	3	2	3	2	1	2	1	3	1	3	2	3	2	1
75	2	1	3	1	3	2	3	2	1	2	1	3	1	3	2
76	1	3	2	3	2	1	3	2	1	2	1	3	1	3	2
77	2	1	3	1	3	2	1	3	2	3	2	1	2	1	3

Continued on page 225

Table A.4 continued from page 224

Row	Column																								
	1	2	3	4	5	6	7	8	9	10	11	12	13	14	15	16	17	18	19	20	21	22	23	24	25
78	3	3	2	1	2	1	3	1	3	2	3	2	1	3	2	1	2	1	3	1	3	2	1	3	2
79	3	3	2	1	3	2	1	2	1	3	1	3	2	1	3	2	3	2	1	2	1	3	3	2	1
80	3	3	2	1	3	2	1	2	1	3	1	3	2	2	1	3	1	3	2	3	2	1	1	3	2
81	3	3	2	1	3	2	1	2	1	3	1	3	2	3	2	1	2	1	3	1	3	2	2	1	3

Row	Column														
	26	27	28	29	30	31	32	33	34	35	36	37	38	39	40
78	3	2	1	2	1	3	2	1	3	1	3	2	3	2	1
79	2	1	3	1	3	2	2	1	3	1	3	2	3	2	1
80	3	2	1	2	1	3	3	2	1	2	1	3	1	3	2
81	1	3	2	3	2	1	1	3	2	3	2	1	2	1	3

A.2 Triangular Tables

The numbers in the triangular tables shown below refer to the columns in which a particular interaction is contained. One column number in an interaction is read from the top row and the other from the left-most column of the table. For example, the interaction between the factors in columns 1 and 2 of an L_{27} array is distributed between columns 3 and 4, as shown in Table A.7. As another example, the interaction between columns 4 and 7 of an L_{27} array is contained in columns 9 and 11.

Table A.5: *Triangular table for the L_8 orthogonal array*

I	Column II					
	2	3	4	5	6	7
1	3	2	5	4	7	6
2		1	6	7	4	5
3			7	6	5	4
4				1	2	3
5					3	2
6						1

Table A.6: *Triangular table for the L_9 orthogonal array*

I	Column II		
	2	3	4
1	3,4	2,4	2,3
2		1,4	1,3
3			1,2

Table A.7: *Triangular table for the L_{27} orthogonal array*

I	Column II											
	2	3	4	5	6	7	8	9	10	11	12	13
1	3,4	2,4	2,3	6,7	5,7	5,6	9,10	8,10	8,9	12,13	11,13	11,12
2		1,4	1,3	8,11	9,12	10,13	5,11	6,12	7,13	5,8	6,9	7,10
3			1,2	9,13	10,11	8,12	7,12	5,13	6,11	6,10	7,8	5,9
4				10,12	8,13	9,11	6,13	7,11	5,12	7,9	5,10	6,8
5					1,7	1,6	2,11	3,13	4,12	2,8	4,10	3,9
6						1,5	4,13	2,12	3,11	3,10	2,9	4,8
7							3,12	4,11	2,13	4,9	3,8	2,10

Continued on page 227

I	Column II											
	2	3	4	5	6	7	8	9	10	11	12	13
8								1,10	1,9	2,5	3,7	4,6
9									1,8	4,7	2,6	3,5
10										3,6	4,5	2,7
11											1,13	1,12
12												1,11

Table A.8: *Triangular table for the L_{81} orthogonal array*[†]

I	Column II																
	14	15	16	17	18	19	20	21	22	23	24	25	26	27	28	29	30
1	15,16	14,16	14,15	18,19	17,19	17,18	21,22	20,22	20,21	24,25	23,25	23,24	27,28	26,28	26,27	30,31	29,31
2	17,20	18,21	19,22	14,20	15,21	16,22	14,17	15,18	16,19	26,29	27,30	28,31	23,29	24,30	25,31	23,26	24,27
3	18,22	19,20	17,21	16,21	14,22	15,20	15,19	16,17	14,18	27,31	28,29	26,30	25,30	23,31	24,29	24,28	25,26
4	19,21	17,22	18,20	15,22	16,20	14,21	16,18	14,19	15,17	28,30	26,31	27,29	24,31	25,29	23,30	25,27	23,28
5	23,32	24,33	25,34	26,35	27,36	28,37	29,38	30,39	31,40	14,32	15,33	16,34	17,35	18,36	19,37	20,38	21,39
6	24,34	25,32	23,33	27,37	28,35	26,36	30,40	31,38	29,39	16,33	14,34	15,32	19,36	17,37	18,35	22,39	20,40

[†] Interactions between factors in columns 1–13 of the L_{81} array are identical to those for the L_{27} array, and are given in Table A.7 on p.226.

I	Column II									
	31	32	33	34	35	36	37	38	39	40
1	29,30	33,34	32,34	32,33	36,37	35,37	35,36	39,40	38,40	38,39
2	25,28	35,38	36,39	37,40	32,38	33,39	34,40	32,35	33,36	34,37
3	23,27	36,40	37,38	35,39	34,39	32,40	33,38	33,37	34,35	32,36
4	24,26	37,39	35,40	36,38	33,40	34,38	32,39	34,36	32,37	33,35
5	22,40	14,23	15,24	16,25	17,26	18,27	19,28	20,29	21,30	22,31
6	21,38	15,25	16,23	14,24	18,28	19,26	17,27	21,31	22,29	20,30

Continued on page 229

Table A.8 continued from page 228

I	Column II																
	14	15	16	17	18	19	20	21	22	23	24	25	26	27	28	29	30
7	25,33	23,34	24,32	28,36	26,37	27,35	31,39	29,40	30,38	15,34	16,32	14,33	18,37	19,35	17,36	21,40	22,38
8	26,38	27,39	28,40	29,32	30,33	31,34	23,35	24,36	25,37	20,35	21,36	22,37	14,38	15,39	16,40	17,32	18,33
9	27,40	28,38	26,39	30,34	31,32	29,33	24,37	25,35	23,36	22,36	20,37	21,35	16,39	14,40	15,38	19,33	17,34
10	28,39	26,40	27,38	31,33	29,34	30,32	25,36	23,37	24,35	21,37	22,35	20,36	15,40	16,38	14,39	18,34	19,32
11	29,35	30,36	31,37	23,38	24,39	25,40	26,32	27,33	28,34	17,38	18,39	19,40	20,32	21,33	22,34	14,35	15,36
12	30,37	31,35	29,36	24,40	25,38	23,39	27,34	28,32	26,33	19,39	17,40	18,38	22,33	20,34	21,32	16,36	14,37
13	31,36	29,37	30,35	25,39	23,40	24,38	28,33	26,34	27,32	18,40	19,38	17,39	21,34	22,32	20,33	15,37	16,35

I	Column II									
	31	32	33	34	35	36	37	38	39	40
7	20,39	16,24	14,25	15,23	19,27	17,28	18,26	22,30	20,31	21,29
8	19,34	17,29	18,30	19,31	20,23	21,24	22,25	14,26	15,27	16,28
9	18,32	18,31	19,29	17,30	21,25	22,23	20,24	15,28	16,26	14,27
10	17,33	19,30	17,31	18,29	22,24	20,25	21,23	16,27	14,28	15,26
11	16,37	20,26	21,27	22,28	14,29	15,30	16,31	17,23	18,24	19,25
12	15,35	21,28	22,26	20,27	15,31	16,29	14,30	18,25	19,23	17,24
13	14,36	22,27	20,28	21,26	16,30	14,31	15,29	19,24	17,25	18,23

Continued on page 230

Table A.8 continued from page 229

I	Column II															
	15	16	17	18	19	20	21	22	23	24	25	26	27	28	29	30
14	1,16	1,15	2,20	3,22	4,21	2,17	4,19	3,18	5,32	6,34	7,33	8,38	9,40	10,39	11,35	12,37
15		1,14	4,22	2,21	3,20	3,19	2,18	4,17	7,34	5,33	6,32	10,40	8,39	9,38	13,37	11,36
16			3,21	4,20	2,22	4,18	3,17	2,19	6,33	7,32	5,34	9,39	10,38	8,40	12,36	13,35
17				1,19	1,18	2,14	3,16	4,15	11,38	12,40	13,39	5,35	6,37	7,36	8,32	9,34
18					1,17	4,16	2,15	3,14	13,40	11,39	12,38	7,37	5,36	6,35	10,34	8,33
19						3,15	4,14	2,16	12,39	13,38	11,40	6,36	7,35	5,37	9,33	10,32
20							1,22	1,21	8,35	9,37	10,36	11,32	12,34	13,33	5,38	6,40

I	Column II									
	31	32	33	34	35	36	37	38	39	40
14	13,36	5,23	7,25	6,24	11,29	13,31	12,30	8,26	10,28	9,27
15	12,35	6,25	5,24	7,23	12,31	11,30	13,29	9,28	8,27	10,26
16	11,37	7,24	6,23	5,25	13,30	12,29	11,31	10,27	9,26	8,28
17	10,33	8,29	10,31	9,30	5,26	7,28	6,27	11,23	13,25	12,24
18	9,32	9,31	8,30	10,29	6,28	5,27	7,26	12,25	11,24	13,24
19	8,34	10,30	9,29	8,31	7,27	6,26	5,28	13,24	12,23	11,25
20	7,39	11,26	13,28	12,27	8,23	10,25	9,24	5,29	7,31	6,30

Continued on page 231

Table A.8 continued from page 230

I	Column II													
	22	23	24	25	26	27	28	29	30	31	32	33	34	35
21	1,20	10,37	8,36	9,35	13,34	11,33	12,32	7,40	5,39	6,38	12,28	11,27	13,26	9,25
22		9,36	10,35	8,37	12,33	13,32	11,34	6,39	7,38	5,40	13,27	12,26	11,28	10,24
23			1,25	1,24	2,29	3,31	4,30	2,26	4,28	3,27	5,14	6,16	7,15	8,20
24				1,23	4,31	2,30	3,29	3,28	2,27	4,26	7,16	5,15	6,14	10,22
25					3,30	4,29	2,31	4,27	3,26	2,28	6,15	7,14	5,16	9,21
26						1,28	1,27	2,23	3,25	4,24	11,20	12,22	13,21	5,17
27							1,26	4,25	2,24	3,23	13,22	11,21	12,20	7,19

I	Column II				
	36	37	38	39	40
21	8,24	10,23	6,31	5,30	7,29
22	9,23	8,25	7,30	6,29	5,31
23	9,22	10,21	11,17	12,19	13,18
24	8,21	9,20	13,19	11,18	12,17
25	10,20	8,22	12,18	13,17	11,19
26	6,19	7,18	8,14	9,16	10,15
27	5,18	6,17	10,16	8,15	9,14

Continued on page 232

Table A.8 continued from page 231

I	Column II											
	29	30	31	32	33	34	35	36	37	38	39	40
28	3,24	4,23	2,25	12,21	13,20	11,22	6,18	7,17	5,19	9,15	10,14	8,16
29		1,31	1,30	8,17	9,19	10,18	11,14	12,16	13,15	5,20	6,22	7,21
30			1,29	10,19	8,18	9,17	13,16	11,15	12,14	7,22	5,21	6,20
31				9,18	10,17	8,19	12,15	13,14	11,16	6,21	7,20	5,22
32					1,34	1,33	2,38	3,40	4,39	2,35	4,37	3,36
33						1,32	4,40	2,39	3,38	3,37	2,36	4,35
34							3,39	4,38	2,40	4,36	3,35	2,37
35								1,37	1,36	2,32	3,34	4,33
36									1,35	4,34	2,33	3,32
37										3,33	4,32	2,34
38											1,40	1,39
39												1,38

B

Probability Histograms for Agglomerate Compression Experiments of Infant Formulae

For reasons of space, none of the probability histograms for force at failure, strain at failure or agglomerate stiffness, obtained by uniaxial compression of individual agglomerates of the four infant formulae described in Table 3.1 (p.50), are shown in Chapter 3. These graphs are instead confined to this appendix. The probability histograms for force at failure, strain at failure and agglomerate stiffness are given in Sections B.1, B.2 and B.3, respectively. Note that the heights of the bars are scaled so that the sum of the bar areas is one. Lognormal distributions were fitted to the data, and the corresponding probability density function is superimposed on each of these histograms as a solid red line. These probability density functions of the compression responses are compared in Chapter 3 on Figures 3.14–3.16 (p.65–66).

B.1 Force at Failure Histograms

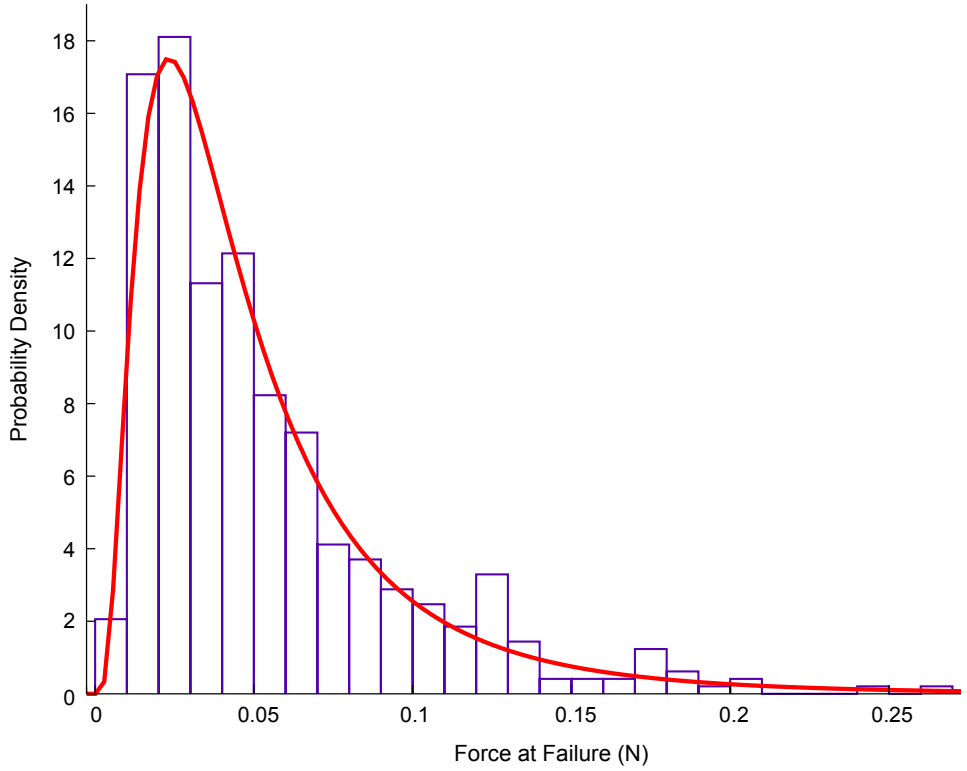

Figure B.1: *Probability histogram of the force at failure data (N) for compression of agglomerates of infant formula A, compared with the PDF of a fitted lognormal distribution*

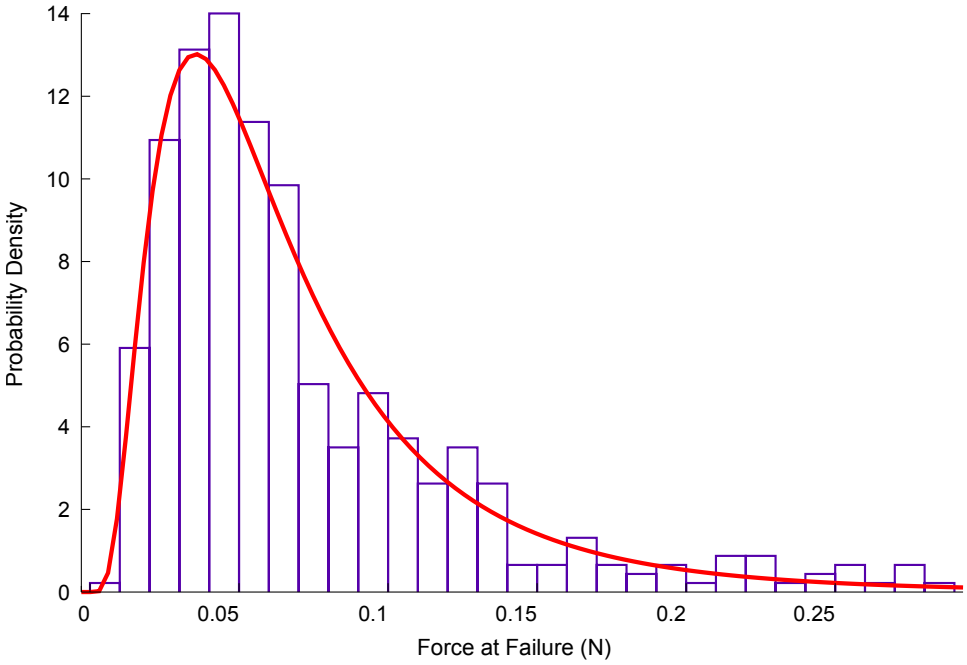

Figure B.2: *Probability histogram of the force at failure data (N) for compression of agglomerates of infant formula B, compared with the PDF of a fitted lognormal distribution*

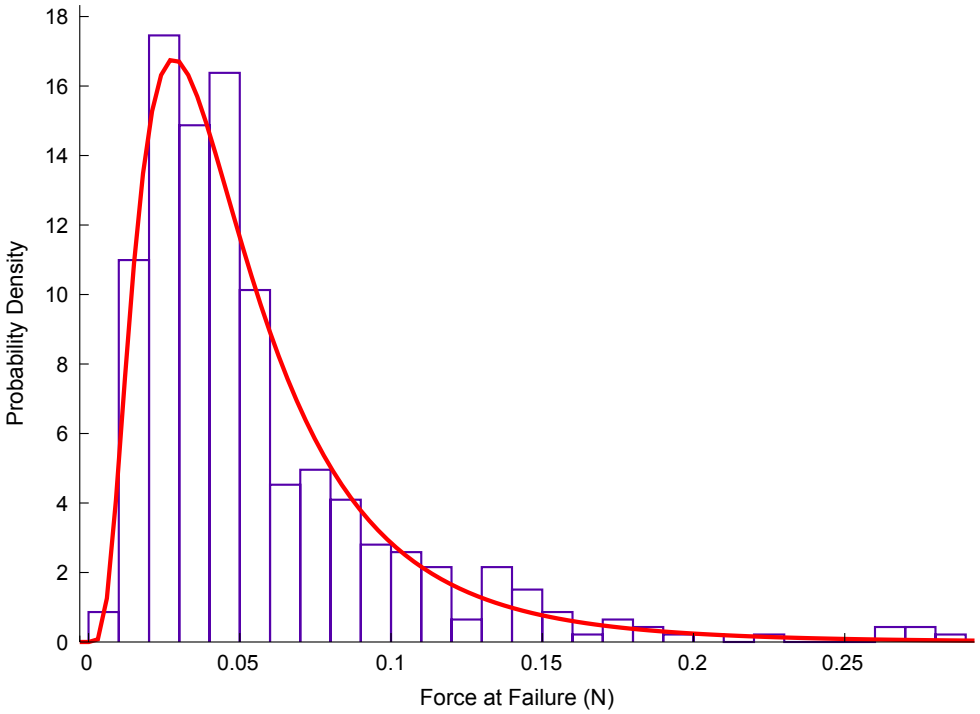

Figure B.3: *Probability histogram of the force at failure data (N) for compression of agglomerates of infant formula C, compared with the PDF of a fitted lognormal distribution*

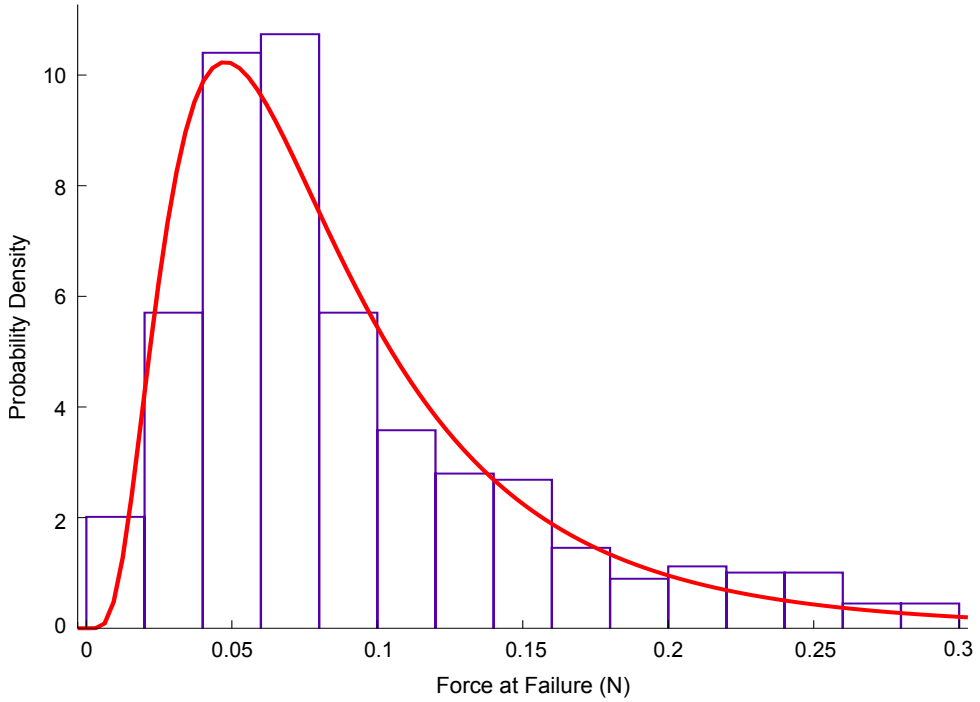

Figure B.4: *Probability histogram of the force at failure data (N) for compression of agglomerates of infant formula D, compared with the PDF of a fitted lognormal distribution*

B.2 Strain at Failure Histograms

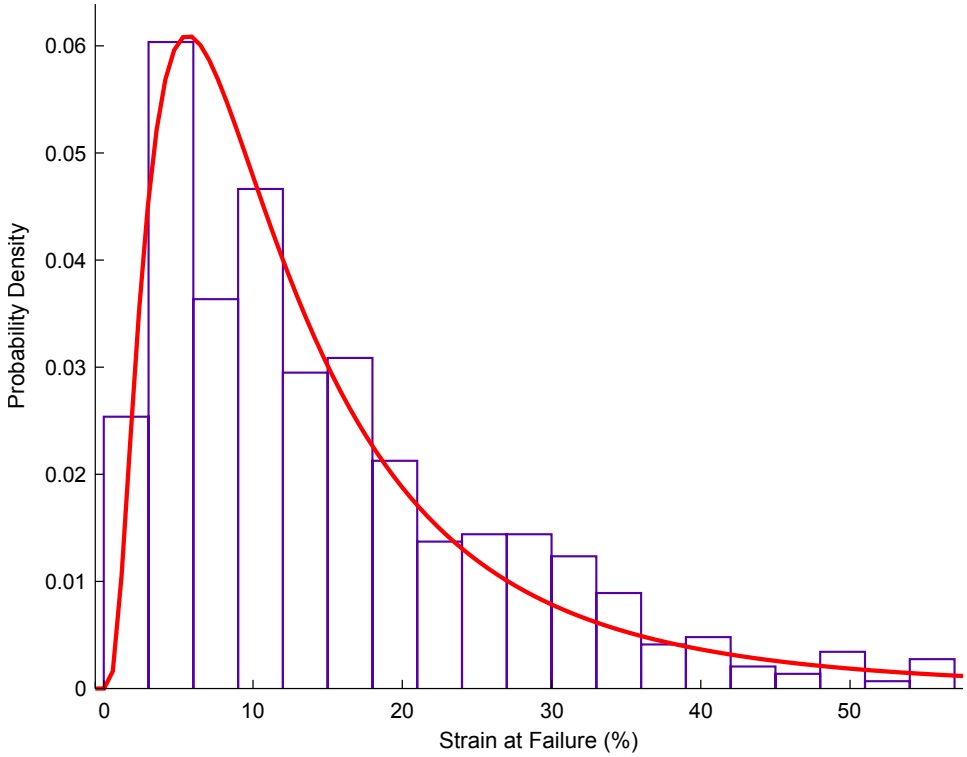

Figure B.5: *Probability histogram of the strain at failure data (%) for compression of agglomerates of infant formula A, compared with the PDF of a fitted lognormal distribution*

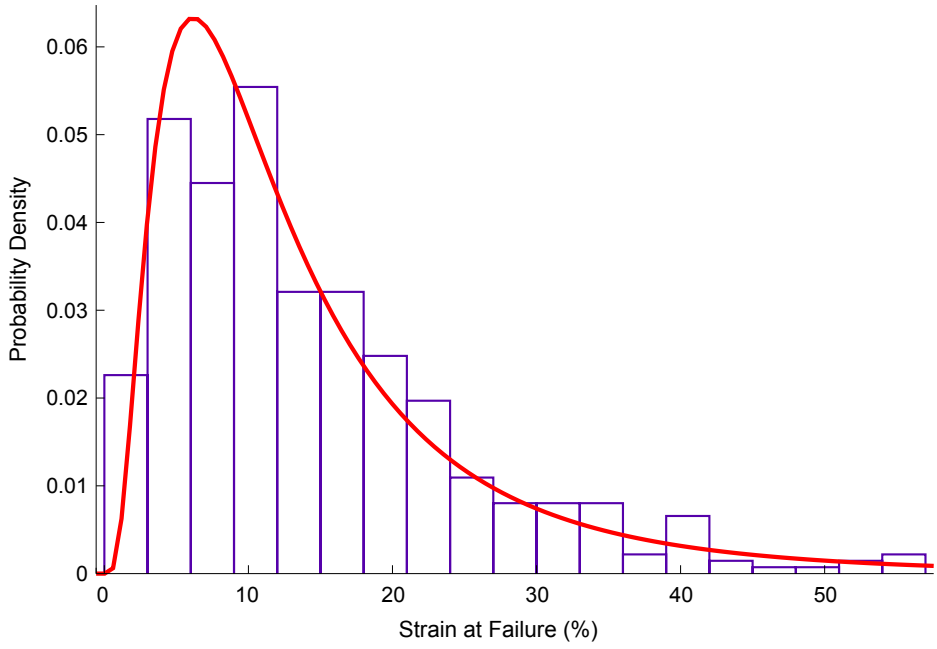

Figure B.6: *Probability histogram of the strain at failure data (%) for compression of agglomerates of infant formula B, compared with the PDF of a fitted lognormal distribution*

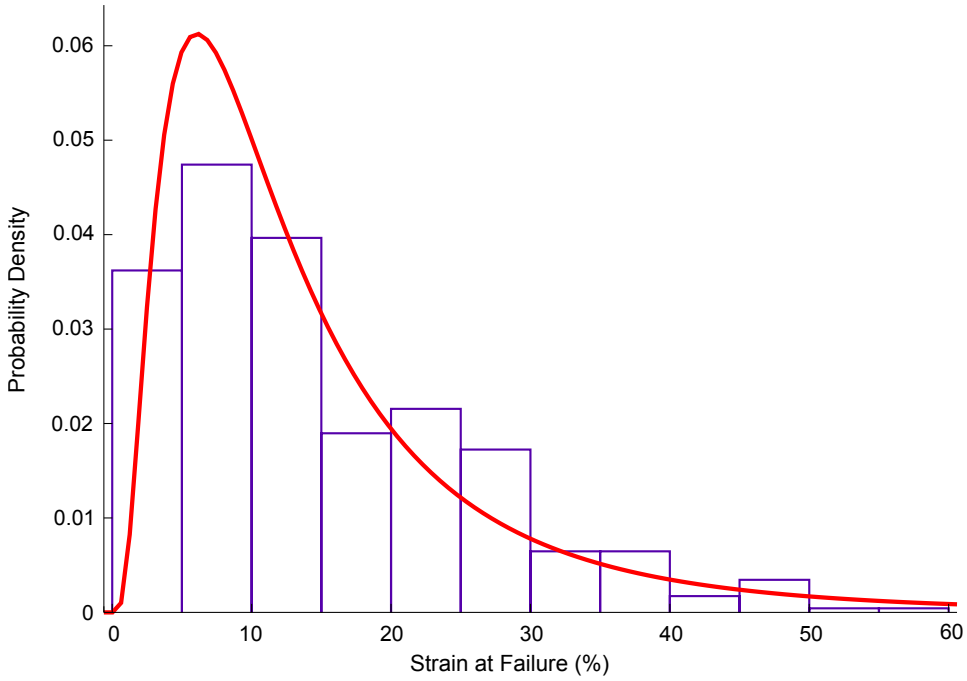

Figure B.7: *Probability histogram of the strain at failure data (%) for compression of agglomerates of infant formula C, compared with the PDF of a fitted lognormal distribution*

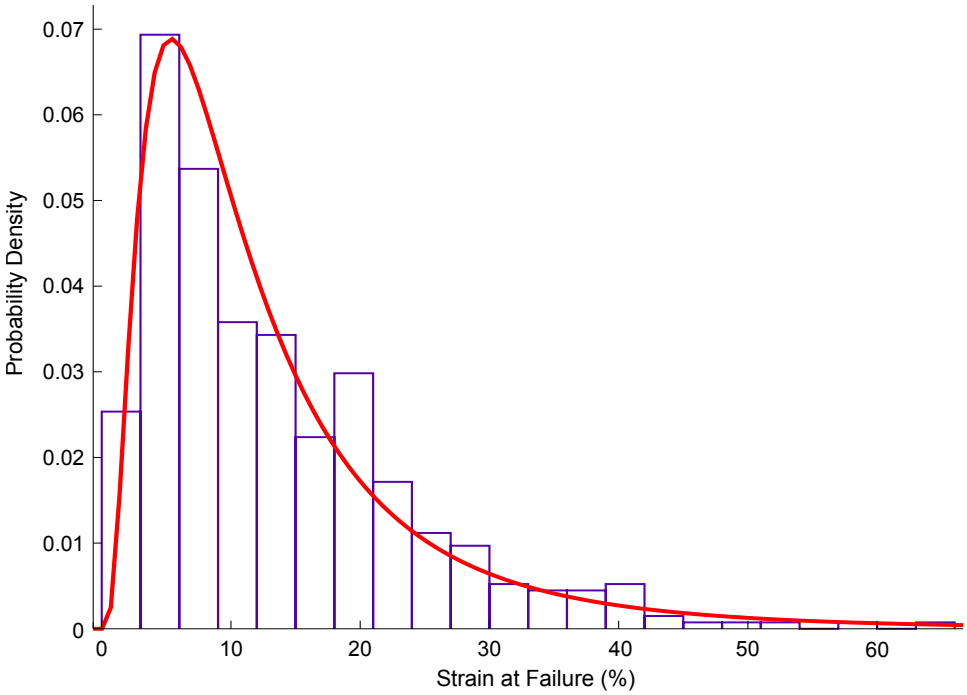

Figure B.8: *Probability histogram of the strain at failure data (%) for compression of agglomerates of infant formula D, compared with the PDF of a fitted lognormal distribution*

B.3 Agglomerate Stiffness Histograms

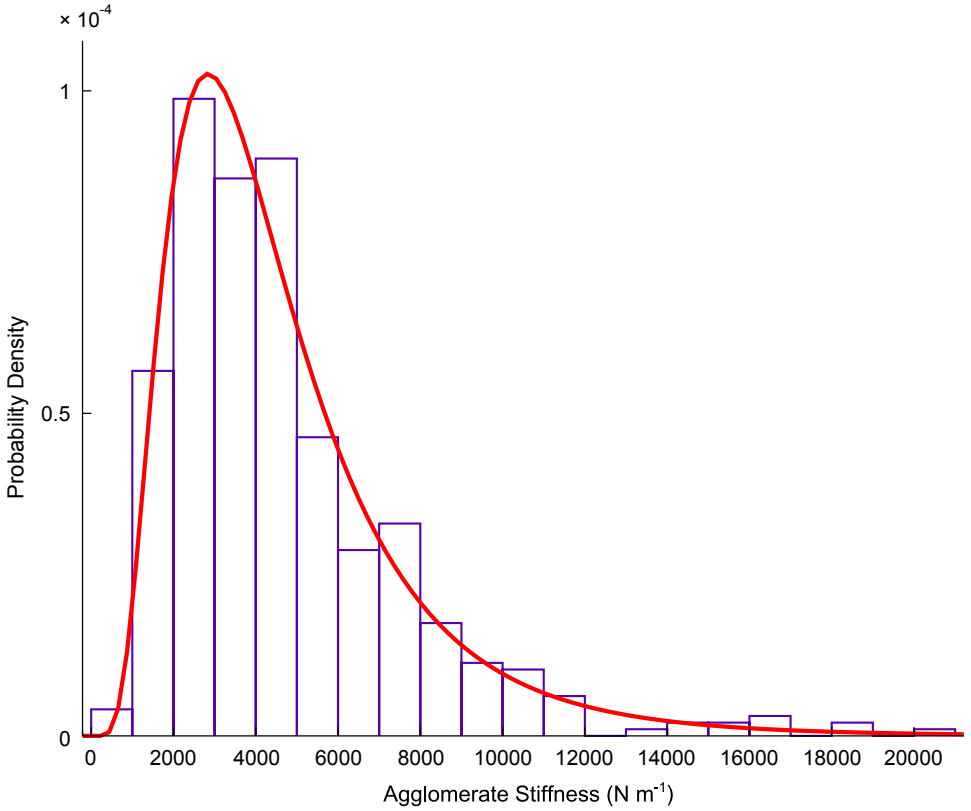

Figure B.9: *Probability histogram of the stiffness data ($N\,m^{-1}$) for compression of agglomerates of infant formula A, compared with the PDF of a fitted lognormal distribution*

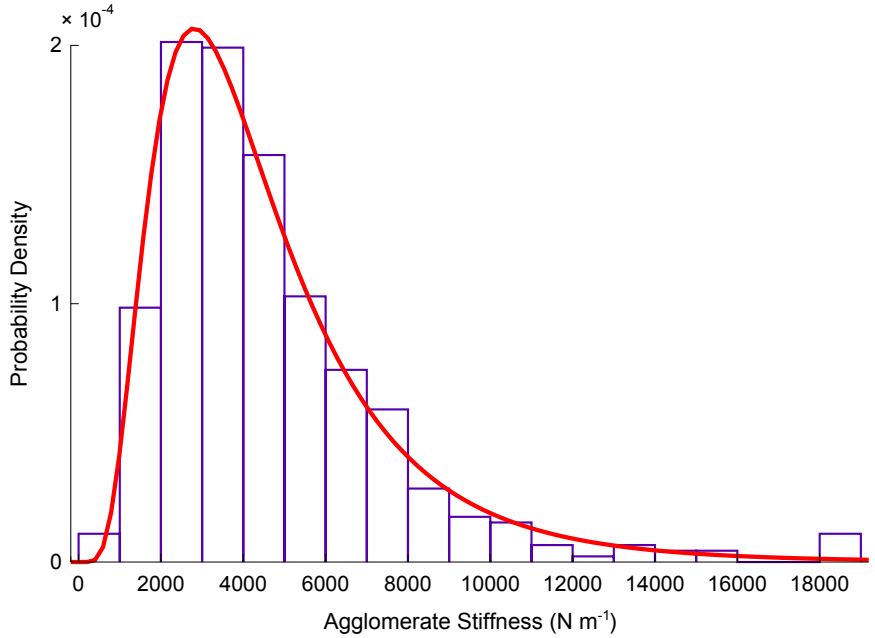

Figure B.10: *Probability histogram of the stiffness data ($N\,m^{-1}$) for compression of agglomerates of infant formula B, compared with the PDF of a fitted lognormal distribution*

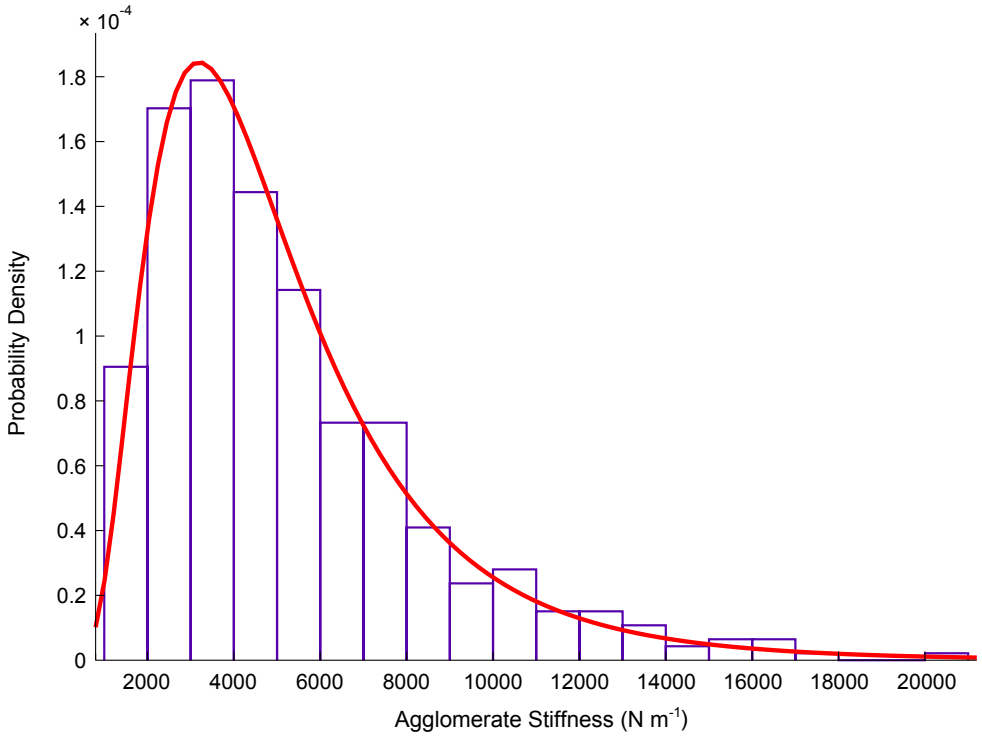

Figure B.11: *Probability histogram of the stiffness data ($N m^{-1}$) for compression of agglomerates of infant formula C, compared with the PDF of a fitted lognormal distribution*

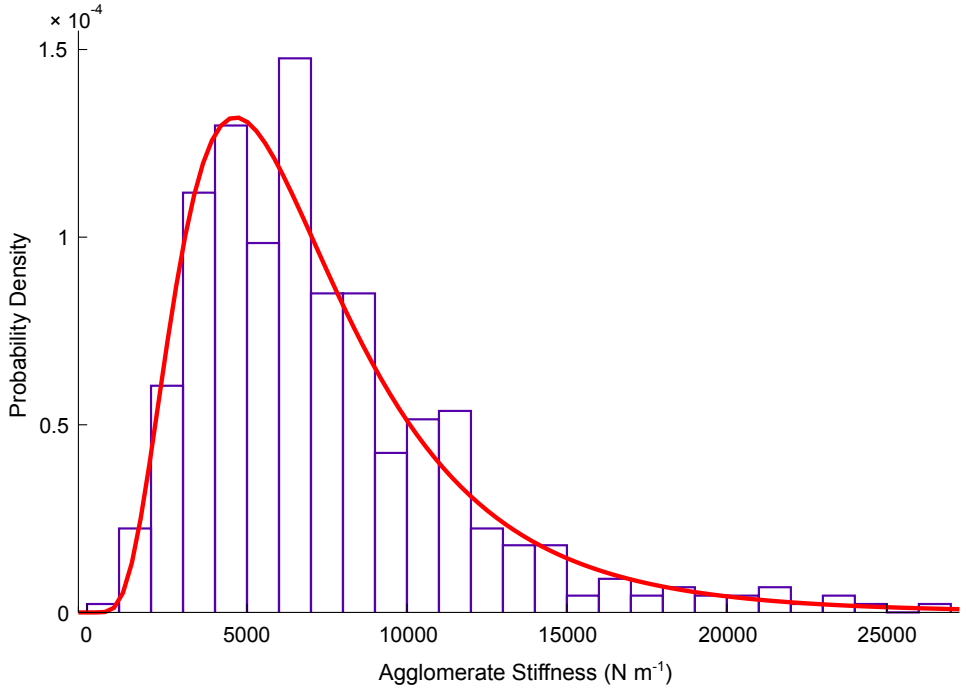

Figure B.12: *Probability histogram of the stiffness data ($N m^{-1}$) for compression of agglomerates of infant formula D, compared with the PDF of a fitted lognormal distribution*

C

Supplementary Information on the Formation of DEM Agglomerates by Sequential Addition

The sequential addition (or deposition) method used to produce agglomerates for the 3D DEM simulations was described briefly in Section 4.1.4 on p.78. One seed sphere is placed at the origin. Other spheres are then placed successively and randomly within an ellipsoidal volume surrounding this seed sphere. Each active sphere is moved randomly until it comes into contact with another sphere, when it is fixed in position (ensuring no overlaps). The random motion of the spheres is modified by point transformation to continuously reduce the distance between the active sphere and the origin until contact occurs with a pre-existing sphere. Russ describes this method of depositing particles on a surface as "diffusion-limited aggregation" (Russ, 1994, p.16), which results in very open, dendritic structures. Such agglomerates exhibit fractal characteristics, having a self-similar appearance.

Figure C.1 (p.242) is a flowchart which shows the principal features of the MATLAB algorithm which was used to produce agglomerates by sequential addition. The number of symbols used on this flowchart was minimised for clarity; those which were required are described below:

i Index of the current active sphere

n Maximum permissible number of spheres in the agglomerate

x Specified length of the agglomerate

y Specified width of the agglomerate

z Specified height of the agglomerate

The complete annotated MATLAB code for an agglomerate of infant formula B is

provided at the end of this appendix for reference. Some other points regarding the MATLAB algorithm are given below:

- If the algorithm was implemented according to Figure C.1, a residual overlap between spheres is possible at the point in the flowchart marked with an asterisk (*). This could occur in either of the following situations:

  1. If moving sphere i to give point contact with sphere j would cause a new overlap with another sphere (k).

  2. If there are multiple simultaneous contacts initially, it would not be possible to give point contact with multiple spheres using the scheme in Figure C.1.

  This was remedied by introducing two additional nested counter-controlled loops, which allows the code segment labelled with an asterisk to be repeated on multiple occasions. Note that although simpler, one loop would not be sufficient and could lead to problems with infinite evaluation, e.g., moving sphere i (from position α to β) to give point contact with sphere j would cause an overlap with sphere k; then moving sphere i to give point contact with sphere k would return sphere i to position α.

- The diameters of the ellipsoid were not equal to x, y and z. If the polar and equatorial diameters were equal to x, y and z, this would yield an agglomerate with quite a tightly-packed structure. By selecting larger ellipsoid diameters, agglomerates with open, highly-porous structures could be generated.

- Pseudo-random numbers were generated as a uniform distribution on the open interval (0,1). The seed of the random number generator was modified each second as a function of time. Negative random numbers were required; these were produced using additional conditional statements which are not shown in Figure C.1.

Since the aim of using this algorithm was to produce loosely-packed agglomerates which closely simulate the structure of real infant formula agglomerates (e.g., SEM micrograph as Figure 1.2 on p.15), the success of this algorithm must be evaluated taking this into consideration. Figure C.2 shows an orthographic projection (front elevation, plan and end views) of one sample agglomerate containing 200 spheres. It is clear that such structures are much less regular than those derived from lattice packing (Section 4.1.4), and are thus closer to real infant formula agglomerates. Furthermore, the density of the packing decreases with distance from the centrepoint of the agglomerate (the origin). This is beneficial as asperities are formed which are easily broken under uniaxial loading. Effects such as asperity failure are also observed on the force–displacement plots for experimental compression of infant formula agglomerates.

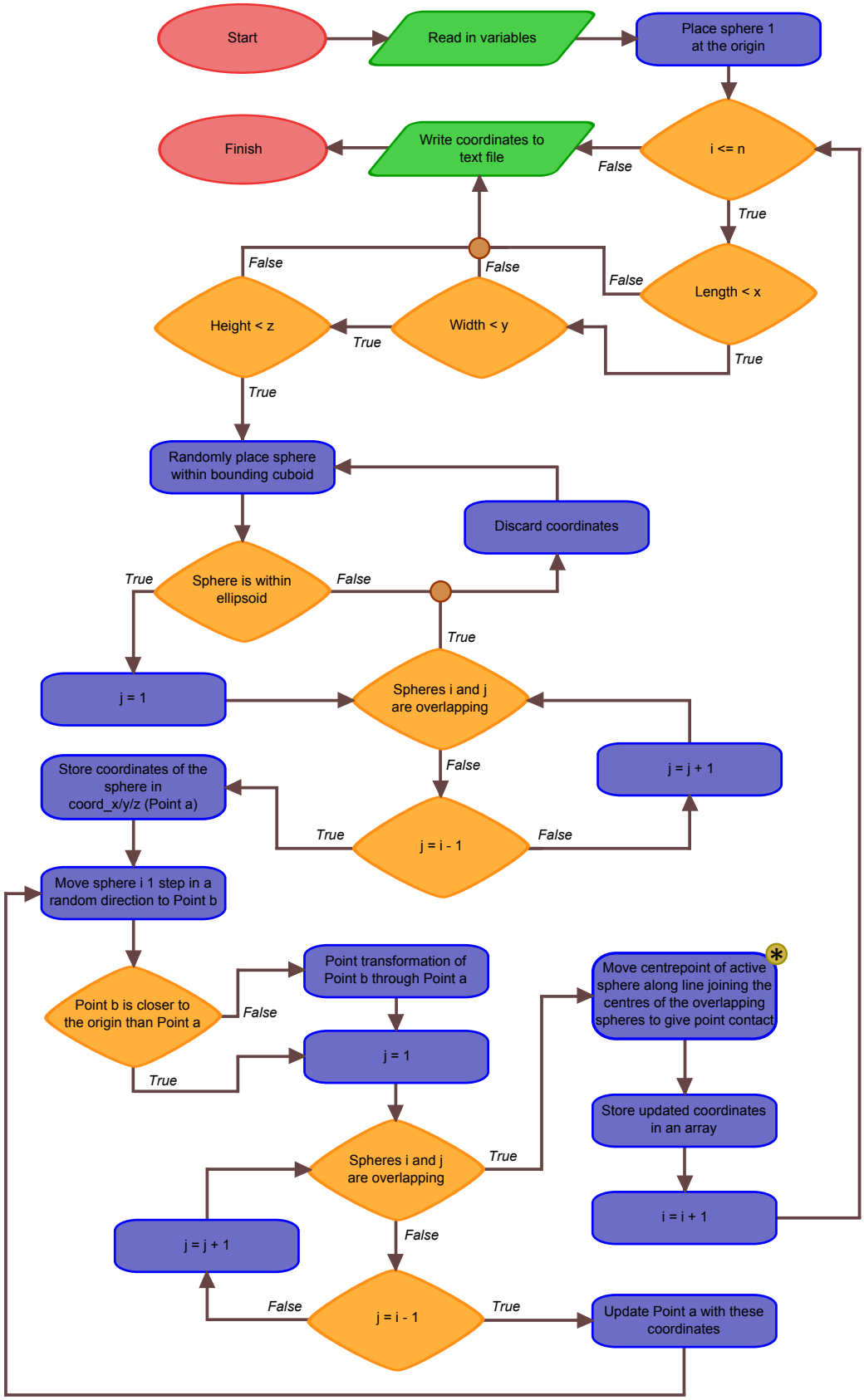

Figure C.1: *Simplified flowchart of the MATLAB code used to form agglomerates by sequential addition*

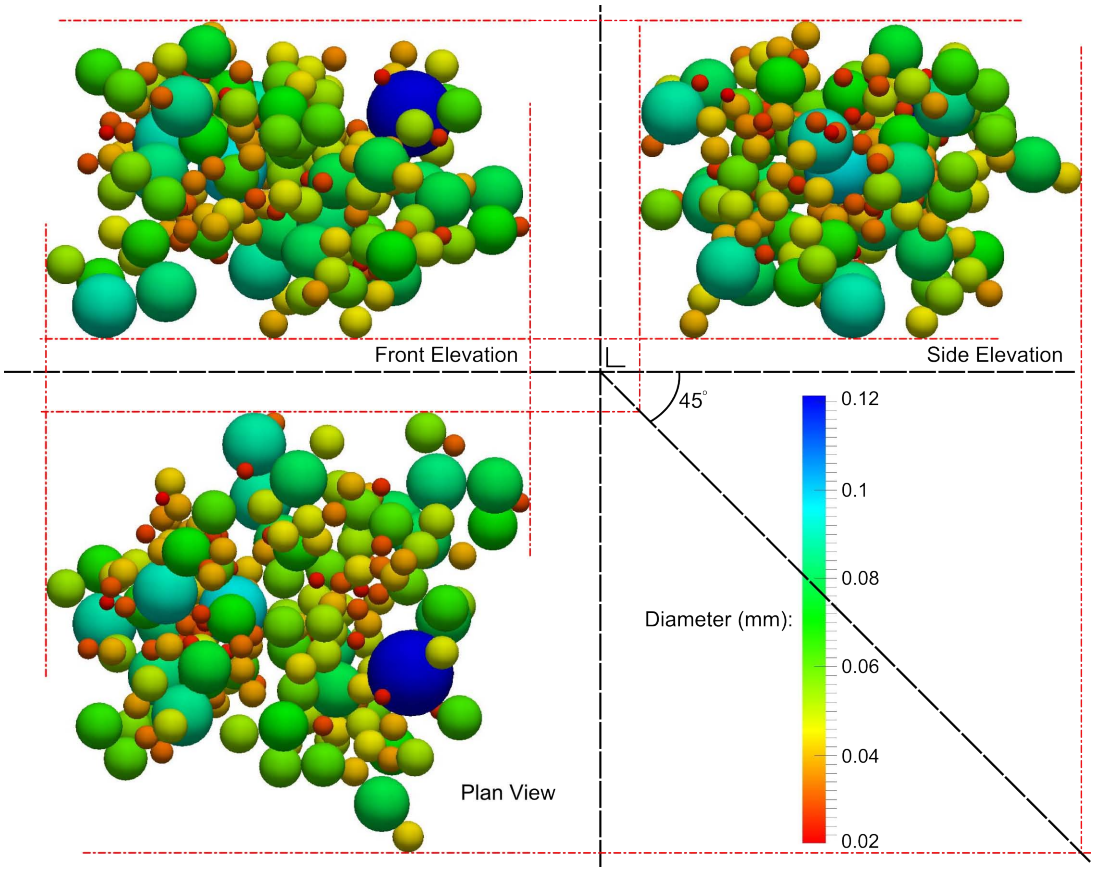

Figure C.2: *Orthographic projection of a sample agglomerate containing 200 spheres produced by sequential addition, in which the colour bar indicates the size of the spheres in mm*

C.1 Annotated MATLAB Code

```
% This is the complete script used to generate an agglomerate
% of any arbitrary size using balls of any size. Most of the
% operations are not vectorised; it was found that vectorising
% many of the for loops, which theoretically should improve
% performance, causes the file to run more slowly.

clear
format long

% Take in the basic variables required.
ball_num = 2000; % The maximum number of balls to generate
exit_cond = 0; % Initialise an exit condition
tolerance = 1e-12; % An overlap tolerance must be defined

% Since the confining shape is an ellipsoid, there are three
% confining radii to be defined (in mm).
mult_factor_x = 1.5; % Multipliers to obtain loose agglomerates
mult_factor_y = 1.2;
mult_factor_z = 1.1;

x = 1.212; % Along x axis
y = 0.937; % Along y axis
z = 0.678; % Along z axis

% Take in parameters for the lognormal distribution in ball
% size where mu and sigma are the mean and standard deviation
% of the associated normal distribution (from lognfit).
mu = -3.1364;
sigma = 0.4372;
lower_cut_off = 0.02; % To truncate the distribution
upper_cut_off = 0.125;

% Call a function to generate a vector of lognormally-distributed
% ball diameters in mm.
ball_diameter = random_variates_lognormal(mu,sigma,...
...lower_cut_off,upper_cut_off,ball_num);

ball_radius = ball_diameter./2;
step_size = min(ball_diameter)/10; % The distance that the active
% ball is moved on each iteration of the loop below

% Randomly reset the random number stream using the clock.
```

```
rand('state',sum(100*clock));

% Place the seed sphere at the origin, and pre-allocate three
% vectors to store the ball coordinates.
coord_x = zeros(ball_num,1);
coord_y = zeros(ball_num,1);
coord_z = zeros(ball_num,1);

i = 2; % Initialise the active ball index (#1 at origin).

% Generate balls successively inside the confining ellipsoid.
while i <= n % While fewer balls generated than the maximum

    exit_cond = 0; % Initialise at 0.

    % Test to see if the agglomerate radii are <= the required
    % confining radii. If not, break out of the while loop.
    if i >= 10
        distance_x_pos = -1000; % Initislise at large values
        distance_x_neg = 1000;
        distance_y_pos = -1000;
        distance_y_neg = 1000;
        distance_z_pos = -1000;
        distance_z_neg = 1000;

        for k = 1:(i-1) % Loop through all balls generated
            if coord_x(k) > distance_x_pos
                distance_x_pos = coord_x(k);
            elseif coord_x(k) < distance_x_neg
                distance_x_neg = coord_x(k);
            end

            if coord_y(k) > distance_y_pos
                distance_y_pos = coord_y(k);
            elseif coord_y(k) < distance_y_neg
                distance_y_neg = coord_y(k);
            end

            if coord_z(k) > distance_z_pos
                distance_z_pos = coord_z(k);
            elseif coord_z(k) < distance_z_neg
                distance_z_neg = coord_z(k);
            end
        end
```

```
    distance_x = abs(distance_x_pos) + abs(distance_x_neg);
    distance_y = abs(distance_y_pos) + abs(distance_y_neg);
    distance_z = abs(distance_z_pos) + abs(distance_z_neg);

    if (distance_x>x) || (distance_y>y) || (distance_z>z)
        break;
    end
end

% Provisionally place the ball randomly within the confining
% ellipsoid. Since rand is a uniform distribution from 0 to 1,
% the full spectrum of pos_x, pos_y and pos_z is a cuboid with
% its centroid at the origin.
pos_x = rand*mult_factor_x*x;
pos_y = rand*mult_factor_y*y;
pos_z = rand*mult_factor_z*z;

% The following ensures that pos_x/y/z are not always positive.
neg_x = rand; % A random number from the uniform distribution
if neg_x <= 0.5
    pos_x = -1*pos_x; % Change to the negative analogue
end

neg_y = rand;
if neg_y <= 0.5
    pos_y = -1*pos_y;
end

neg_z = rand;
if neg_z <= 0.5
    pos_z = -1*pos_z;
end

% Firstly, check whether the ball is inside the confining
% ellipsoid. It could potentially lie inside the cuboid but
% outside the ellipsoid.
distance = sqrt((pos_x^2)+(pos_y^2)+(pos_z^2));

% intersec_x/y/z are the coordinates of the point of
% intersection between the line joining the origin and
% the ball coordinates, and the ellipsoid. Note that the
% sign is unimportant.
intersec_x = 1/sqrt((1/((mult_factor_x*x)^2))+...
```

```
((pos_y^2)/((pos_x^2)*((mult_factor_y*y)^2)))+...
...((pos_z^2)/((pos_x^2)*((mult_factor_z*z)^2))));

intersec_y = 1/sqrt((1/((mult_factor_y*y)^2))+...
...((pos_x^2)/((pos_y^2)*((mult_factor_x*x)^2)))+...
...((pos_z^2)/((pos_y^2)*((mult_factor_z*z)^2))));

intersec_z = 1/sqrt((1/((mult_factor_z*z)^2))+...
...((pos_x^2)/((pos_z^2)*((mult_factor_x*x)^2)))+...
...((pos_y^2)/((pos_z^2)*((mult_factor_y*y)^2))));

intersection = sqrt((intersec_x^2) +...
...(intersec_y^2) + (intersec_z^2));

if distance < intersection % Ball inside confining ellipsoid

    % Now cycle through all existing balls to check that the
    % ball does not overlap with any of those that have
    % already been generated.
    for j = 1:(i-1)
        ball_dist = sqrt(((pos_x-coord_x(j))^2)+...
        ...((pos_y-coord_y(j))^2)+((pos_z-coord_z(j))^2));

        if ball_dist < (ball_radius(i)+ball_radius(j))
            exit_cond = 1; % To skip the computations below
            break; % Exit the inner for loop
        end
    end

    % If the ball is inside the confining ellipsoid and is
    % not overlapping any other balls, provisionally
    % write the ball coordinates to the storage vectors.
    if exit_cond == 0
        coord_x(i) = pos_x;
        coord_y(i) = pos_y;
        coord_z(i) = pos_z;

        % Now move the ball randomly from its starting
        % position until it contacts another ball.
        overlap = 0;

        while overlap == 0 % Loop while there is no contact
            x_step = rand; % Random numbers for moving the ball
            y_step = rand;
```

```
z_step = rand;

% As before, rand always returns positive numbers.
neg_x = rand;
if neg_x <= 0.5
    x_step = -1*x_step;
end

neg_y = rand;
if neg_y <= 0.5
    y_step = -1*y_step;
end

neg_z = rand;
if neg_z <= 0.5
    z_step = -1*z_step;
end

% Now provisionally move the ball to a position
% which is incrementally different from the
% starting coordinates. Over-write pos_x/y/z to
% save variables.
pos_x = coord_x(i) + x_step*step_size;
pos_y = coord_y(i) + y_step*step_size;
pos_z = coord_z(i) + z_step*step_size;

% Find the distance between the ball and the origin
% before and after motion. If the distance after is
% greater, use a point transformation to bring the
% ball closer to the origin.
distance_old = sqrt(((coord_x(i))^2)+...
...((coord_y(i))^2)+((coord_z(i))^2));

distance_new = sqrt((pos_x^2)+(pos_y^2)+(pos_z^2));

if distance_old < distance_new
    pos_x = coord_x(i) - x_step*step_size;
    pos_y = coord_y(i) - y_step*step_size;
    pos_z = coord_z(i) - z_step*step_size;
end

% Check for overlaps between the ball in its new
% position and all other balls. If there is one
% overlap, the looping will continue at least once
```

```
                % more until it is certain that there are no
                % additional ball overlaps.
                redo = 0;
                passes = 0;
                while redo == passes
                    passes = passes + 1;

                    % Sometimes, a loop may be established whereby
                    % moving a ball one way could move it into the
                    % path of another. By re-generating the ball
                    % if passes > 100, this problem is avoided.
                    if passes > 100
                        break; % Exit the while loop
                    end

Unindent the section of code between the lines for readability.
~~~~~~~~~~~~~~~~~~~~~~~~~~~~~~~~~~~~~~~~~~~~~~~~~~~~~~~~~~~~~~~
for k = 1:(i-1)
    ball_dist = sqrt(((pos_x-coord_x(k))^2)+...
    ...((pos_y-coord_y(k))^2)+((pos_z-coord_z(k))^2));

    if ball_dist < (ball_radius(i)+ball_radius(k))-tolerance
        % If there is an overlap, must move active ball to give a
        % touching contact. Move the centrepoint of the active
        % ball away from the contacting ball along the line joining
        % their centres.
        pos_x = coord_x(k)+(pos_x-coord_x(k))*...
        ...(ball_radius(i)+ball_radius(k))/ball_dist;
        pos_y = coord_y(k)+(pos_y-coord_y(k))*...
        ...(ball_radius(i)+ball_radius(k))/ball_dist;
        pos_z = coord_z(k)+(pos_z-coord_z(k))*...
        ...(ball_radius(i)+ball_radius(k))/ball_dist;

        overlap = 1; % Change variable to record the overlap
        redo = redo + 1; % If no overlap on a loop, redo < passes
        break; % Exit the for loop
    end
end
~~~~~~~~~~~~~~~~~~~~~~~~~~~~~~~~~~~~~~~~~~~~~~~~~~~~~~~~~~~~~~~

                end

                % Even if there is no overlap, the positions must
                % still be updated.
```

```
                coord_x(i) = pos_x;
                coord_y(i) = pos_y;
                coord_z(i) = pos_z;

                % Increment the active ball index if there has
                % been an overlap.
                if overlap == 1
                    i = i + 1;
                end
            end
        end
    end
end

% Write the ball coordinates to a text file.
fid = fopen('Ball_Coordinates.txt','wt');
for m = 1:(i-1)
    fprintf(fid,'%1.10f\t %1.10f\t %1.10f\t %1.10f\n',...
    ...coord_x(m),coord_y(m),coord_z(m),ball_diameter(m));
end
fclose(fid);

% Show a plot of the generated agglomerate.
figure
hold on
axis('equal'); % Make the axes equal
axis('off'); % Turn the axes off

for i =1:m
    [a,b,c] = sph_coords(coord_x(i),coord_y(i),coord_z(i),...
    ...ball_radius(i));
    surf(a,b,c,'LineWidth',0.1,'EdgeColor',[0.2,0.2,0.2]);
    colormap(summer);
    brighten(0.3);
    view([90 30]);
end
hold off

return

~~~~~~~~~~~~~~~~~~~~~~~~~~~~~~~~~~~~~~~~~~~~~~~~~~~~~~~~~~~~~~~~~~~~

function diameters = random_variates_lognormal(m,sig,lower,...
...upper,num_balls)
```

```
% lognrnd requires the Statistics Toolbox

var = 1;

while var <= num_balls
    diameters(var) = lognrnd(m,sig,1,1);

    if (diameters(var) >= lower) && (diameters(var) <= upper)
        var = var + 1;
    end
end

~~~~~~~~~~~~~~~~~~~~~~~~~~~~~~~~~~~~~~~~~~~~~~~~~~~~~~~~~~~~~~~~~~~~~~~~

function [x,y,z] = sph_coords(xcenter,ycenter,zcenter,rad)

phi = 0:pi/20:pi;
theta = 0:pi/10:2*pi;
[Phi,Theta] = meshgrid(phi,theta);

x = xcenter + rad*sin(Phi).*cos(Theta);
y = ycenter + rad*sin(Phi).*sin(Theta);
z = zcenter + rad*cos(Phi);
```

D

Correlations of Compression Responses and Physical Characteristics of the Agglomerates

In Section 3.2.2, correlations between each combination of responses (force at failure, strain at failure and agglomerate stiffness) were determined, beginning on p.68: the Spearman R and Kendall τ coefficients were reported for each of the four formulae in Tables 3.9–3.12. Since a range of physical characteristics of individual agglomerates could be measured, it was possible to evaluate two additional types of correlation:

1. Correlations between one of the three agglomerate compression responses and any measurable physical characteristic of the agglomerates
2. Correlations between pairs of measurable physical characteristics of the agglomerates

Spearman R coefficients were calculated in both cases as none of the experimental compression responses were normally distributed (Table 3.8) and the same was true for many of the agglomerate physical characteristics. These correlations were evaluated only for 92 agglomerates from the 710–850 µm sieve fraction of infant formula B due to the practical difficulties involved:

- The agglomerates were individually characterised before compression using the Malvern PharmaVision 830 instrument introduced in Section 5.1.1. Since this apparatus was not in the same laboratory as the texture analyser, the exposure of the agglomerates to atmosphere was prolonged. Experiments were performed only when the relative humidity of the air was low. However, it was difficult to ascertain whether the agglomerates had absorbed sufficient moisture to affect the results during this period of exposure.
- The necessity of having to transfer agglomerates between two widely-separated

pieces of equipment made these experiments very time-consuming. It would have been impractical to conduct a larger, more statistically-significant number of experiments for four formulae without changing the arrangement of the apparatus, which was infeasible in this case.

D.1 Measured and Calculated Agglomerate Characteristics

Nine physical characteristics of the agglomerates were obtained:

1. Mean diameter (μm)
2. Length (μm)
3. Width (μm)
4. Projected area (μm^2)
5. Roundness (–)
6. Convexity (–)
7. Aspect ratio (–)
8. Box fractal dimension of the agglomerate outline (–)
9. Box fractal dimension of the compressive force response (–)

The first six characteristics were obtained directly from the PharmaVision, while aspect ratio was obtained from a trivial calculation. These seven characteristics are described collectively in Section D.1.1, while the fractal dimensions are discussed in Sections D.1.2–D.1.4.

D.1.1 Characteristics Obtained Directly from PharmaVision[†]

1. Mean diameter: This was calculated by measuring the distance from the centre of mass of the agglomerate to each pixel on its perimeter, and then multiplying the arithmetic mean of these distances by two.
2. Length: All possible lines that may be drawn between points on the agglomerate perimeter were projected onto the major axis[‡]. The length of the agglomerate was the maximum length of any projection.
3. Width: As for length, except projections were onto the minor axis[‡]. The width of the agglomerate was the maximum length of any projection.

[†]All details of the calculations in Section D.1.1 were obtained from Malvern Instruments Ltd. (2004).
[‡]The major and minor axes were defined in # 5 as part of the explanation of roundness.

4. Projected area: This was the projected surface area of the agglomerate.

5. Roundness: A perfect circle has a roundness of one, and narrow, elongated objects have roundness values which approach zero. Roundness was calculated as $\frac{|\lambda_1 - \lambda_2|}{\lambda_1 + \lambda_2}$, where λ_1 and λ_2 were the eigenvalues of the covariance matrix, M:

$$M = \begin{pmatrix} I_{xx} & I_{xy} \\ I_{xy} & I_{yy} \end{pmatrix} \tag{D.1}$$

$$I_{xx} = \sum_{i,j} x_i x_j \tag{D.2}$$

$$I_{xy} = \sum_{i,j} x_i y_j \tag{D.3}$$

$$I_{yy} = \sum_{i,j} y_i y_j \tag{D.4}$$

   x_i and y_j were the coordinates of the agglomerate pixel p_{ij} relative to the centre of mass of the agglomerate. The major axis of the agglomerate was the eigenvector of the maximum eigenvalue of matrix M. The minor axis was orthogonal to the major axis.

6. Convexity: This was found as the projected area divided by the area of the convex hull enclosing the agglomerate.

7. Aspect ratio: This was calculated by dividing the length by the width.

D.1.2 Fractal Analysis

In Euclidean geometry, every structure may be defined by an integer dimension: 0 for a point in space, 1 for a line, 2 for an area or 3 for a volume (Peleg, 1993). Fractals have dimensions which are not exact integers. While the concept of fractals has existed for a long time in fields such as mathematics, fractals were popularised, and the term itself was coined, by Benoît Mandelbrot (Russ, 1994, p.1) in his book *The Fractal Geometry of Nature* (Mandelbrot, 1982). A fractal dimension between 1 and 2 corresponds to an irregular, convoluted line which partially fills an area (Barrett and Peleg, 1995; Peleg, 1993). Any truly fractal object must be self-similar, which requires the physical appearance of the object to remain unchanged irrespective of the magnification or length scale used (Barletta and Barbosa-Cánovas, 1993). This condition is satisfied only by mathematical constructs such as the Koch curve, Sierpinski triangle and Mandelbrot set. In nature, there are always physical restrictions; a common lower limit for self-similarity is the size of an atom, molecule, cell, or pixel for image analysis. Apparent fractal dimensions may still be calculated for such objects, which are described as self-affine rather than self-similar (Peleg and McClements, 1997), and which may be treated as fractals within a restricted range of scale.

There are many methods used to calculate fractal dimensions; further information regarding most of these is provided by Russ (1994). Only one method was used in this work: the box-counting method. This is widely used, is relatively straightforward to implement and may be applied to patterns which lack self-similarity (Foroutan-pour et al., 1999). As an example, the box-counting fractal dimension for an agglomerate outline may be estimated by the following four-step process:

1. A grid of identical square boxes, each of side length ε, is overlaid on the image and the number of boxes which intersect the agglomerate outline is recorded as N_ε.
2. The size of the boxes is progressively reduced, and the number of boxes which contain part of the agglomerate outline is recorded for each box size.
3. A graph is plotted of $\log(N_\varepsilon)$ against $\log(\varepsilon)$.
4. The (apparent) fractal dimension is the absolute slope of the linear regression of this graph. Strictly, the box-counting dimension is defined as $\lim_{\varepsilon \to 0} \frac{\log(N_\varepsilon)}{\log(\varepsilon)}$ (Karperien, 2007).

D.1.3 Particle Outline Box Dimension (FracLac)

The PharmaVision saved a *.tif* file of each agglomerate, as stated in Section 5.1.1. These files were opened in ImageJ (previously mentioned in Section 5.1.2). Each image was converted to a binary form and holes inside the agglomerate boundary were filled to leave a solid black agglomerate against a white background. An example of this process is shown in Figure D.1.

Once the agglomerate images were prepared, the fractal dimensions were calculated using the FracLac ImageJ plug-in (v.2.5, r.4, A. Karperien (auth.), http://rsb.info.nih.gov/ij/plugins/fraclac/fraclac.html). The standard box count option was selected with the default linear progression of box sizes and 8 grid positions. This number specified that eight fractal dimensions were calculated for each agglomerate by using this number of random sampling orientations for the grid. The fractal dimension used in the results is the arithmetic mean of these eight dimensions. Figure D.2 shows an example of the linear regression used to calculate the fractal dimension for one agglomerate scan. The box-counting fractal dimension for this scan is 1.6853 (the mean of all scans of this agglomerate is 1.6716).

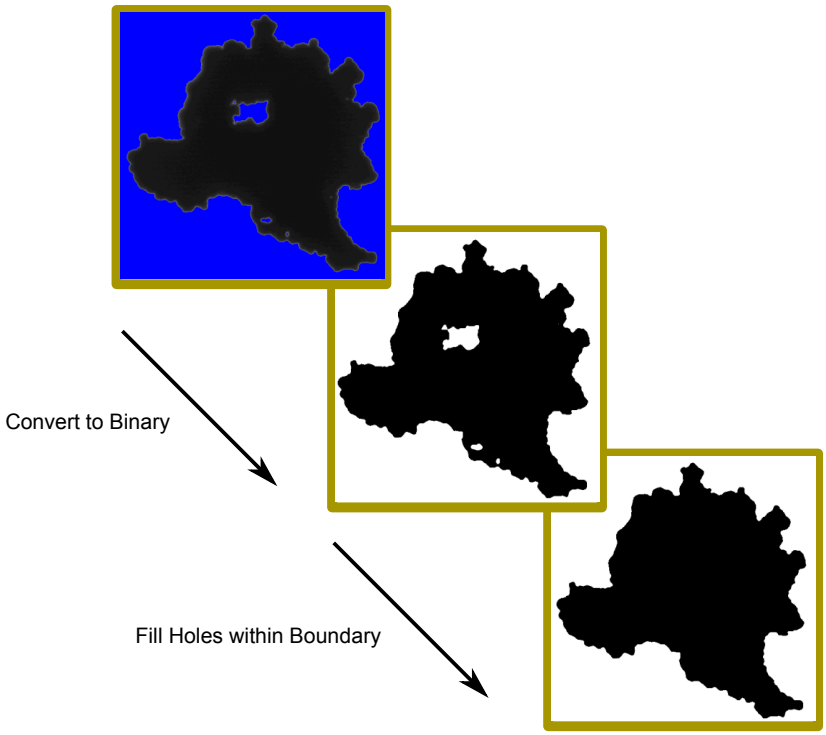

Figure D.1: *Preparation of the* .tif *images for calculating the fractal dimensions of agglomerate outlines using ImageJ*

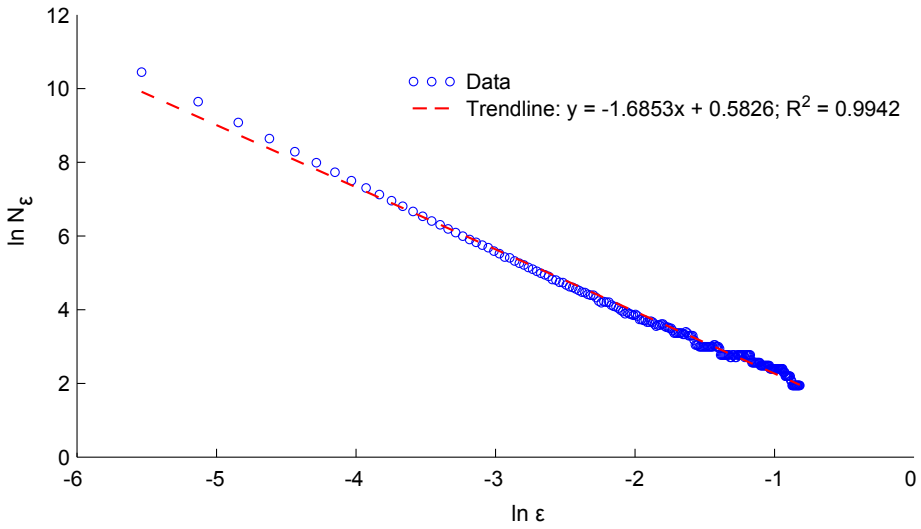

Figure D.2: *Logarithmic plot showing the data calculated by FracLac for N_ε and ε, where the fractal dimension of the agglomerate outline is the absolute slope of the linear regression*

D.1.4 Compressive Response Box Dimension (FracLab)

It is also possible to calculate a box counting fractal dimension for a mechanical crushing signature (e.g., Nussinovitch et al., 2000; Peleg, 2003). This was done using the FracLab plug-in for MATLAB (v.2.04, INRIA, Saclay, France), an established plug-in which has been used in many academic studies, e.g., Devaux et al. (2006), and Feng et al. (2010).

The force data were imported to FracLab from the MATLAB workspace as a column

vector. The raw data for displacement, strain or time were not required since the compression and data acquisition rates were constant for all tests at 0.01 mm s^{-1} and 500 points/s, respectively. The option was selected in FracLab to use an affine transformation to map all input forces to the range [0,1], which is recommended for correct calculation of the fractal dimension. The *boxdim_classique* function was used with a power law progression of box sizes. 21 boxes were specified in the software, with a maximum size of 1, a minimum size of 1/1024 and the least-squares linear regression option. The resulting output is shown in Figure D.3 for one set of agglomerate data. The user was required to select a range of points which was used to fit a linear trendline to the results. The same region, between box sizes of 1/2 and 1/16, was selected in most cases (> 90%) for consistency. These points are shown in red on Figure D.3 and the corresponding linear fit is shown in blue. This agglomerate has a fractal dimension of 1.15, which was automatically calculated from the slope of the linear fit.

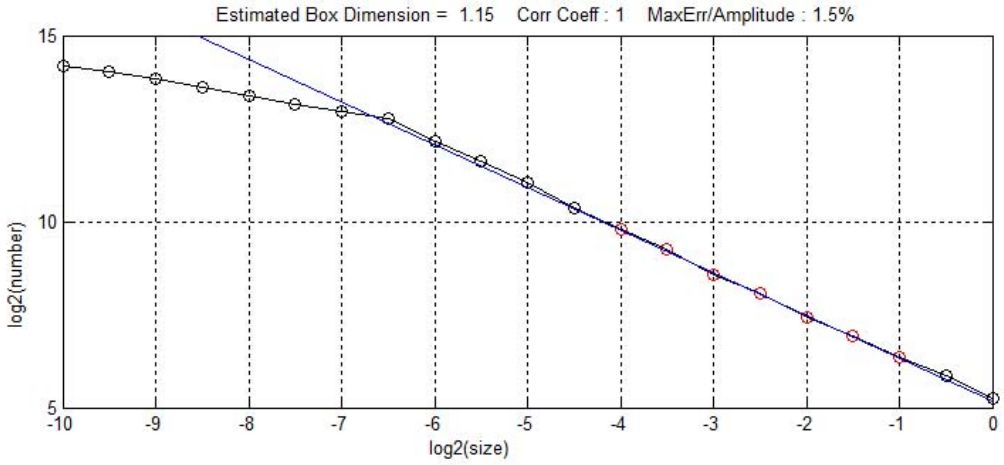

Figure D.3: *An example of fractal dimension calculation for agglomerate compression data using FracLab*

D.2 Correlation Results and Discussion

Table D.1 shows the Spearman R rank correlations between the three responses recorded and the physical characteristics of the agglomerates. Most of the correlation results in Table D.1 were not statistically-significant, which was largely attributable to the small number of agglomerates tested. However, two correlations were significant: between force at failure and convexity, and between strain at failure and the fractal dimension of the force response. Neither correlation coefficient was strong at approximately 0.23. It was also possible to calculate correlations between pairs of agglomerate characteristics, and these results are shown in Table D.2.

Many of these correlations are intuitively obvious if the relationships between physical characteristics of the agglomerates are considered. Some of these are listed below:

Table D.1: *Spearman R rank correlations of force at failure, strain at failure or agglomerate stiffness, and the physical characteristics of 92 agglomerates of infant formula B. Statistically-significant correlations at a 95% significance level are denoted in bold and with an asterisk*

Correlation	Force at Failure		Strain at Failure		Agglomerate Stiffness	
	R	p-value	R	p-value	R	p-value
Mean Diameter	-0.0038	0.9719	0.1118	0.2996	0.0596	0.5815
Length	-0.0211	0.8456	0.1631	0.1288	0.0599	0.5793
Width	0.0794	0.4623	0.0050	0.9632	0.1488	0.1665
Projected Area	0.0192	0.8593	0.1028	0.3406	0.0534	0.6214
Roundness	0.0165	0.8784	-0.1212	0.2606	0.0101	0.9255
Convexity	0.2266	**0.0337***	0.0548	0.6122	0.0089	0.9344
Aspect Ratio	-0.0313	0.7724	0.1268	0.2392	-0.0233	0.8297
Outline F. Dim.	0.1395	0.1948	0.1034	0.3378	-0.0362	0.7375
Force F. Dim.	0.0391	0.7177	0.2328	**0.0291***	0.0520	0.6304

Table D.2: *Spearman R rank correlations of pairs of agglomerate physical characteristics, where p-values are given in parentheses after the R coefficients. Statistically-significant correlations at a 95% significance level are denoted in bold and with an asterisk*

	Force F. Dim.	Outline F. Dim.	Aspect Ratio	Convexity
Mean Diameter	0.097 (0.367)	0.216 (**0.043***)	0.505 (**0.000***)	-0.196 (0.067)
Length	0.158 (0.142)	0.244 (**0.022***)	0.781 (**0.000***)	-0.382 (**0.000***)
Width	0.082 (0.446)	-0.401 (**0.000***)	-0.438 (**0.000***)	-0.200 (0.062)
Projected Area	0.082 (0.448)	0.214 (**0.045***)	0.395 (**0.000***)	-0.109 (0.313)
Roundness	-0.131 (0.222)	-0.441 (**0.000***)	-0.936 (**0.000***)	0.236 (**0.027***)
Convexity	-0.034 (0.750)	0.529 (**0.000***)	-0.198 (0.064)	
Aspect Ratio	0.085 (0.433)	0.465 (**0.000***)		
Outline F. Dim.	-0.029 (0.788)			

	Roundness	Projected Area	Width	Length
Mean Diameter	-0.525 (**0.000***)	0.966 (**0.000***)	0.423 (**0.000***)	0.873 (**0.000***)
Length	-0.797 (**0.000***)	0.789 (**0.000***)	0.150 (0.164)	
Width	0.341 (**0.001***)	0.498 (**0.000***)		
Projected Area	-0.422 (**0.000***)			

- Mean diameter had a quadratic relationship with projected area; therefore, the correlation coefficient for these two characteristics should be almost 1. The calculated coefficient was 0.966. Similarly, a strong negative correlation was expected between roundness and aspect ratio, since by definition, agglomerates with high roundness values are required to have aspect ratios close to unity, and those with low roundness values must have large aspect ratios.
- Length and roundness had a strong, statistically-significant R coefficient of -0.797. This negative correlation indicates that, on average, longer particles had relatively low roundness values.
- Projected area showed a strong positive correlation with agglomerate length (0.789).

A small number of the statistically-significant results provided more insight. Fractal dimension of the agglomerate outlines showed a moderate correlation with aspect ratio (0.465), agglomerate width (-0.401), roundness (-0.441) and convexity (0.529). Roundness and mean diameter had a moderate negative correlation of -0.525.

E

Convexities of Simulated Agglomerates before Mechanical Loading

The convexities of the simulated agglomerates generated using the sequential addition algorithm were stated to lie between 0.14 and 0.18 in Section 5.2.1. These convexities were calculated using Eq. E.1:

$$\text{Convexity} = \frac{\text{Total volume occupied by spheres}}{\text{Volume enclosed by the bounding convex hull}} \tag{E.1}$$

The convex hull of a set of points is defined as the smallest convex polyhedron which contains all of the points in the set. This was calculated in MATLAB using the *convhulln* function. Figure E.1 shows an example of a convex hull fitted to a set of 100 randomly-generated points in three dimensions drawn from the uniform distribution.

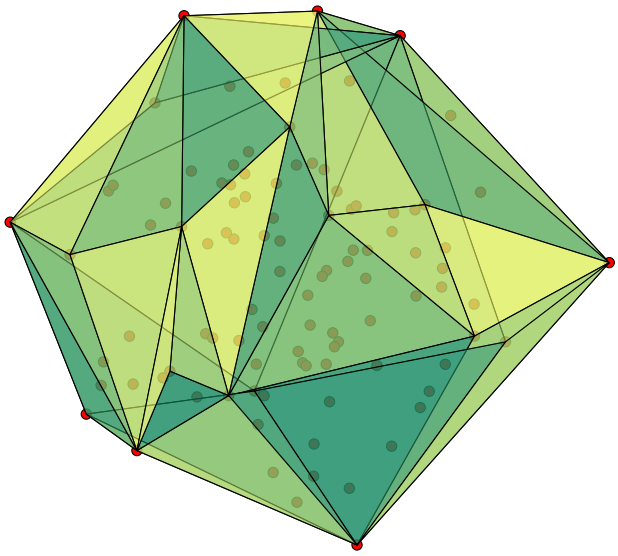

Figure E.1: *Example of a convex hull fitted to 100 randomly-generated points*

Although this method made use of an inbuilt MATLAB function, finding an accurate value for the convexity was not as straightforward as this fact may imply. The convexity

was calculated directly from the output of the sequential addition algorithm shown in Appendix C. Each row in the output file corresponded to one sphere and there were four columns: the first three contained x, y and z coordinates of the sphere centres while the fourth column gave the diameters of the spheres. To find the total volume occupied by all m spheres, V_s, the volumes of each individual sphere were summed:

$$V_s = \sum_{i=1}^{m} \frac{\pi}{6} d_i^3 \tag{E.2}$$

If the convex hull was fitted using only the sphere centres as potential vertices, parts of those spheres on the periphery of the agglomerate would protrude beyond the hull. However, the entirety of these peripheral spheres would be included in the calculation of V_s; hence, the resulting convexity would be overestimated and quite inaccurate, particularly for agglomerates containing relatively few spheres. This issue was avoided by replacing each sphere centrepoint with a set of points having the following properties:

- Each point was a distance equivalent to the sphere radius from the centrepoint of the sphere.
- The points were evenly distributed on the surface of the sphere.

This method necessitated finding an appropriate compromise between accuracy and computational requirements. For example, if an agglomerate contains 700 spheres, the number of potential vertices would increase to 700,000 if each centrepoint was replaced with 1000 points on the sphere surface. Moreover, the number of possible facets for the convex hull would increase from $\binom{700}{3}$ to $\binom{700000}{3}$, i.e., from 5.7×10^7 to 5.7×10^{16}. Despite the large number of permutations for the convex hull, the *qhull* algorithm used by MATLAB for the *convhulln* function is efficient and quick, even with large data sets. Most of the calculation time required is for other operations, including reading data from text files, basic manipulations of matrices, plotting figures and writing the results to output files. This is illustrated by Table E.1, which shows times required to fit convex hulls and find their volumes for large sets of 3D coordinates on the range [0, 1] which were randomly selected from the uniform distribution. These computations were performed on a single 3 GHz Intel Pentium 4 processor and the times recorded were the medians of three replicates. These times were measured using the inbuilt MATLAB *tic…toc* construct and exclude the time required for data generation.

While it is inefficient to use an excessively large number of points to find the convex hull, it is important that the number is sufficient to ensure accurate convexity results. This may be illustrated by the simple idealised agglomerate shown in Figure E.2. This agglomerate is composed of two identical spheres in contact and has a convexity which may be calculated theoretically.

If the spheres have diameters of d, V_s is given by Eq. E.3. The volume of the hull, V_h, is

Table E.1: *Median times required to fit convex hulls and find their enclosed volumes using the MATLAB function* convhulln. *Hulls were fitted to sets of randomly-generated data with lengths varying between 10^4 and 10^7*

Number of Points $\times 10^{-4}$	Time (s)
1	0.015
2	0.031
5	0.062
10	0.125
20	0.203
50	0.516
100	1.156
200	2.110
500	5.078
1000	9.750

found by adding the volume of a cylinder of height d (highlighted in blue on Figure E.2) to the volume of two hemispherical heads, or equivalently one sphere (Eq. E.4). Thus, the convexity is 0.8, irrespective of the value of d:

$$V_s = 2\frac{\pi}{6}d^3 = \frac{\pi}{3}d^3 \tag{E.3}$$

$$V_h = \pi\frac{d^2}{4}(d) + \frac{\pi}{6}d^3 = \frac{5\pi}{12}d^3 \tag{E.4}$$

$$\text{Convexity} = \frac{V_s}{V_h} = \frac{\frac{\pi}{3}}{\frac{5\pi}{12}} = 0.8 \tag{E.5}$$

Each sphere may now be replaced by a set of points at a distance $d/2$ from their centres to assess the effect of changing the number of points used on the convexities calculated. This is shown on Figure E.3, where the number of points used per sphere varied from 25 to 4225 and the convexity changed correspondingly from 1.056 to 0.8009. Note that for each sphere, if the increment is given as π/n, the number of points per sphere is $(n+1)^2$ for this simple agglomerate.

For actual simulated agglomerates, such as the example shown in Figure 5.6 on p.109, only a minority of the spheres form part of the convex hull. For these peripheral hull spheres, the MATLAB algorithm used 4225 points for accuracy, whereas the number of points used for the core spheres was relatively unimportant, and therefore was set at 25 for computational efficiency. Those spheres which formed part of the hull could be distinguished from those which did not by initially fitting a crude convex hull to the agglomerate using 25 points for all spheres. Spheres were identified as hull spheres if at least one of the 25 points composing the sphere was a vertex of the convex hull. Then a second convex hull was fitted, increasing the number of points used for the hull

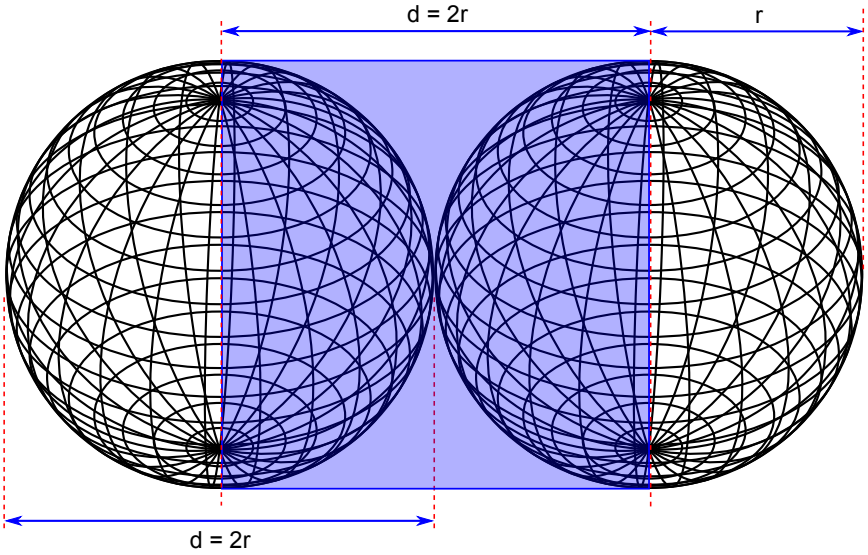

Figure E.2: *An agglomerate composed of two identical contacting spheres, the convexity of which may be calculated theoretically as 0.8 (Eq. E.5)*

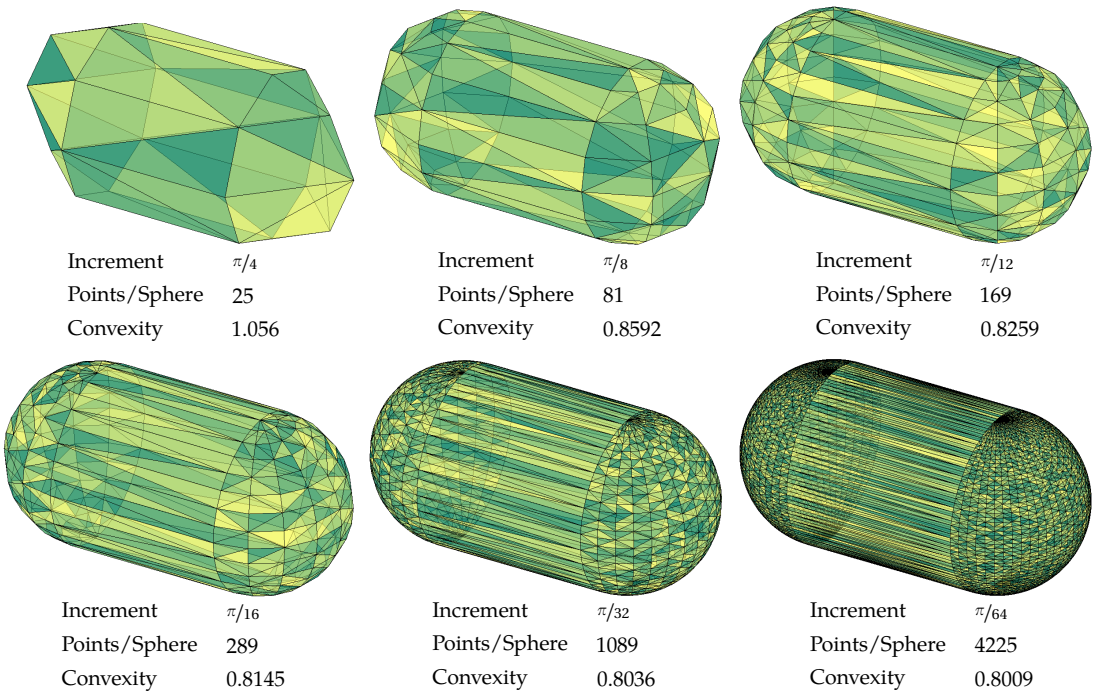

Figure E.3: *Effect of varying the number of points used per sphere on the calculated convexity*

spheres to 4225. The complete MATLAB code, with annotations, is shown in Section E.1.

E.1 Annotated MATLAB Code

```
% This is the complete script used to calculate convexities of
% DEM agglomerates with high accuracy.

clear
format long

% Read in the ball coordinate data. The first 3 columns contain
% the x, y and z coordinates and column 4 contains the
% ball diameters.
coord_data = dlmread('Ball_Coordinates.txt',' ',0,0);
points = size(coord_data,1);

% Find the volume occupied by all the balls.
ball_volume = 0; % Initialise at 0.

for i = 1:points
    ball_volume = ball_volume + (pi/6)*((coord_data(i,4))^3);
end

% Now fit a crude convex hull to the points.
counter = 0; % Initialise at 0.

% For each sphere, generate 25 points on the sphere surface to
% replace the centrepoint. Store these points in the
% expanded_data matrix.
for i = 1:points
    % Multiply coord_data(i,4) by 0.5 to convert to radii.
    [a,b,c] = sph_coords_convex_hull(coord_data(i,1),...
    ...coord_data(i,2),coord_data(i,3),0.5*coord_data(i,4),(pi/4));
    for j = 1:size(a,1)
        for k = 1:size(a,2)
            counter = counter + 1;
            expanded_data(counter,1) = a(j,k);
            expanded_data(counter,2) = b(j,k);
            expanded_data(counter,3) = c(j,k);
            % Also store the index of the ball.
            expanded_data(counter,4) = i;
        end
    end
end

expanded_points = size(expanded_data,1);
```

```
% Use the convhulln function to fit the convex hull.
[the_hull, hull_volume] = convhulln(expanded_data...
...((1:expanded_points),(1:3)));
hull_length = size(the_hull,1);

% Create a matrix of zeros which will be overwritten with indices
% of the hull spheres.
indices = zeros(3*expanded_points,1);
counter = 1; % Re-initialise at 1.

% Cycle through all the points in the crude convex hull and write
% indices of the balls which form part of the hull to the indices
% matrix, overwriting the zero values.
for i = 1:hull_length
    for j = 1:3
        indices(counter) = expanded_data(the_hull(i,j),4);
        counter = counter + 1;
    end
end

% Use the ismember command to identify those spheres which form
% part of the hull.
counter = 0;  % Reinitialise for further use.
balllist = [1:points]; % Create a vector of all ball indices.

% ismember returns a vector of 0s and 1s which is the same
% size as balllist. 1 is returned if that index is contained in
% both balllist and indices; otherwise, 0 is returned.
spherelist = ismember(balllist,indices);

% Clear and re-use some variables for efficiency.
clear expanded_data a b c expanded_points the_hull hull_volume...
... hull_length

% Now increase the number of points for the hull spheres.
for i = 1:points
    if spherelist(i) == 1 % Sphere is part of convex hull
        [a,b,c] = sph_coords_convex_hull(coord_data(i,1),...
        ...coord_data(i,2),coord_data(i,3),0.5*coord_data(i,4),...
        ...(pi/64));
    else
        [a,b,c] = sph_coords_convex_hull(coord_data(i,1),...
        ...coord_data(i,2),coord_data(i,3),0.5*coord_data(i,4),...
        ...(pi/4));
```

```
    end

    % Append the coordinates of sphere i to a matrix named
    % expanded_data.
    for j = 1:size(a,1)
        for k = 1:size(a,2)
            counter = counter + 1;
            expanded_data(counter,1) = a(j,k);
            expanded_data(counter,2) = b(j,k);
            expanded_data(counter,3) = c(j,k);
        end
    end
end

expanded_points = size(expanded_data,1);
% Fit a more precise convex hull.
[the_hull, hull_volume] = convhulln(expanded_data...
...((1:expanded_points),(1:3)));
hull_length = size(the_hull,1);

% Show a plot of the agglomerate, with full spheres and the
% bounding convex hull.
figure
hold on
axis('equal'); % Make the axes equal
axis('off'); % Turn the axes off

for i =1:points
    [a,b,c] = sph_coords_convex_hull(coord_data(i,1),...
    ...coord_data(i,2),coord_data(i,3),0.5*coord_data(i,4),(pi/8));
    surf(a,b,c,'LineWidth',0.1,'EdgeColor',[0.2,0.2,0.2]);
    colormap(summer);
    brighten(0.3);
end

for i =1:size(the_hull,1)
    j = the_hull(i,[1 2 3 1]);
    patch(expanded_data(j,1),expanded_data(j,2),...
    ...expanded_data(j,3),rand,'FaceAlpha',0.6);
end

hold off

% Finally, calculate the convexity.
```

```
convexity = ball_volume/hull_volume;
disp(['The agglomerate convexity is ',num2str(convexity),'.']);

return

~~~~~~~~~~~~~~~~~~~~~~~~~~~~~~~~~~~~~~~~~~~~~~~~~~~~~~~~~~~~~~~~~~~~

function [x,y,z] = sph_coords_convex_hull(xcenter,ycenter,...
...zcenter,rad,increment)

phi = 0:increment:pi;
theta = 0:2*increment:2*pi;
[Phi,Theta] = meshgrid(phi,theta);

x = xcenter + rad*sin(Phi).*cos(Theta);
y = ycenter + rad*sin(Phi).*sin(Theta);
z = zcenter + rad*cos(Phi);
```

E.2 Convexity Results

The distribution in convexities of the agglomerates before compression is shown in Figure E.4. For example, approximately 66% of agglomerates in the full set had a convexity less than 0.16. The convexities lay within a narrow range from 0.14–0.18, as mentioned at the start of this appendix.

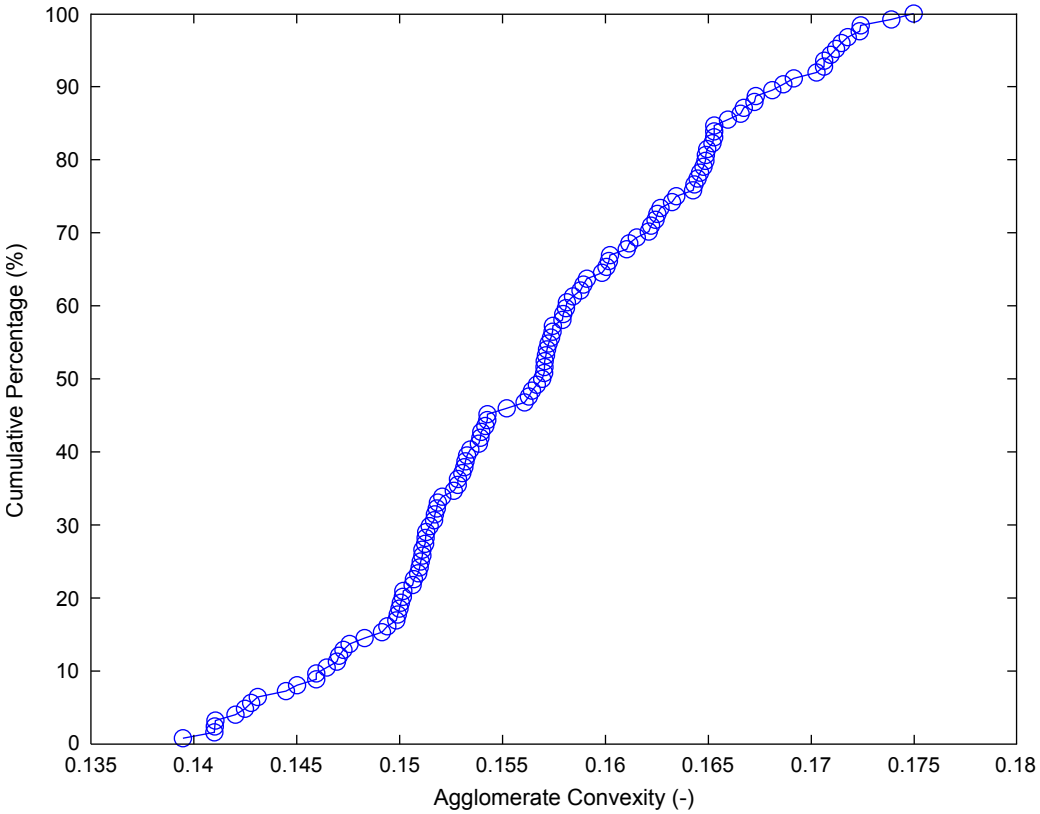

Figure E.4: *Plot showing the percentages of simulated agglomerates which had convexities ≤ the corresponding values given on the x-axis*

F

Illustration of DEM Calibration Difficulties in Chapter 5

The inherent variability of the simulated agglomerates in Chapter 5 made it extremely difficult to calibrate the model. This appendix illustrates this point using two randomly-generated agglomerates containing 633 and 746 spheres. The parameters selected for both agglomerates were varied according to an L_8 Taguchi array (Table A.1 on p.211). The array was saturated, and the levels of the seven factors were chosen as their settings in set II of Table 5.3 ± 20%. The factors and levels are shown in Table F.1 and the assigned array is shown as Table F.2. For conciseness, the seven factors are denoted as A–G in accordance with Table F.1. Therefore, 16 experiments were necessary since the eight experiments in the L_8 array were run for each agglomerate.

Table F.1: *Control factors and levels used for the L_8 experimental design*

Control Factors	Levels	
	1	2
Ball normal stiffness, A ($N m^{-1}$)	3.2×10^7	4.8×10^7
Ball shear stiffness, B ($N m^{-1}$)	3.2×10^7	4.8×10^7
Bond normal strength, C ($N m^{-2}$)	8×10^8	1.2×10^9
Bond shear strength, D ($N m^{-2}$)	8×10^8	1.2×10^9
Bond normal stiffness, E ($N m^{-3}$)	2.4×10^{15}	3.6×10^{15}
Bond shear stiffness, F ($N m^{-3}$)	2.4×10^{15}	3.6×10^{15}
Ball friction, G	0.56	0.84

The data were analysed by ANOVA and the results are shown in Tables F.3 and F.4.

Table F.2: *L_8 array showing the columns used after assigning all factors to the array*

Row	Column						
	B ($\mathrm{N\,m^{-1}}$)	C ($\mathrm{N\,m^{-2}}$)	E ($\mathrm{N\,m^{-3}}$)	D ($\mathrm{N\,m^{-2}}$)	F ($\mathrm{N\,m^{-3}}$)	A ($\mathrm{N\,m^{-1}}$)	G
1	3.2×10^{7}	8×10^{8}	2.4×10^{15}	8×10^{8}	2.4×10^{15}	3.2×10^{7}	0.56
2	3.2×10^{7}	8×10^{8}	2.4×10^{15}	1.2×10^{9}	3.6×10^{15}	4.8×10^{7}	0.84
3	3.2×10^{7}	1.2×10^{9}	3.6×10^{15}	8×10^{8}	2.4×10^{15}	4.8×10^{7}	0.84
4	3.2×10^{7}	1.2×10^{9}	3.6×10^{15}	1.2×10^{9}	3.6×10^{15}	3.2×10^{7}	0.56
5	4.8×10^{7}	8×10^{8}	3.6×10^{15}	8×10^{8}	3.6×10^{15}	3.2×10^{7}	0.84
6	4.8×10^{7}	8×10^{8}	3.6×10^{15}	1.2×10^{9}	2.4×10^{15}	4.8×10^{7}	0.56
7	4.8×10^{7}	1.2×10^{9}	2.4×10^{15}	8×10^{8}	3.6×10^{15}	4.8×10^{7}	0.56
8	4.8×10^{7}	1.2×10^{9}	2.4×10^{15}	1.2×10^{9}	2.4×10^{15}	3.2×10^{7}	0.84

For each response, the factor with the smallest sum of squares (SS shown in grey) was pooled ($\mathbb{P}$) with the error to allow the statistical significance to be evaluated.

Table F.3: *Partial ANOVA table for the three simulation responses for the agglomerate containing 633 spheres. υ is the number of degrees of freedom, SS the sum of squares and p the p-value. Statistically-significant effects at a 95% confidence level are denoted in bold and with an asterisk*

Factor	υ	Normal Force at Failure		Strain at Failure		Agglomerate Stiffness	
		$\mathrm{SS}\times10^{6}$	p	SS	p	$\mathrm{SS}\times10^{-4}$	p
A	1 (0 $\mathbb{P}$)	1.13	—	16.2	0.140	168	0.110
B	1 (0 $\mathbb{P}$)	37.5[†]	0.110	0.805	—	26.4 [‡]	0.264
C	1 (0 $\mathbb{P}$)	609	**0.027***	1.12	0.448	5.12	—
D	1	1.07	0.509	2.92	0.308	44.4	0.209
E	1	25.2	0.133	8.88	0.186	11.3	0.377
F	1	29.8	0.122	5.42	0.234	47.9	0.201
G	1	38.3	0.108	16.6	0.138	596	0.059
Error	1 ($\mathbb{P}$)	1.13		0.805		5.12	
Total	7	742		51.9		900	

[†]Note that this entry is equal to 3.75×10^{-5} to prevent ambiguity.

[‡]This entry is equal to 2.64×10^{5}.

The ANOVA results were quite consistent, particularly for the force and strain at failure responses. For normal force at failure, bond normal strength had the highest sum of squares for both agglomerates, and was statistically-significant at the 95% level for the agglomerate containing 633 spheres. The ball friction had the second-highest SS for

Table F.4: *Partial ANOVA table for the three simulation responses for the agglomerate containing 746 spheres. υ is the number of degrees of freedom, SS the sum of squares and p the p-value. Statistically-significant effects at a 95% confidence level are denoted in bold and with an asterisk*

Factor	υ	Normal Force at Failure		Strain at Failure		Agglomerate Stiffness	
		$SS \times 10^4$	p	SS	p	$SS \times 10^{-5}$	p
A	1 (0 $\mathbb{P}$)	5.21	0.266	56.8	**0.045***	5.89	—
B	1 (0 $\mathbb{P}$)	1.03	—	0.287	—	18.2	0.329
C	1	49.2	0.091	6.44	0.133	17.4	0.335
D	1	2.28	0.376	7.46	0.123	72.4	0.177
E	1	3.16	0.330	27.6	0.065	97.7	0.153
F	1	3.01	0.336	22.4	0.072	7.47	0.462
G	1	12.7	0.176	85.0	**0.037***	28.1	0.273
Error	1 ($\mathbb{P}$)	1.03		0.287		5.89	
Total	7	76.6		206		247	

both agglomerates. The results for strain at failure corresponded almost exactly for the two simulated agglomerates. When the factors were ordered by increasing SS, the same hierarchy was seen in both cases: ball shear stiffness (which was pooled) → bond normal strength → bond shear strength → bond shear stiffness → bond normal stiffness → ball normal stiffness → ball friction. The last two were significant at the 95% level for the agglomerate containing 746 spheres. The results for agglomerate stiffness did not compare as well, although none of the factors were statistically-significant for either agglomerate. Although this reasonable correspondence between the ANOVA results for the two agglomerates may imply that calibration ought to be straightforward, Figure F.1 demonstrates why this was not the case.

Even for those factors identified as being statistically-significant, increasing the setting of a factor often had opposite effects on the two agglomerates, e.g., increasing the ball friction caused an increase in the strain at failure of the agglomerate containing 633 spheres whereas the strain at failure decreased for the agglomerate containing 746 spheres. Thus, even though a factor might be identified as influential, it may be unclear what the effect of changing its setting would be on a typical agglomerate. This behaviour made the calibration process difficult and time-consuming.

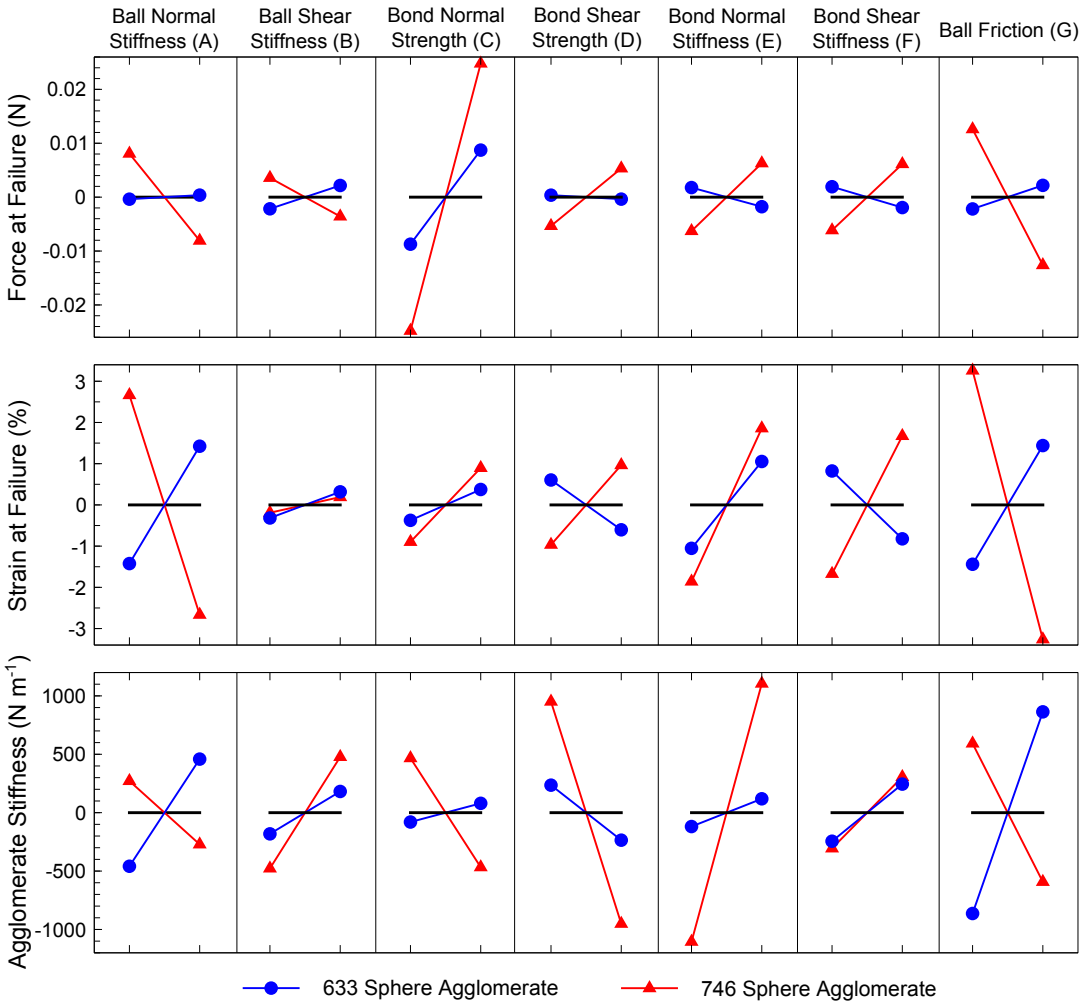

Figure F.1: *ANOVA contributions plots for three responses: force at failure (N), strain at failure (%) and agglomerate stiffness ($N m^{-1}$)*

G

Mathematical Derivations for Probabilistic Model of Pneumatic Conveying

CHAPTER 6 contains the development of a probabilistic model of pneumatic conveying. Most of the detailed mathematical workings were not given in this chapter for reasons of space, and are instead provided in this appendix for reference.

G.1 Probability Density Function of Fluid Velocity

The fluid velocity, u_f, is related to the maximum velocity along the centreline, u_m, by the $1/7^{\text{th}}$ power law given as Eq. 6.1.

$$u_f = u_m \left(1 - \frac{r}{R}\right)^{\frac{1}{n}} \tag{6.1}$$

The first derivative with respect to r was found as Eq. G.1:

$$\begin{aligned} \frac{du_f}{dr} &= -\frac{u_m}{nR}\left(1-\frac{r}{R}\right)^{\frac{1}{n}-1} \\ &= -\frac{u_m}{nR}\left(1-\frac{r}{R}\right)^{\frac{1}{n}}\left(1-\frac{r}{R}\right)^{-1} \end{aligned} \tag{G.1}$$

The two substitutions identified below were made:

$$u_m \left(1 - \frac{r}{R}\right)^{\frac{1}{n}} = u_f \tag{G.2}$$

$$\left(1 - \frac{r}{R}\right)^{-1} = \left(\frac{u_m}{u_f}\right)^{n} \tag{G.3}$$

Thus, Eq. G.4 was obtained:

$$\begin{aligned} \frac{du_f}{dr} &= -\frac{{u_f}^{1-n}{u_m}^n}{nR} \\ \therefore dr &= -\frac{nR\,du_f}{{u_f}^{1-n}{u_m}^n} \end{aligned} \tag{G.4}$$

The fraction of the pipe cross-section in which the velocity lies between u_f and $u_f + du_f$ is given by Eq. G.5:

$$\frac{2\pi r\,dr}{\pi R^2} = \frac{2r\,dr}{R^2} = -\frac{2nRr\,du_f}{R^2{u_f}^{1-n}{u_m}^n} \tag{G.5}$$

Eq. 6.1 was rearranged to obtain $r = R\left(1 - \frac{{u_f}^n}{{u_m}^n}\right)$ and this was substituted into Eq. G.5:

$$\frac{2r\,dr}{R^2} = -\frac{2nR^2({u_m}^n - {u_f}^n)\,du_f}{R^2{u_f}^{1-n}{u_m}^{2n}} = \frac{2n({u_f}^n - {u_m}^n)\,du_f}{{u_f}^{1-n}{u_m}^{2n}} \tag{G.6}$$

Finally, the probability density function is given by Eq. 6.3:

$$P(u_f) = \frac{2n({u_f}^n - {u_m}^n)}{{u_f}^{1-n}\,{u_m}^{2n}} \tag{6.3}$$

Eq. 6.3 satisfies the basic requirement of a PDF that its zeroth moment equals one:

$$\begin{aligned} \int_{u_m}^{0} P(u_f)\,du_f &= \frac{2n}{{u_m}^{2n}} \int_{u_m}^{0} \left({u_f}^{2n-1} - {u_m}^n {u_f}^{n-1}\right) du_f \\ &= \frac{2n}{{u_m}^{2n}} \left[\frac{{u_f}^{2n}}{2n} - \frac{{u_m}^n {u_f}^n}{n}\right]_{u_m}^{0} \\ &= \frac{2}{{u_m}^{2n}} \left[{u_m}^n {u_f}^n - \frac{1}{2}{u_f}^{2n}\right]_{0}^{u_m} \\ &= \frac{2}{{u_m}^{2n}} \left({u_m}^{2n} - \frac{1}{2}{u_m}^{2n}\right) \\ &= \frac{2}{{u_m}^{2n}} \left(\frac{{u_m}^{2n}}{2}\right) \\ &= 1 \end{aligned}$$

G.2 Derivation of Mean Fluid Velocity

The mean fluid velocity, μ_{uf}, could be found using two different methods, which had to give the same result:

1. By a method based on integration of the probability density function of u_f
2. By integrating the spatial variation of u_f

G.2.1 Method One

$$\begin{aligned}
\mu_{uf} &= \int_0^{u_m} P(u_f)\, u_f \, d\, u_f \\
&= \frac{2n}{{u_m}^{2n}} \int_0^{u_m} \left({u_f}^{2n} - {u_m}^n {u_f}^n \right) d\, u_f \\
&= \frac{2n}{{u_m}^{2n}} \left[\frac{{u_f}^{2n+1}}{2n+1} - \frac{{u_m}^n {u_f}^{n+1}}{n+1} \right]_0^{u_m} \\
&= \frac{2}{{u_m}^{2n}} \left[\frac{{u_m}^{2n+1}}{2n+1} - \frac{{u_m}^{2n+1}}{n+1} \right]_0^{u_m} \\
&= \not{} \frac{2n^2}{(n+1)(2n+1)} u_m
\end{aligned} \tag{6.4}$$

G.2.2 Method Two

$$\begin{aligned}
\mu_{uf} &= \frac{1}{\pi R^2} \int_0^R u_f \cdot 2\pi r \, d\, r \\
&= \frac{1}{\pi R^2} \int_0^R u_m \left(1 - \frac{r}{R} \right)^{\frac{1}{n}} 2\pi r \, d\, r \\
&= \frac{2u_m}{R^2} \int_0^R \left(1 - \frac{r}{R} \right)^{\frac{1}{n}} r \, d\, r
\end{aligned} \tag{G.7}$$

A substitution was made to do this integration. Let $y = 1 - \frac{r}{R}$. Therefore, $r = R(1-y)$ and $d\, r = -R\, d\, y$. The limits also needed to be modified:

$$\begin{aligned}
r &= 0 \quad &\longrightarrow \quad & y = 1 \\
r &= R \quad &\longrightarrow \quad & y = 0
\end{aligned}$$

Thus, Eq. G.7 was rewritten as Eq. G.8:

$$\begin{aligned}
\mu_{uf} &= -2u_m \int_1^0 y^{\frac{1}{n}} (1-y)\, d\, y \\
&= 2u_m \int_0^1 \left(y^{\frac{1}{n}} - y^{\frac{n+1}{n}} \right) d\, y \\
&= 2u_m \left[\frac{n y^{\frac{n+1}{n}}}{n+1} - \frac{n y^{\frac{2n+1}{n}}}{2n+1} \right]_0^1 \\
&= 2u_m \left(\frac{n}{n+1} - \frac{n}{2n+1} \right) \\
&= \frac{2n^2}{(n+1)(2n+1)} u_m
\end{aligned} \tag{G.8}$$

$$\tag{6.4}$$

G.3 Derivation of Variance in Fluid Velocity

As for the mean fluid velocity in Section G.2, the variance in fluid velocity, σ^2_{uf}, could be found using two different methods.

G.3.1 Method One

$$\sigma^2_{uf} = \int_0^{u_m} P(u_f)(u_f - \mu_{uf})^2 \, du_f \tag{G.9}$$

Eqs. 6.3 and 6.4 were substituted for $P(u_f)$ and μ_{uf}, respectively:

$$\sigma^2_{uf} = \frac{2n}{{u_m}^{2n}} \int_0^{u_m} \left({u_f}^2 - \frac{4n^2 u_m u_f}{(n+1)(2n+1)} + \frac{4n^4 {u_m}^2}{(n+1)^2(2n+1)^2} \right) \left(\frac{{u_m}^n - {u_f}^n}{{u_f}^{1-n}} \right) du_f \tag{G.10}$$

This integral was divided into six parts, as follows:

$$\begin{aligned}
\sigma^2_{uf} = {} & \frac{2n}{{u_m}^n} \int_0^{u_m} {u_f}^{n+1} \, du_f - \frac{2n}{{u_m}^{2n}} \int_0^{u_m} {u_f}^{2n+1} \, du_f - \frac{8n^3 {u_m}^{1-n}}{(n+1)(2n+1)} \int_0^{u_m} {u_f}^n \, du_f \dots \\
& + \frac{8n^3 {u_m}^{1-2n}}{(n+1)(2n+1)} \int_0^{u_m} {u_f}^{2n} \, du_f + \frac{8n^5 {u_m}^{2-n}}{(n+1)^2(2n+1)^2} \int_0^{u_m} {u_f}^{n-1} \, du_f \dots \\
& - \frac{8n^5 {u_m}^{2-2n}}{(n+1)^2(2n+1)^2} \int_0^{u_m} {u_f}^{2n-1} \, du_f \\
\sigma^2_{uf} = {} & \frac{2n{u_m}^2}{n+2} - \frac{2n{u_m}^2}{2n+2} - \frac{8n^3 {u_m}^2}{(n+1)^2(2n+1)} + \frac{8n^3 {u_m}^2}{(n+1)(2n+1)^2} + \frac{8n^5 {u_m}^2}{n(n+1)^2(2n+1)^2} \dots \\
& - \frac{8n^5 {u_m}^2}{2n(n+1)^2(2n+1)^2}
\end{aligned} \tag{G.11}$$

Eq. G.11 was manipulated algebraically, gathering all of the terms, to give Eq. 6.5:

$$\sigma^2_{uf} = \frac{n^2(5n+1)}{(n+1)^2(n+2)(2n+1)^2} {u_m}^2 \tag{6.5}$$

G.3.2 Method Two

$$\sigma^2_{uf} = \frac{1}{\pi R^2} \int_0^R (u_f - \mu_{uf})^2 \cdot 2\pi r \, dr \tag{G.12}$$

Eq. 6.1 was substituted for u_f and μ_{uf} was replaced by Eq. 6.4. The integral was divided into three parts:

$$\begin{aligned}
\sigma^2_{uf} = {} & \frac{2{u_m}^2}{R^2} \int_0^R r \left(1 - \frac{r}{R}\right)^{\frac{2}{n}} dr - \frac{8n^2 {u_m}^2}{R^2(n+1)(2n+1)} \int_0^R r \left(1 - \frac{r}{R}\right)^{\frac{1}{n}} dr \dots \\
& + \frac{8n^4 {u_m}^2}{R^2(n+1)^2(2n+1)^2} \int_0^R r \, dr
\end{aligned}$$

For the first two of these integrals, the same substitution was made as in Section G.2.2, i.e., $y = 1 - \frac{r}{R}$:

$$\begin{aligned}
\sigma_{uf}^2 &= \frac{2{u_m}^2}{R^2}\int_1^0 -R^2(1-y)y^{\frac{2}{n}}\,dr - \frac{8n^2{u_m}^2}{R^2(n+1)(2n+1)}\int_1^0 -R^2(1-y)y^{\frac{1}{n}}\,dr \ldots \\
&\quad + \frac{8n^4{u_m}^2}{R^2(n+1)^2(2n+1)^2}\left[\frac{r^2}{2}\right]_0^R \\
&= 2{u_m}^2\left(\frac{n}{n+2} - \frac{n}{2(n+1)}\right) + \frac{8n^2{u_m}^2}{(n+1)(2n+1)}\left(\frac{n}{2n+1} - \frac{n}{n+1}\right) + \frac{4n^4{u_m}^2}{(n+1)^2(2n+1)^2} \\
&= 2n{u_m}^2\left(\frac{1}{n+2} - \frac{1}{2(n+1)} + \frac{4n^2}{(n+1)(2n+1)^2} - \frac{4n^2}{(n+1)^2(2n+1)} + \frac{2n^3}{(n+1)^2(2n+1)^2}\right)
\end{aligned}$$

When similar terms were gathered and this equation was rearranged, the same expression was obtained as in Section G.3.1, i.e.:

$$\sigma_{uf}^2 = \frac{n^2(5n+1)}{(n+1)^2(n+2)(2n+1)^2}{u_m}^2 \tag{6.5}$$

G.4 Derivation of Effective Fluid Velocity

The effective fluid velocity is the average fluid velocity acting on the cross-section of a particle normal to the axial fluid velocity. Consider a particle of radius r_p, with its centre at a distance of r from the centreline of a pipe of radius R. The inner edge of the particle is a radial distance of $r - r_p$ from the centreline of the pipe, while its outer edge is a radial distance of $r + r_p$ from the centreline. The effective fluid velocity acting on this particle is approximately equal to the mean velocity in an annular band with inner and outer radii of $r - r_p$ and $r + r_p$, respectively. This is shown in Figure G.1.

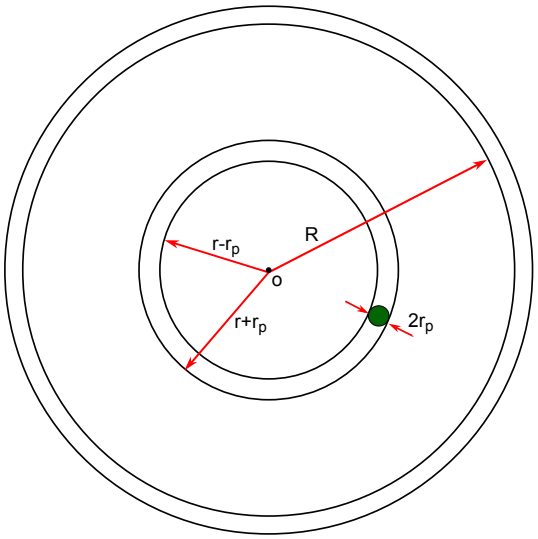

Figure G.1: *Illustration of a spherical particle in the cross-section of the pipeline*

Thus, u_e was approximated by Eq. 6.7:

$$u_e(r) = \int_{r-r_p}^{r+r_p} \frac{u_m \left(1-\frac{r}{R}\right)^{\frac{1}{n}} \cdot 2\pi r \, dr}{\pi\left[(r+r_p)^2-(r-r_p)^2\right]} \tag{6.6}$$

$$= \frac{u_m}{2\left(1+\frac{1}{n}\right)\frac{r_p}{R}} \left[\left(1+\frac{r_p}{R}-\frac{r}{R}\right)^{\frac{n+1}{n}} - \left(1-\frac{r_p}{R}-\frac{r}{R}\right)^{\frac{n+1}{n}}\right] \tag{6.7}$$

Note that u_e is defined only for $0 \leq r \leq R - r_p$ since the particles are in contact with the pipe wall at the upper limit. Eq. 6.7 is a simplification as it assumes that each particle has a cross-section which is an annular segment rather than a circle. This difference is illustrated by Figure G.2.

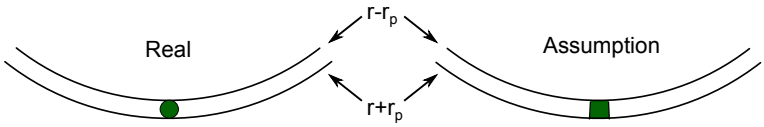

Figure G.2: *Diagram showing the assumption made that the cross-section of each particle is a segment of an annulus rather than a circle*

This assumption is reasonable if the particle radius is considerably smaller than the pipe radius. A more accurate expression was obtained by substituting the annular rings of thickness dr with narrow strips of length L and thickness ds, as shown on Figure G.3. s is the radial distance between the centreline of the pipe and any such strip, while r is the value of s when at the centrepoint of the particle.

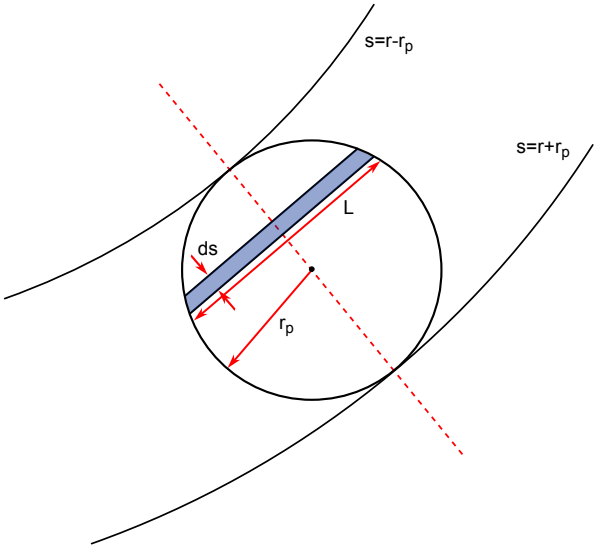

Figure G.3: *Geometry for more accurate integration used to quantify u_e*

L varies with radial distance, from 0 at $r - r_p$ and $r + r_p$ to a maximum of $2r_p$ at a radial distance of r. Figure G.4 graphically shows the relationship between L and s, while Eq. G.13 is the equation relating these variables.

$$L = 2\sqrt{{r_p}^2 - (s-r)^2} \tag{G.13}$$

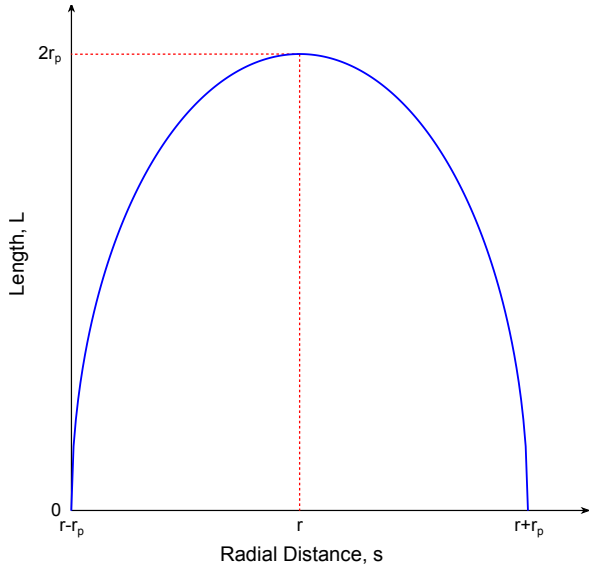

Figure G.4: *Relationship between L and s which is quantified by Eq. G.13*

Thus, the integral given as Eq. 6.6 was changed to the form of Eq. G.14:

$$\begin{aligned} u_e(r) &= \frac{1}{\pi {r_p}^2} \int_{s=r-r_p}^{s=r+r_p} u_f L \, ds \qquad\qquad r - r_p \le s \le r + r_p \\ &= \frac{2u_m}{\pi {r_p}^2} \int_{s=r-r_p}^{s=r+r_p} \left(1 - \tfrac{s}{R}\right)^{\frac{1}{n}} \sqrt{{r_p}^2 - (s-r)^2} \, ds \end{aligned} \tag{G.14}$$

Although it appears to be relatively straightforward, it was not possible to evaluate an analytical solution using Mathematica and therefore, Eq. G.14 required numerical evaluation.

G.5 Probability Density Function of Effective Fluid Velocity

The first derivative with respect to r was obtained as Eq. G.15:

$$\frac{du_e}{dr} = \frac{u_m}{2r_p} \left[\left(1 - \frac{r_p}{R} - \frac{r}{R}\right)^{\frac{1}{n}} - \left(1 + \frac{r_p}{R} - \frac{r}{R}\right)^{\frac{1}{n}} \right] \tag{G.15}$$

The fraction of the pipe cross-section in which the velocity lies between u_e and $u_e + du_e$ was obtained as follows:

$$\frac{2\pi r \, dr}{\pi R^2} = \frac{2r \, dr}{R^2} = \frac{2r \cdot 2r_p \, du_e}{R^2 u_m \left[\left(1 - \frac{r_p}{R} - \frac{r}{R}\right)^{\frac{1}{n}} - \left(1 + \frac{r_p}{R} - \frac{r}{R}\right)^{\frac{1}{n}} \right]}$$

Since $r = R\left(1 - \frac{{u_f}^n}{{u_m}^n}\right)$ from the $1/7^{\text{th}}$ power law:

$$\begin{aligned}\frac{2r\,dr}{R^2} &= \frac{2R\left(1-\frac{{u_f}^n}{{u_m}^n}\right)\cdot 2r_p\,du_e}{R^2 u_m\left[\left(1-\frac{r_p}{R}-\left(1-\frac{{u_f}^n}{{u_m}^n}\right)\right)^{\frac{1}{n}}-\left(1+\frac{r_p}{R}-\left(1-\frac{{u_f}^n}{{u_m}^n}\right)\right)^{\frac{1}{n}}\right]} \\ &= \frac{4r_p({u_m}^n-{u_f}^n)R^{\frac{1}{n}-1}\,du_e}{{u_m}^n\left[\left(R{u_f}^n-r_p{u_m}^n\right)^{\frac{1}{n}}-\left(R{u_f}^n+r_p{u_m}^n\right)^{\frac{1}{n}}\right]}\end{aligned}$$

Finally, the PDF was obtained as Eq. 6.9:

$$P(u_e) = \frac{4r_p({u_m}^n-{u_f}^n)R^{\frac{1}{n}-1}}{{u_m}^n\left[\left(R{u_f}^n-r_p{u_m}^n\right)^{\frac{1}{n}}-\left(R{u_f}^n+r_p{u_m}^n\right)^{\frac{1}{n}}\right]} \tag{6.9}$$

G.6 Proof that Effective Fluid Velocity Tends to Fluid Velocity for Infinitesimal Particles

This could be proved in a number of ways, one of which was to apply l'Hôpital's rule. This states that for two functions, $a(r_p)$ and $b(r_p)$:

$$\lim_{r_p\to 0}\frac{a(r_p)}{b(r_p)} = \lim_{r_p\to 0}\frac{a'(r_p)}{b'(r_p)} \tag{G.16}$$

if $\lim_{r_p\to 0} a(r_p) = \lim_{r_p\to 0} b(r_p) = 0$ or $\pm\infty$ **and** $\lim_{r_p\to 0}\frac{a'(r_p)}{b'(r_p)}$ exists.

Writing u_e as $\frac{a(r_p)}{b(r_p)}$:

$$\begin{aligned}\frac{da}{dr_p} &= \frac{u_m(n+1)}{nR}\left[\left(1+\frac{r_p}{R}-\frac{r}{R}\right)^{\frac{1}{n}}+\left(1-\frac{r_p}{R}-\frac{r}{R}\right)^{\frac{1}{n}}\right] \\ \frac{db}{dr_p} &= \frac{2(n+1)}{nR}\end{aligned}$$

Thus:

$$\begin{aligned}\lim_{r_p\to 0} u_e &= \lim_{r_p\to 0}\frac{a'(r_p)}{b'(r_p)} \\ &= \lim_{r_p\to 0}\frac{u_m}{2}\left[\left(1+\frac{r_p}{R}-\frac{r}{R}\right)^{\frac{1}{n}}+\left(1-\frac{r_p}{R}-\frac{r}{R}\right)^{\frac{1}{n}}\right] \\ &= \frac{u_m}{2}\left[2\left(1-\frac{r}{R}\right)\right] \\ &= u_f\end{aligned}$$

G.7 Outline Derivation of Mean and Variance of Particle Velocity

Eq. 6.24 shows that the effective fluid velocity, u_e, at any time is the sum of the mean effective fluid velocity, μ_{ue}, and a random component, denoted as $u_e^*(t)$:

$$u_e(t) = \mu_{ue} + u_e^*(t) \tag{G.17}$$

When Eq. 6.17 was substituted into Eq. G.17, Eq. G.18 was obtained, in which $W(t)$ is a random variate drawn from the normal distribution with a mean of 0 and a variance of σ_{ue}^2, i.e., $W(t) \backsim N[0, \sigma_{ue}^2]$.

$$\frac{d}{dt} u_e^*(t) + \phi u_e(t) = W(t) \tag{G.18}$$

This stochastic differential equation has the same form as an equation developed for lumped capacitance heat transfer by Nicolaï et al. (2007). Nicolaï et al. solved the differential equation using the variance propagation algorithm, and the analogous result for Eq. G.18 is shown as Eqs. 6.26 and 6.27:

$$\mu_{up} = \mu_{ue} \tag{6.26}$$

$$\sigma_{up}^2 = \frac{p_e}{p_e + \phi} \sigma_{ue}^2 + \frac{p_e}{p_e - \phi} \sigma_{ue}^2 e^{-2p_e t} - \frac{2p_e^2}{(p_e + \phi)(p_e - \phi)} \sigma_{ue}^2 e^{-(p_e + \phi)t} \tag{6.27}$$

G.8 Mean Fall Height and Velocity of Particle

Since the pipe cross-section is symmetrical, half was disregarded in the derivation. A vertical strip of width dx and of height $2y$ was selected, which is a distance x from the vertical axis passing through the centrepoint of the cross-section. This is shown in Figure G.5.

The mean fall height for particles in this strip is y, since there is an equal probability of any particle within this area being above or below the horizontal area bisector. y is a function of x: $y = R - r_p$ when $x = 0$ and $y = 0$ when $x = R - r_p$. Pythagoras's theorem gives the relationship $y^2 = (R - r_p)^2 - x^2$. The average fall height for any particle, μ_h,

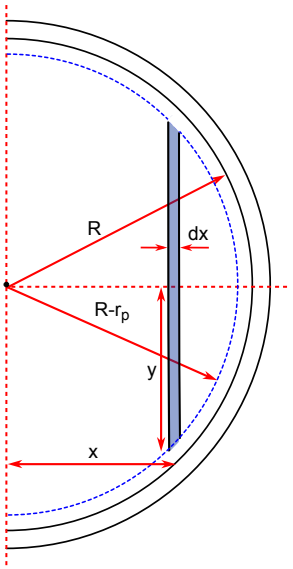

Figure G.5: *Geometry for the integral used to quantify the mean fall height of a particle under gravity,* μ_h

was found as Eq. 6.34, noting that the area of the strip is $2y\,dx$:

$$\begin{aligned}
\mu_h &= \frac{2}{\pi(R-r_p)^2}\int_{x=0}^{x=R-r_p} y\cdot 2y\,dx \\
&= \frac{4}{\pi(R-r_p)^2}\int_{x=0}^{x=R-r_p} \left((R-r_p)^2 - x^2\right)dx \\
&= \frac{4}{\pi(R-r_p)^2}\left[(R-r_p)^2 x - \frac{x^3}{3}\right]_0^{R-r_p} \\
&= \frac{4}{\pi(R-r_p)^2}\left(\frac{2(R-r_p)^3}{3}\right) \\
&= \frac{8(R-r_p)}{3\pi}
\end{aligned} \tag{6.34}$$

For a particle falling under gravity, its vertical velocity is given by Eq. 6.32 for a suitable range of Reynolds numbers. Note that the particle has zero initial velocity, i.e., falls from rest.

$$u_v = u_t \tanh\left(\frac{g\,t}{u_t}\right) \tag{6.32}$$

$$\frac{dy}{dt} = u_t \tanh\left(\frac{g\,t}{u_t}\right) \tag{G.19}$$

This first-order differential equation was solved to yield Eq. G.20, where H represents the fall height corresponding to a fall time of t.

$$H = \frac{{u_t}^2}{g}\ln\left(\cosh\left(\frac{g\,t}{u_t}\right)\right) \tag{G.20}$$

Rearranging:

$$t = \frac{u_t}{g}\operatorname{arccosh}\left(e^{\frac{gH}{{u_t}^2}}\right) \tag{G.21}$$

If any vertical strip is selected, the mean velocity of a particle in that strip is **not** $\frac{y}{t(y)}$ since there is a non-linear relationship between u_v and H. Hence, the mean velocity of a particle was found as Eq. G.22, noting that mean velocity was calculated by dividing the total fall height by the fall time.

$$\frac{1}{2y}\int_{H=0}^{H=2y}\frac{H}{t}\,dH=\frac{1}{2y}\int_{H=0}^{H=2y}\frac{gH}{u_t\,\text{arccosh}\left(e^{\frac{gH}{u_t{}^2}}\right)}\,dH \tag{G.22}$$

These were summed by integration for all strips of thickness dx, noting that $y=\sqrt{(R-r_p)^2-x^2}$ and again the area of each strip is $2y\,dx$:

$$u_\phi=\frac{2}{\pi(R-r_p)^2}\int_{x=0}^{x=R-r_p}\frac{1}{\cancel{2y}}\int_{H=0}^{H=2y}\frac{gH}{u_t\,\text{arccosh}\left(e^{\frac{gH}{u_t{}^2}}\right)}\,dH\cdot\cancel{2y}\,dx \tag{G.23}$$

$$u_\phi=\frac{2}{\pi(R-r_p)^2}\int_{x=0}^{x=R-r_p}\int_{H=0}^{H=2\sqrt{(R-r_p)^2-x^2}}\frac{gH}{u_t\,\text{arccosh}\left(e^{\frac{gH}{u_t{}^2}}\right)}\,dH\,dx \tag{6.35}$$

Eq. 6.35 required numerical solution.

G.9 Probability Density Function of Impact Angle

The cross-sectional area of the pipe of inner radius R within which the centrepoint of any particle of radius r_p may be located is $\pi(R-r_p)^2$. The cross-section was divided into horizontal strips of length $2L$ and width dy, as shown in Figure G.6. The area of each such strip is $2L\,dy$. Pythagoras's theorem was applied to relate L to y (the vertical displacement from the centrepoint of the cross-section):

$$L=\sqrt{(R-r_p)^2-y^2} \tag{G.24}$$

The proportion of the particles in any horizontal strip at a distance y from the centrepoint of the pipeline, and hence the proportion of the particles subjected to the commensurate impact angle, θ, is given by Eq. G.25:

$$\text{Proportion of particles in strip}=\frac{2\sqrt{(R-r_p)^2-y^2}\,dy}{\pi(R-r_p)^2} \tag{G.25}$$

A relationship was found between θ and y by reference to Figure 6.7:

$$\theta(y)=\arccos\left[\frac{1-\frac{y}{R_b}}{1+\frac{R-r_p}{R_b}}\right] \tag{6.42}$$

This equation was rearranged to find y explicitly and differentiated to obtain dy:

$$y=R_b-(R_b+R-r_p)\cos\theta \tag{6.42}$$

$$dy=(R_b+R-r_p)\sin\theta\,d\theta \tag{G.26}$$

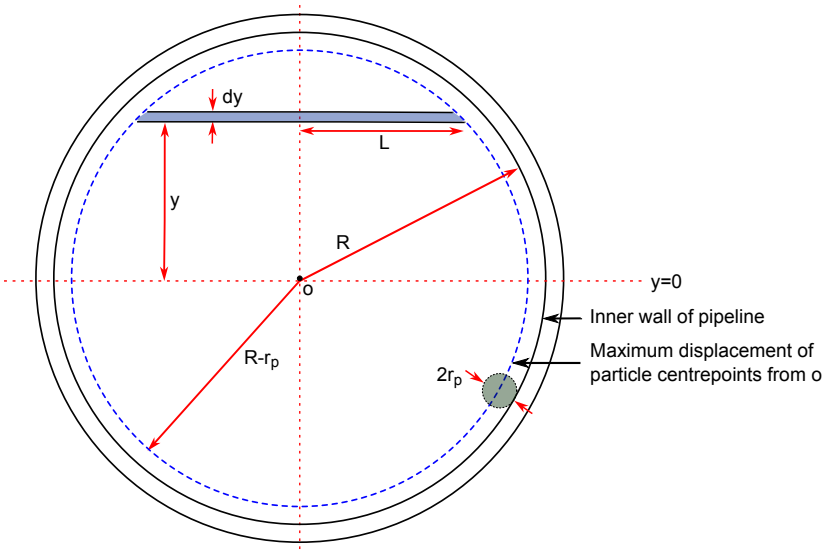

Figure G.6: *Cross-section through the pipe bend showing the geometry used to derive Eq. 6.45 for $P(\theta)$*

Thus, Eq. G.25 could be rewritten as Eq. G.27:

$$\begin{aligned}\text{Proportion} &= \frac{2\sqrt{(R-r_p)^2-y^2}}{\pi(R-r_p)^2}(R_b+R-r_p)\sin\theta\, d\theta \\ &= \frac{2\sin\theta\, d\theta}{\pi(R-r_p)^2}\sqrt{(R-r_p-y)(R-r_p+y)}(R_b+R-r_p)\end{aligned}$$

Substituting y with $R_b-(R_b+R-r_p)\cos\theta$:

$$\text{Proportion} = \frac{2\sin\theta\, d\theta}{\pi(R-r_p)^2}\sqrt{(R-r_p-R_b+(R_b+R-r_p)\cos\theta)(1-\cos\theta)}(R_b+R-r_p)^{\frac{3}{2}} \tag{G.27}$$

Finally, the PDF was found as Eq. 6.45:

$$P(\theta) = \frac{2\sin\theta}{\pi(R-r_p)^2}\sqrt{\left(R-r_p-R_b+(R_b+R-r_p)\cos\theta\right)(1-\cos\theta)}(R_b+R-r_p)^{\frac{3}{2}} \tag{6.45}$$

G.10 Derivations for Kelvin-Voigt Model

The governing second-order differential equation for the Kelvin-Voigt model is Eq. 6.48:

$$mx''(t)+cx'(t)+kx(t)=0 \tag{6.48}$$

This could be rewritten as Eq. G.28:

$$x''(t)+2\zeta\omega_n x'(t)+\omega_n^2 x(t)=0 \tag{G.28}$$

where:

$$\omega_n = \sqrt{\frac{k}{m}} \tag{G.29}$$

$$\zeta = \frac{c}{2m\omega_n} = \frac{c}{2\sqrt{mk}} \tag{G.30}$$

Impacts of particles with the bend are always underdamped ($\zeta < 1$); thus, the solutions for velocity and deflection are given by Eq[s]. G.31 and 6.49, respectively.

$$x'(t) = e^{-\zeta\omega_n t}\left[\frac{-\zeta\omega_n u_n}{\omega_d}\sin(\omega_d t) + u_n\cos(\omega_d t)\right] \tag{G.31}$$

$$x(t) = \frac{u_n}{\omega_d}e^{-\zeta\omega_n t}\sin(\omega_d t) \tag{6.49}$$

In these equations, $u_n = x'(0)$ and ω_d is defined by Eq. G.32.

$$\omega_d = \omega_n\sqrt{1-\zeta^2} \tag{G.32}$$

It was necessary to derive suitable expressions for k and c. It is known that the damping coefficient, c, is related to the coefficient of restitution, ε, which is in turn a function of the material parameters, the particle mass and radius, and the impact velocity (Schwager and Pöschel, 2007). A relationship between the coefficient of restitution of the impacting bodies and the damping coefficient could be found readily for an underdamped system.

Consider a particle which is initially at its equilibrium position, $x(t) = 0$. It is projected in the positive x-direction, towards the wall of the pipeline. A maximum displacement from the equilibrium position is reached, which corresponds to the point of maximum compression of the particle or spring, after which motion commences in the negative x-direction. The particle is unstressed (spring at its natural length) again when the equilibrium position is reached. The contact time between the particle and the wall of the pipeline, t_c, could be found as the difference between the two times when $x(t) = 0$:

$$x(t_c) = \frac{u_n}{\omega_d}e^{-\zeta\omega_n t_c}\sin(\omega_d t_c) = 0$$

$$\sin(\omega_d t_c) = 0$$

$$t_c = 0 \text{ (trivial) or } \frac{\pi}{\omega_d}$$

By subsection, Eq. G.33 was obtained:

$$t_c = \frac{\pi}{\omega_d} = \frac{\pi}{\omega_n\sqrt{1-\zeta^2}} = \frac{\pi}{\sqrt{\frac{k}{m}}\sqrt{1-\left(\frac{c}{2\sqrt{mk}}\right)^2}} = \frac{2\pi m}{\sqrt{4mk-c^2}} \tag{G.33}$$

The coefficient of restitution is defined as the magnitude of the normal velocity after impact divided by the normal velocity before impact. The latter is u_n, whereas the normal velocity after impact was found by substituting t_c from Eq. G.33 into Eq. G.31:

$$x'(t_c) = e^{-\zeta\omega_n\frac{\pi}{\omega_d}}\left[\frac{-\zeta\omega_n u_n}{\omega_d}\sin\pi + u_n\cos\pi\right] = -u_n e^{-\zeta\omega_n\frac{\pi}{\omega_d}}$$

Thus, the coefficient of restitution may be found from Eq. G.34:

$$\varepsilon = \left| \frac{-u_n e^{-\zeta\omega_n \frac{\pi}{\omega_d}}}{u_n} \right| = e^{-\zeta\omega_n \frac{\pi}{\omega_d}} \tag{G.34}$$

ζ, ω_n and ω_d were all substituted into Eq. G.34 to obtain an equivalent expression which is more commonly seen in the literature (e.g., Marhefka and Orin, 1996):

$$\varepsilon = e^{-\frac{c\pi}{\sqrt{4mk-c^2}}} \tag{G.35}$$

Note that the denominator of the exponential quotient in Eq. G.35 is identical to the denominator in Eq. G.33. Eq. G.33 was rearranged and substituted into Eq. G.35 to yield an explicit equation for c in terms of m, ε and t_c only:

$$\sqrt{4mk-c^2} = \frac{2\pi m}{t_c} \tag{G.33}$$

$$\varepsilon = e^{-\frac{c\pi}{\sqrt{4mk-c^2}}} = e^{-\frac{ct_c}{2m}}$$

$$c = -\frac{2m\ln\varepsilon}{t_c} \tag{6.51}$$

Eq. 6.51 was, in turn, substituted into Eq. G.33 to obtain a similar equation for k in terms of m, ε and t_c only:

$$4mk - c^2 = \frac{4\pi^2 m^2}{t_c^2}$$

$$4mk = \frac{4\pi^2 m^2}{t_c^2} + \frac{4m^2 \ln^2\varepsilon}{t_c^2}$$

$$k = \frac{m}{t_c^2}(\ln^2\varepsilon + \pi^2) \tag{6.52}$$

The force on the particle according to the Kelvin-Voigt model is given by Eq. 6.50:

$$F(t) = m u_n e^{-\zeta\omega_n t}\left[\left(\frac{\zeta^2\omega_n^2}{\omega_d} - \omega_d\right)\sin(\omega_d t) - 2\zeta\omega_n\cos(\omega_d t)\right] \tag{6.50}$$

The first derivative of this function was found as Eq. G.36 using the product rule:

$$F'(t) = -\zeta m u_n \omega_n e^{-\zeta\omega_n t}\left[\left(\frac{\zeta^2\omega_n^2}{\omega_d} - \omega_d\right)\sin(\omega_d t) - 2\zeta\omega_n\cos(\omega_d t)\right]$$
$$+ m u_n e^{-\zeta\omega_n t}\left((\zeta^2\omega_n^2 - \omega_d^2)\cos(\omega_d t) + 2\zeta\omega_n\omega_d\sin(\omega_d t)\right) \tag{G.36}$$

As $c \to 0$, $\zeta \to 0$ and $\omega_d \to \omega_n$. Thus:

$$F'(t) \to -m u_n \omega_n^2 \cos(\omega_n t) = -\frac{\cancel{m} u_n k}{\cancel{m}}\cos(\omega_n t) = -u_n k\cos(\omega_n t) \tag{G.37}$$

Eq. G.37 is equal to 0, indicating a point of maximum or minimum of $F(t)$, when $\omega_n t = \frac{\pi}{2}$ or $\frac{3\pi}{2}$. $F''(t) = u_n\omega_n k\sin(\omega_n t)$ where $c = 0$; thus, a local maximum exists ($F''(t) < 0$) where $\omega_n t = \frac{3\pi}{2}$. Finally, the maximum force is given by Eq. G.38, again noting that this is for the special case of $c \to 0$:

$$F(t)\big|_{\max} = -m u_n \omega_n \sin(\tfrac{3\pi}{2}) = m u_n \omega_n = \sqrt{km}\, u_n \tag{G.38}$$